The Influence of Morphology on Polyurethane Foam Heat Transfer

by

Jeffrey Stewart

B.S.E.Sci., Penn State University (1992)

Submitted to the Department of Mechanical Engineering
in partial fulfillment of the requirements for the degree of

Master of Science in Mechanical Engineering

at the

MASSACHUSETTS INSTITUTE OF TECHNOLOGY

January, 1994

Author .....
Department of Mechanical Engineering
January 14, 1994

Certified by .....
Professor Leon R. Glicksman
Department of Mechanical Engineering
Thesis Supervisor

Accepted by .....
Professor Anin Sonin
Chairman, Graduate Thesis Committee
Department of Mechanical Engineering

The Influence of Morphology on Polyurethane Foam Heat Transfer

by

Jeffrey Stewart

Submitted to the Department of Mechanical Engineering on
January 14, 1994, in partial fulfillment of the requirements for the
degree of Master of Science in Mechanical Engineering

Abstract

To better understand the impact of foam structure on heat transfer, the geometry of polyurethane foam is analyzed. Specifically, means to measure and characterize parameters that affect solid and radiative conductivity are developed. The predicted thermal conductivity based on measured morphology characteristics are compared to measured thermal conductivities for a series of foams. In conjunction with these comparisons, parameters of solid polyurethane that affect radiative conductivity are analyzed.

A two-dimensional solid conductivity program is presented to calculate the solid conductivity given Scanning Electron Microscope or confocal microscope images of the foam. The increase in solid conductivity due to anisotropy is apparent in results from this program.

From measured intercept area distributions, the actual cell size distribution is calculated. For each of the small celled foams, the distribution is narrow, close to the mean intercept length. From numerical analysis of extreme cell segregation, less than 11% error in the extinction coefficient calculated from the mean cell diameter is expected due to cell size distribution.

A means to measure the fraction of solid in the strut from strut cross sectional areas is derived. For the small-celled foams analyzed, the fraction of solid in the strut decreases from0.67 to 0.34 as mean cell diameter decreases from 0.363mm to 0.109mm. Smaller celled foams blown with HCFC-141b and perfluoropentane show a redistribution of polymer from the struts to the cell walls as cell size decreases.

Predictions of total conductivity from morphology measurements and transmission measurements agree within 11% to measured total conductivities for six small-celled foams. Redistribution of polymer from the struts to the cell walls and large blowing agent conductivities account for the lack of thermal improvement with smaller cell sizes even though the radiative conductivity decreases from 1.96mW/mK to 1.12mW/mK.

Thesis Supervisor: Leon R. Glicksman
Title: Professor, Mechanical Engineering

Acknowledgements

This research could not have been possible without funding, technical support, and guidance from Dr Cunningham and associates at ICI Polyurethanes. Their constant involvement helped make many of the results possible.

Many people provided technical information and help during the course of this research and so cannot all be noted here. But the help of Bill Westphal, Wendel Rhine, Steve Rudolph, Walter Eastes at Owens Corning, Mark at the Whitehead Institute, and all in the Heat Transfer Lab is greatly appreciated.

The support and love of my family also helped make this work successful.

Most importantly, I will long be indebted to Professor Glicksman, not only for the educational opportunities which he provided me, but for the concern, involvement, and guidance in every aspect of this research.

Table of Contents

List of Tables

List of Figures

Chapter 1

Introduction

1.1 Background

Closed cell polyurethane foam is used extensively in the appliance and roofing industry as a thermal insulant because of its low thermal conductivity compared to other conventional insulating systems. Thermal conductivity is a measure of the insulating ability of the material, with lower thermal conductivity indicating the better performing insulant. It is a ratio of the thermal flux across a material to the applied temperature gradient. The thermal conductivity of freshly made closed cell foam insulation is roughly half that of fibrous or cellular glass insulation [1].

The insulating ability of closed cell foams derives from the large fraction of trapped low-conductivity gas. That is, high molecular weight gases such as CFC-11 are trapped in pockets or cells as the foam is formed. The thermal conductivity of such gases is typically a third of the conductivity of air [1]. Then, since these gases comprise a large volume fraction of the foam, the conductivity of the foam can be as much as one-half the conductivity of low density fibrous insulation.

In the past the recommended trapped gas, or blowing agent, has been CFC-11. However, there is now great concern over the destructive influence that CFC-11 has on the Earth's ozone layer. In response, governments and industry have called for the use of alternative blowing agents that exhibit similar thermal properties as CFC-11 without the environmental impact. Unfortunately, CFC-11 has the lowest thermal conductivity of most known blowing agents. As a result, foams blown with alternative gases such as HCFC-141b, CO_2, or HCFC-123a will not exhibit the same insulating ability as CFC-11. The purpose of research that has been underway at MIT since 1982 is to consider other

modes of heat transfer in the closed cell foams and develop means to reduce these modes. Ideally, the loss in foam insulating ability due to alternative blowing agents can be offset by reducing other modes of heat transfer.

1.2 Literature Review and Objectives

There are three modes of heat transfer in closed cell polyurethane foams. One mode is conduction across the gases trapped in the foam cells. The second is conduction through the solid polymer surrounding the trapped gas, the cell walls and strut-like members that define the outline of the cells. These will be described in further detail in Chapter 2. There is also radiation across the foam. Gas conduction comprises roughly 40% to 50% of the total with radiation and solid conduction contributing to the balance in roughly equal proportions.

In the past, models of heat transfer based on simplified geometries were developed. However, these neglected radiation and generally underestimated the total heat transfer because of it. Some of the earlier inclusions of radiation in the heat transfer model by Doherty et al. [2] and by Skochdopole [3] modeled radiation by treating cell walls as series of opaque plates with separation distances of the order of the cell diameter. Treating cell walls as opaque plates again seriously underpredicted the total heat transfer. The cell walls are in actuality highly transparent as was shown by Glicksman et al. [4] who measured the transmissivity of foam cell walls 1.5μm thick, still three times thicker than most conventional cell walls. As can be seen in figure 1.1 even this section is highly transparent. Williams and Aldo [5] included the effects of transparent cell walls, but ignored the effects of the struts, the thick linear elements resulting from the intersection of three cell walls. The struts, as shown later in work by Glicksman and Torpey [6] dominate

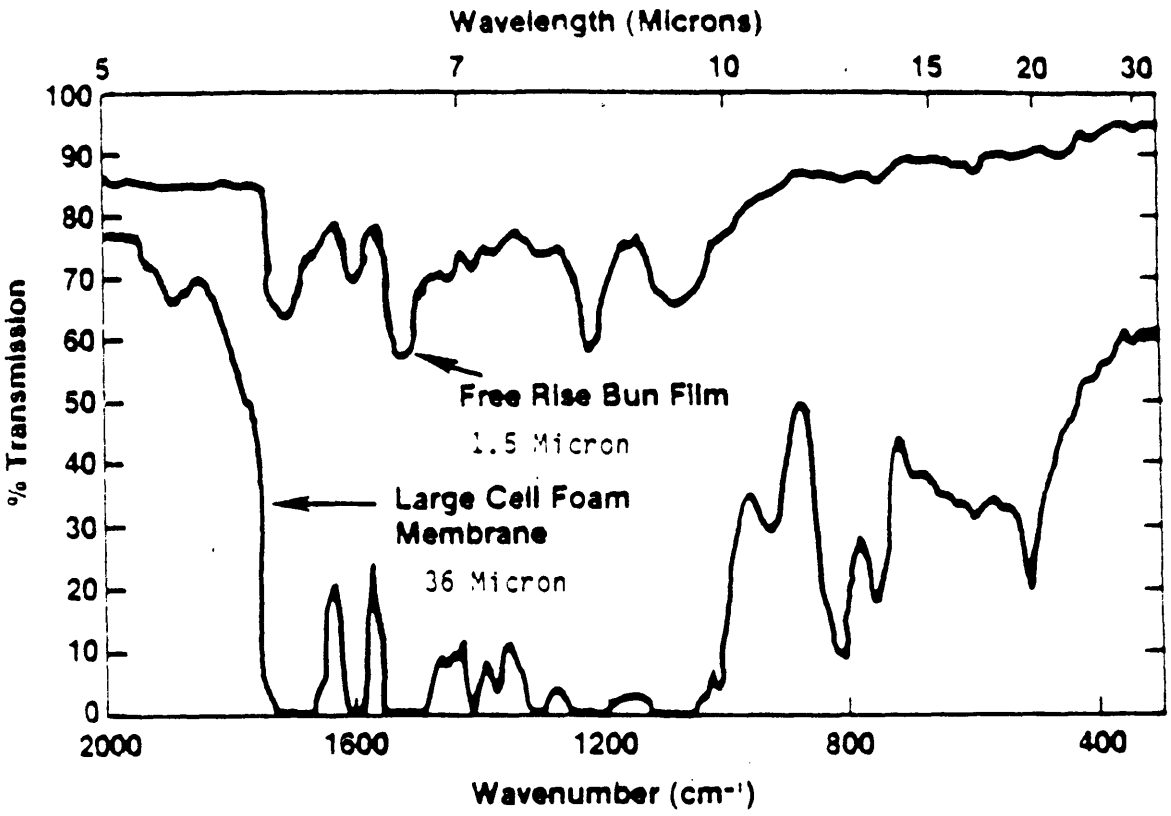

Figure 1.1: *Transmission of Radiation Through Polyurethane Cell Wall 1.5μm Thick*

the radiative process accounting for most of the absorption. Glicksman and Torpey [6] modeled the total heat transfer in foams including the effects of transparent cell walls and blackbody struts on radiation. Glicksman et al. extended this relation [7] to account for the effects of cell wall absorption.

From the work of Glicksman et al [7], it was proposed that a reduction in foam cell size, the size of bubbles encompassing the trapped gas, reduces the radiative conductivity as well as the overall conductivity. Unfortunately, the overall conductivity of some small celled foams produced by ICI Polyurethanes have not shown the expected decrease in overall conductivity. The purpose of this research therefore was to further examine the model as well as to characterize the small celled foams measured and account for the lack of thermal improvement with reduced cell size. The objectives of this work are threefold. The first goal is to accurately characterize the microscopic geometry of the foam, such parameters as cell size, cell size distribution, the distribution of solid in the cell borders, and cell anisotropy. The second goal is to determine how changes in these geometric parameters, or in the morphology, affect the conductivity components in the foam. Specifically, is the overall conductivity of the foam reduced by some changes in the morphology? The final purpose is to further explore methods that characterize the solid and radiative conductivity components. Since most measurement techniques either interfere with the conductivity environment or are incapable of extracting individual components, calculation of solid or radiative conductivity now requires combinations of optical and thermal measurements and use of models to characterize the solid or radiative conductivity. There is a need therefore for a technique to directly describe either radiative or solid conductivity.

Chapter 2

Heat Transfer Model

2.1 Conductivity Components

There are three mechanisms of heat transfer through polyurethane foam: conduction through the gases trapped in the foam cells, conduction across the solid polymer enclosing the cells, and radiation across the foam. Gas conductivity is the largest contribution being usually 40-50% of the total for foams filled with low conductivity gases. Natural convection does not play any significant role until the foam cell sizes reach about 4 or 5mm, roughly ten times larger than the typical foam cell size [1].

Except in cases where low emissivity boundaries are used, past work by Glicksman et al. [8] have shown that ignoring coupling between the heat transfer components provides an accurate description of heat transfer. That is, each conductivity component can be considered separately, and simply added to account for the total conductivity across the foam.

$$q_{total} = -k_{foam}\frac{dT}{dx} \tag{2.1}$$

$$k_{foam} = k_{solid} + k_{gas} + k_{radiation} \tag{2.2}$$

It will be shown later that the radiative process for optically thick media like polyurethane foam will act as a diffusion process and there is an effective expression for the radiative conductivity ($k_{radiation}$).

2.2 Foam Morphology

The foam structure, or morphology, has a great impact on the heat transfer properties. Relationships between thermal conductivity and some of the most important characteristics, such as the void fraction, the mean cell diameter, the anisotropy of the cells, and the fraction of solid in the strut, have been formulated in past work at MIT and are presently being examined.

The void fraction, or porosity, is the fraction of total foam volume occupied by trapped gas. In terms of densities of the solid polymer (ρ_s), of the ambient air (ρ_a), of the trapped gas (ρ_g), and of the foam (ρ_f), the void fraction is

$$\delta = \frac{\rho_s - \rho_a - \rho_f}{\rho_a - \rho_g} \tag{2.3}$$

For low density foams, expression 2.2.1 can be simplified

$$\delta \approx 1 - \frac{\rho_f}{\rho_s} \tag{2.4}$$

The shape and size of the cells defining the foam are of great importance in determining the conductivity components. Some emphasis has been placed on defining the shape of the cells [9,10]. Rather than being spherical in shape, polyurethane cells are better described by regular polyhedra. Reitz [11] has shown that the shape of

polyurethane foam cells can be accurately defined by a pentagonal dodecahedron which is shown in figure 2.1.

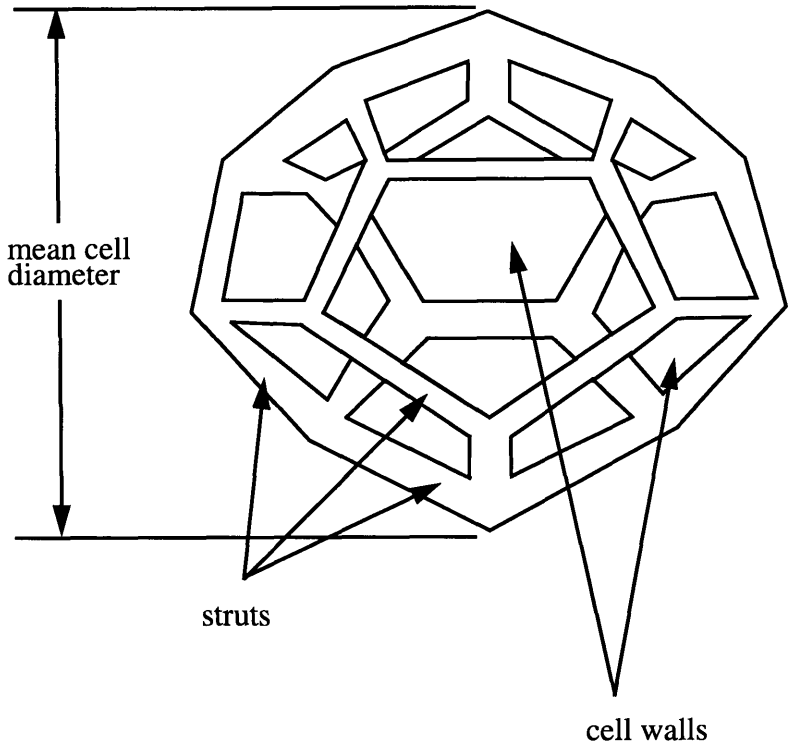

Figure 2.1: *Pentagonal Dodecahedron Foam Cell Shape*

Several measured and statistical quantities could be termed the cell diameter. However, the cell diameter used should be one that relates the physical properties of the foam to the heat transfer process. As will be shown in Chapter 4, for radiative conductivity this physical property is the surface area to volume ratio of the foam. As described in *Quantitative Stereology* [12], the cell diameter is a quantity related to the surface-to-volume ratio

$$d = \frac{3.46}{S_V} \tag{2.5}$$

This mean cell diameter is displayed in figure 2.1. It relates the true number of particles per unit volume (N_V) to the number of particles per unit area (N_A) when the foam is intersected by a section plane[12].

$$N_A = N_V d \tag{2.6}$$

Underwood also calls it the mean projected height for a system of particles [12]. This terminology stems from the derivation of equation 2.6 which is given in Appendix A. It relates spatial quantities and planar quantities when a system of cells are intersected by random test planes. For spherical particles, it is the mean sphere diameter.

Another important parameter in describing the heat transfer process is the distribution of the solid polymer through the foam. As represented in figure 2.1, the solid surrounding the cell can be thought of as divided between two regions. The solid region that separates two cells, the cell walls, is in many cases approximately a constant thickness region on the order of 1μm. The second region is where three cells intersect. There is a thickening of the walls in this region resulting in much thicker rodlike regions called struts. These two regions influence both conduction through the solid polymer and radiation in different ways. Therefore it is worthwhile to describe the fraction of material in the struts and the fraction in the cell walls. For typical CFC-11 blown foams of diameter greater than 0.3mm, the strut mass fraction (f_s) is usually on the order of f_s=0.8. For phenolics and HCFC blown polyisocyanerate foams, Page [13] found the strut mass fraction to be closer to f_s=0.6.

A final parameter that has an important influence at least on the conduction through the solid polymer is the degree of anisotropy of the foam cells. For most polyurethane foams, there is a preferred rise direction when the foam is blown. This results in cells with an elongated axis with the other axes being isotropic as in figure 2.2. This anisotropy can be included in the heat transfer model with the term relating the major to minor axes, *a/b*.

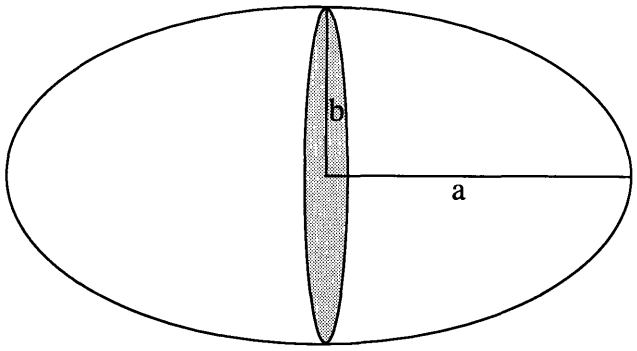

Figure 2.2: *Major and Minor Axes Used to Describe Cell Elongation*

2.3 Gas Conductivity

Of the three conductivity components, the gas conductivity is the largest component. It is an intricate quantity in that not only do the physical properties of the component gases present have to be accurately considered, but the effects of diffusion of the blowing agent out of the cells and diffusion of air into the cells have to be considered to determine the gas concentration distribution. Since the emphasis of this work is the solid conductivity and radiation properties of small-celled foams, the Lindsay Bromley expression was used to calculate the gas conductivity as a function of the local gas concentration. It is an

expression that has been found to be accurate to within 5% of experimental values for gas mixtures containing CFC [1]. Therefore, the gas conductivity is described by

$$k_{gas} = \delta k_{mix} \tag{2.7}$$

where

$$k_{mix} = \sum_{i=1}^{N} \left[\frac{y_i k_{gi}}{\sum_{j=1}^{N} y_j A_{ij}} \right] \tag{2.8}$$

$$A_{ij} = \frac{1}{4} \left\{ 1 + \left[1 + \frac{\mu_i}{\mu_j} \left(\frac{M_j}{M_i} \right)^{3/4} \frac{(1 + \frac{S_{ij}}{T})}{(1 + \frac{S_j}{T})} \right]^{1/2} \right\}^2 \frac{(1 + \frac{S_{ij}}{T})}{(1 + \frac{S_i}{T})} \tag{2.9}$$

$$S_{ij} = \sqrt{(1.5T_{bi})\ (1.5T_{bj})} \tag{2.10}$$

y_i is the molar fraction of the i^{th} component,

N is the number of components,

k_{gi} is the thermal conductivity of the pure i^{th} component,

μ_i is the viscosity of the pure i^{th} component,

M_i is the molecular weight of the pure i^{th} component,

T is the absolute temperature, and

T_{bi} is the absolute boiling temperature of the ith component at 1 atmosphere pressure.

2.4 Solid Conductivity

Solid conductivity for typical polyurethane foams accounts for roughly 25% of the total heat transfer. Therefore, considerable effort in the past has been placed on relating this conductivity component to the foam morphology [14,15,16]. Modeling struts as rods randomly oriented in three dimensions, Schuetz [14] determined the solid conductivity due to struts in an isotropic foam to be related to the morphology as

$$k_{s-struts} = \frac{1}{3} k_p f_s (1-\delta) \tag{2.11}$$

Similarly considering random plates in three dimensions, Schuetz determined the solid conductivity due to the cell walls in an isotropic foam to be

$$k_{s-cw} = \frac{2}{3} k_p (1-f_s)\ (1-\delta) \tag{2.12}$$

where k_p is the solid polymer conductivity (k_p=0.263 W/mK), f_s is the mass fraction of solid material in the struts, and δ is the void fraction of the foam. These expressions are upper limits for the conduction heat transfer; lower limit expressions for the conductivity differ by less than 20% percent [1]. The solid conductivity model was then modified to account for anisotropy [1]

$$k_s = \frac{(1-\delta)}{3} k_p \left[2(1-f_s) \left(\frac{a}{b}\right)^{1/4} + f_s \sqrt{\frac{a}{b}} \right] \tag{2.13}$$

2.5 Radiative Conductivity

In addition to conduction through the solid and trapped gas, there exists radiative heat transfer through polyurethane foam. The situation is simplified in that foams are highly absorbing material. It will be shown that this will reduce the radiative process to a diffusion one, yielding an effective radiative conductivity similar to solid and gas conductivity.

Consider radiation incident upon a thin slice of polyurethane foam of thickness dx as in figure 2.3. The decrease in spectral radiant intensity passing through this thin slice is related to a parameter known as the extinction coefficient (K_λ). The extinction coefficient provides a measure of the amount of attenuation of radiant energy within a material. The attenuation of incident radiant energy is

$$di_\lambda = -K_\lambda i_\lambda dx \tag{2.14}$$

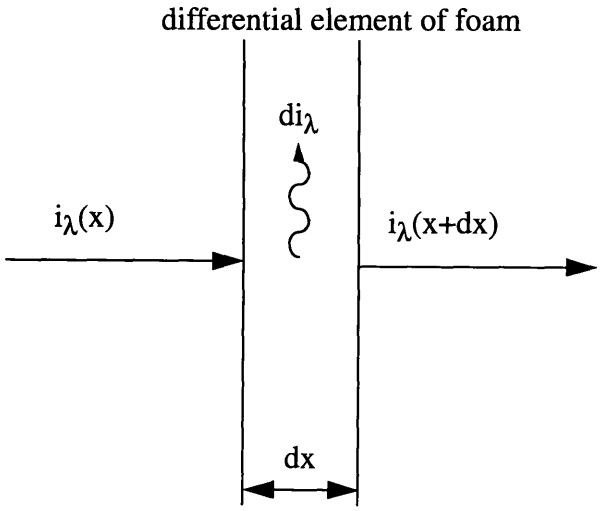

Figure 2.3: *Radiant Energy Incident Upon Differential Thickness of Foam*

As long as the medium is homogenous so that K_λ does not vary with position and the medium is cold so that it emits negligible radiation, this expression can be integrated to yield

$$\frac{i_\lambda(L)}{i_{\lambda o}} = e^{-K_\lambda L} \tag{2.15}$$

for a thickness L of foam. Here, $i_{\lambda 0}$ is the intensity of radiation incident on the foam sample. The ratio of intensity to incident intensity is also the transmissivity, or τ_1, of a specimen of foam of thickness L.

The extinction coefficient can also physically understood as the reciprocal of the mean free path length of a photon of energy, or the average distance a photon of energy travels in the material before being absorbed, l_{mf}. The extinction coefficient can also be understood as the sum of coefficients that express distinct modes of attenuation. These are the absorption coefficient a_λ and the scattering coefficient σ_λ. The absorption coefficient describes attenuation of energy due to the material absorbing the energy. The scattering coefficient accounts for energy that is redirected or scattered out of the path of radiation. So the extinction coefficient can also be understood as

$$K_\lambda = a_\lambda + \sigma_\lambda \tag{2.16}$$

The nondimensional optical thickness of a material τ_2 is the thickness of the material times the extinction coefficient

$$\tau_2 = KL \tag{2.17}$$

The optical thickness can be viewed as the ratio of material thickness to photon mean free path. ($\tau_2=L/l_{mf}$). For an optically thick material ($\tau_2>>1$), the diffusion process described below is applicable.

2.6 Radiative Equation of Transfer

In an optically thick medium, radiant energy emitted within an area is reabsorbed and reemitted by the surroundings. In this way, although direct radiation incident upon a sample of foam is absorbed within the first millimeter of foam, the radiant energy propagates through the foam in infinitesimal increments of absorption and reemission. One only needs to look at a differential element to describe the radiative process, reducing the integro-differential equations of radiation to differential ones and the properties affecting the radiative process to local ones.

With true optically thick material with negligible phonon conduction and steady state one-dimensional radiation flux across it, a linear T^4 profile across the foam results as in figure 2.4. Similarly, since i_b is proportional to T^4, a linear profile in the black body intensity of emitted radiation results. That is

$$i_b = c_o x \tag{2.18}$$

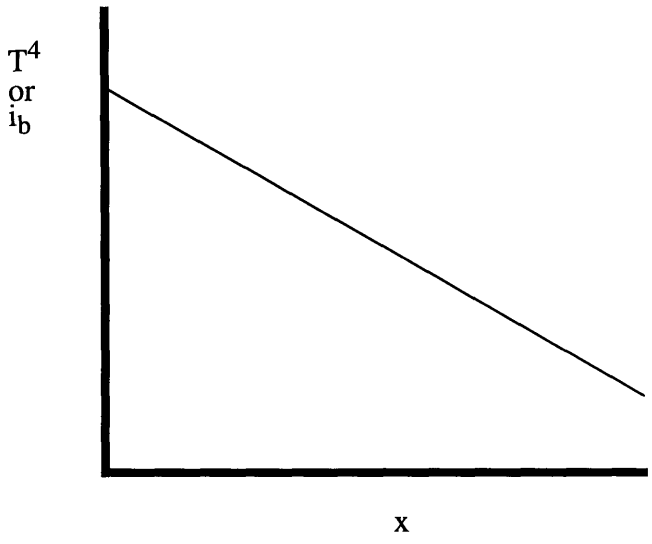

Figure 2.4: *T^4 (or i_b) Profile in Optically Thick Material*

Now at any point x,

$$\frac{di}{dx} = -Ki + Ki_b \tag{2.19}$$

where i is the intensity at x, K is the extinction coefficient of the foam, and i_b is the blackbody intensity at x. Combining equations 2.18 and 2.19 and integrating,

$$i(x) = i_b(x - \frac{1}{K}) = i_b(x - l_{mf}) \tag{2.20}$$

Along any path, the intensity at a point x is equal to the blackbody intensity at one mean free path upstream of x (see figure 2.5).

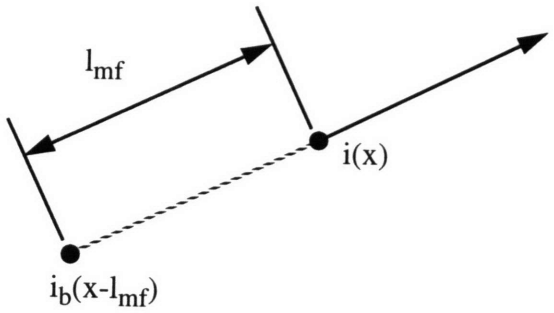

Figure 2.5: *Intensity at Location x in Absorbing Media (Foam)*

Consider the flux crossing a plane A as shown in figure 2.6. The net flux crossing this plane is

$$q_R = q_R(+x) - q_R(-x) \tag{2.21}$$

where

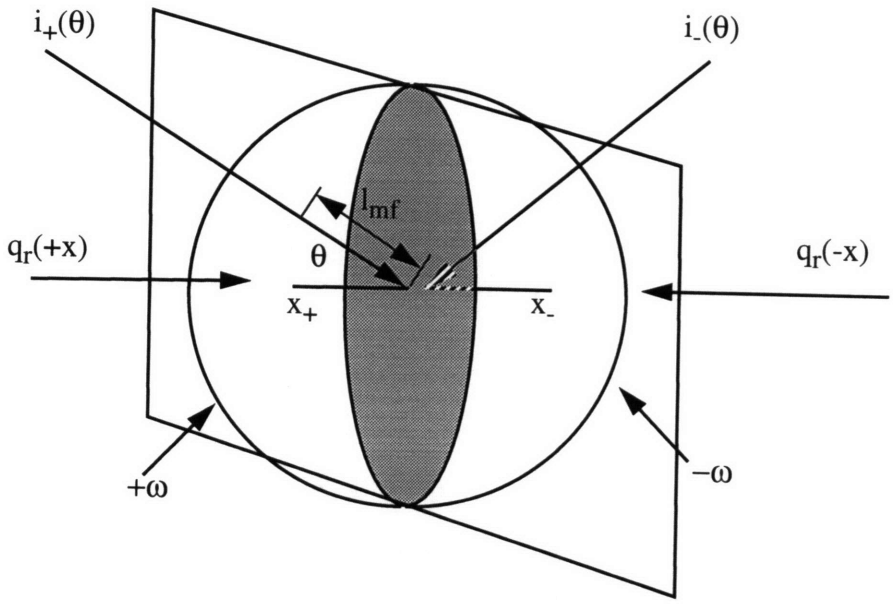

Figure 2.6: *Radiant Flux at Any Plane x in Optically Thick Medium*

$$q_R(+x) = \int_{+\omega} i_+(\theta)\cos(\theta)\,d\omega \tag{2.22}$$

$$q_R(-x) = \int_{-\omega} i_-(\theta)\cos(\theta)\,d\omega \tag{2.23}$$

Equation 2.21 then becomes

$$q_R = \int_{+\omega} i_+(\theta)\cos(\theta)\,d\omega - \int_{-\omega} i_-(\theta)\cos(\theta)\,d\omega \tag{2.24}$$

From equation 2.20, $i_-(\theta)$ and $i_+(\theta)$ can be written

$$i_+(\theta) = i_b(x - l_{mf}) \tag{2.25}$$

$$i_-(\theta) = i_b(x + l_{mf}) \tag{2.26}$$

respectively. Expanding $i_b(x)$ using Taylor series expansion limiting this to the first three terms,

$$i_b(x) = i_b(0) + x\left(\frac{di_b}{dx}\right)_{x=0} + \frac{x^2}{2}\left(\frac{d^2 i_b}{dx^2}\right)_{x=0} \tag{2.27}$$

and realizing that x_+ and x_- are respectively

$$x_+ = -\frac{\cos(\theta)}{K} \tag{2.28}$$

$$x_{-} = \frac{\cos(\theta)}{K} \tag{2.29}$$

Then $i_{+}(\theta)$ and $i_{-}(\theta)$ are

$$i_{+}(\theta) = i_b(0) - \frac{\cos(\theta)}{K}\left(\frac{di_b}{dx}\right)_{x=0} + \frac{1}{2}\left(\frac{\cos(\theta)}{K}\right)^2\left(\frac{d^2 i_b}{dx^2}\right)_{x=0} \tag{2.30}$$

$$i_{-}(\theta) = i_b(0) + \frac{\cos(\theta)}{K}\left(\frac{di_b}{dx}\right)_{x=0} + \frac{1}{2}\left(\frac{\cos(\theta)}{K}\right)^2\left(\frac{d^2 i_b}{dx^2}\right)_{x=0} \tag{2.31}$$

Substituting these expressions into equation 2.24, assuming K does not vary with θ, and integrating yields

$$q_R = 2\pi\left[\left\{-\frac{i_b(0)}{2} - \frac{1}{3K}\left(\frac{di_b}{dx}\right)_{x=0} - \frac{1}{8K}\left(\frac{d^2 i_b}{dx^2}\right)_{x=0}\right\} - \left\{-\frac{i_b(0)}{2} + \frac{1}{3K}\left(\frac{di_b}{dx}\right)_{x=0} - \frac{1}{8K}\left(\frac{d^2 i_b}{dx^2}\right)_{x=0}\right\}\right] \tag{2.32}$$

$$q_R = -\frac{4\pi}{3K_R}\frac{di_b}{dx} = -\frac{4}{3K_R}\frac{de_b}{dx} \tag{2.33}$$

$$q_R = -\frac{4}{3K_R}\frac{d(\sigma T^4)}{dx} \tag{2.34}$$

$$q_R = -\frac{16\sigma}{3K_R}T^3\frac{dT}{dx} \tag{2.35}$$

This is the Rosseland diffusion equation for isotropic media which holds for nongray media if K_R is defined as the Rosseland mean extinction coefficient or

$$\frac{1}{K_R} = \int_0^\infty \frac{1}{K_\lambda(\lambda)} \left(\frac{\partial e_{b\lambda}}{\partial e_b} \right) d\lambda \tag{2.36}$$

The Rosseland mean extinction coefficient weighs spectral attenuation by the amount of blackbody energy at that wavelength compared to the rest of the spectrum. This definition derives from

$$\frac{1}{K_R} \frac{de_b}{dx} = \int \frac{1}{K_\lambda} \frac{de_{b\lambda}}{dx} d\lambda \tag{2.37}$$

Using the chain rule defining $\frac{de_{b\lambda}}{dx} = \frac{de_{b\lambda}}{de_b} \frac{de_b}{dx}$, recognizing that de_b/dx is independent of wavelength and can be removed from both sides of the equation, the expression for the Rosseland mean extinction coefficient results. So an effective radiative conductivity term k_r can be defined

$$k_r = \frac{16\sigma}{3K_R} T^3 \tag{2.38}$$

and added to the solid and gas conductivity component terms to yield an effective thermal conductivity of optically thick polyurethane foams. For more explanation of radiative

heat transfer in absorbing/emitting/scattering media, the reader is referred to Thermal Radiation Heat Transfer[17].

2.7 Morphology Impact on Extinction Coefficient

To judge the impact of foam structure on radiative conductivity, consider first the impact of strut regions on radiative conductivity then the impact of the cell wall regions. The reader is referred to [1] and Torpey [16] for the original derivations.

For the struts, consider randomly oriented members with a cross section as in the SEM photograph in figure 2.7. Torpey [16] found the strut cross-sectional area to be roughly 2/3 the area of the enclosing triangle of side a shown in the picture, or $0.29a^2$. For such randomly oriented linear elements, the extinction coefficient can be expanded as,

$$K = CL_V Q \tag{2.39}$$

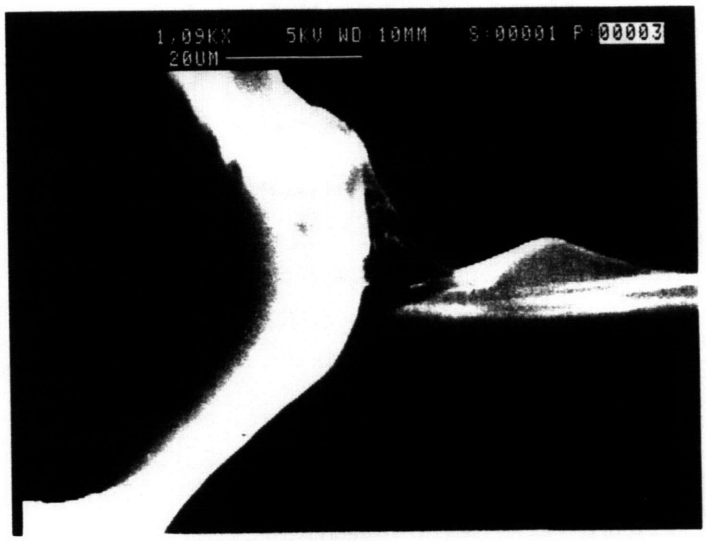

Figure 2.7: *SEM photograph of Strut Cross Section*

where C is the strut projected area per unit length, L_V is the strut length per unit volume, and Q is the efficiency factor. The efficiency factor is the ratio of the effective cross sectional area for extinction of radiation to the geometric cross sectional area. For larger celled foams, the efficiency factor has been found to be close to unity [16] as it would be for blackbody elements where the dimensions are much greater than the wavelength of energy (λ). It is a parameter that will be more closely examined in Appendix H for

smaller celled foams. With the strut axis normal to the direction of heat transfer propagation, the strut projected area per unit length is

$$C = \frac{3}{\pi}a = 0.955a \tag{2.40}$$

To express the length-to-volume ratio, a cell shape has to be assumed. For the pentagonal dodecahedron with each strut shared by three cells, L_V can be expressed as

$$L_V = \frac{8.62}{d^2} \tag{2.41}$$

where the cell diameter is related to the surface-to-volume ratio as described in equation 2.5.

To account for random orientations of struts, rather than all being aligned in the heat transfer direction, the projection of the length-to-volume ratio in the heat transfer direction is used, after averaging over all possible alignments one obtains,

$$L_m = \frac{\pi}{4}L_V \tag{2.42}$$

The strut mass from strut volume considerations can be related to the mass from overall density considerations or

$$0.29a^2 L_V \rho_s V_f = f_s \rho_f V_f \tag{2.43}$$

which can be rearranged to express the strut edge length a in terms of measurable properties of the foam

$$a = \sqrt{\frac{f_s \rho_f / \rho_s}{0.29 L_V}} \tag{2.44}$$

So combining expressions 2.40, 2.41, 2.42, and 2.44 into equation 2.39 yields the strut contribution to extinction coefficient as a function of foam geometry

$$K = \frac{4.10\sqrt{f_s \rho_f / \rho_s}}{d} Q \tag{2.45}$$

The cell wall contribution to the extinction coefficient can also be expressed in terms of the morphology of the foam and in terms of the extinction coefficient of the solid polyurethane polymer K_w. For a detailed description of the derivation of the impact of morphology on the cell wall extinction coefficient, see [18]. In the optically thin limit ($K_w t_{cw} << 1$ where t_{cw} is the cell wall thickness) neglecting reflections at the gas/cell wall interface, the homogeneous extinction coefficient is

$$K_H = \left[\frac{(1 - f_s)\, \rho_f}{\rho_s} \right] K_w \tag{2.46}$$

where the term in brackets is the ratio of volume occupied by the cell walls to the total foam volume. The term homogeneous extinction coefficient means the hypothetical extinciton coefficient of a homogeneous material occupying the same volume as the foam with the same attenuation as the collection of cell wall. In the optically thick limit ($K_w t_{cw} >> 1$), radiation originates from neighboring cells and the emissive power incident on a cell can be expanded using a Taylor series [1]. For isotropic cells ignoring reflection and scattering and assuming cells to be pentagonal dodecahedrons, the extinction coefficient can be expressed in terms of the geometry as

$$K = \frac{3.46}{d}\frac{1-e^{-2K_w t}}{1+e^{-2K_w t}} \tag{2.47}$$

where the cell wall thickness is

$$t = \frac{(1-f_s)\,\rho_f d}{3.46\rho_s} \tag{2.48}$$

As the optical thickness approaches the optically thin limit, equation 2.47 yields the same results as equation 2.46.

The extinction coefficient for foams with optically thin cell walls can therefore be expressed in terms of the morphology. The extinction coefficient is the sum of the extinction coefficient due to the struts plus the extinction coefficient due to the cell walls or

$$K = K_{struts} + K_{\text{cell}\,walls} \tag{2.49}$$

$$K = \frac{4.10\sqrt{f_s \rho_f / \rho_s}}{d} Q + \left[\frac{(1-f_s)\,\rho_f}{\rho_s}\right] K_w \tag{2.50}$$

Parameters such as cell size, the solid polymer extinction coefficient, and fraction of solid in the strut will be analyzed in greater depth in Chapter 4. Methods to measure these parameters will be explored and the impact of varying these on the foam conductivity will be shown as well as the results predicted by equations 2.36, 2.38, and 2.50.

Chapter 3

Solid Conductivity and Morphology Influence

3.1 Attempts to Model Solid Conductivity

Two methods to obtain the contribution of the solid conductivity were considered. The first consists of modeling the two-dimensional solid conductivity from actual foam geometries with a system of linear equations. The development, implementation, and results of this approach is described in the next few sections. The second method is based on measuring the electrical conductivity across the foam and relating this to the solid conductivity. This technique will be described in Sections 3.11 through 3.15.

3.2 Solid Conductivity Matrix Theory

If one were to cut a volume of foam with an imaginary section plane parallel to the heat transfer direction, a section plane would appear with solid borders connecting nodal intersections (see figure 3.1). These solid borders could be either cell walls or struts that are intersected by the test plane. The nodes are where cells intersect. For this matrix program, locations where borders intersect y=0 or y=Δy are also defined as nodes, boundary nodes. That is, as in figure 3.2, border *b* does not intersect another border at y=0 but instead extends below y=0. The boundary node *n* is defined at y=0 as shown in the figure. When boundary conditions are imposed, something will be said of the temperature at these border nodes which will allow one to solve for the solid conductivity. Of course when an actual intersection of borders occurs at y=0 or at y=Δy, this intersection will also be treated as a boundary node.

The resulting section gives an accurate picture of the foam morphology in two dimensions. On this section plane, the solid conductivity would follow the tortuous path of solid borders from the higher temperature boundary to the lower temperature boundary.

And although this is a two dimensional representation of the three dimensional picture, this should give a fair indication of solid conduction in the foam and of the influence of a preferred rise direction as long as the section is aligned with the temperature gradient.

3.3 Conductivity Matrix Equations

To solve for the full conductivity in the section plane, first look at how heat flows across the borders, which again can be either cell walls or struts intersected by the test plane. A solid border connecting nodes *i* and *j* is shown in figure 3.3. Neglecting interaction of solid conduction with radiation heat transfer and gas conduction, heat transfer along this strut would then be

$$q_{ij} = \frac{k_{ij} A_{ij} (T_i - T_j)}{L_{ij}} \tag{3.1}$$

where

k_{ij} = conductivity of solid member, i.e. $k_{polymer}$ (W/mK)

T_i, T_j = temperature at nodes *i,j* (K)

L_{ij} = length of solid border (m)

q_{ij} = heat transfer from node *i* to node *j* (W)

A_{ij} = two-dimensional cross-sectional area
which is the thickness of the border times
unit depth for two dimensions (m^2)

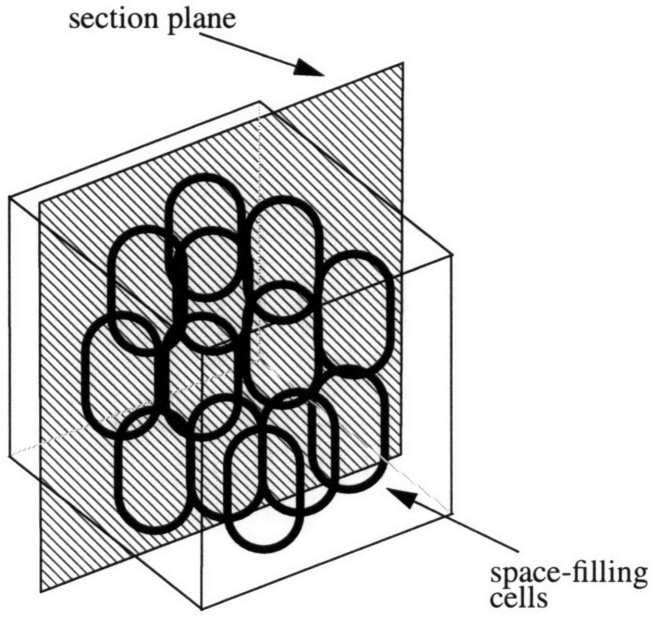

(a) volume of cells intersected by section plane

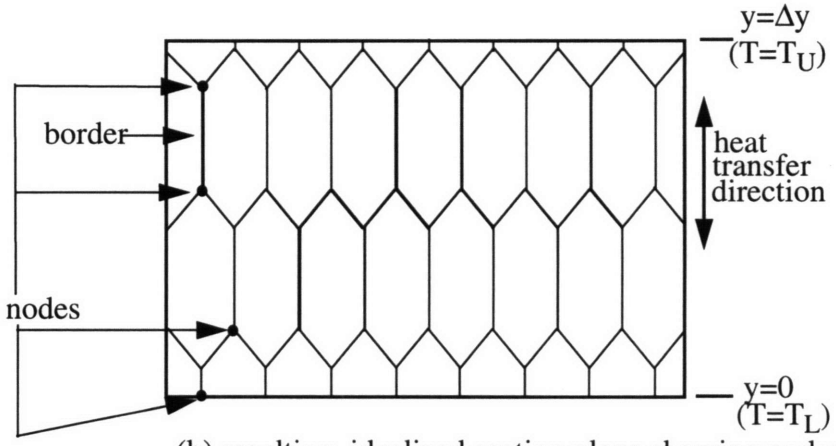

(b) resulting idealized section plane showing nodes and borders

Figure 0.1: *Section Plane Yielding Two-Dimensional Geometry Used with Solid Conductivity Model*

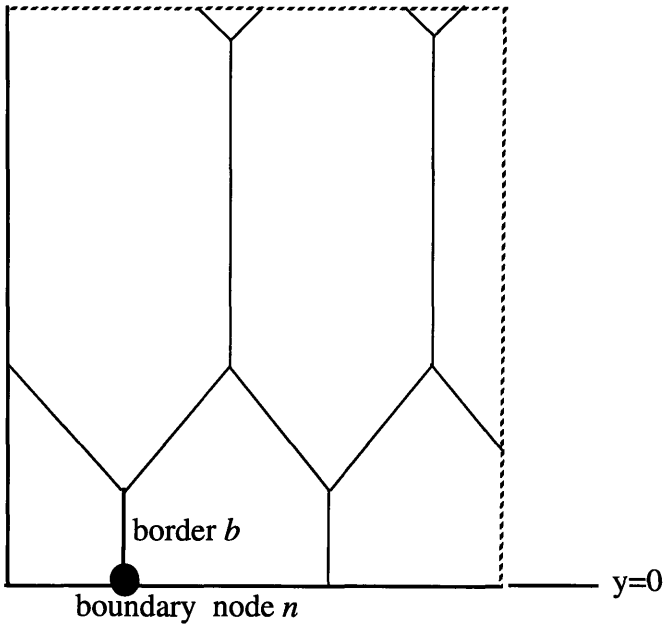

Figure 0.2: *Boundary Node Defined at y=0 or y=Δy Boundaries*

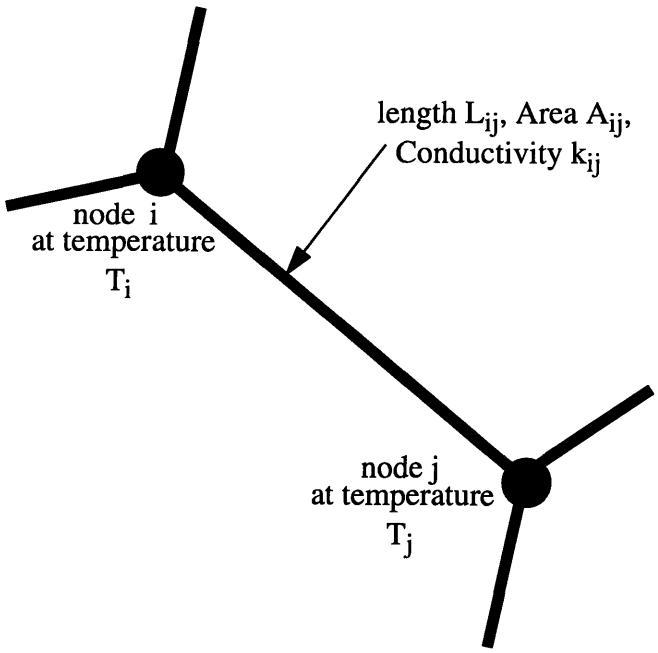

Figure3.3: *Solid Border Between Nodes of Two-Dimensional Foam Section*

Turning attention now to the nodes, the energy balance for any node i at steady state neglecting other forms of heat transfer is

$$q_{out} = \sum q_{ij} = 0 \tag{3.2}$$

where the summation is carried out over all nodes j directly connected to node i by solid borders. Or, substituting expression 3.1 for the heat transfer out of the node,

$$\sum \frac{k_{ij}A_{ij}(T_i - T_j)}{L_{ij}} = 0 \quad , \tag{3.3}$$

where again the summation is performed for all nodes j directly connected to node i. Rearranging equation 3.3 in terms of the temperatures,

$$\left(\sum \frac{k_{ij}A_{ij}}{L_{ij}}\right)T_i + \ldots - \left(\frac{k_{ik}A_{ik}}{L_{ik}}\right)T_k \ldots - \left(\frac{k_{i(k+1)}A_{i(k+1)}}{L_{i(k+1)}}\right)T_{(k+1)} = 0 \tag{3.4}$$

where nodes k and k+1 are connected to node i. The summation is over all nodes connected to node i, and if a node $k+n$ is not connected to node i, the T_{k+n} term is zero in equation 3.4.

After writing similar equations for all nodes, a matrix equation relating the temperatures at the nodes to the net heat transfer out of the nodes can be written:

$$[C][T] = [Q] \tag{3.5}$$

where [C] is the connectivity matrix such that

$$C_{ij} = \begin{cases} \sum_k \frac{k_{ik}A_{ik}}{L_{ii}} & i=j, \text{ summed over nodes k directly connected to node } i \\ -\frac{k_{ij}A_{ij}}{L_{ij}} & \text{nodes } i \text{ and } j \text{ are connected and } i \neq j \\ 0 & \text{nodes } i \text{ and } j \text{ are not connected} \end{cases} \tag{3.6}$$

[T] is a one-dimensional vector comprised of the nodal temperatures T_j. The [Q] matrix is a one-dimensional vector that has all entries equal to zero for internal nodes, not boundary nodes.

3.4 Boundary Conditions

To solve this matrix equation, boundary conditions have to be invoked. That is, something has to be said of the rate of heat transfer or of the temperature at the boundary nodes where y=0 or y=Δy as in figures 3.1 and 3.2. A first simple boundary condition is to consider the temperature gradient across the entire foam and use it to fix the temperatures at both boundaries. First, a one-dimensional linear temperature profile across the foam is assumed. Such an assumption is an extension of the locally linear temperature profile assumed in the Rosseland radiation equation derivation. Next, a temperature gradient from typical thermal conductivity testing equipment is used. Specifically, the 50K (ΔT) temperature difference across the Δt=1" (0.0254m) foam panels quoted by Bhattacharjee, et al [19] was used. Then, for a two-dimensional section of length Δy in the heat transfer

direction as represented in figure 3.1 and for a linear temperature profile, the temperature difference across the boundary nodes is

$$\Delta T = \frac{\Delta T_{total} \Delta y}{\Delta t} = \frac{(50K)\,\Delta y}{0.0254m} \tag{3.7}$$

Since the thermal testing was done at T=283K and many properties are reported at T=300K, the temperature at the lower nodes is set to a temperature near this condition T_L=290K. Then the temperature at the upper boundary nodes can be set to

$T_U=T_L + \Delta T$.

These boundary conditions have to be incorporated into the matrix equation 3.5. As with the energy balance of equation 3.2, an energy balance for boundary nodes can be expressed.

$$q_{out} = \sum q_{ij} \tag{3.8}$$

where now, the heat transfer out of the boundary node is no longer zero. But the temperature at the boundary node, T_i is known. Inserting the conductive rate of heat transfer along each border into equation 3.8, the energy balance for any boundary node is

$$\left(\sum \frac{k_{ij} A_{ij}}{L_{ij}}\right) T_i + \ldots - \left(\frac{k_{ik} A_{ik}}{L_{ik}}\right) T_k \ldots - \left(\frac{k_{i(k+1)} A_{i(k+1)}}{L_{i(k+1)}}\right) T_{(k+1)} \ldots = q_{out,\,i} \tag{3.9}$$

where again nodes k and k+1 represent those nodes connected to node i by borders, the temperature terms for nodes not directly connected to node i are zero, and $q_{out,i}$ is the unknown rate of heat transfer at the boundary. This equation is appended to the matrix equation for every boundary node. The appended matrix equation becomes

$$[M]\ [T]\ =\ [b] \tag{3.10}$$

The entries of [M] are

$$M_{ij} = \begin{cases} \sum_k \dfrac{k_{ik}A_{ik}}{L_{ik}} & \text{if } i = j \text{, Summed over nodes } k \text{ connected to node } i. \\ -\dfrac{k_{ij}A_{ij}}{L_{ij}} & \text{if nodes } i \text{ and } j \text{ are connected} \\ 0 & \text{if nodes } i \text{ and } j \text{ are not connected} \end{cases} \tag{3.11}$$

The entries of [T] are the temperatures at the nodes. With the boundary equations appended to equation 3.5, this vector includes both known and unknown temperatures. That is, T_i is known if node i is a boundary node, T_i is unknown otherwise. The entries of [b] are

$$b_i = \begin{cases} 0 & \text{if node i is not a boundary node} \\ q_{out,\,i} & \text{if node } i \text{ is a boundary node} \end{cases} \tag{3.12}$$

This system of linear equations is solved for the unknown $q_{out,i}$'s for the boundary nodes as well as for the unknown T_i for the internal nodes. Remember that the temperatures at the boundary nodes are known. So a solution routine was set up to rearrange knowns in a single vector and unknowns in a single vector and then solve for the resulting matrix equation. This matrix equation was solved using a simple Gauss-Seidel solver. After the heat transfer rate at the boundaries are determined, the rates of heat transfer at the lower

boundary are summed and the rates of heat transfer at the upper boundary are summed. Both sums should be the same for conservation of energy in the foam section. Then from the Fourier relation, the solid conductivity is

$$k_s = \frac{(\sum q_{boundary})\,\Delta y}{A_{xs}\Delta T} \tag{3.13}$$

where for the two-dimensional section, the cross-sectional area is the total length of the section perpendicular to the heat transfer direction or Δx. So the effective solid conductivity from a two-dimensional section of foam can be calculated from

$$k_s = \frac{(\sum q_{boundary})\,\Delta y}{\Delta x \Delta T} \tag{3.14}$$

3.5 Conductivity Model Validation

To determine how well the solid conductivity matrix program determines the conductivity of a two-dimensional section, several simple geometries where an analytical solution can be determined were run with the program and tested against the analytical results. Specifically, Mark Schuetz [14] solved the analytical conductivities for three simplified geometries. The first was a collection of cubic foam "cells" in an inline geometry (see figure 3.4(a)). The second geometry was an array of these cubic cells in a staggered arrangement (figure 3.4(b)). Finally Schuetz looked at an array of these cubes at an oblique angle to the heat transfer direction, specifically at 45^{o} to the heat transfer direction (see figure 3.4(c)). These three geometries were run with the solid conductivity program and the results were compared to Schuetz's results.

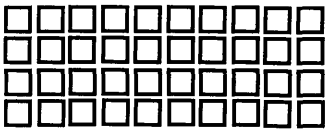

(a) inline cubic geometry

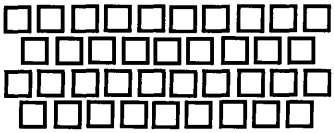

(b) staggered cubic geometry

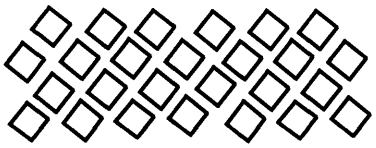

(c) oblique (45^{o}) cubic geometry

Figure 3.4: *Geometries Used to Compare Solid Conductivity Program with Schuetz's Analysis*

To be consistent with Schuetz's work, some program parameters had to be specified. The first parameter that had to be determined was the cross-sectional areas of the solid

borders. For the two-dimensional case, this area is the thickness of the solid borders. From Schuetz's analysis, assuming all of the polymer is in the cell walls, the border thickness t, cell diameter d, and void fraction δ for a two-dimensional cubic geometry are related

$$\delta = \frac{d^2}{(d+t)^2} \tag{3.15}$$

So, for a certain void fraction and cell diameter the cell border thickness can be set to

$$t = d\left(\frac{1}{\sqrt{\delta}} - 1\right) \tag{3.16}$$

The second parameter that has to be determined for the Schuetz analysis and the computer model to be consistent is the gas conductivity. Schuetz's analysis actually looked at the coupled gas and solid thermal conductivity across the cells. The solid conductivity matrix program implicitly assumes that the solid and gas conductivities can be uncoupled. This is similar to the gas conductivity term being ignored or set to zero in Schuetz's analysis.

For each geometry, Schuetz looked at the repeating element, or symmetric part of the cell that was repeated to form the array. Using the electrical analogy to heat transfer (V=IR) where V=ΔT, I=q, and R=1/kA, Schuetz determined the resistances to heat transfer across the repeating element. From this he determined the overall solid and gas conductivity for the repeating element and thus for the entire array. To deal with elements perpendicular to the heat transfer direction, Schuetz considered the upper and lower limits. The upper limit was the case where conductivity across these perpendicular elements were considered infinite, thus contributing as much as possible to heat transfer. The lower limit

considered the conductivities along these perpendicular elements to be zero, thus providing as much resistance to heat transfer as possible.

The first geometry considered is the inline cubic geometry where the cubic cells are aligned as in figure 3.4(a). The repeating element for this geometry is pictured in figure 3.5(a). The upper and lower limit analogous electrical circuits are depicted in figure 3.5(b) and 3.5(c). Considering the upper limit, these thermal resistances are

$$R_{s1} = \frac{\frac{t}{2}}{k_s \frac{(d+t)}{2}} = \frac{t}{k_s (d+t)} \tag{3.17}$$

$$R_{s2} = \frac{\frac{d}{2}}{k_s \frac{t}{2}} = \frac{d}{k_s t} \tag{3.18}$$

$$R_{g1} = \frac{1}{k_g} \tag{3.19}$$

In this analysis consider k_g approaching zero which means R_{g1} approaches infinity. Then the overall resistance between isotherms T_1 and T_2 is, with k_g approaching zero,

$$R_{UL} = R_{s1} + \frac{1}{\frac{1}{R_{s2}} + \frac{1}{R_{g1}}} = R_{s1} + R_{s2} \tag{3.20}$$

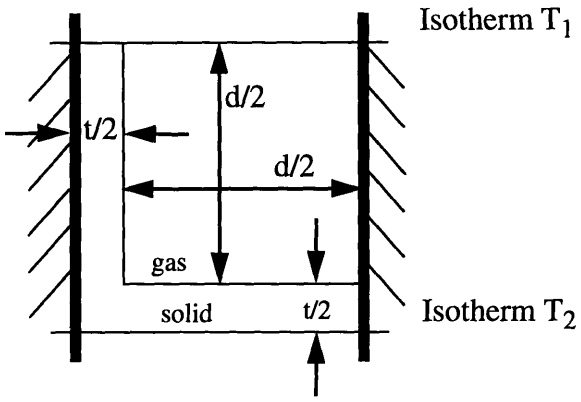

(a) repeating element

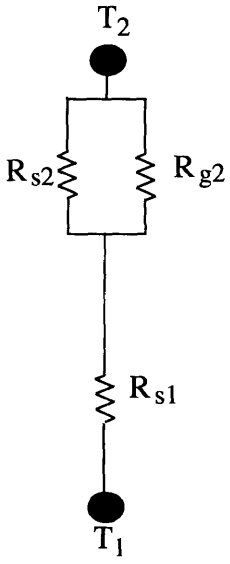

(b) upper limit equivalent circuit

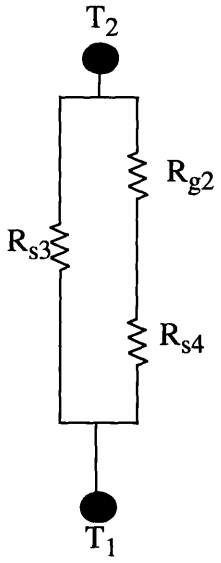

(c) lower limit equivalent circuit

Figure3.5: *Repeating Element and Equivalent Circuits for Inline Cubic Geometry*

Considering the lower limit, the thermal resistances become

$$R_{s3} = \frac{\frac{d+t}{2}}{k_s \frac{t}{2}} = \frac{d+t}{k_s t} \tag{3.21}$$

$$R_{s4} = \frac{\frac{t}{2}}{k_s \frac{d}{2}} = \frac{t}{k_s d} \tag{3.22}$$

$$R_{g2} = R_{g1} \rightarrow \infty \tag{3.23}$$

and with R_{g1} approaching infinity, the overall resistance is

$$R_{LL} = \left(\frac{1}{R_{s3}} + \frac{1}{R_{s4} + R_{g2}}\right)^{-1} = R_{s3} \tag{3.24}$$

For both the upper and lower limit, the conductivity is related to the overall resistance (R being R_{UL} or R_{LL})

$$k_s = \frac{\frac{d+t}{2}}{R\frac{d+t}{2}} = \frac{1}{R} \tag{3.25}$$

The geometry in figure 3.4(a) was run with the solid conductivity matrix program for different void fractions and different cell diameters. The calculated solid conductivity as a function of void fraction was then compared to that predicted by the repeating element analysis. The results are shown in figure 3.6 and in Table 3.1.

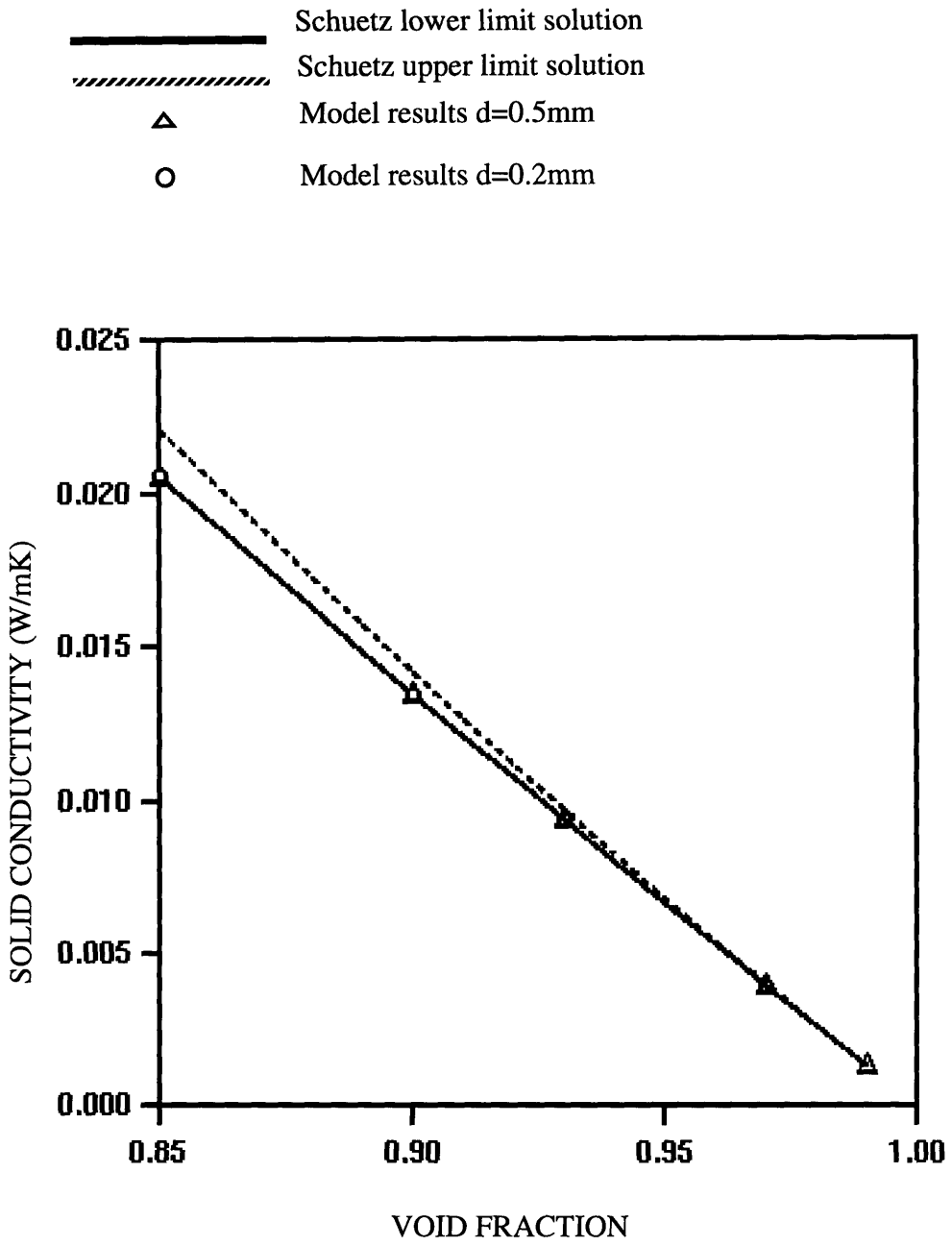

Figure 3.6: *Comparison of Inline Cubic Geometry Solid Conductivity from Matrix Program and from Schuetz's Analysis*

Void Fraction	Matrix Solid Conductivity (W/mK)	Lower Limit Analytical Conductivity (W/mK)
0.85	0.0205	0.0205
0.9	0.0135	0.0135
0.93	0.00938	0.00937
0.95	0.00666	0.00666
0.97	0.00398	0.00398
0.99	0.001318	0.001318

Table 3.1: *Comparison of Matrix Solid Conductivity and Analytical Results for Inline Cubic Geometry*

As can be seen, the solid conductivity matrix results are the same as predicted by the lower limit analysis. Upon closer inspection of the two solution methods, the correspondence between the lower limit and the matrix solution should be expected. As seen in figure 3.7, the cross-sectional area for heat transfer is different in the lower region of the cell for the upper and lower limit cases. In the upper limit case, with conductivity being as large as possible, the cross-sectional area is the entire (d+t)/2 segment. In the lower limit, since there is no lateral heat transfer, the effective cross section for heat transfer is the t/2 member. Similarly, in the solid conductivity program, the endpoints of the transverse member are at the same y location and are therefore at the same temperature. So the temperature gradient across the transverse element is zero, heat transfer across the member is zero, and the member does not contribute to heat transfer. That is, the cross-sectional area for heat transfer becomes the t/2 member.

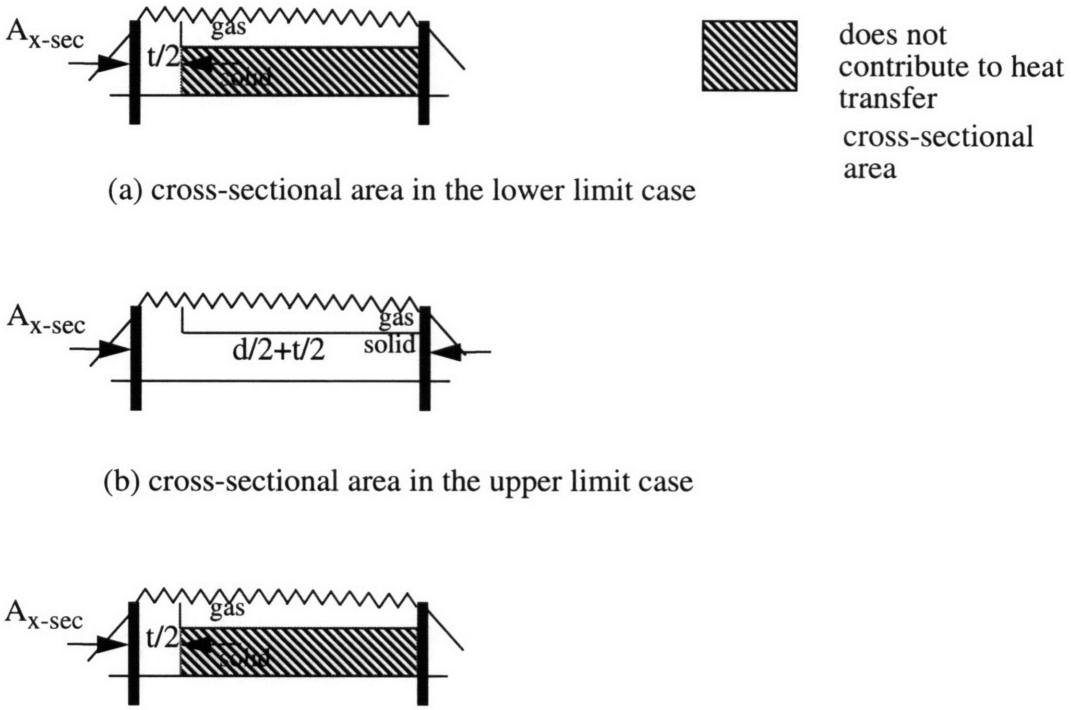

Figure 3.7: *Cross Sectional Areas for Heat Transfer in Upper Limit, Lower Limit, and Matrix Program Cases*

The next geometry which Schuetz considered was the staggered cube alignment where the cells are once again cubes but aligned as in figure 3.4(b). The repeating element for this geometry is shown in figure 3.8. The upper limit for this staggered geometry is exactly the same as for the inline cubic geometry. That is, for conductivities of infinity perpendicular to the heat transfer direction, isotherms are lines of constant x. However, due to the tortuosity of the geometry, the lower limit conductivity is considerably lower than the lower limit of the inline geometry especially when k_g=0.

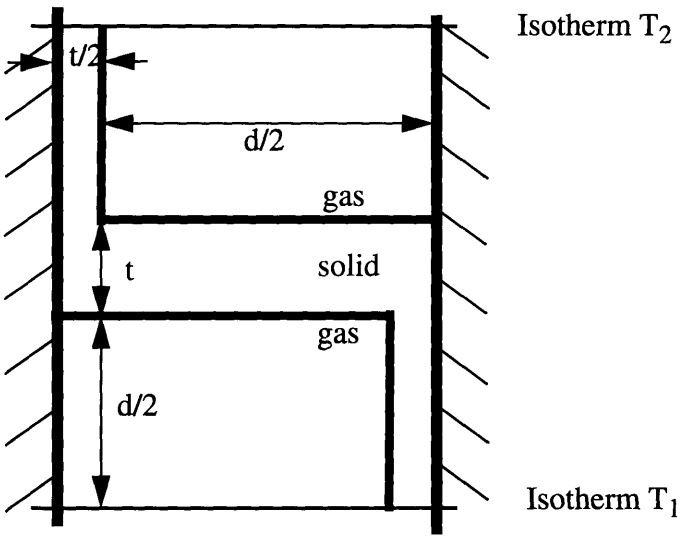

Figure 3.8: *Repeating Element for Staggered Cubic Geometry*

The detailed description of this lower limit geometry is outlined in Schuetz's work [14]. In summary, the lower limit takes advantage of the fact that the conductivity problem is a linear one and can be treated as the superposition of two simpler problems. The requirement being that the differential equations and boundary conditions of the sum of the two simpler variables are the same as the staggered geometry's governing equations and boundary conditions. The lower limit considered then is the sum of the lower limits of these two component cases. These component cases are shown in figure 3.9. The sum solution of the lower limits of these cases is then

$$R_A = 2\left(\frac{d+t}{k_s t}\right) + \frac{\frac{d}{2}}{k_s t} = \frac{2.5d+2t}{k_s t} \tag{3.26}$$

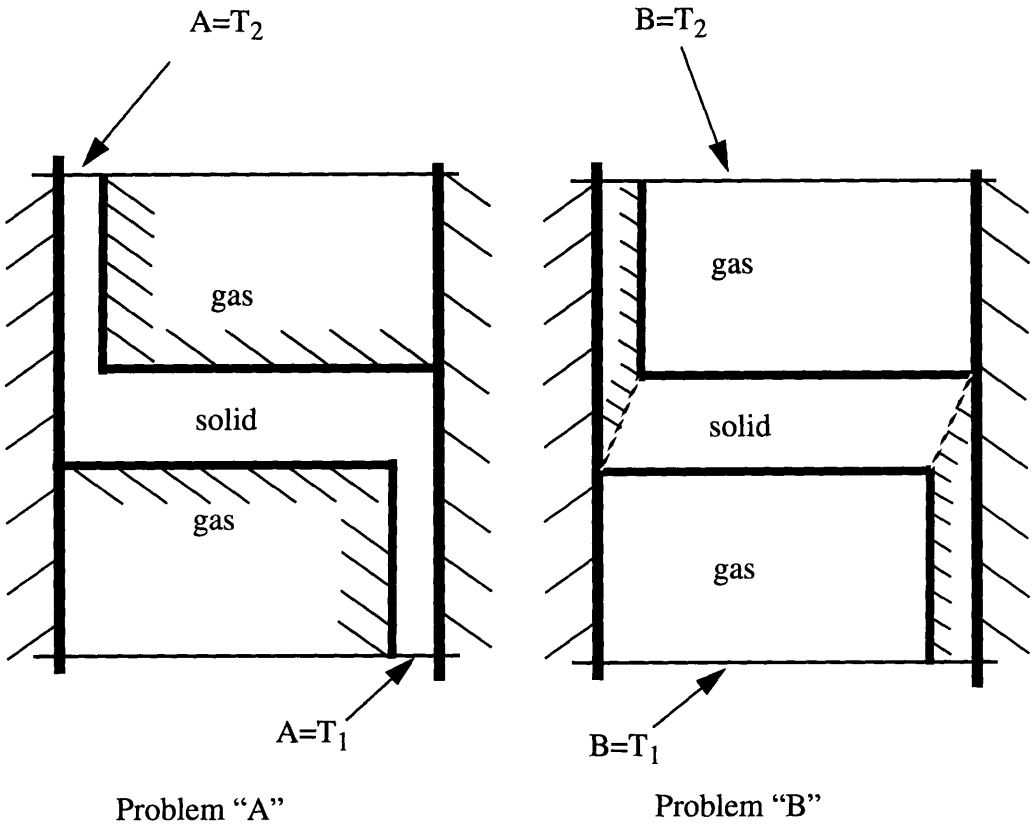

Figure 3.9: *Cases Superimposed for Staggered Geometry Lower Limit*

$$R_B = 2\left(\frac{d}{k_g d}\right) + \frac{t}{k_s d} \rightarrow \infty \tag{3.27}$$

where again, to compare with the solid conductivity model, k_g approaches zero so R_B approaches infinity. By superposition of the solutions it is meant that the overall flux for the staggered case is the flux of case A plus the flux of case B. That is

$$q_T = q_A + q_B = \frac{T_1 - T_2}{R_A} + \frac{T_1 - T_2}{R_B} = \frac{T_1 - T_2}{R_{s+g}} \tag{3.28}$$

which gives an expression for the overall thermal resistance

$$R_{s+g} = \left(\frac{1}{R_A} + \frac{1}{R_B}\right)^{-1} \tag{3.29}$$

which reduces to $R_{s+g}=R_A$ for the limit of k_g approaching zero. Then the solid conductivity lower limit for the staggered geometry is

$$k_{s+g} = \frac{d+t}{R_{s+g}\frac{d+t}{2}} = \frac{2}{R_{s+g}} = \frac{2}{R_A} \tag{3.30}$$

For the staggered geometry, the solid conductivity predicted by the model as a function of void fraction is compared to the analytical conductivity of Schuetz in figure 3.10 and Table 3.2. The matrix program values and the lower limit values agree within 3.6%. The small discrepancy is due to a problem unique to this test case. The present solid conductivity model treats the cross sectional area of every border as the same. In these test cases, the area is the thickness, t, of a cell border. This is true even for borders on the sides of the test image as shown in figure 3.11. In the analytical result from the repeating element, only one-half of the thickness is used in analyzing every cell. So the thicknesses of the borders on the side of the image are different in the two cases (see figure 3.11). Once the matrix program can be extended to include the thickness of every border individually, the border areas used in the analytical results can be incorporated into the matrix program. So for all practical purposes, the results of the matrix program and the lower limit analytical results can be considered equivalent.

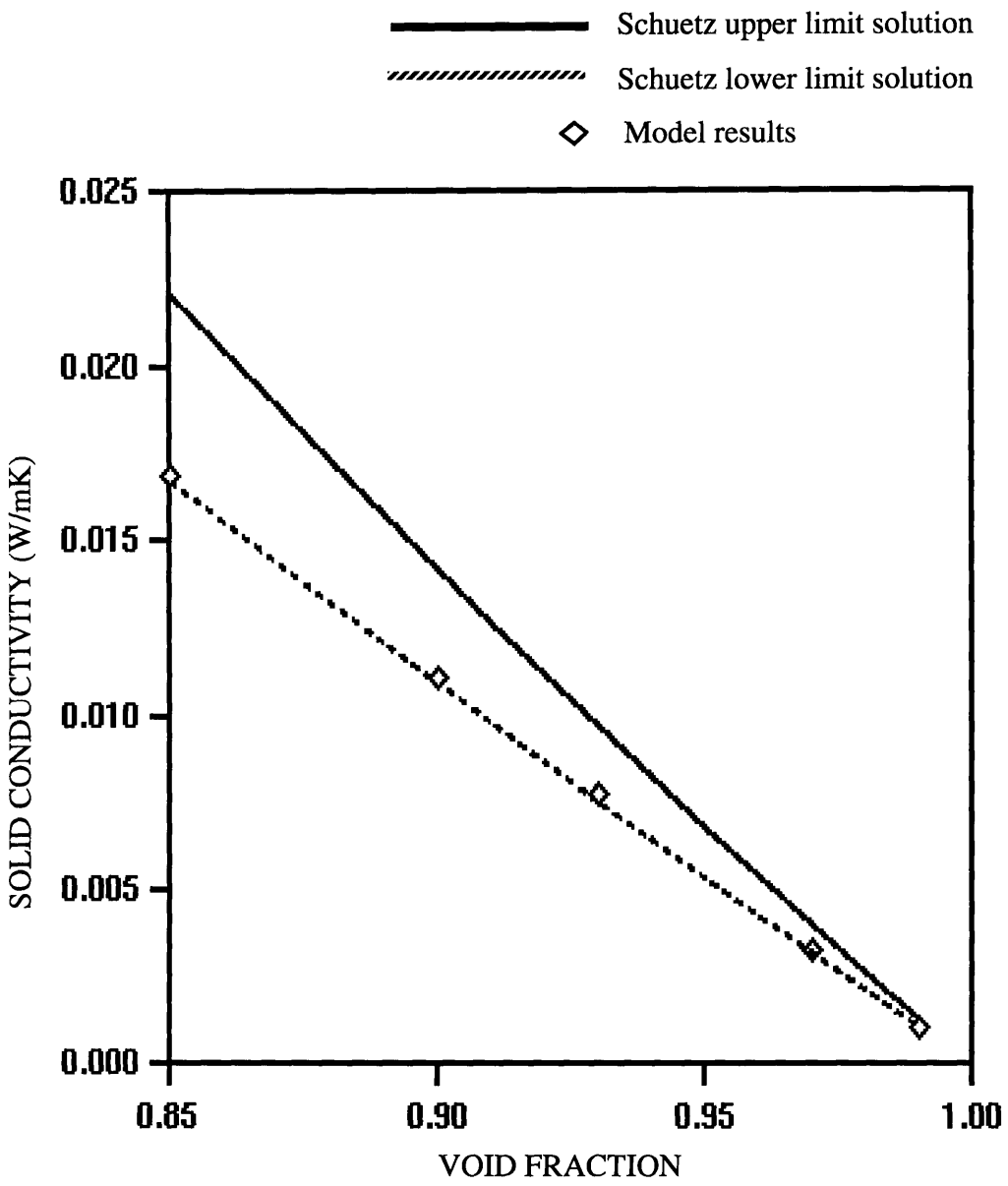

Figure 3.10: *Comparison of Staggered Cubic Geometry Solid Conductivity from Matrix Program and from Schuetz's Analysis*

Void Fraction	Matrix Solid Conductivity (W/mK)	Lower Limit Analytical Conductivity (W/mK)
0.85	0.01688	0.01668
0.90	0.01114	0.010909
0.93	0.007754	0.007551
0.97	0.003298	0.003189
0.99	0.0010954	0.001058

Table 3.2: *Comparison of Matrix Solid Conductivity and Analytical Results for Staggered Cubic Geometry*

Looking at the methods used in each case, the agreement between the lower limit results and the matrix program results makes some intuitive sense. Having a finite solid conductivity, struts perpendicular to the heat transfer direction have to have a temperature gradient along their lengths for there to be heat transfer from the lower to upper boundary. Therefore, isotherms for the solid conductivity model are not lines of constant x as in the upper limit case. With gas conductivity being negligible in the lower limit case, one can see that the lower limit reduces to case A which is the same case solved by the solid conductivity model.

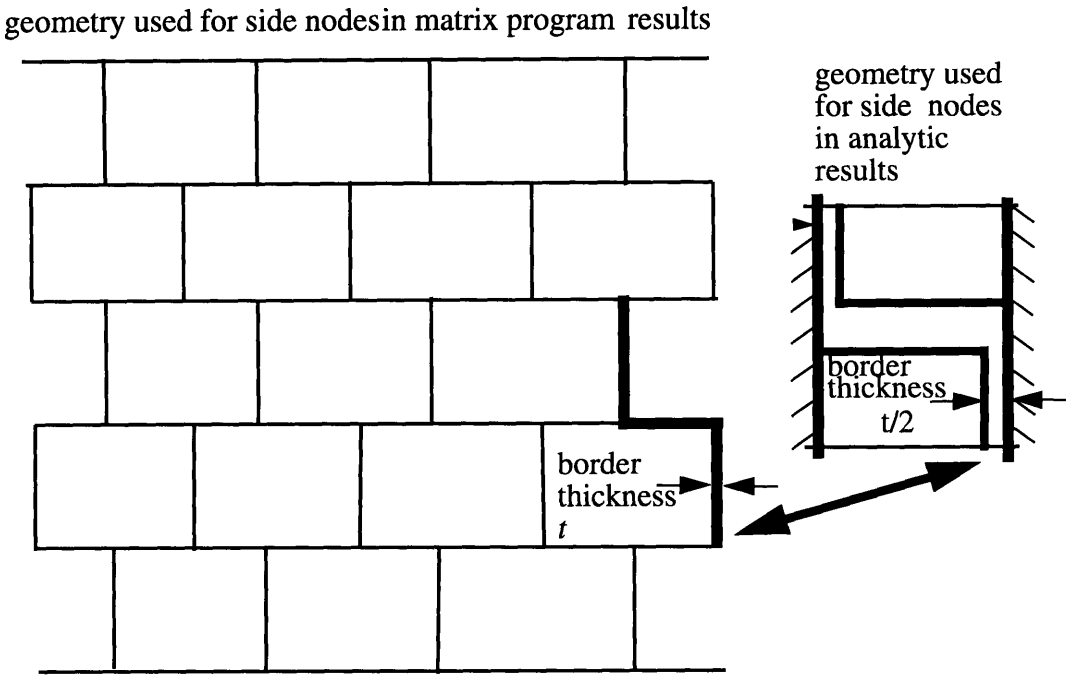

Figure 3.11: *Differences in Side Border Thicknesses for Staggered Geometry Validation*

For a final comparison of a simple geometry with analytical results developed by Schuetz, the oblique cubic geometry which is shown in figure 3.4(c) is considered. An angle of 45° is chosen for simplicity of analysis. This geometry provides the feature that nodes at the same y are not directly connected and each border is obliquely oriented to the heat transfer direction. The repeating element for this geometry is shown in figure 3.12. For this geometry, both the upper and lower limits converge to the same solution, which can be considered the exact analytical solution for this geometry. The resulting conductivity for this geometry is

$$k_{s+g} = k_g + \frac{k_{polymer} t}{d} \tag{3.31}$$

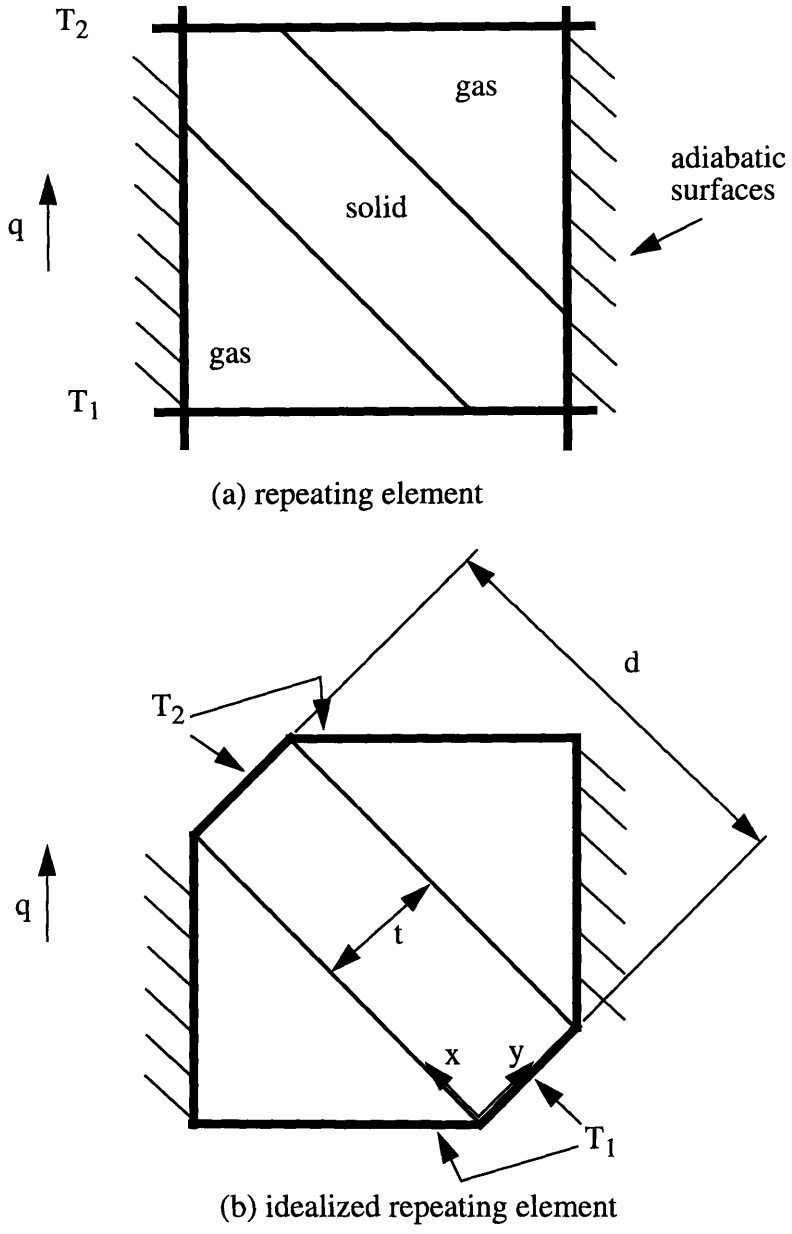

Figure 3.12: *Repeating Element for Oblique Cubic Geometry*

Again the case where k_g approaches zero is considered to compare to the solid conductivity model. This limiting case yields the analytical conductivity for the 45^o cubic geometry

$$k_s = \frac{k_{polymer}{}^t}{d} \tag{3.32}$$

The results from the solid conductivity program compared to this analytical result as a function of void fraction are shown in figure 3.13 and in Table 3.3. As can be seen, the solid conductivity program predicts the same solid conductivity as the analytical prediction.

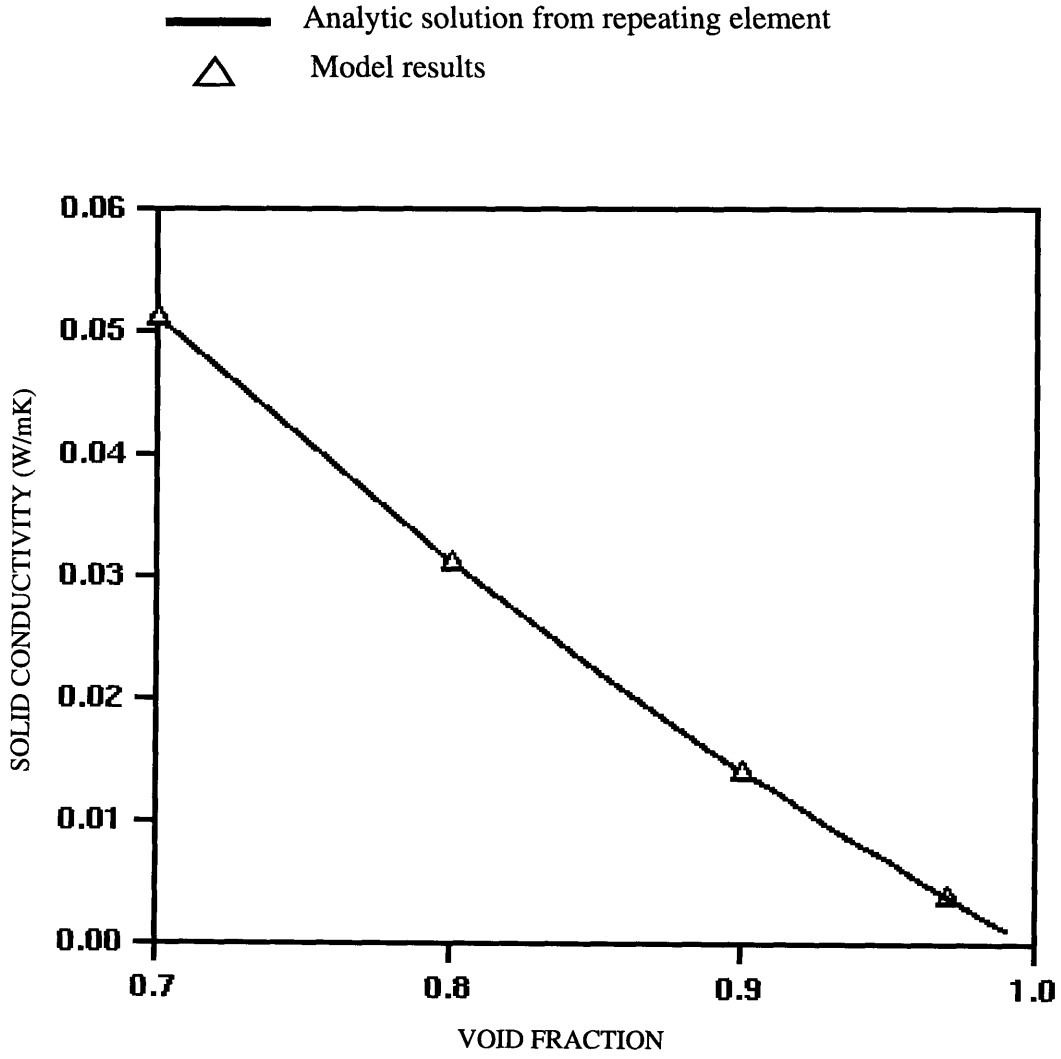

Figure 3.13: *Comparison of Oblique Cubic Geometry Solid Conductivity from Matrix Program and from Schuetz's Analysis*

Void Fraction	Matrix Solid Conductivity (W/mK)	Lower Limit Analytical Conductivity (W/mK)
0.70	0.051347	0.051345
0.80	0.031048	0.031043
0.90	0.014225	0.014226
0.97	0.004036	0.004036

Table 3.3: *Comparison of Matrix Solid Conductivity and Analytical Results for Oblique Cubic Geometry*

3.6 Foam Solid Conductivity Prediction

The solid conductivity model was next used with morphology images from actual foams supplied by ICI Polyurethanes. Specifically, two-dimensional optical sections of foams were digitized using a confocal microscope (see Section 3.6 where the confocal microscope is described). The digitized system of nodes and borders were then inputs to the solid conductivity matrix program. The program outputted the rate of heat transfer out of the lower boundary of the image and the rate of heat transfer into the upper boundary, which both should be equal for conservation of energy. Using either one of these heat transfer rates and the geometry of the image, the two-dimensional solid conductivity can be predicted.

3.7 Confocal Images

Since the solid conductivity model is a two-dimensional routine, an acceptable two-dimensional foam geometry has to be used with the program. SEM micrographs of foam geometry add a depth-of-field problem that would have to be accounted for in considering what are two-dimensional features of the foam. This can be seen in figure 3.14. Here,

not only are cell boundaries seen, but also the interior of the cells with boundaries of cell faces. That is, a projection of the three-dimensional cell features are seen, not a planar section of the foam. The confocal microscope was therefore investigated as a means of achieving a two-dimensional foam section without a depth-of-view problem.

In brief, the confocal microscope consists first of a scanning laser with a high numeric aperture condenser lens that focuses the light into a small section of the sample [20]. This illuminating setup causes the sample to autofluoresce, or emit energy at a certain wavelength range. In our case the laser causes a sample to autofluoresce at a wavelength of 488nm. A filter in the collecting portion of the microscope allows only the spectrum of energy in which the sample autofluoresces to be detected. In collecting the autofluorescence, the confocal microscope uses a high numeric objective lens to focus on the section autofluorescing.

The amount of light reaching the image also depends on the stops. These are openings on an opaque screen as in figure 3.15. The screen prevents light from out-of-focus sources and from severely scattered rays from reaching the image (see figure 3.15), improving detail and reducing background light. There are two stops, an illumination stop reducing the light coming from the source and an image stop reducing the amount of light reaching the image. When both stops are made small enough, imaging information will come from a sharply peaked region around the in-focus object plane.

The illumination stop is filled with light from the laser and focused through the high numerical aperture condensor lens on a small portion of the sample. The sample section is imaged with an identical numerical aperture objective lens, through a diameter D image stop. Remember that if the stops are large, fluorescent light from other portions of

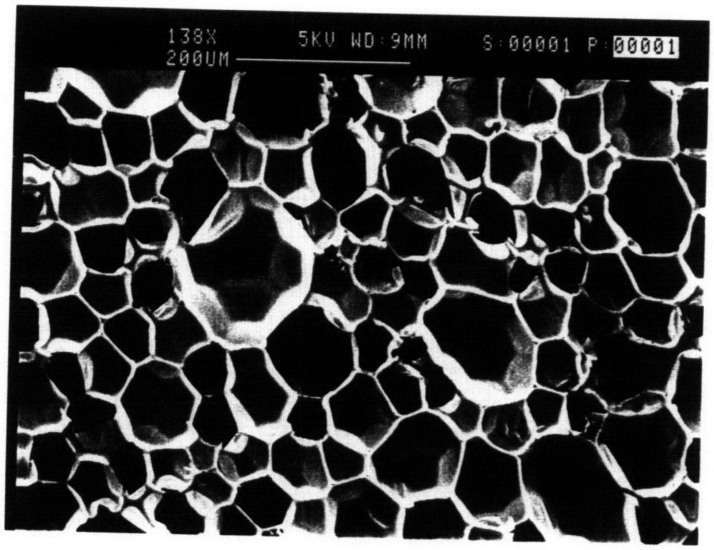

Figure 3.14: *SEM Photograph Showing Depth-of-Field*

the sample (out-of-focus images) intercepted by the illumination beam will pass through the image stop and obscure the image (the dashed path in figure 3.15). The lateral resolution is $\Delta X=D/M$ where D is the diameter of the image stop and M is the lens magnification. The axial resolution or depth-of-field is $\Delta Z=D\cot(\alpha)/M$ where α is the lens aperature[20]. For $\alpha=64^{o}$ which is a typical example in water immersion cases, to get a 1μm depth-of-field with 63X magnification, the stop diameter should be 66μm [20].

Unfortunately only a 1μm diameter section of sample (the lateral resolution) can be imaged at a time. This is where the confocal microscope improves the image obtainable from a conventional light microscope. The stop sizes are reduced to very small diameters. The small field of view is scanned around the specimen in order to image the larger structure. In our particular confocal setup the laser itself is moved and scans around the specimen rather than the specimen being moved as in some other setups. The confocal microscope's computer records sequentially the small patches imaged as the laser scans. A view of the larger structure is then assembled from the patches line by line by the computer and displayed on the video screen. This allows one to image larger structures, such as several cells, with the small depth-of-field scanned in each patch. Proper combinations of lenses and stops allows the depth of focus of such a section to reach as small as 100 nanometer optical thickness. A schematic of this basic operation of the confocal microscope, as presented by Shuman et al [20], is shown in figure 3.15.

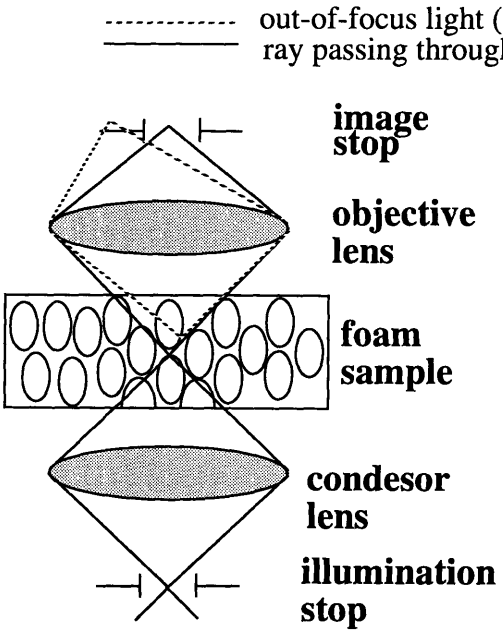

Figure 3.15: *Schematic of Confocal Microscope Operation*

This setup allows a photomicrograph of a section of foam with a small depth of field to be recorded. A typical resulting optical section of foam is displayed in figure 3.16.

Note also the potential of the confocal microscope to reconstruct the three-dimensional view of the foam structure by reconstructing an image from patches not only from a lateral scan, but also from scans in the axial dimension as well. Such three-dimensional reconstructions are outlined by Schuman [20].

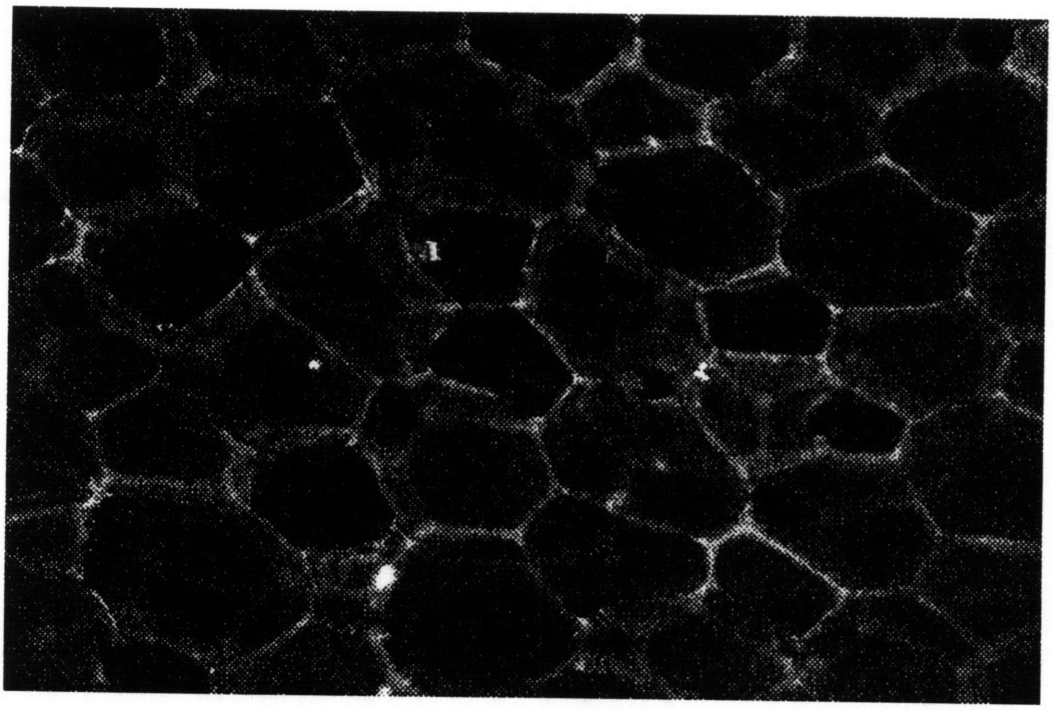

Figure 3.16: *Typical Image Recorded with Confocal Microscope* (10X *Magnification*)

3.8 Imaging Technique

Several foams were prepared so that resulting confocal images displayed cells with elongated and isotropic dimensions showing. With the first samples examined, only the mechanical parameters of the confocal microscope were used to try to enhance the image such as increasing the gain of the equipment, playing with computer filters, and decreasing the aperture of the confocal microscope filter. However, the autoflourescence of the foam cell walls did not register well with these images. So the foam samples were later prepared in a fluoroscene dye, which adds autofluorescence in the wavelength range of interest. This increased the amount of autofluorescence and allowed an image with an even smaller depth-of-field. Once an acceptable optical section of foam had been collected, the section displayed by the confocal microscope computer screen was digitized to disk.

3.9 Preparing Optical Sections for Solid Conductivity Model

Upon further optimization of the present technique, the digitized confocal images will be used as input into a computer code that recognizes the locations of nodes and borders. This will allow automation of the solid conductivity model. However, at present, the two-dimensional images from the confocal microscope have gaps in cell walls and other problems that leave such automation presently unworkable. So for now there is an intermediate step in the use of confocal two-dimensional images to predict the solid conductivity component. This step is the use of an image analysis software, presently NIH Image 1.47, to determine the locations of nodes and borders.

The digitized confocal images are transferred to the image analysis software. After setting the scale for the photomicrograph which is a function of the lenses of the confocal

microscope, borders are marked by hand. That is, the software includes a cross-hair tool that marks x-y location in the image. By marking the endpoints of a border, it and the endpoint nodes defining it are marked. The endpoints of every border are labeled in this manner. Once all borders have been labeled, the x-y coordinates of the border endpoints are written to a file. As can be seen in the solid conductivity matrix program included in Appendix B this file allows borders and nodes to be located and the solid conductivity to be determined.

Also shown in Appendix B is a code that automates the node and border finding functions directly from the digitized images. That is, the intermediate step of marking x-y coordinates is eliminated using images with clearly defined borders. At the present, suitable images have not been found so the intermediate x-y marking step is still necessary.

Note that for the present model, one paramter has to be assigned that should, in future versions of the program, be obtained directly from the digitized images. This parameter is the border area, A_{ij} in expression 3.11, which was considered the border thickness, t, in the validation cases. Once suitable digitized images can be found, the node finding routine can be expanded to calculate the border thickness of each individual border. However, for the present situation where x-y coordinates of border endpoints are marked using IMAGE, the thickness is assigned and is considered the same for every border. The thickness is determined in the following manner. The section image is considered to be of a differential depth, dz, as shown in figure 3.17. The borders are assumed to have this same depth also. So the border area is

$$A_{ij} = (t)\ (dz) \tag{3.33}$$

The total dimensions of the borders are now related to the foam overall density. That is,

$$\rho_f = \frac{m_{solid}}{V_{image}} = \frac{\rho_{solid} V_{borders}}{V_{image}} \tag{3.34}$$

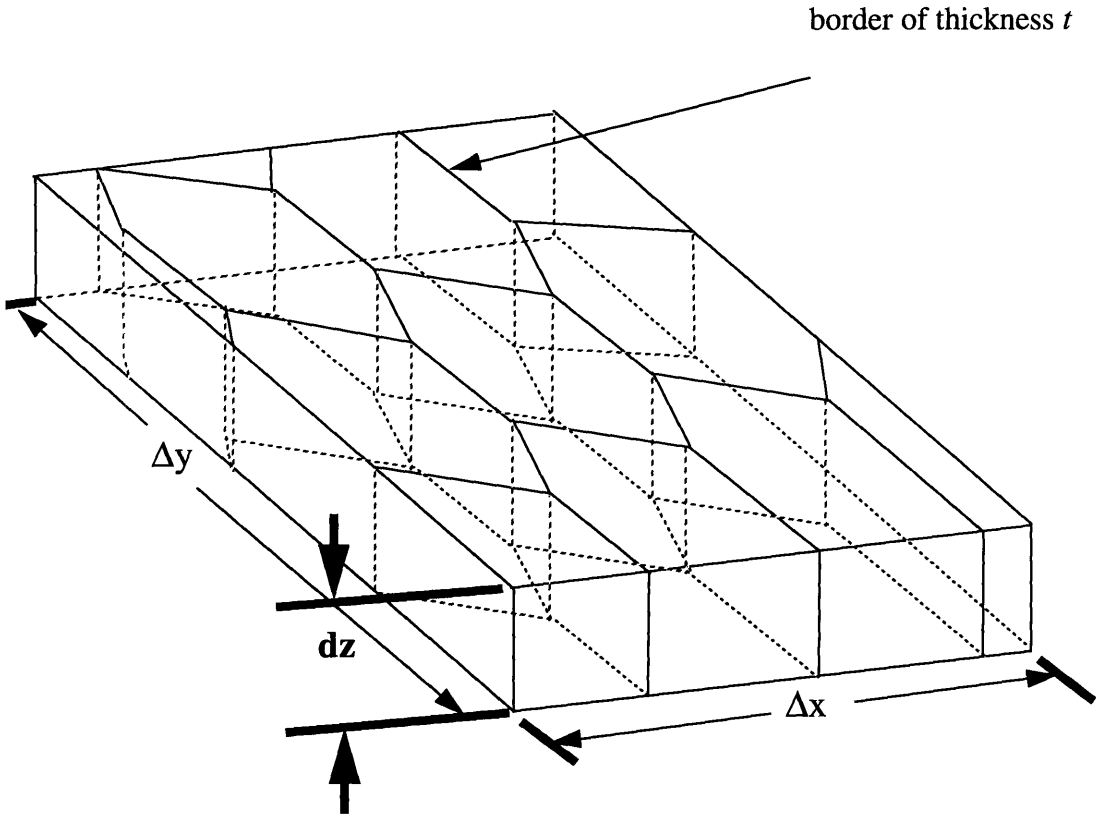

Figure 3.17: *Idealized Confocal Image Volume Showing Differential Depth Used in Calculating Border Areas*

The volume of the borders are the border areas times the total length of borders, L_T,

$$V_{borders} = L_T A_{ij} = L_T t dz \tag{3.35}$$

while the volume of the image is

$$V_{image} = \Delta x \Delta y dz \tag{3.36}$$

Then the foam density can be written as

$$\rho_f = \frac{\rho_{solid} L_T t dz}{\Delta x \Delta y dz} = \frac{\rho_{solid} L_T t}{\Delta x \Delta y} \tag{3.37}$$

Rearranging to express the border thicknesses

$$t = \frac{\rho_f \Delta x \Delta y}{\rho_{solid} L_T} = \frac{\Delta x \Delta y (1 - \delta)}{L_T} \tag{3.38}$$

So the length of all of the borders are summed and the border thickness is calculated.

3.10 Solid Conductivity Model Results for Foams Analyzed

Two-dimensional foam solid conductivities were calculated using the above technique from several confocal images of planes parallel and perpendicular to the heat transfer direction. Images displaying the plane parallel to the heat transfer direction were gathered from samples cut perpendicular to the rise direction of the foam, the elongated direction. Similarly images displaying the plane perpendicular to the heat transfer direction were obtained from samples parallel to the rise direction as in figure 3.18. Typical images of both planes are shown in figures 3.19 and 3.20. These results are displayed in Table 3.4, graphically in figure 3.21 where predicted solid conductivity is plotted against void fraction. Each foam represents a different void fraction. The number of data points at each void fraction represents different confocal images of the same foam. The degree of anisotropy measured for each foam sample (see Chapter 4) is also displayed in the figure. The trend with these foams is that as void fraction increases, the solid conductivity

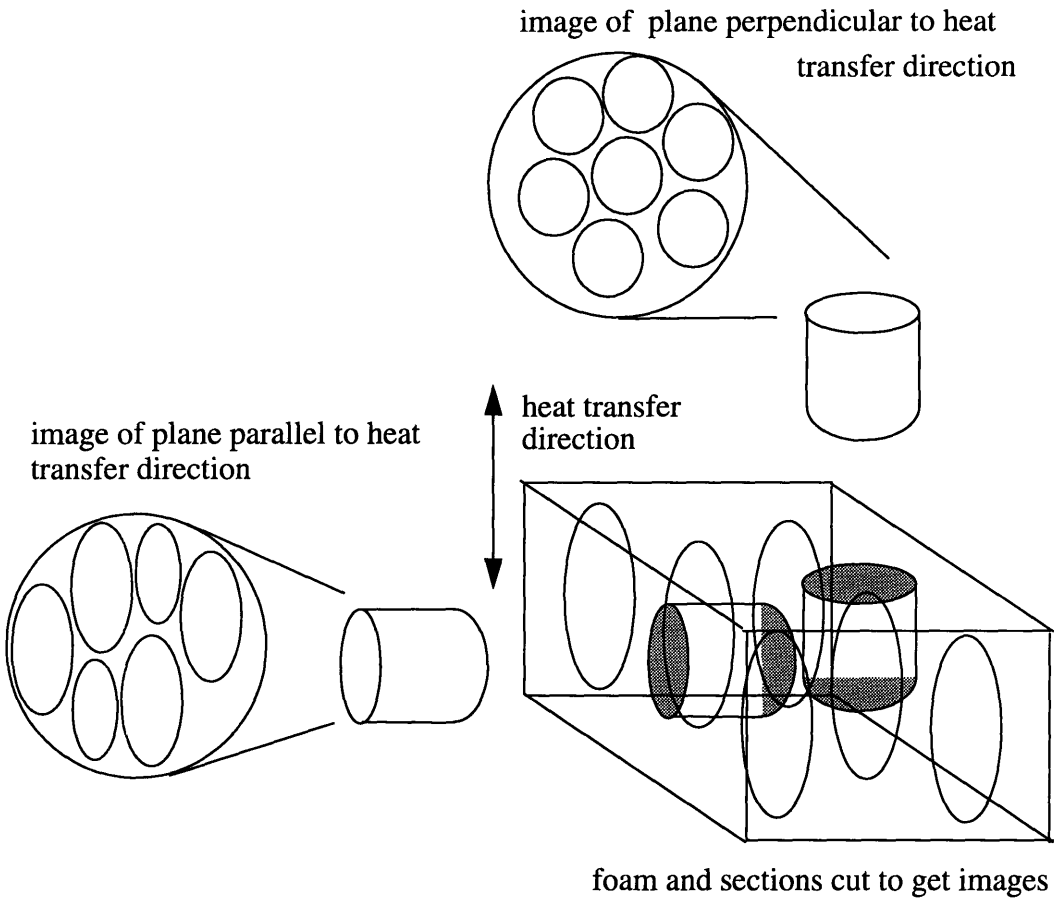

Figure 3.18: *Sketch of Section Orientations Used to Obtain Confocal Images Parallel and Perpendicular to Heat Transfer*

in the rise direction (parallel to the heat transfer) decreases. Also shown in figure 3.21 is the result of Schuetz's analysis of two-dimensional conduction through randomly oriented cell walls [14]. The analysis is

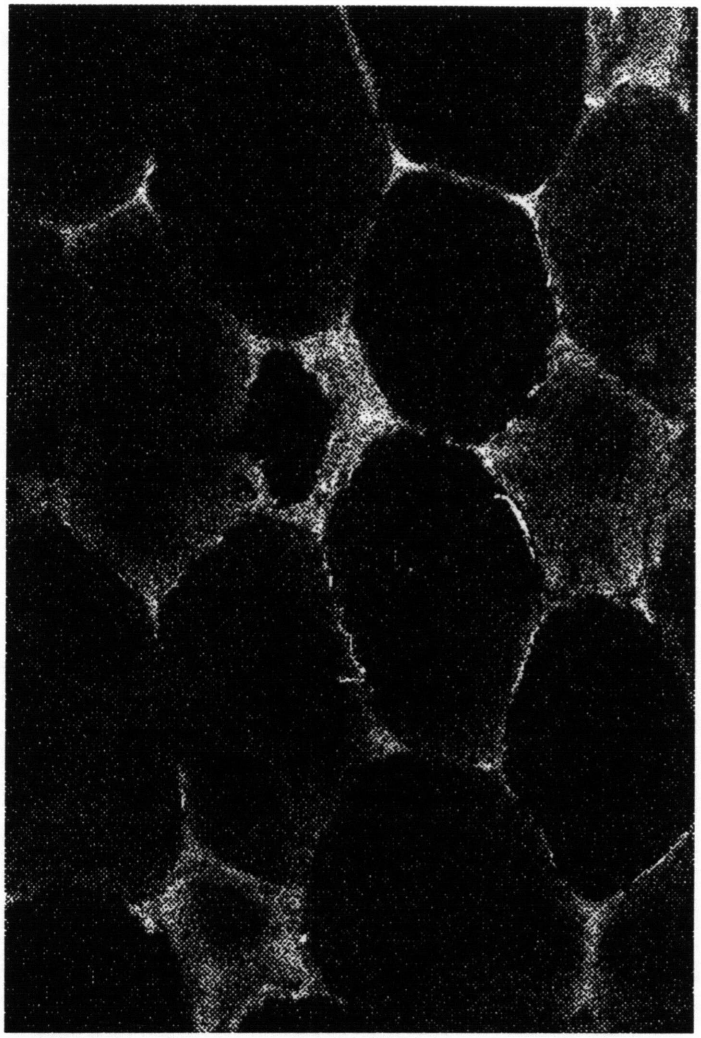

Figure 3.19: *Typical Confocal Image Showing Plane Parallel to Heat Transfer*

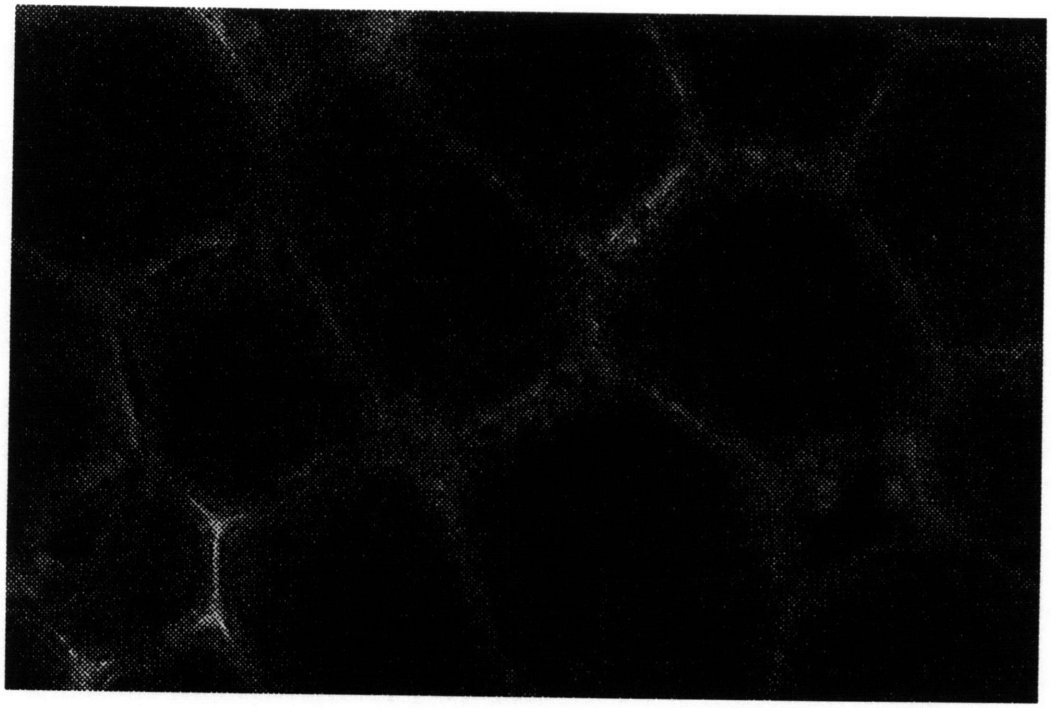

Figure 3.20: *Typical Confocal Image Showing Plane Perpendicular to Heat Transfer*

Foam Designation (NBE ...)	Foam Void Fraction	Anisotropy *a/b*	Plane Parallel or Perpendicular to Heat Transfer Direction	Predicted Solid Conductivity (mW/mK)
863/13/1	0.9710	1.70	Perpendicular	1.59
863/13/1	0.9710	1.70	Perpendicular	1.74
819/16/1	0.9713	1.70	Perpendicular	1.94
819/16/1	0.9713	1.70	Perpendicular	1.95
819/16/2	0.9718	1.80	Perpendicular	2.37
785/206	0.9734	1.11	Perpendicular	3.10
678/21/47	0.9741	1.35	Perpendicular	2.44
785/204	0.9765	1.29	Perpendicular	2.49
785/204	0.9765	1.29	Perpendicular	3.38
863/13/1	0.9710	1.70	Parallel	4.73
863/13/1	0.9710	1.70	Parallel	5.02
819/16/1	0.9713	1.70	Parallel	3.48
819/16/1	0.9713	1.70	Parallel	3.81
819/16/1	0.9713	1.70	Parallel	4.35
819/16/1	0.9713	1.70	Parallel	4.40
819/16/2	0.9718	1.80	Parallel	3.75
819/16/2	0.9718	1.80	Parallel	4.04
819/16/2	0.9718	1.80	Parallel	4.33
819/16/2	0.9718	1.80	Parallel	4.44
819/16/2	0.9718	1.80	Parallel	4.59
678/21/47	0.9741	1.35	Parallel	2.86
678/21/47	0.9741	1.35	Parallel	2.87

Table 3.4: *Solid Conductivities of ICI Foams Predicted by Solid Conductivity Matrix Model*

Foam Designation (NBE ...)	Foam Void Fraction	Anisotropy *a/b*	Plane Parallel or Perpendicular to Heat Transfer Direction	Predicted Solid Conductivity (mW/mK)
678/21/47	0.9741	1.35	Parallel	2.89
678/21/47	0.9741	1.35	Parallel	3.38

Table 3.4: *Solid Conductivities of ICI Foams Predicted by Solid Conductivity Matrix Model*

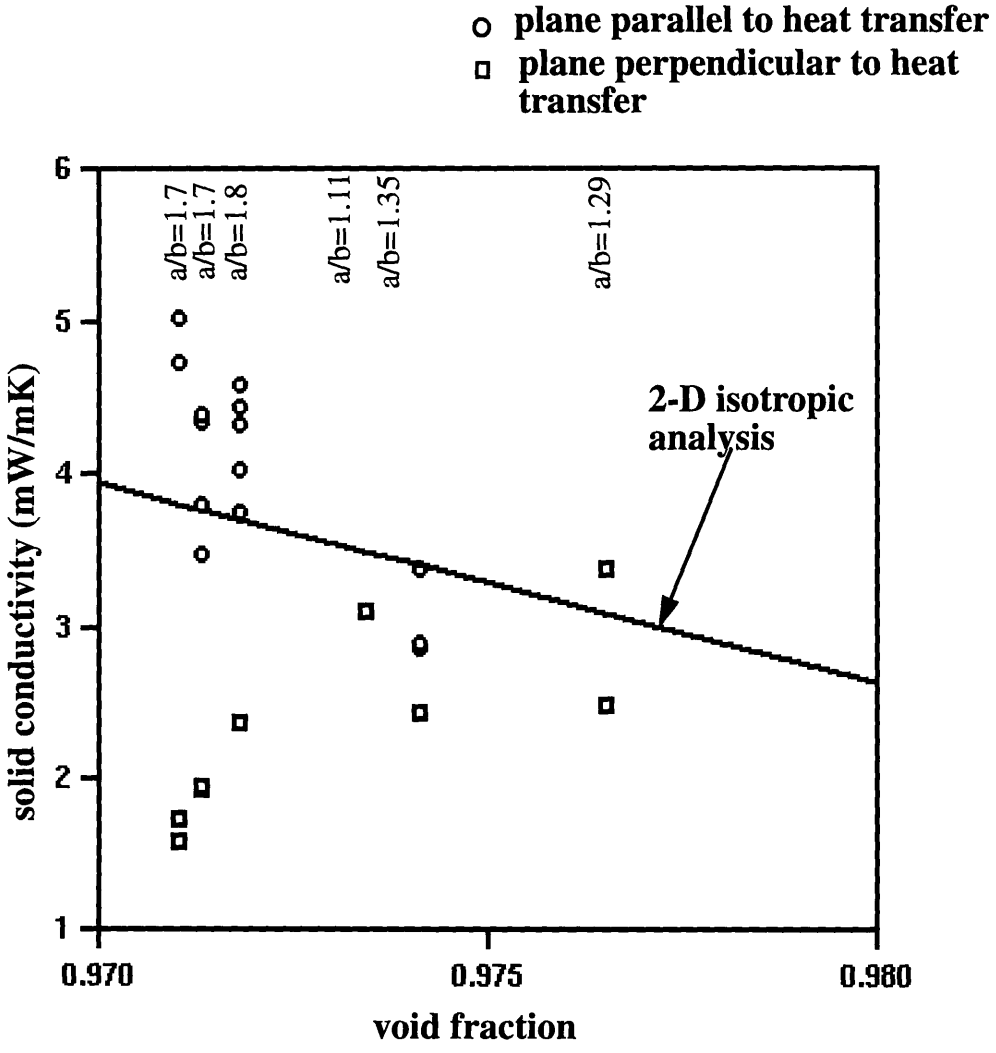

Figure 3.21: *Predicted Foam Solid Conductivities from Confocal Images and from Schuetz Two-Dimensional Analysis (Note: Anisotropy, a/b, Given for Each Foam)*

shown in Appendix C. Schuetz determined that

$$k_{solid} = k_{polymer}\left(\frac{1-\delta}{2}\right) \tag{3.39}$$

This analysis assumes random cell wall orientations, so does not account for anisotropy. One can see that the two-dimensional analysis captures the conductivity features of the matrix solutions for the elongated direction or the plane parallel to the direction of heat transfer. Anisotropy should increase the conductivity from Schuetz's isotropic results. In the foams with the largest degree of anisotropy, which are the foams with void fractions of 0.9710, 0.9713, and 0.9718 respectively, this increase from the isotropic predictions is apparent. In the foam with the small degree of anisotropy, with a void fraction of 0.9741, the conductivities from the matrix program are only 16% lower than the analytical result in the worst case and 0.9% lower in the closest case.

A comparison of conductivities from the images of the two planes helps quantify the effects of cell orientation on solid conduction. From figure 3.21 notice that as the void fraction increases (amount of anisotropy decreases), the ratio of conductivity in the plane perpendicular to the heat flux to the conductivity in the plane parallel to the heat flux increases from 37% to between 72% and 85%.

To see how these results compare to the predictions of theory, consider the three-dimensional anisotropic model of solid conductivity (equation 2.13).

$$k_{s//} = \frac{(1-\delta)}{3} k_p \left[f_s \sqrt{\frac{a}{b}} + 2(1-f_s)\left(\frac{a}{b}\right)^{1/4} \right] \tag{3.40}$$

This is for conductivity in the rise direction. The expression for conductivity in the plane perpendicular to heat transfer is

$$k_{s\perp} = \frac{(1-\delta)}{3} k_p \left[f_s \sqrt{\frac{b}{a}} + 2(1-f_s)\left(\frac{b}{a}\right)^{1/4} \right] \tag{3.41}$$

The ratio of conductivity in the plane parallel to heat transfer to conductivity in the plane perpendicular to heat transfer as predicted by the three-dimensional model is then

$$\frac{k_{s//}}{k_{s\perp}} = \frac{f_s \sqrt{\frac{a}{b}} + 2(1-f_s)\left(\frac{a}{b}\right)^{1/4}}{f_s \sqrt{\frac{b}{a}} + 2(1-f_s)\left(\frac{b}{a}\right)^{1/4}} \tag{3.42}$$

For the six foams analyzed, the predicted ratio of solid conductivity in the plane parallel to heat transfer to the plane perpendicular to heat transfer is presented in Table 3.5.

foam	f_s	a/b	k_s/k_s
NBE 678/21/47	0.34	1.35	1.198
NBE 785/206	0.65	1.11	1.080
NBE 819/16/2	0.54	1.80	1.496
NBE 819/16/1	0.77	1.70	1.539
NBE 863/13/1	0.36	1.70	1.382
NBE 785/204	0.67	1.29	1.211

Table 3.5: *Predicted Solid Conductivity Ratios from Equation 3.42*

These predicted ratios are plotted versus anisotropy factor, *a/b*, in figure 3.22. Also shown in the figure are the ranges of calculated solid conductivity ratios ($K_{//}/K_{\perp}$) from the two-dimensional matrix program. These ranges are represented by the error bars in the figure. Note that the two-dimensional results exaggerate the influence of anisotropy in each case. So care must be taken in extending the quantitative results of the two-dimensional program to the three-dimensional analysis.

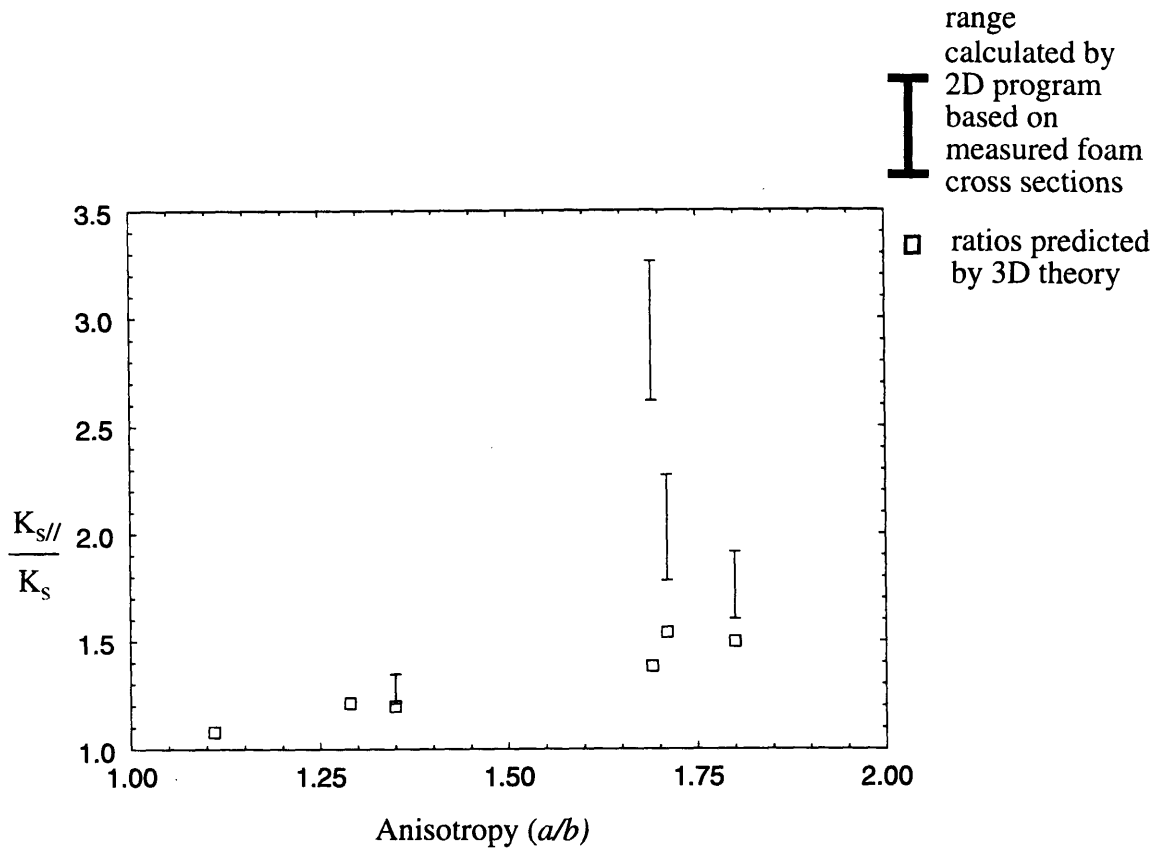

Figure 3.22: *Comparison of Calculated Solid Conductviiy Ratios (Plane Parallel to Heat Transfer Direction to Plane Perpendicular to Heat Transfer Direction) to Solid Conductivity Ratios Predicted by Three-Dimensional Theory*

It is believed that the decrease in solid conductivity with increasing void fraction for the plane perpendicular to the heat flux is due to anisotropy. That is, consider how anisotropy affects the cell walls parallel and perpendicular to the temperature gradient.

The influence of anisotropy will be discussed for cubic foam cells but the same effect of anisotropy on foam structure should be the seen with other cell shapes. Treat isotropic foam cells as a collection of two-dimensional cubes with cell walls of thickness t as in figure 3.23(a). Here, the solid conductivity parallel to the temperature gradient is equal to the solid conductivity perpendicular to the temperature gradient because there is the same amount of solid polymer to conduct heat in both directions. Consider now an anisotropic cell with a major axis parallel to the temperature gradient. For the cells to keep the same density at the same cell wall thickness t the cell walls perpendicular to the temperature gradient will become shorter as in figure 3.23(b). There is now more solid polymer aligned parallel to the temperature gradient in the anisotropic cells than in the isotropic cells. The number of cell walls per unit volume has increased in the direction of the temperature gradient. Therefore there is greater solid conductivity parallel to the temperature gradient. By the same argument, there is less solid polymer aligned perpendicular to the temperature gradient with greater degrees of anisotropy. This results in lower solid conductivity perpendicular to the heat transfer direction with greater degrees of anisotropy. Both trends with anisotropy are seen in the results of figure 3.21.

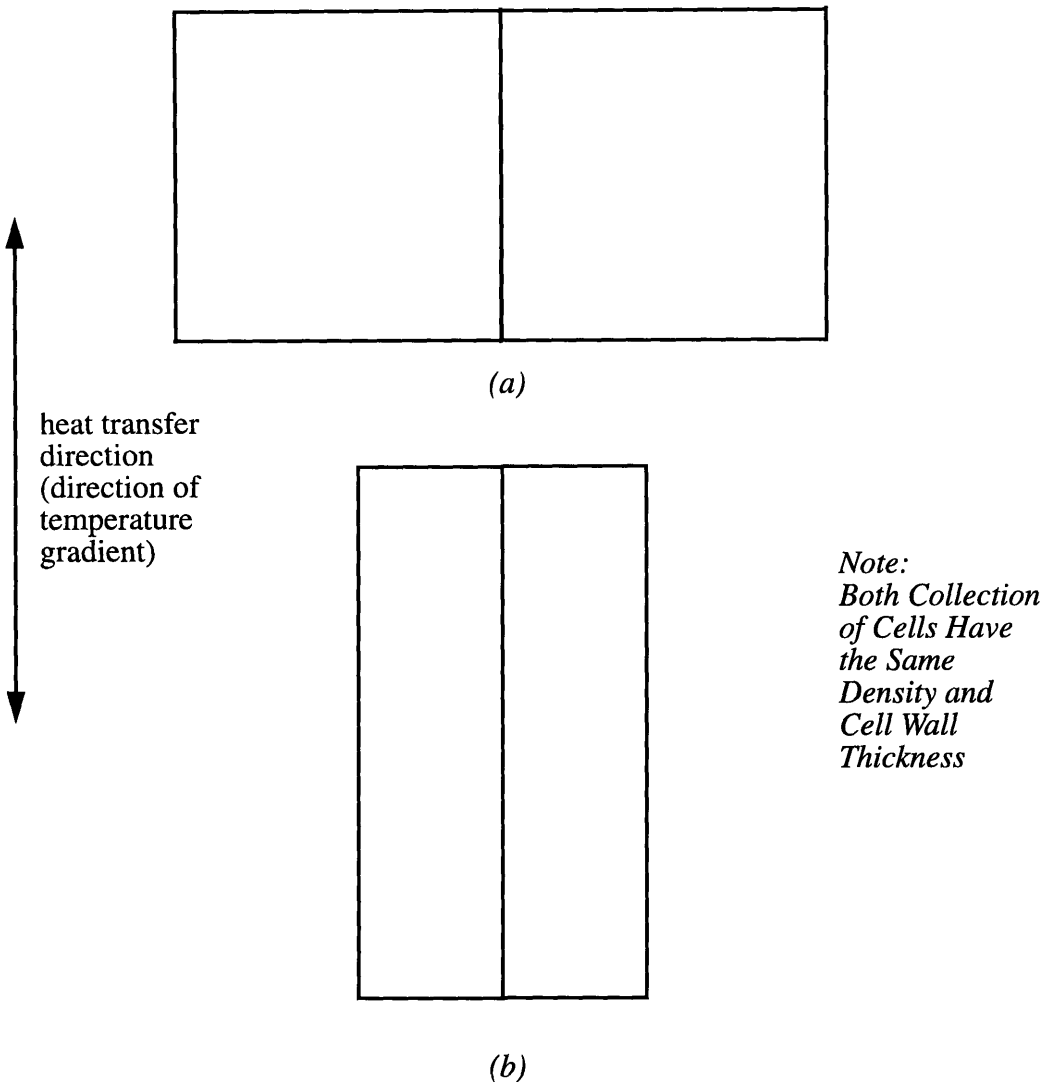

Figure 3.23: *Collection of Idealized Foam Cells (a) Isotropic; (b) Anisotropic*

From measurements of polymer distributions in optical microscope photographs, Torpey similarly concluded that anisotropy redistributes polymer from the plane perpendicular to heat transfer to the plane parallel to heat transfer [16]. His results indicated that anisotropy would increase the conductivity in the plane parallel to heat transfer while decreasing the conductivity in the plane perpendicular to heat transfer.

This analysis does not yet account for relative distribution of solid polymer between the struts and cell walls. Such a factor is accounted for in the theoretical solid conductivity model. As will be shown in Chapter 4, the amount of solid in the cell walls, which is higher than was anticipated, significantly affects the solid conductivity component. Once the solid conductivity matrix program can be automated, this effect can be incorporated into the analysis in the border area variable.

3.11 Electrical Conductivity Measurement Theory

Before the solid conductivity program was developed, the use of electrical conductivity measurements to separate the heat transfer components was attempted. In the early stages of this project, the need for a direct and simple test to accurately assess either the solid or radiative conductivity became apparent. Means to directly examine the radiative contribution were analyzed, but none found to directly measure the radiation without a probe or technique that would alter the radiation environment and skew the test results. The use of electrical conductivity to measure the quantity analogous to the solid conductivity term was much more appealing in that it is a simple test that would not alter the foam makeup or environment.

The use of electrical conductivity to measure the thermal conductivity is an extension of the use of the analogy between electrical and thermal conduction already stated in section 3.4. That is, when subjected to a potential, either a voltage in the case of electrical conduction or temperature difference in the case of thermal conduction, a flux ensues, either electrical current or heat flux, with the material providing a resistance. Thus an analogy between thermal resistance ($1/kA$) and electrical resistance ($1/\sigma A$) exists. Furthermore, since the electrical conductivity of the gas in the foam cells is much lower than that of the solid polyurethane in the struts and cell walls it can be treated as negligible [21]. Then the electrical conductivity really becomes analogous to thermal conductivity through the solid struts and cell walls. This analogy is only strictly true if the polymer acts

as an ohmic conductor, not exhibiting the polarization and high surface conductivity of dielectrics which unfortunately is not the case as will be shown in Section 3.12. The reasoning then is that if the electrical resistance across a foam can be measured, by calibrating the resistance measurements with thermal conductivity measurements, a direct test for the solid thermal conductivity is available.

The electrical resistance across liquid foams which are good conductors has already been extensively analyzed [22]. In a foam comprised of gelatin struts and cell walls, where most of the material is located in the cell walls, Lemlich experimentally measured the foam resistance. He also derived a relationship predicting the electrical conductivity of the foam based upon the foam structure. These foams are solely rod-like members or 100% struts. This relationship is

$$\frac{\sigma_f}{\sigma_s} = \frac{A_{xs-struts} L_V}{3} \tag{3.43}$$

where

σ_f = foam electrical conductivity (Ω-1)

σ_s = solid electrical conductivity (Ω-1)

A_{xs} = cross-sectional area of strut (conducting member)

L_V = total length of struts per unit volume

The predicted relationship agrees with Lemlich's data well [23] at low foam densities. Even though these results were carried out for liquid gelatin foam, the author claims that the technique also applies to "solid foam of sufficiently low density and sufficiently open cell structure as to approach a lattice" [22].

Assuming that electrical conductivity does provide a reasonable analogy to solid thermal conductivity, how would the foam electrical conductivity relate to the solid foam morphology? The reader is referred to the article in the *Journal of Colloid and Interface*

Science [22] where Lemlich relates the electrical conductivity through an array of struts to the strut dimensions (equation 3.43). Comparing two polyurethane foams where the solid electrical conductivities (σ_s) are the same and the structures are 100% struts, the ratio of electrical conductivities is

$$\frac{\sigma_{f1}}{\sigma_{f2}} = \frac{A_{xs1}L_{V1}}{A_{xs2}L_{V2}} \tag{3.44}$$

The mass fraction of polyurethane in the struts is related to the dimensions of the strut (see equation 2.43)

$$f_s = \frac{\rho_s L_V A_{xs}}{\rho_f} \tag{3.45}$$

where ρ_s is the density of the solid polyurethane and ρ_f is the density of the foam. Substituting the mass fractions for the strut dimensions ($A_{xs}L_V$) and recognizing that ρ_s is the same for both foams, the ratio of electrical conductivities through the struts of two foams is simply related to the foam morphologies,

$$\frac{\sigma_{f1}}{\sigma_{f2}} = \frac{f_{s1}\rho_{f1}}{f_{s2}\rho_{f2}} \tag{3.46}$$

Note that other structural properties like anisotropy factor are assumed to be the same for both foams.

3.12 Polyurethane as a Dielectric

Experimentally, several factors have to be established for the electrical conductivity analogy to be useful. First, it has to be established that the conductivity of polyurethane foam can be measured. Next it has to be established whether the measured conductivity of polyurethane follows a simple relation as Lemlich proposed for aqueous foams, or

whether spurious effects overwhelm the measured value. Finally, a clear relation between the thermal and electrical conductivities has to be established to calibrate electrical measurements for thermal measurement use.

Unfortunately, difficulties arise in establishing the first experimental factor, being able to measure the resistance of polyurethane foam. Polyurethane is a *dielectric*, a material that as an insulator has a conductivity well below $10^{-8}\Omega^{-1}cm^{-1}$. Furthermore, as a current is applied to a dielectric, bound charges such as reorienting dipoles contribute to the apparent current for a time. This causes the apparent measured current to decay exponentially as in figures 3.25 through 3.27. For more detailed information on the actual processes involved in the current decay associated with dielectrics, the reader is referred to [24] or any of the other many sources on dielectric responses to applied fields.

Equipment to measure the electrical resistance of polyurethane must not only be able to measure the resistance as the field is directly applied, but the "steady" value after much of the polarization current has decayed. Steady is taken with care here since it is not at all obvious whether this steady current is not the result of further polarization with a time constant much larger than the amount of time of measurement. It is steady electronic or ionic conduction that is needed however for there to be an analogy to heat transfer processes.

We again get back to the problem of dielectrics having by their nature a very low conductivity. For standardization purposes, in the literature the conductivity that is reported is that after the electric field has been applied to a sample for one minute. Even with this short arbitrary choice of electrification, highly sensitive equipment is needed. *The Encyclopedia of Electrical Insulating Materials* [25] reports one minute conductivities of polyurethane foam less than $10^{-15}\ \Omega^{-1}cm^{-1}$. *Insulating Materials for Design and Engineering Practice* [26] reports one minute conductivities less than $10^{-14}\Omega^{-1}cm^{-1}$. With a typical testing slab of area 6"x6" ($232.26cm^2$) and thickness 0.02" (0.0508cm), this would correspond to having to measure a resistance of

$$R = \rho\frac{t}{A} = 2.2\times10^{10}\Omega \tag{3.47}$$

Since megohmeters do not typically measure resistances this high, and since the steady resistance is expected to be several orders of magnitude smaller than this, we resorted to measurements on a DC electrometer and amplifier.

As described in "Measurement of Multimegohm Resistors" [27], a vibrating reed DC electrometer and amplifier is a combined device that converts DC potentials into AC potentials by means of the vibrating reed. The AC potential is then amplified and rectified and the resulting DC resistance becomes measurable. The General Radio Type 1230A DC Electrometer and Amplifier used in this experiment allowed measurements up to $5x10^{14}\Omega$

.

Since the measured current is so low and sources of error can be on the order of or greater than the desired current, a special test setup is required. First, the foam sample has to be shielded from outside stray currents. Even electromagnetic interference caused by passing one's hand over an exposed sample causes the measurements to jump drastically. So the electrodes are placed in a closed metal box insulated from ground as in figure 3.24. Next, the effects of contact resistance has to be carefully avoided. Therefore, to ensure contacts between the brass electrodes of the electrometer and the sample, aluminum electrodes are attached to the surfaces of the sample using a paper-thin layer of silicon vacuum grease. Better, but much more expensive, contacts can be fabricated by thermally depositing a layer of gold, silver, or platinum on the sample surfaces or by painting on a layer of silver paint as outlined in the ASTM dielectric measurement guide [28]. To further ensure that proper contact was achieved, plates ranging in weight from 4 to 13.5 pounds were placed upon the electrodes to apply pressure. The complete test setup is again shown in figure 3.24.

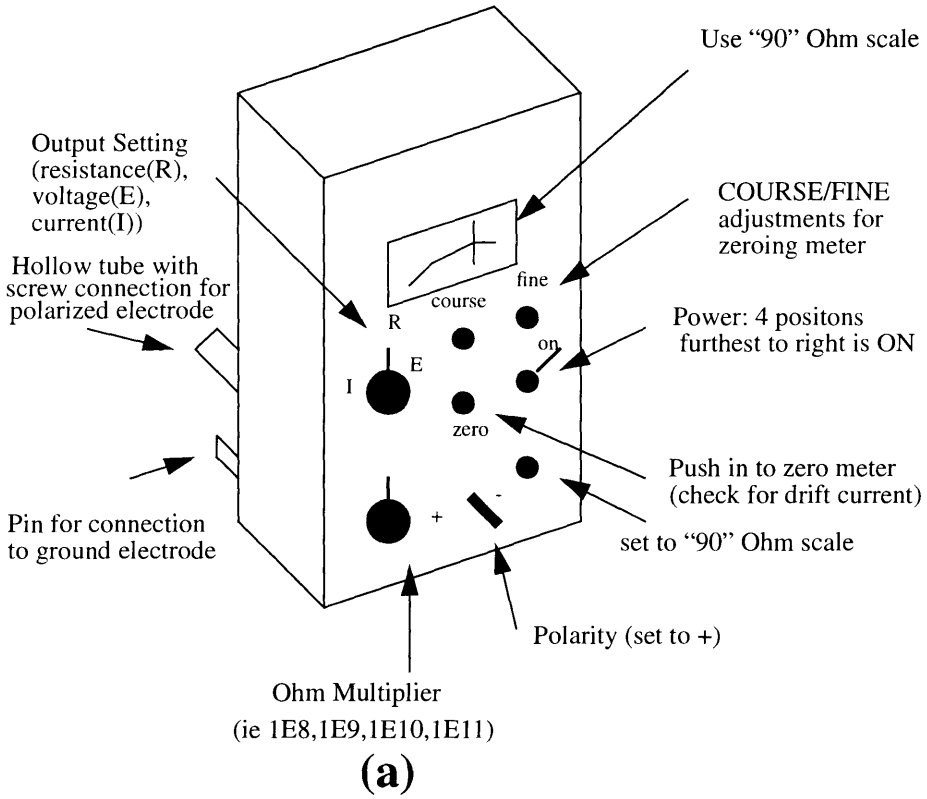

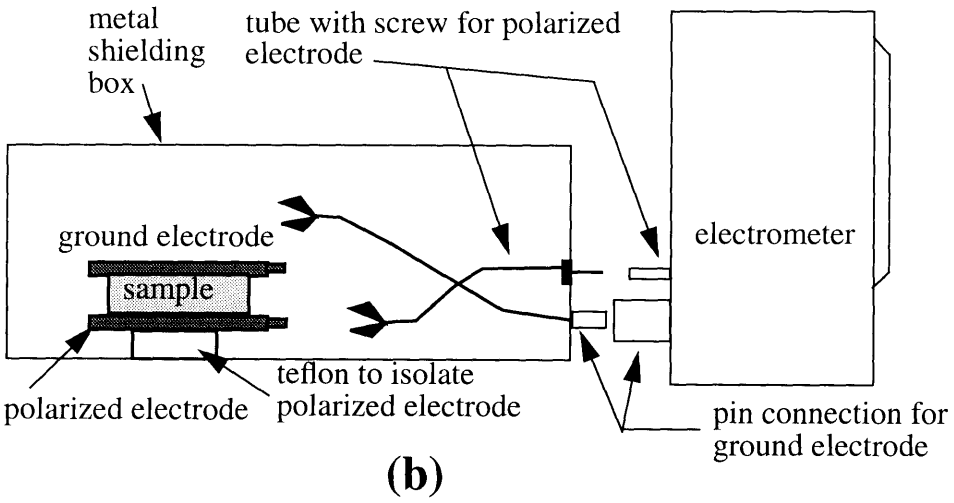

Figure3.24: *Setup for Electrical Conductivity Tests: (a) Electometer; (b) Shielding and Connections*

3.13 Electrical Test Procedure

After the foam specimen had been cut to the proper dimensions of 6"x6" and thickness near 1/4", the aluminum electrodes were applied to the foam faces by means of a thin layer of Dow Corning silicon grease. The electrometer was warmed up for several hours and then short circuited to accommodate for any drift potential. The specimen was then placed between the brass electrodes, weights, if any, placed on the electrode, and the top shielding plate placed on the test box. The current was then applied to the specimen and allowed to exponentially decay until the current did not change noticeably for several hours. In a few instances, the current was allowed to decay for two days. During the course of current decay, measurements were periodically taken to chart the exponential decay.

3.14 Electrical Test Results

Since equation 3.46 predicts that the steady electrical conductivity would be directly proportional to the foam density, three foams of densities 32kg/m^3, 45kg/m^3, and 60kg/m^3 were tested. The characteristics of the morphologies of these foams are listed in Table 3.6.

Foam	Density (kg/m^3)	Cell Diameter (mm)	Strut Area (mm^2)	f_s
1	32	0.422	4.49E-4	0.84
2	45	0.402	3.59E-4	0.53
3	60	0.527	5.29E-4	0.34

Table 3.6: *Characteristics of Foams Used in Electrical Conductivity Tests*

Typical resistance versus time curves for each of the foams are displayed in figures 3.25 through 3.27. The conductivities of each foam with applied weights is shown in

figure 3.28.

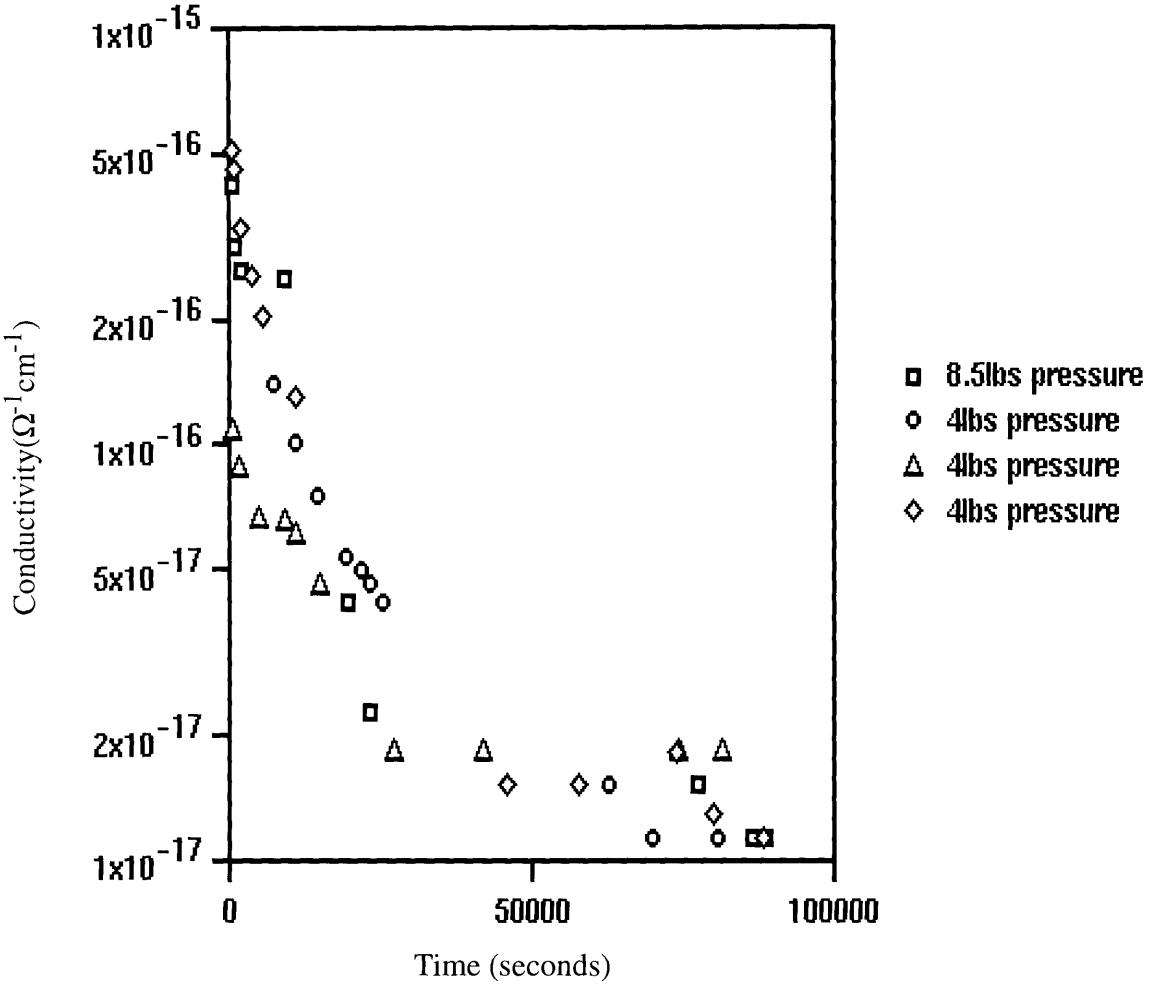

Figure3.25: *32kg/m^3 Conductivity Time Histories*

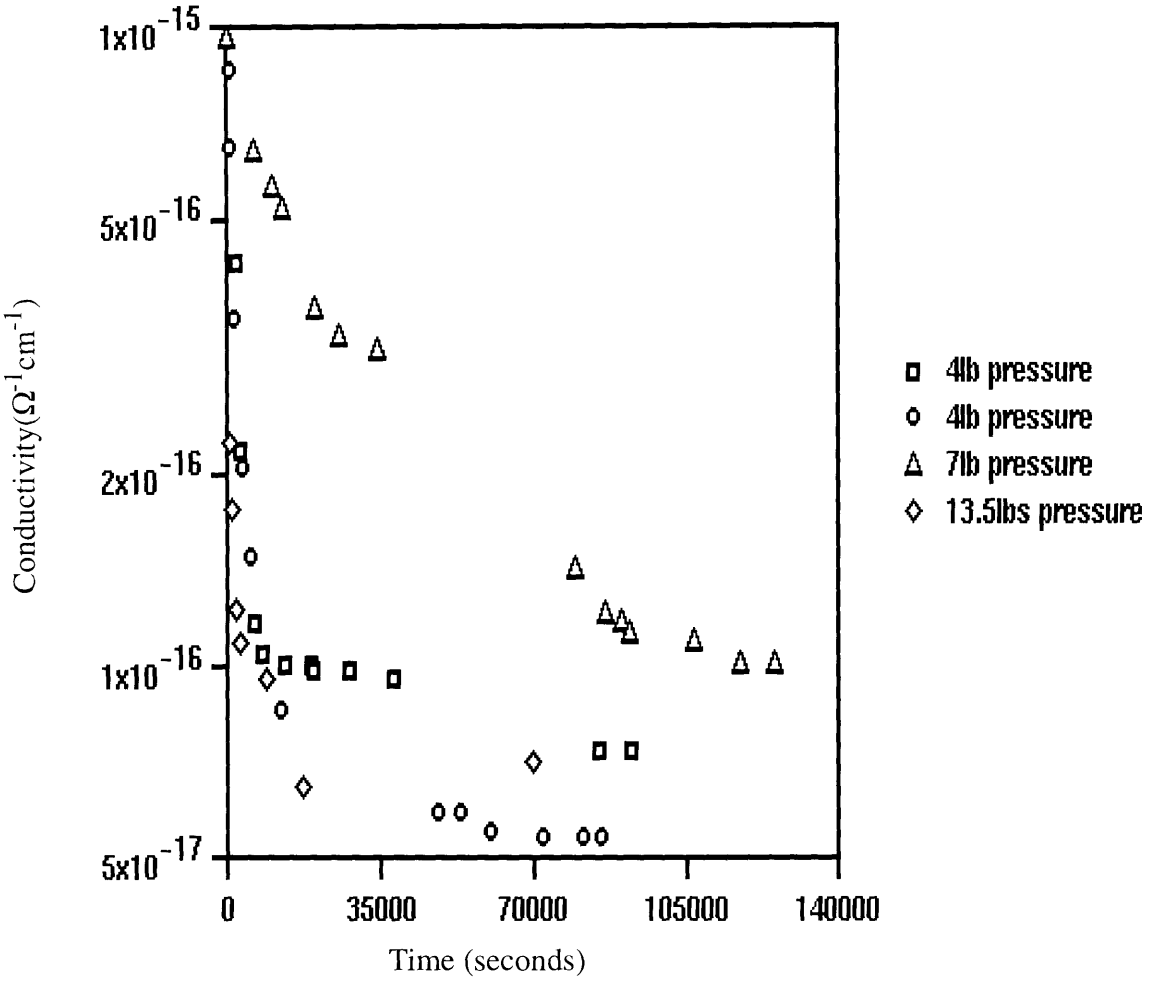

Figure3.26: *45kg/m^3 Conductivity Time Histories*

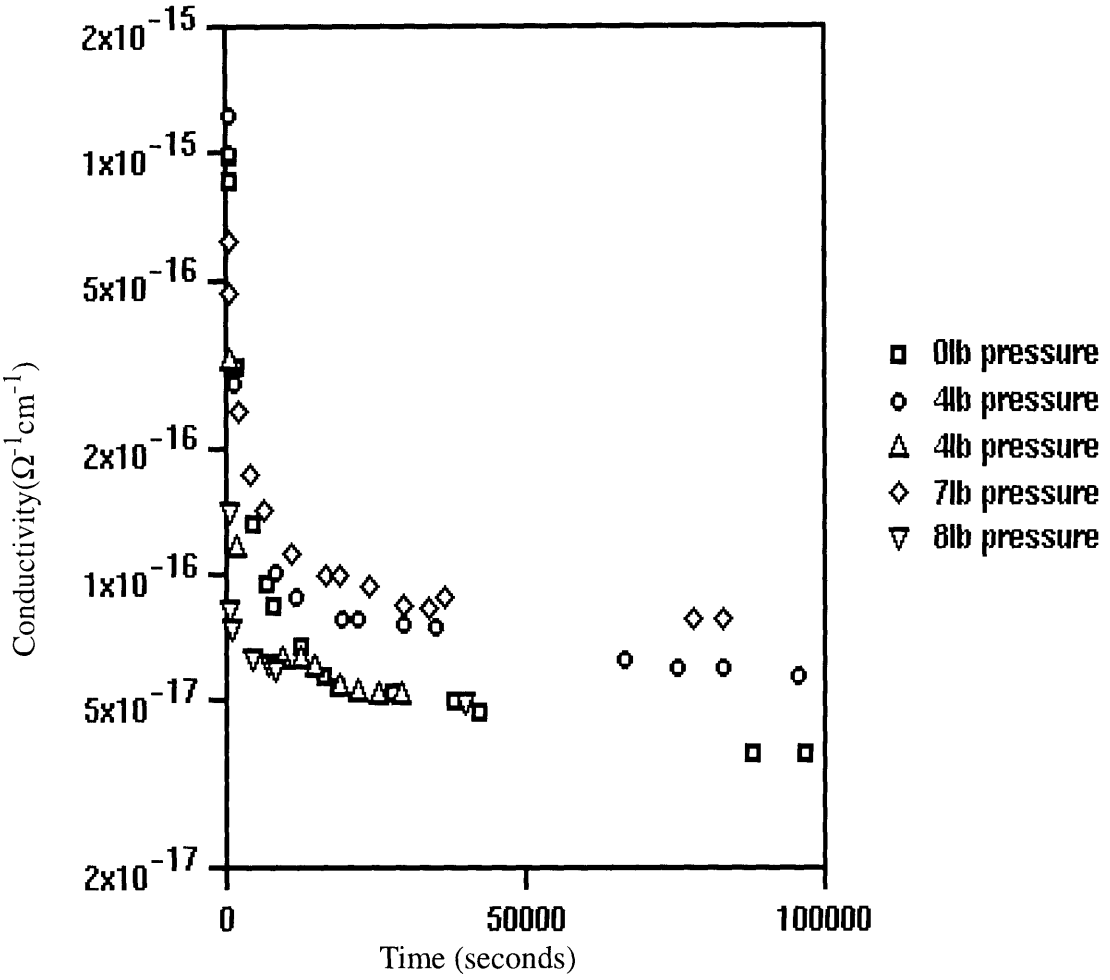

Figure3.27: *60kg/m^3 Conductivity Time Histories*

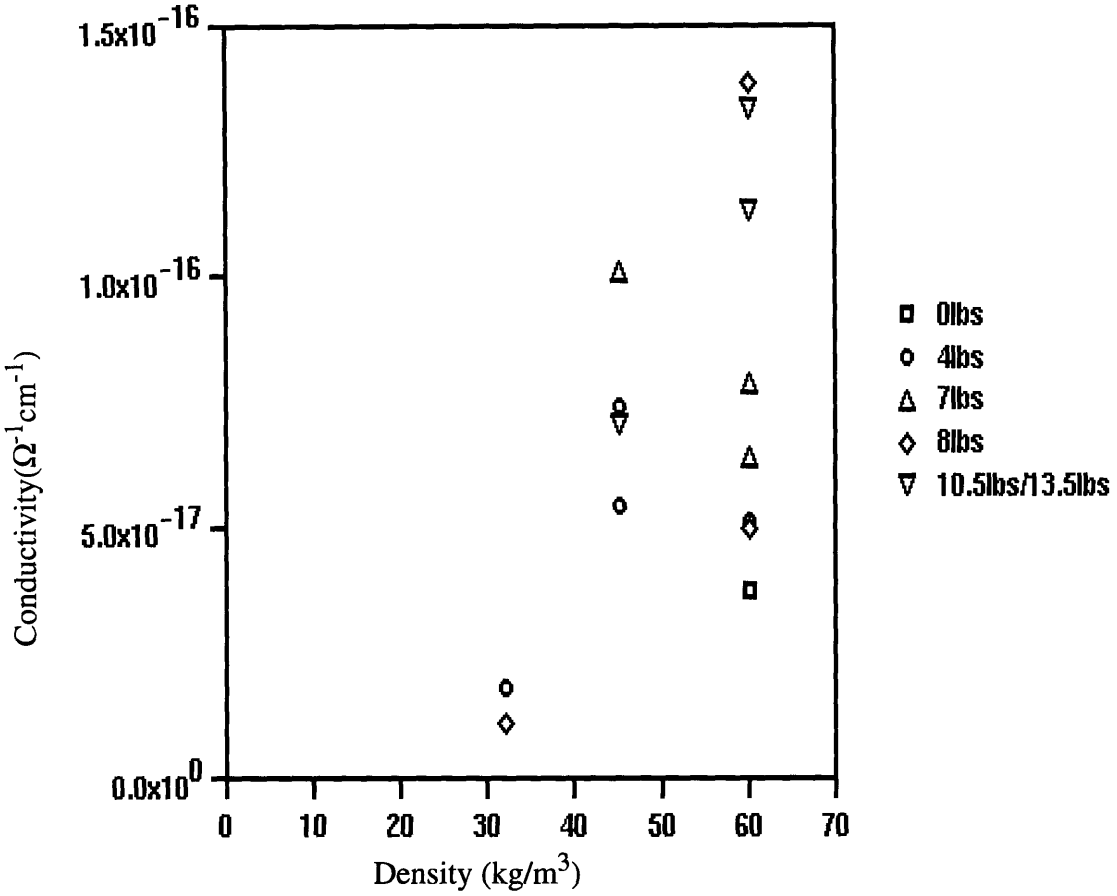

Figure3.28: *Electrical Conductivity Vs. Foam Density for Different Applied Pressures*

As can be seen in figure 3.28, the conductivity does increase with increasing foam density. However, even allowing for a considerable mass redistribution as foam density increases, the observed conductivity increase is much greater than expected. This can be seen in Table 3.7 where the ratios of the measured 60kg/m^3 electrical conductivity to the measured 45kg/m^3 conductivity and to the 32kg/m^3 conductivity are listed. Also listed are the conductivity ratios predicted by equation 3.46 with the measured strut mass fractions, with the mass fractions remaining constant, and with the mass fractions increasing linearly from f_s=0.3 at ρ_f=32kg/m^3 to f_s=0.9 at ρ_f=60kg/m^3.

conductivity ratio	Ratio of Measured σ's	Predicted Ratio from Equation 3.46 using Measured Strut Mass Fractions	Predicted Ratio from Equation 3.46 using Constant Strut Mass Fractions	Predicted ratio from Equation 3.46 using Linearly Increasing Strut Mass Fractions
σ_{60}/σ_{45}	1.33	0.855	1.33	2.07
σ_{60}/σ_{32}	7.87	0.759	1.88	5.63
σ_{45}/σ_{32}	5.90	0.887	1.41	2.71

Table 3.7: *Predicted vs Measured Conductivity Ratios*

For calibration with thermal conductivity, the solid polyurethane conductivity would have to be measured as well. ICI Polyurethanes sent a solid polyurethane laminate of the same chemistry as the solid polymer in foams but without the surfactants and catalysts found in foams. This 15"x15" 0.17" thick block was then tested for electrical conductivity. The conductivity history for this solid polyurethane is shown in figure 3.29 with two test runs shown. The conductivity was determined to be $3.25 \times 10^{-17} \Omega^{-1} cm^{-1}$.

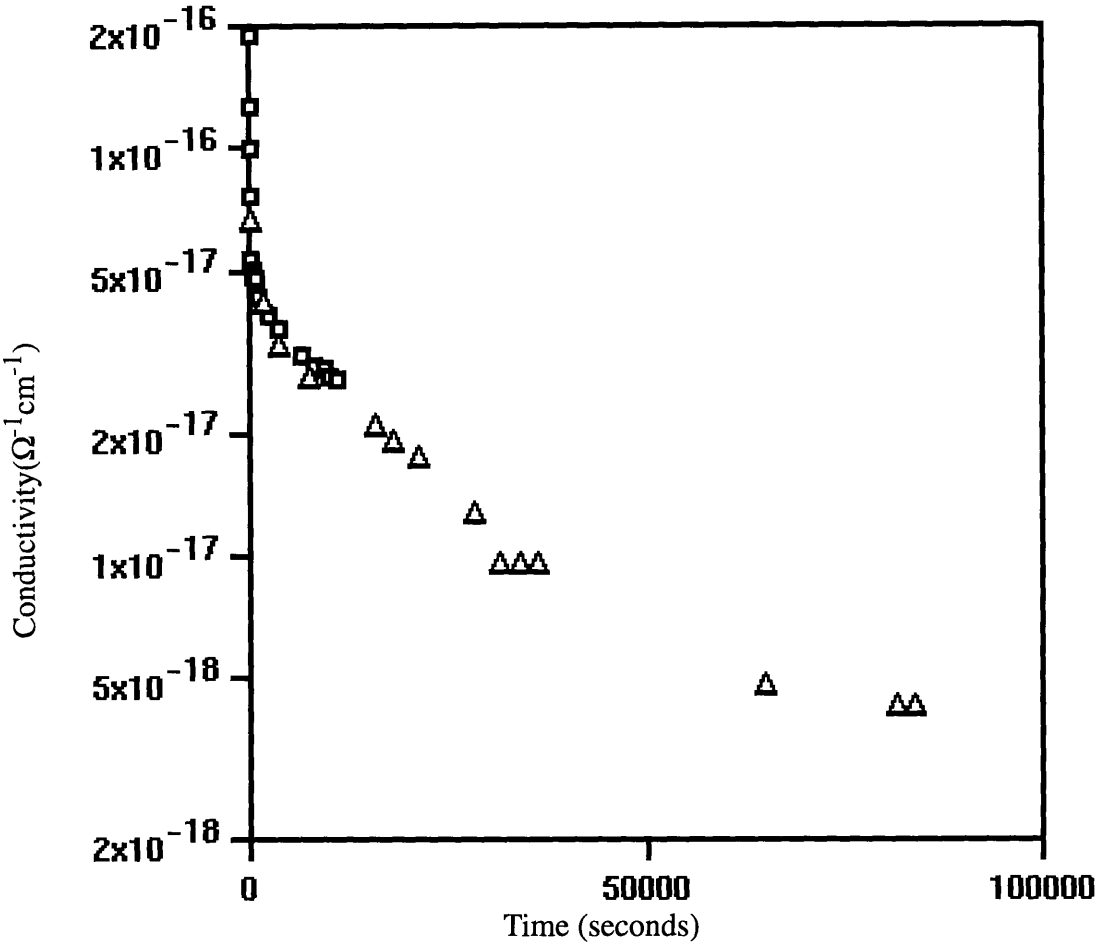

Figure3.29: *Solid Polyurethane Electrical Conductivity History*

3.15 Electrical Conductivity Conclusions

In looking at the data, a problem arises. The conductivity ratios are well above the expected ratios, even accounting for a large mass fraction redistribution. Adding to the problem is the fact that the solid electrical conductivity is not much larger than foam conductivities as would be expected but instead is lower than the denser foams.

It was at this point that the technique was reanalyzed. The influence of moisture on the measured conductivity has not been taken into consideration. Contact resistance is not

thoroughly eliminated. The influence of trace impurities could also be the dominating factor. The setup could be adjusted to eliminate the effects of changes in humidity. Specimens can be dried in a desiccated oven for several weeks at temperatures above 373K and below 403K for several days and then stored in a desiccated bell jar. This was done with some later samples but it is likely that moisture again played a significant role as the tests were in progress and the samples were exposed to ambient humidity. To eliminate the possibility of moisture during testing the setup can be wrapped in a plastic glove bag. Then a dry gas such as N_2 could be circulated around the specimen for the duration of the testing. Contact resistance could be minimized by implementing the electrodes paints used in electron microscope work or thermally evaporating electrodes onto the specimen.

Judging from the time necessary to adapt the setup and the expense involved in eliminating contact resistance, electrical conductivity experts at the National Institute of Standards and Technology (NIST) were consulted as to the mechanisms of conductivity and methods to eliminate errors. According to Fred Mopsik [29], in the experience of testing at NIST it is not likely that it is electronic/ionic conduction but rather a polarization, the buildup of space charge, that is causing the apparent conductivity. The only polymer with which NIST has seen true electronic/ionic conduction are some dielectric epoxies. Furthermore, warnings were given that the possible errors could be the compound effect of polyurethanes sensibility to both impurities and to moisture. Given that the goal of implementing this technique is to provide a simple measurement on production foams, further development of this technique was halted. Further work could be done to see if indeed the errors are accounted for solely by moisture and contact resistance, which could be eliminated in the setup and allow for the simple measurement technique posed. It is likely however that a simple measuring technique is not possible from this method.

Chapter 4

Radiative Conductivity and Morphology Influence

4.1 Direct Transmission Measurement of Radiative Conductivity

The first approach to determining the radiative conductivity of small-celled foams is one that has been developed over the course of a decade at MIT. The method is to measure the optical properties of the polyurethane foam and calculate the radiative conductivity from the model described in Chapter 2. This in conjunction with thermal measurements of the overall heat transfer and with morphology measurements of the foam allows a full description of the conductivity components. So, to determine the radiative conductivity, the transmissivity of the foam in the infrared spectrum is measured, allowing the calculation of the extinction coefficient. The infrared spectrum is important since, for a source radiating at 300K, roughly 95% of the energy is in the infrared spectrum.

The procedure of calculating the extinction coefficient from transmission data is as follows. First several samples of a foam are sliced very thin (0.021" to 0.06"), but using a technique that minimizes surface damage. Surface damage from the tearing of cell walls causes scattering of radiation and skewing the transmission results [18]. Next the spectral transmissivities of several samples of a foam having different thicknesses are measured and recorded using an infrared spectrometer. The thicknesses of these samples are measured using a paper micrometer. Finally, using the data from several samples of different thicknesses, the Rosseland mean extinction coefficient is calculated.

Several techniques have been explored at MIT in providing foam sections of uniform thickness while at the same time trying to minimize surface damage that causes scattering. Cutting foam slices using a cryogenic microtome appears to satisfy both requirements [14]. The reader is referred to Mark Schuetz's thesis [14] as to a full description of the

equipment. Basically, the microtome allows a foam sample to be mounted on a moveable stage. The stage temperature is set to 248K while the ambient chamber is at 238K. The moveable stage then slides down to a stationary blade that slices through the sample. The process of freezing the sample and then slicing helps to prevent the tearing of cell walls that accompanies slicing foam samples with a razor at room temperature or by cutting the sample with a low-speed saw.

Once several thicknesses of foam have been sectioned on the microtome, the transmission characteristics of each sample is recorded using a Nicholett IR44 Spectrometer. Much of the operation of the IR44 Spectrometer is discussed by Mozgowiec [18]. The spectrometer consists of a high temperature source emitting infrared radiation as sketched in figure 4.1. Mirrors collect this radiation into a beam. The beam is sent through a chamber purged of carbon dioxide and water. Two beams are collected and recorded by the spectrometer. The first, which is collected before the sample is set in place is the *background* spectrum. The second beam which is collected is passed through the sample. A set of mirrors collects a finite solid angle of radiation leaving the sample. The collection angle and beam divergence which define the solid angle reaching the detector (shown in figure 4.2) were both determined to be between 15^{o} and 40^{o} by Mark Sinofsky [15]. Prisms break both beams down into spectral elements while detectors measure the intensity of radiation as a function of wavelength. The transmissivity is the ratio of intensity collected from the sample to the intensity of the background. The spectral transmissivities are then displayed and recorded as functions of wavenumber which is the inverse of the wavelength. The spectral range of the Nicholett Spectrometer is $400cm^{-1}$ to $4800cm^{-1}$ (25μm to 2.1μm). This covers roughly 85% of the energy emitted by a source at room temperature (T=300K).

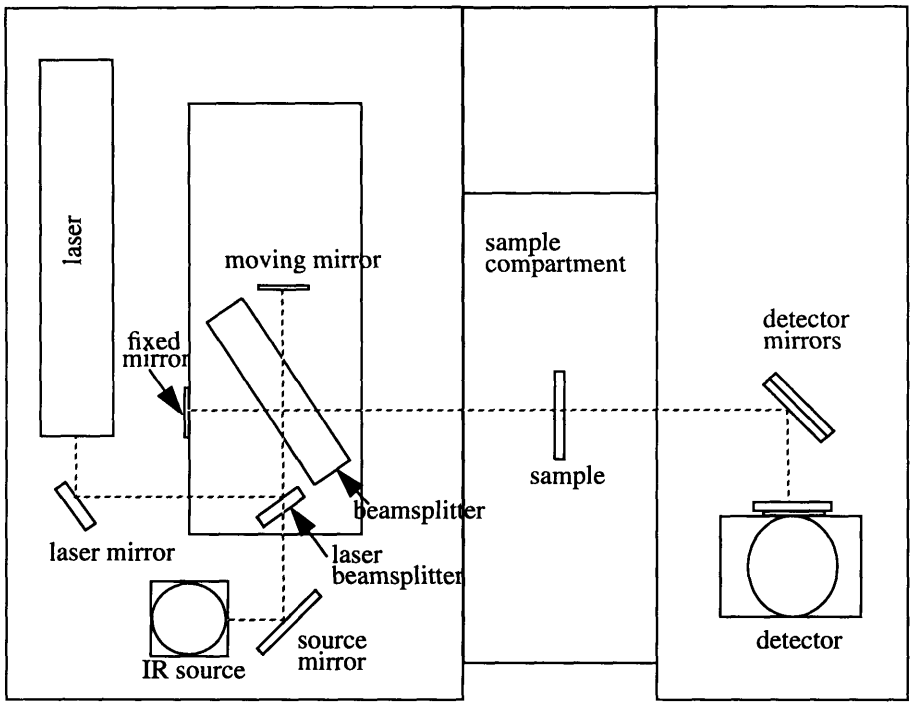

Figure 4.1: *Sketch of IR44 Spectrometer (Reproduced from* [40])

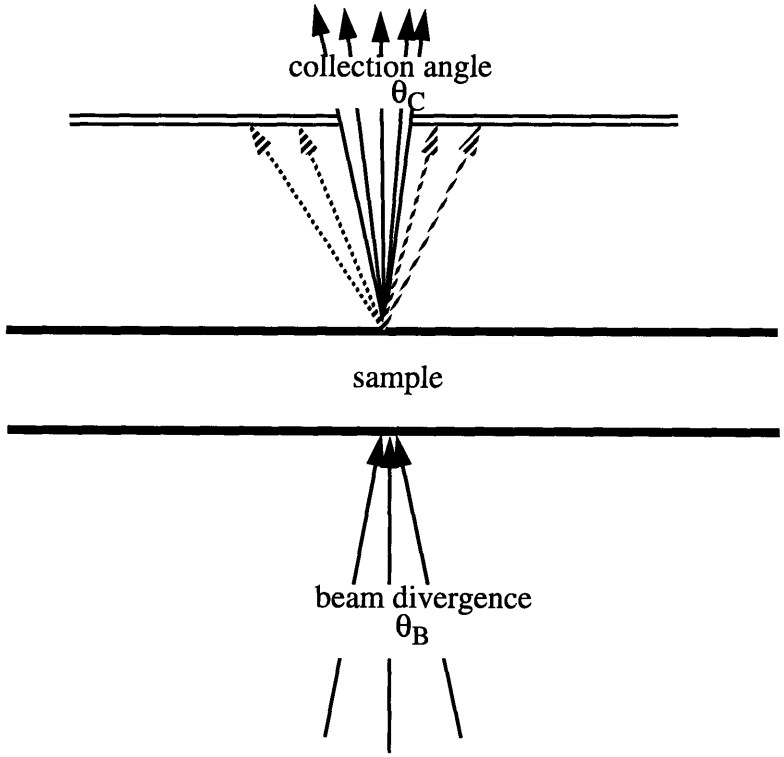

Figure 4.2: *Sketch of Spectrometer Collection Angle and Beam Divergence* [15]

The first step in operating the spectrometer is to allow it to purge water and carbon dioxide from the sample chamber for 10 minutes. After the resolution and number of scans used to get an average result are set, $2cm^{-1}$ and 128 respectively, the background spectrum is collected. This is done only once. Next, the first sample is loaded in the chamber and the chamber is given time to purge. The transmissivity of the sample is recorded, displayed, and stored to disk in a form similar to that shown in Appendix D. A sample transmissivity spectrum is shown in figure 4.3. Following the first sample, each of the other samples are loaded and their transmissivities recorded in the same manner.

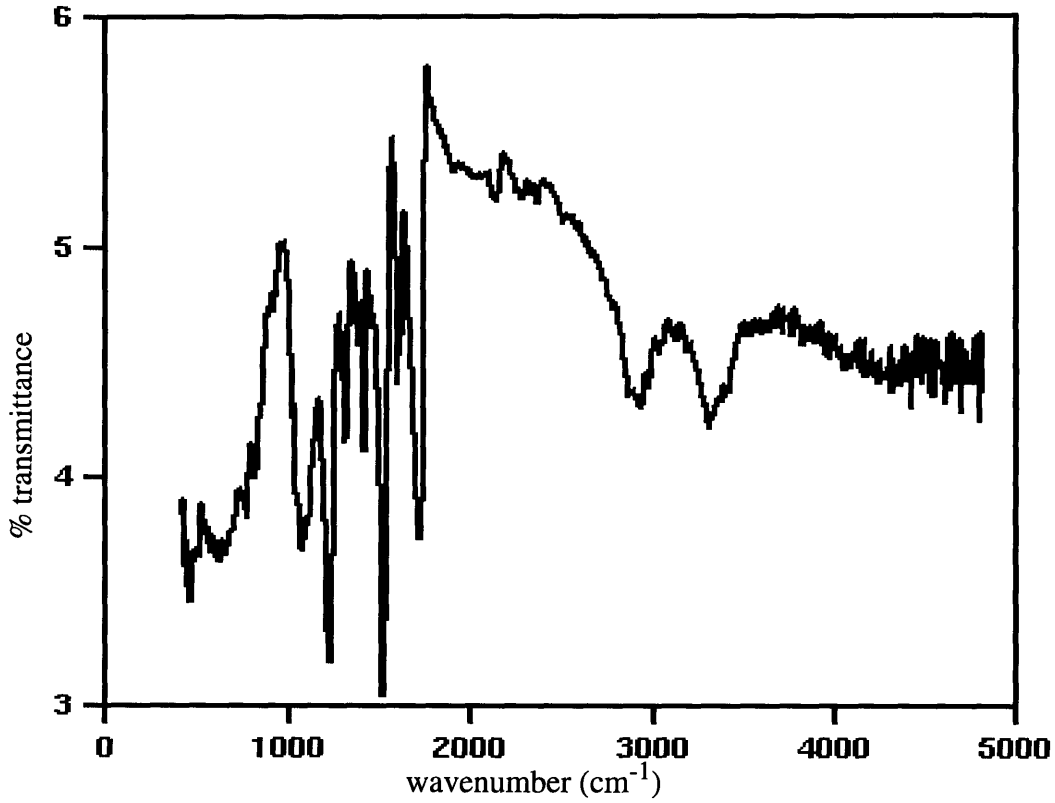

Figure 4.3: *Sample Spectral Transmissivity (Foam NBE 819/16/2, Thickness=0.30")*

A rough wavelength averaged transmissivity can be obtained from the spectrometer. Specifying the wavenumber range over which averaging is to take place and using the "integrate" command, the spectrometer outputs a "peak area", A_p. The peak area is the

value of the area above the spectrum shown in figure 4.3 (on a zero-to-one scale) to a horizontal line at a transmissivity of one. The units of the area are obtained by multiplying the units of wavenumber by the transmissivity on a zero-to-one scale. For example, if the spectrum in figure 4.3 were a horizontal line at 10% transmittance, the peak area from $400cm^{-1}$ to $2000cm^{-1}$ would be

$$A_p = (2000cm^{-1} - 400cm^{-1})\ (1 - 0.1) = 1440 \tag{4.1}$$

The average transmissivity is then

$$\bar{\tau} = 1 - \frac{A_p}{\eta_2 - \eta_1} \tag{4.2}$$

where $(\eta_2 - \eta_1)$ is the wavenumber range over which averaging takes place. In the plot of $-\ln(\bar{\tau})$ versus sample thickness, the slope is a measure of the wavelength average extinction coefficient. As shown in Appendix G for the results of the six foam samples tested, this rough approximation provides a rather good estimate of the Rosseland mean extinction coefficient.

The sample thicknesses are then measured using a paper micrometer. The paper micrometer allows thickness measurements to be made with an accuracy of 0.001". The transmissivity files from the spectrometer are then modified by deleting the header and inserting the sample thickness at the top of each file (see Appendix D).

All of the transmissivity files for a given foam are then used as input for the program "Rosseland" which is given in Appendix D. With L the thickness of a sample, K_λ the spectral extinction coefficient, and τ_λ the spectral transmissivity, the extinction coefficient is calculated for each wavenumber interval of width $\Delta\eta = 5.79cm^{-1}$ such that

$$K_\lambda = -\frac{ln(\tau_\lambda)}{L} \tag{4.3}$$

The average of the spectral extinction coefficient for the different slices is calculated making sure that at zero thickness the transmissivity would be zero. The spectral extinction coefficients are then Rosseland averaged. That is, the Rosseland mean extinction coefficient is determined from

$$\frac{1}{K_R} = \frac{\int_{\Delta\lambda} \frac{1}{K_\lambda}\left(\frac{\partial e_{\lambda b}}{\partial e_b}\right) d\lambda}{\int_{\Delta\lambda}\left(\frac{\partial e_{\lambda b}}{\partial e_b}\right) d\lambda} \tag{4.4}$$

This procedure was followed for six small-celled foams provided by ICI. Extinction coefficients were measured parallel to the rise direction or perpendicular to the foam facers as shown in figure 4.4. This direction would correspond to the direction of heat transfer for foams placed *in situ* and corresponds to the cell's elongated direction as can be seen in SEM photographs showing this direction (figure 4.5). First samples were cored with a 21/32" cork borer parallel to the rise direction. The cored sample was then cut with the cryogenic microtome as described earlier yielding thin slices as shown in figure 4.4. These samples were then measured in the spectrometer with the beam parallel to the rise direction, or the cell's elongated direction. A few of the foams, which are marked, fell apart when sectioning with the microtome was attempted. So for these, sections were obtained using razor blades at room temperature, so some error due to surface damage

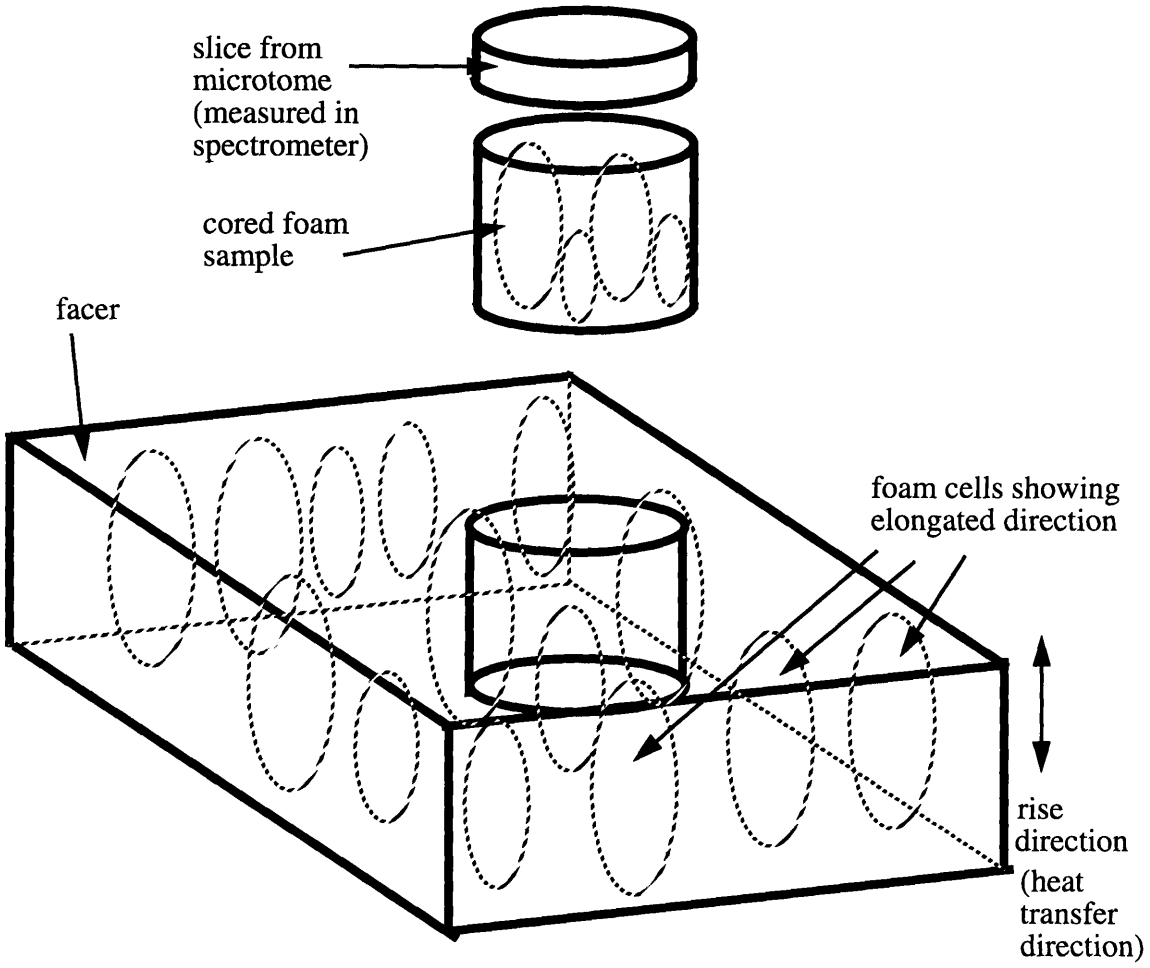

Figure 4.4: *Sketch of Sample Preparation for Transmission Measurements*

Figure 4.5: *SEM Photograph Showing Elongated Direction (Parallel to Rise Direction or Orientation Axis)*

should be expected. The extinction coefficients for four of the foams were also measured perpendicular to the heat transfer (rise) direction. The extinction coefficients measured parallel and perpendicular to the heat transfer direction are listed in Table 4.1. Also listed in Table 4.1 are the correlation coefficients for the extinction coefficients. These are a factor from 0 to 1 that describe how much individual sample measurements deviate from

the calculated slope (extinction coefficient). A factor of 1 indicates perfect correlation. The calculation procedure for the correlation coefficient is listed in the code in Appendix D. Even though extinction coefficients measured in both directions are listed, predictions of the radiative conductivity are based on the extinction coefficient parallel to the rise direction, $K_{//}$.

foam	mean cell diameter (mm)	$K_{//}$ (cm^{-1})	correlation coefficient	$K_{perp.}$ (cm^{-1})	correlation coefficient
NBE 678/21/47	0.109	61.0	0.9161	65.0	0.8470
NBE 785/206	0.188	49.0	0.9925	--	--
NBE 819/16/2	0.192	40.7	0.9545	50.5	0.9448
NBE 819/16/1	0.238	38.4	0.8741	--	--
NBE 863/13/1	0.284	27.0	0.8277	35.5	0.9872
NBE 785/204	0.363	34.9	0.8544	36.9	0.9820

Table 4.1: *Extinction Coefficients Calculated from Measured Transmission Data*

Measurements parallel to the heat transfer direction are also shown in Table 4.14 at the end of the chapter along with the results of morphology measurements explained in following sections. Notice that the radiative conductivity calculated from the Rosseland equation using the measured extinction coefficient decreases with cell size. This can be seen in figure 4.6.

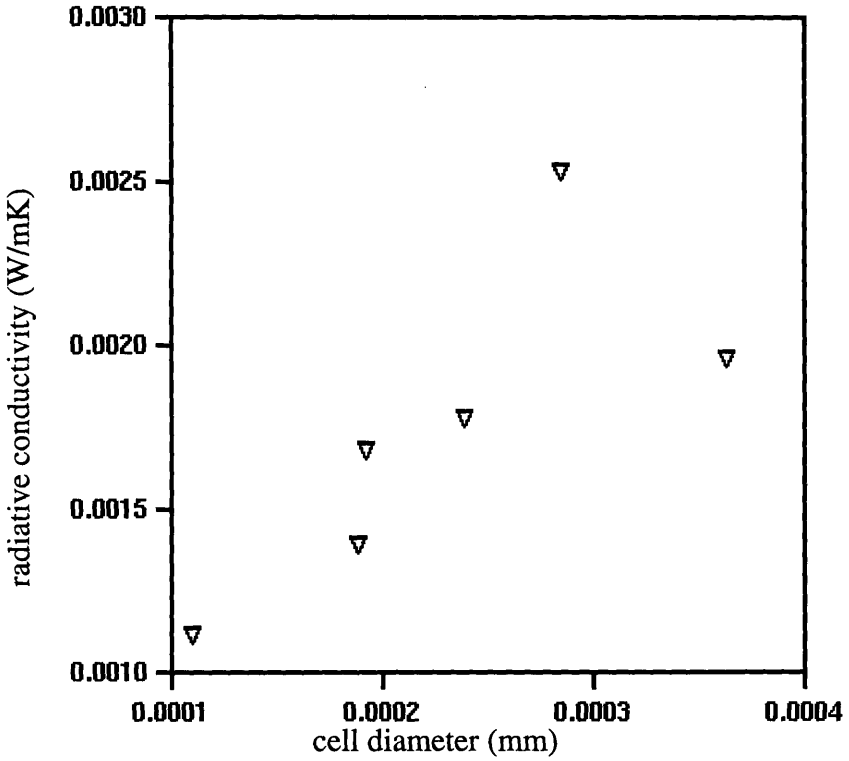

Figure 4.6: *k_{rad} Predicted from Rosseland Equation and Transmission Measurements*

4.2 Measurement of Solid Polymer Extinction Coefficient

In past work, there has been a wide variation as to what should be considered the solid polymer extinction coefficient, K_w in equation 2.50. Values have ranged from 1100cm^{-1} to 1633cm^{-1} [1]. Recent measurements conducted at ICI Polyurethanes [30] indicated that K_w was closer to 300cm^{-1}. A further cause of concern stemmed from the fact that radiative conductivity data from Cunningham and Sparrow indicated an even lower solid polymer extinction coefficient (see figure 4.7). So measurements of the solid polymer extinction coefficient were carried out at MIT in conjunction with ICI Polyurethanes to more accurately assess the solid polymer extinction coefficient.

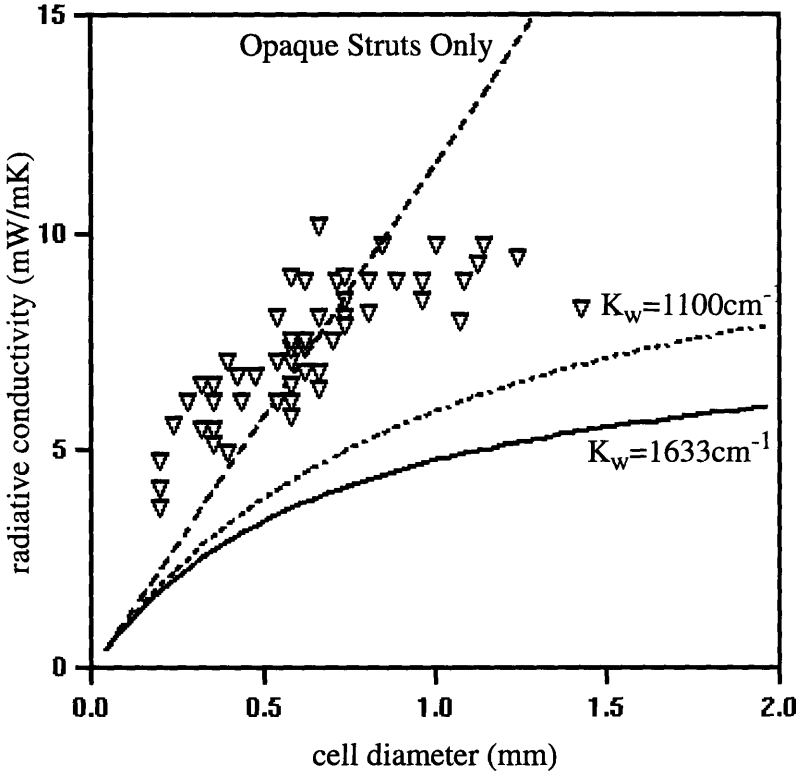

Figure4.7: *Comparison of Radiative Conductivity Measured by Cunningham and Sparrow* [31] *with Theory Using Earlier K_w Values*

The values of K_w reported in the literature, 1100cm^{-1} and 1633cm^{-1}, were calculated from transmission measurements of a 36μm large cell foam membrane and of 1.5μm free rise bun film respectively [1]. The transmission characteristics of these two polyurethane films is reproduced from [4] in figure 4.8. The reason why these measurements are suspect are different for each sample. It is likely with the 1.5μm film that since the film is so thin that attenuation due to reflection is considerable. An estimate of reflectivity from the complex index of refraction measured by Mark Torpey [16] at each wavelength was calculated (see Appendix E) and subtracted from the measured

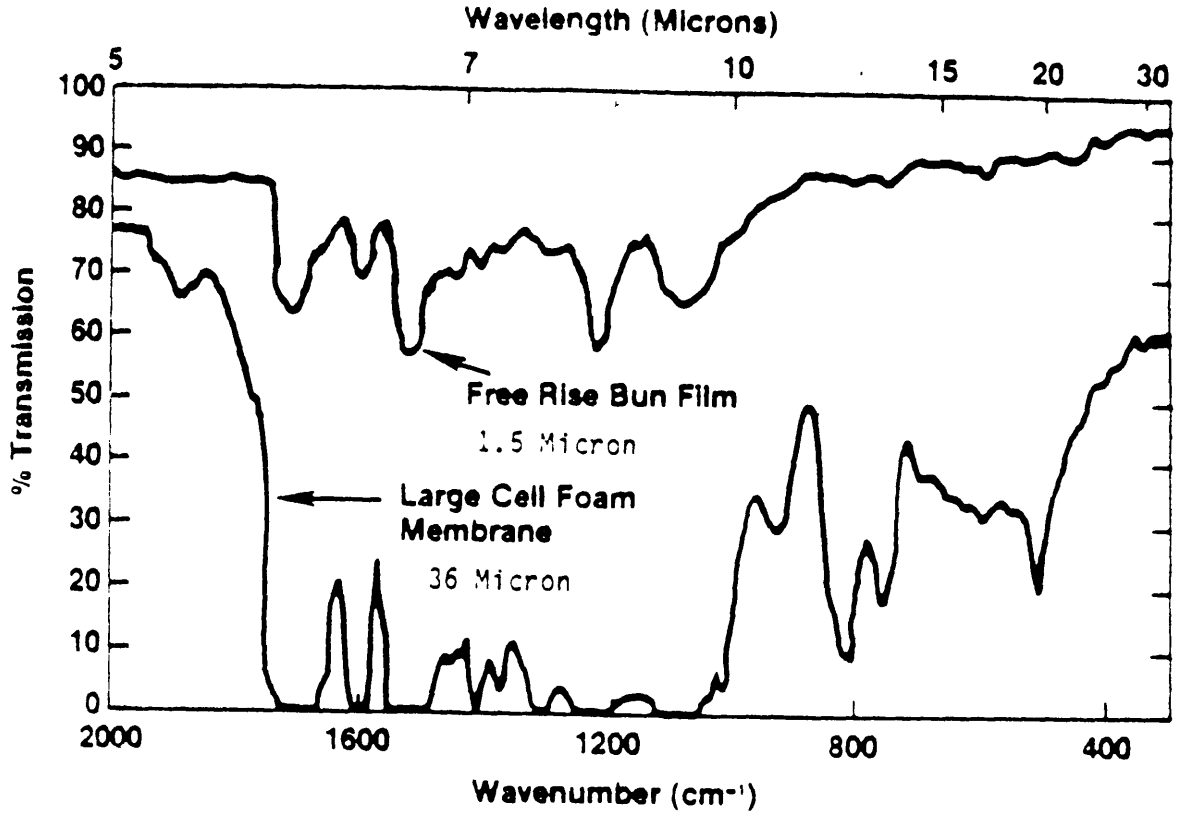

Figure 4.8: *Transmission Measurements of Large Cell Foam Membrane and Free Rise Bun Film* [4]

spectral extinction coefficient. The modified Rosseland averaged extinction coefficient accounting for the estimated reflectivity was $612cm^{-1}$. The extinction coefficient calculated from the 36μm large cell foam membrane is suspect because the membrane is too thick. That is, it is difficult to get an accurate assessment of the extinction coefficient in the wavenumber range $1100cm^{-1}$ to $1700cm^{-1}$ because little energy is transmitted in this

range. So it was decided to measure the extinction coefficient from films of thicknesses between the range reported in the literature.

ICI Polyurethanes provided four thin specimens of solid polyurethane. Micrometer thickness measurements of these samples carried out at ICI were provided and are listed in Table 4.2 [30]. Measurements of the solid polymer extinction coefficient were carried out for Sample 1 at ICI. The spectrometer used covered a wavenumber range of $4000cm^{-1}$ to $300cm^{-1}$ (2.5μm to 33μm wavelength). Roughly 96% of the blackbody energy from a source at 283K lies in this spectral range. The calculated Rosseland average extinction coefficient was determined to be $280cm^{-1}$. The spectral profile of this measured extinction coefficient is shown in Appendix G. When truncated to the spectral range of the spectrometer used at MIT ($4000cm^{-1}$ to $415cm^{-1}$ which represents roughly 85% of the energy emitted by a blackbody at 283K), the Rosseland average extinction coefficient was determined to be $310cm^{-1}$ [30].

Sample	Thickness (μm)
1	26.5
2	33.8
3	25.1
4	28.3

Table 4.2: *ICI Measurements of Solid Polyurethane Extinction Coefficient*

Using the same technique applied in Section 4.1, the solid polymer extinction coefficient was measured at MIT for each sample. The extinction coefficient profiles with respect to wavelength are shown in figure 4.9. The results of the extinction coefficient measurements are displayed in Table4.3

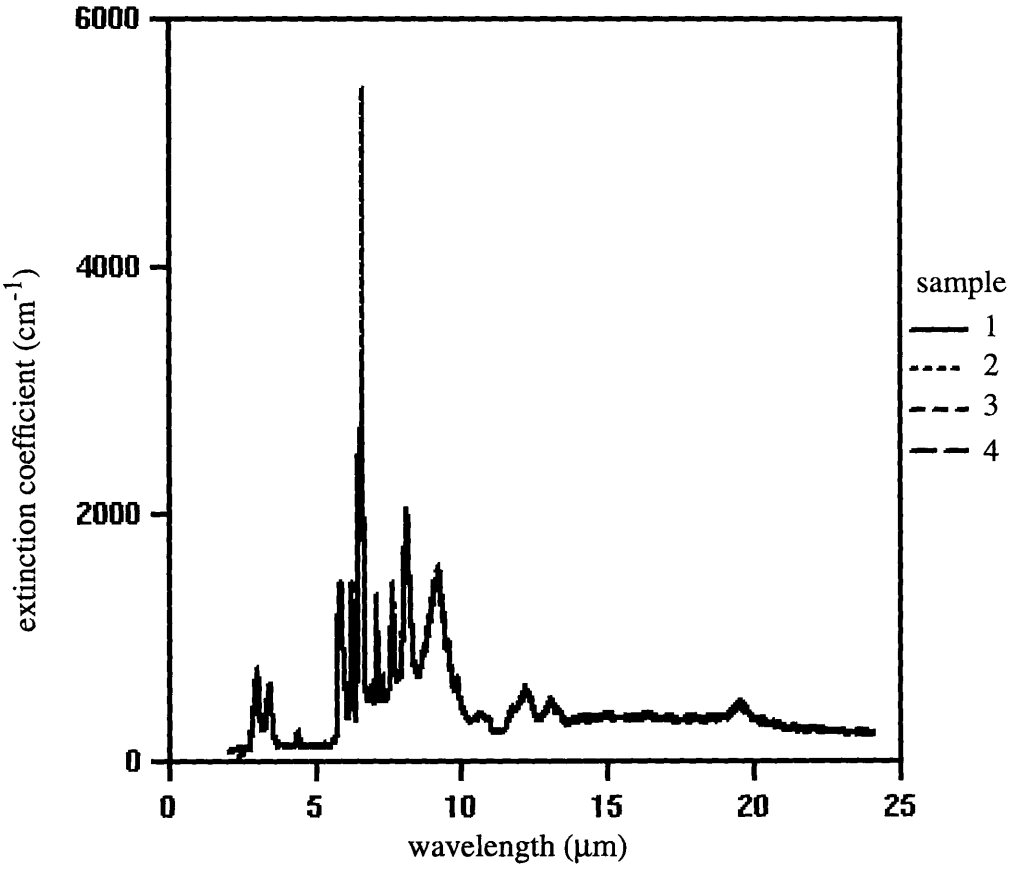

Figure 4.9: *Comparison of Spectral Extinction Coefficients of ICI Polyurethane Film Samples*

Sample	K_R (cm^{-1})
1	347
2	323
3	359
4	347

Table 4.3: *MIT Measurements of Solid Polyurethane Extinction Coefficient*

Using the mean Rosseland averaged extinction coefficient of $337cm^{-1}$, the comparison of predicted radiative conductivity (f_s=0.8, ρ_f=35kg/m^3, and ρ_s=1240kg/m^3) with the data

of Cunningham and Sparrow is shown in figure 4.10. The comparison of predicted radiative conductivity with a Rosseland mean extinction coefficient of $280cm^{-1}$ is also shown. Note that the agreement with measured radiative conductivities is much better than with the larger values of the solid polymer extinction coefficient. A Rosseland mean extinction coefficient of $337cm^{-1}$ for the solid polymer will be used in tandem with equations 2.2, 2.38, and 2.50 to predict the overall conductivity of the six foams provided by ICI in Chapter 5.

4.3 Morphology and Radiative Conductivity

From equations 2.7, 2.13, 2.38, and 2.50, one can see that a detailed relationship between the foam structure and the conductivity components has been developed. So to see how well this model predicts conductivity as cell-sizes decrease, the morphology is measured, the conductivity components calculated, and then the components are compared to measured thermal and optical properties. The influence of some parameters on conductivity are rather well documented, such as the effects of mean cell diameter and the fraction of solid in the struts. The influence of others are not yet developed such as the influence of cell size distribution, anisotropy of the cells, and the

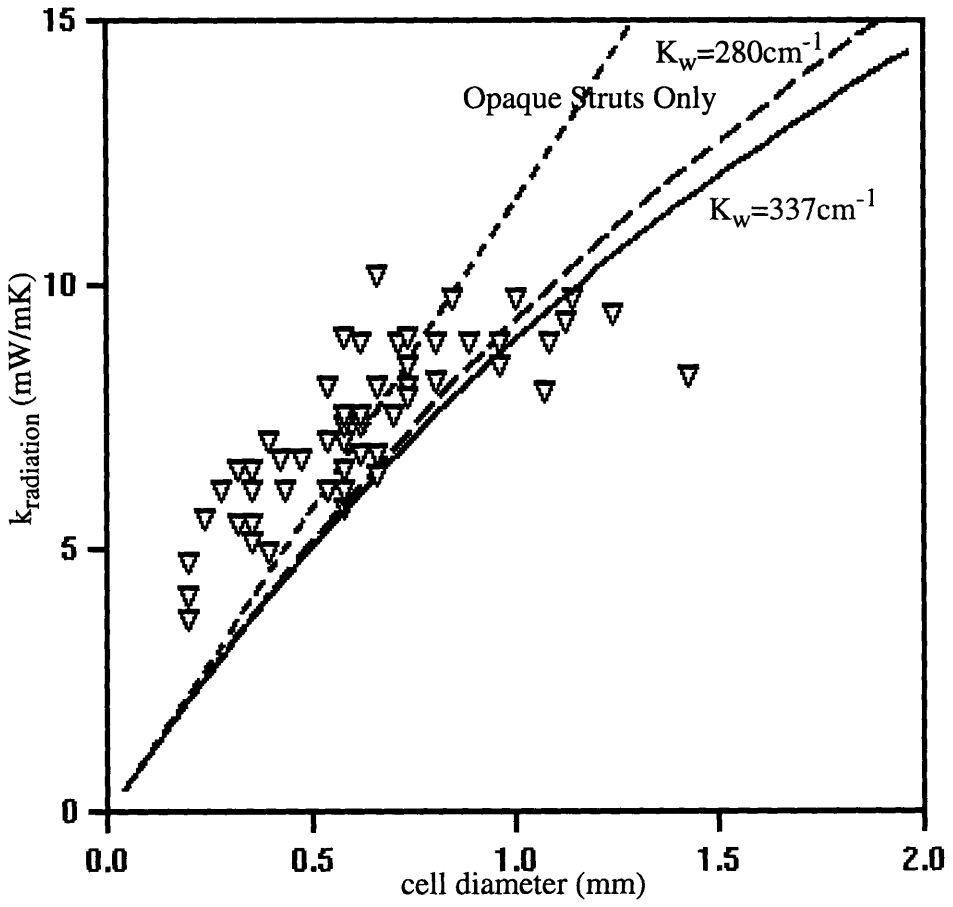

Figure 4.10: *Comparison of Cunningham and Sparrow Data with Theory (K_w=337cm^{-1})*

solid polymer extinction coefficient. So there are three goals to the morphology work of this chapter. First is to measure parameters like mean cell diameter for six foams provided by ICI using the methods already developed and to see if the predicted thermal conductivities compare well with measured values. Next, for parameters whose influence is well modeled but which have not yet been clearly measured such as the fraction of solid in the strut and solid polymer extinction coefficient measurement techniques are explored. Finally, both means of measurement and the influence of parameters like cell size distribution and extinction efficiency are detailed. The effects of parameters measured in

this chapter on the solid conductivity component and on the overall heat transfer will be presented in Chapter 5.

4.4 Mean Cell Diameter Measurement

Measurement of the mean cell diameter, as can be seen from equation 2.5 entails measuring the surface-to-volume ratio of the foam. Scanning Electron Microscope (SEM) photographs showing the plane parallel to the heat transfer direction are taken of foam samples as described in Mozgowiec [18]. A typical SEM photograph is pictured in figure 4.11. Shown in the figure, are lines drawn parallel and perpendicular to the orientation axis. The number of intersections with cell boundaries per unit length of line (N_L) is related to the mean intercept length as described in *Quantitative Stereology* [12]. That is, for an isotropic structure, the mean intercept length is the inverse of the number of intersections per unit length

$$\bar{l} = \frac{1}{N_L} \tag{4.5}$$

In determining the number of intersections, if a test line passes through a cell wall, it is counted as one intersection. If the test line is tangent to a cell wall, it is counted as one-half of an intersection. If a test line intersects a strut, where three or more cells come together, it is counted as one and one-half of an intersection. As outlined in *Quantitative Stereology* [12], the surface-to-volume ratio is

$$S_V = \frac{2}{\bar{l}} = 2N_L \tag{4.6}$$

For structures like foam cells which have an orientation axis, the number of intersections with cell walls parallel and perpendicular to the orientation axis are counted ($N_L//$ and $N_L \perp$ respectively). Then the surface-to-volume ratio is

$$S_V = 1.571 N_{L\perp} + 0.429 N_{L//} \tag{4.7}$$

The mean cell diameter is then calculated using equation 2.5. The results of the mean cell diameter calculations for the six small-celled foams sent by ICI are shown in Table 4.14 along with the predicted radiative conductivity.

4.5 Fraction of Solid in the Struts Measurement

The effect on radiative and solid conductivity of polymer distribution between the cell walls and strut regions is well developed theoretically (equations 2.13 and 2.50). However, whether this parameter changes drastically with smaller-celled foams or not is not clear. The fraction of solid in the struts, f_s, as measured by Mark Mozgowiecs and by Melissa Page is plotted versus decreasing cell size in figures 4.12 and 4.13. Both measured cell wall thicknesses from which an estimate of the fraction of solid in the strut can be calculated, as will be shown below. A general trend with smaller-celled foams is not apparent from these figures. So f_s measurements for the smaller-celled foams is necessary.

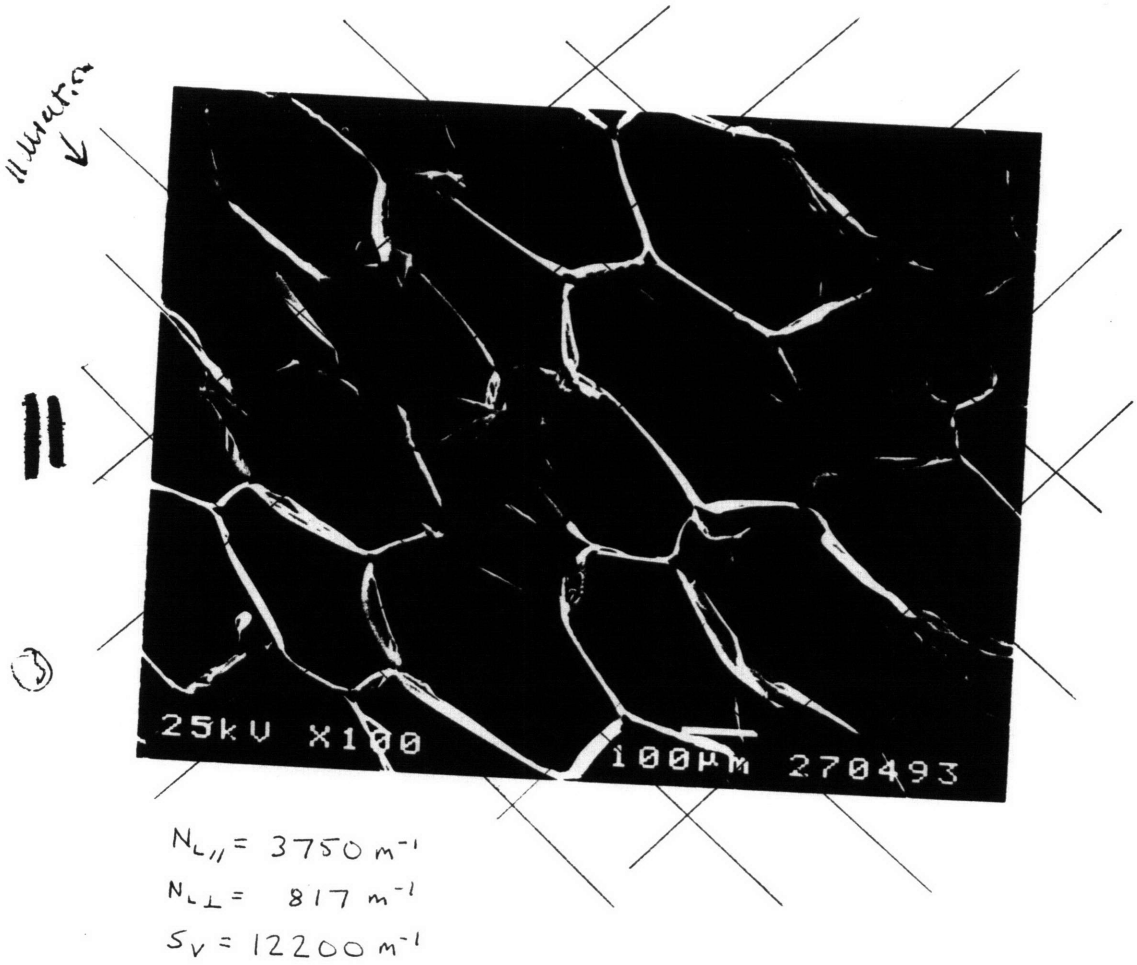

Figure 4.11: *SEM Photograph Showing S_V Calculation Method*

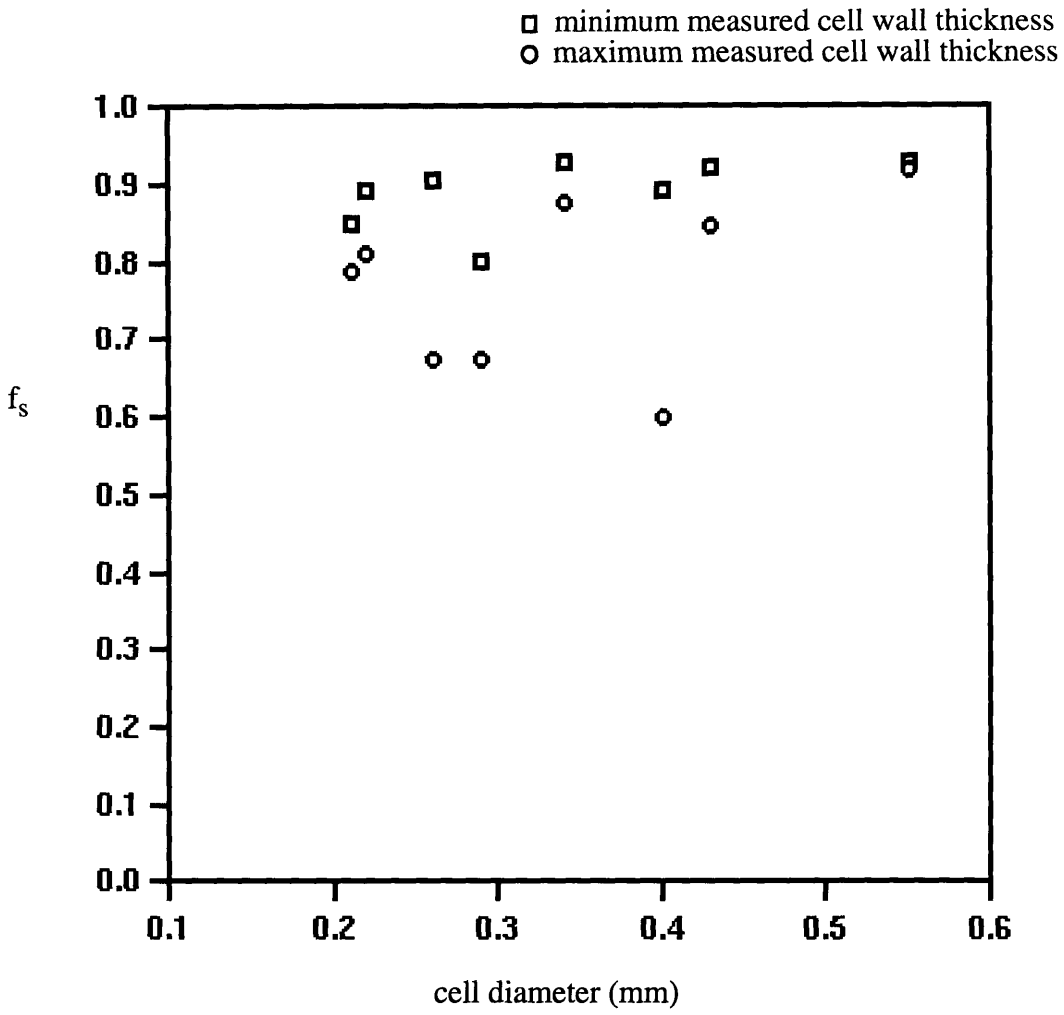

Figure 4.12: *Fraction of Solid in Strut Measured By Mark Mozgowiec* [18]

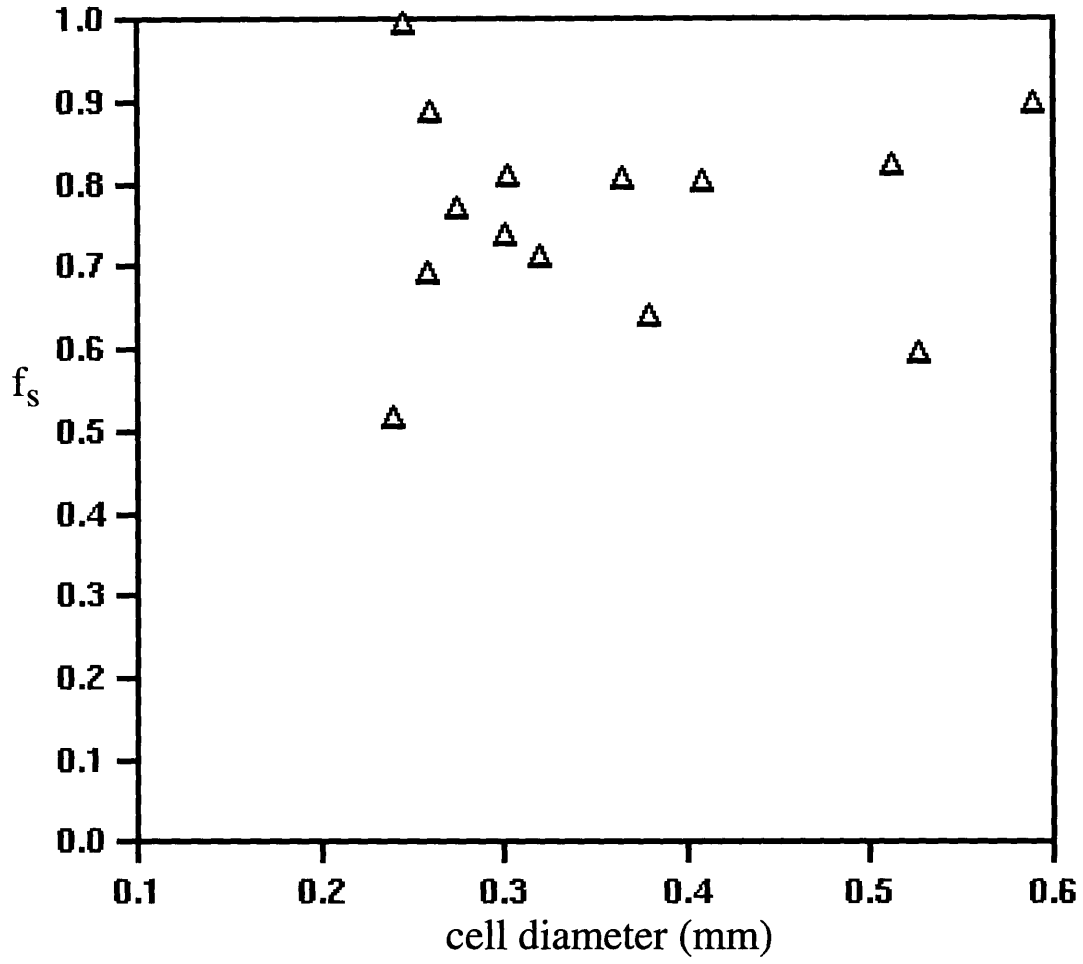

Figure 4.13: *Fraction of Solid in Strut Measured by Melissa Page* [13]

Presently f_s is calculated from SEM images of cell wall thicknesses,t. The relationship between f_s and t is outlined in Page [13]. With thickness measurements perpendicular to cell walls, the fraction of solid in the struts is

$$f_s = 1 - \frac{S_V t}{1 - \delta} \tag{4.8}$$

However, the method is limited by large variations in measured thicknesses. Both Page [13] and Mozgowiec [18] cite cell wall thickness variations of a factor of three in some foams. A technique to measure f_s with greater precision was analyzed in this project and the trend of f_s with smaller cells examined. This technique involved relating the strut cross sectional area observed in SEM photographs to f_s.

To relate strut cross-sectional area measurements to f_s, first look at the definition of strut mass fraction. The fraction of solid in the struts is the ratio of total mass in the struts to the total mass of the polymer or

$$f_s = \frac{m_{strut}}{m_{total}} \tag{4.9}$$

The total mass of the polymer is the total mass of the foam minus the total mass of the gas trapped in the foam or

$$m_{total} = \rho_f V_f - \rho_g V_g = V_f(\rho_f - \delta\rho_g) \tag{4.10}$$

The mass of the struts is the density of the solid polymer multiplied by the total volume of polymer in the struts or

$$m_{strut} = \rho_s V_{strut} = \rho_s A_{strut} L_{total} \tag{4.11}$$

where A_{strut} is the cross sectional area of the strut which is assumed to be the same for all of the struts, and L_{total} is the total length of the struts in the foam. Taking the length of each strut to be equivalent to L_{strut} and the total number of struts being N_{strut}, L_{total} can be written as

$$L_{total} = L_{strut} N_{strut} \tag{4.12}$$

Using these definitions and rearranging, equation 4.9 can be written

$$f_s = \frac{\rho_s}{\rho_f - \delta\rho_g}\left(\frac{N_{strut}}{V_f} L_{strut}\right) A_{strut} \tag{4.13}$$

For a pentagonal dodecahedron, L_{strut} is an edge length of a face, which is related to the mean cell diameter

$$L_{strut} = \frac{d}{2.57} \tag{4.14}$$

The number of struts N_{strut} per foam volume can be expressed in terms of the number of struts per cell and the number of cells per volume or

$$\frac{N_{strut}}{V_f} = \frac{N_{strut}}{cell}\frac{N_{cell}}{V_f} \tag{4.15}$$

For typical foams, each cell has three neighbors, so the number of struts per cell has to be divided by the three cells. So for pentagonal dodecahedron foam cells with 30 struts per cell,

$$\frac{N_{strut}}{cell} = \frac{N_{strut,\mathrm{pd}}}{3} = \frac{30}{3} = 10 \tag{4.16}$$

The number of cells per unit volume, N_{cell}/V_f, can be expressed in terms of the measured surface-to-volume ratio of the foam. That is, the surface-to-volume ratio is the number of cells times the *internal surface area* ($S_{internal}$) of the cell divided by the total volume or

$$S_V = \frac{N_{cell} S_{internal}}{V_f} = \frac{N_{cell}(\frac{1}{2} S_{cell})}{V_f} \tag{4.17}$$

The factor of one-half comes from Underwood's definition of the surface-to-volume ratio [12]. In defining the surface-to-volume ratio in terms of the number of intersections per unit test line (N_L), the internal surface areas are treated as two-dimensional surfaces separating space-filling cells. That is, two cells share the same cell wall surface area. The surface area per cell is one-half the surface area of a single stand-alone cell (S_{cell}). Equation 4.17 can be rearranged to yield

$$\frac{N_{cell}}{V_f} = \frac{2S_V}{S_{cell}} \tag{4.18}$$

For a pentagonal dodecahedron, the measured surface-to-volume ratio is $3.46/d$ where d is the cell diameter. The surface area of a single cell is $3.126d^2$. So for several pentagonal dodecahedron cells,

$$\frac{N_{cell}}{V_f} = \frac{2(\frac{3.46}{d})}{3.126d^2} = \frac{2.214}{d^3} \tag{4.19}$$

Combining expressions 4.15, 4.16, and 4.19, the number of struts per unit volume is

$$\frac{N_{strut}}{V_f} = \frac{N_{strut}}{cell}\frac{N_{cell}}{V_f} = 10\frac{2.214}{d^3} = \frac{22.14}{d^3} \tag{4.20}$$

In terms of measurable geometric properties of the foam like cell diameter (d), foam density (δ), and strut cross-sectional area (A_{strut}), the fraction of solid in the strut is

$$f_s = \left(\frac{\rho_s}{\rho_f - \delta\rho_g}\right)\left(\frac{22.14}{d^3}\right)\left(\frac{d}{2.57}\right)A_{strut} \tag{4.21}$$

Since the foam density ρ_f is much greater than $\delta\rho_g$ this measure of strut mass fraction is roughly

$$f_s = \left(\frac{\rho_s}{\rho_f}\right)\left(\frac{8.62}{d^2}\right)A_{strut} \tag{4.22}$$

This relationship is useful when measurements are made of strut cross sectional areas with the SEM. A typical SEM photograph of strut cross sectional area is shown in figure 4.14.

The cross section pictured on an SEM photograph may not be normal to the length of the strut, but may be a cut at some other angle as shown in figure 4.15. So to account for angular orientations, several strut cross sections are measured for each foam. Then, the actual cross sectional area can be related to the average measured cross sectional area as will be shown below.

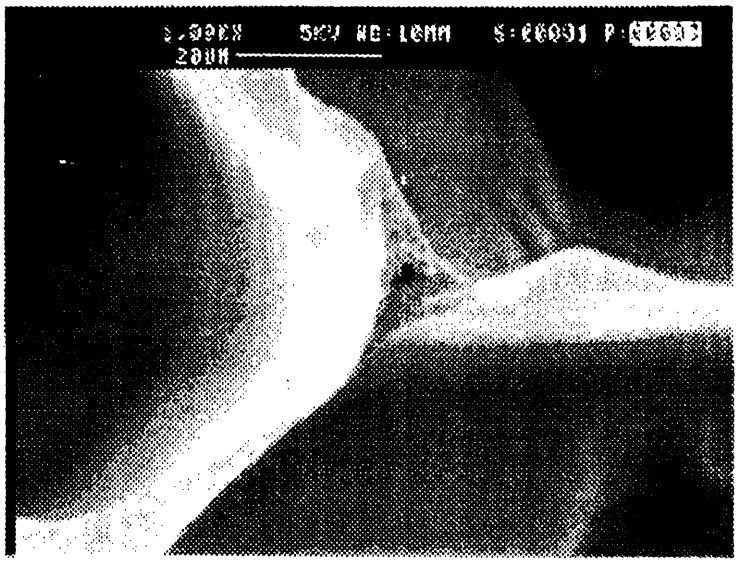

Figure 4.14: *Typical SEM Photograph of Strut Cross-Sectional Area*

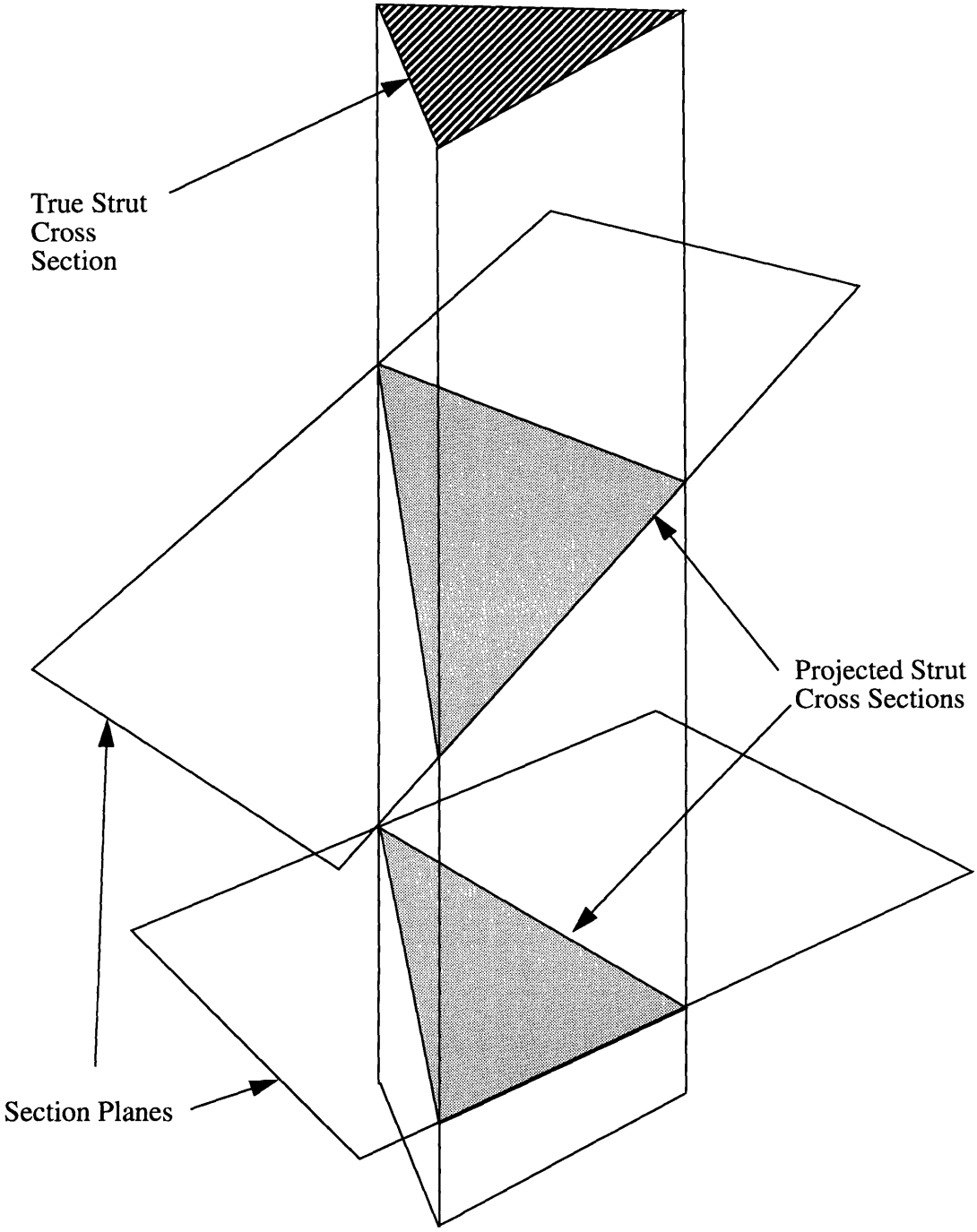

Figure 4.15: *Cross Section of Strut Intersected at Different Orientations*

To derive a relationship between measured average strut cross sectional area and the actual strut cross sectional area, consider the strut intersected by a plane, the base of a hemisphere, in figure 4.16.

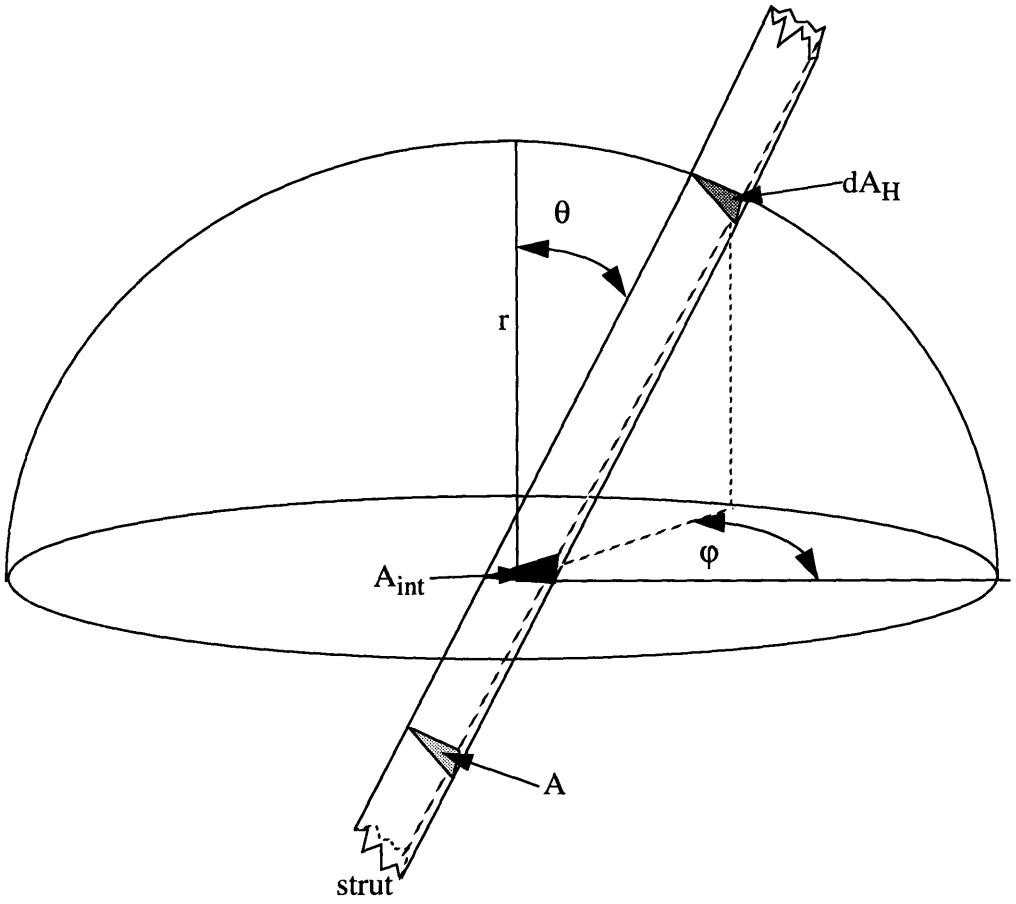

Figure 4.16: *Sections (A_{int}) Used To Represent Average Intercepted Orientation*

The area of intersection between the strut and the hemispherical base, A_{int}, represents the sectional areas when struts are intersected by random planes. It is related to the true cross sectional area of the strut, A, by

$$A_{int} = A \sec\theta \tag{4.23}$$

The strut projects a differential element onto the surface of the hemisphere, dA_H. Finding the average section area is the same as weighing the intersected area from each orientation by the fraction of total hemispherical area that this element represents and summing over all possible orientations. That is,

$$\overline{A}_{int} = \frac{\int_{A_H} A_{int} dA_H}{\int_{A_H} dA_H} \tag{4.24}$$

the differential element dA_H is

$$dA_H = r^2 \sin\theta d\theta d\varphi \tag{4.25}$$

So the average intersected area is

$$\overline{A}_{int} = \frac{\int_{\theta=0}^{\theta_2} \int_{\varphi=0}^{2\pi} A \sec\theta r^2 \sin\theta d\theta d\varphi}{\int_{\theta=0}^{\theta_2} r^2 \sin\theta d\theta d\varphi} \tag{4.26}$$

Carrying out the integration gives the average area as a function of A,θ_2,

$$\bar{A}_{int} = \left(\frac{ln|\sec\theta_2|}{1-\cos\theta_2} \right) A \tag{4.27}$$

The reason this expression is written in terms of a maximum angle θ_2 rather than integrated to $\pi/2$ is that mathematically the intersected area becomes infinitely large with $\theta_2=\pi/2$. In real SEM work this would correspond to the cross sectional area incorporating the entire length of the strut. Mathematically then, the expression for $\bar{A}_{int}$ becomes infinite. Practically however, there is a maximum θ_2 to which one measures. The key is to determine this maximum angle from the statistical distribution of measured areas and then to use expression 4.27 to get the true strut cross sectional area from the average measured strut cross sectional area.

The maximum area measured, considering all struts to be of the same cross sectional area, should correspond to the plane that intersects the strut at angle θ_2. This maximum area is then

$$A_{max} = A\sec\theta_2 \tag{4.28}$$

Then the ratio of maximum to average measured area is a function of θ_2 only. That is,

$$R = \frac{A_{max}}{\bar{A}_{int}} = \frac{\sec\theta_2}{\dfrac{ln|\sec\theta_2|}{1-\cos\theta_2}} \tag{4.29}$$

So to determine the cross sectional area of struts from SEM photographs the following procedure is used. First measure a number of strut areas from a local area having similar cell sizes like the one pictured in figure 4.17. Determine the average area and the ratio

Figure 4.17: *SEM Photograph of Local Area Having Similar Cell Sizes*

of maximum to average area. From the ratio, determine θ_2 using expression 4.29. Knowing θ_2 and the average measured area, the cross sectional area of the strut is simply

$$A = \bar{A}_{int} \frac{(1 - \cos\theta_2)}{ln|\sec\theta_2|} \tag{4.30}$$

It is this area that is appropriate for the fraction of solid in the strut calculation.

Fraction of solid in the strut calculations using this method were compared to results Page [13] obtained for two foams using cell wall thickness measurements. Cell wall thicknesses were also measured for two of the foams provided by ICI. The comparison of results for the two methods are shown in Table 4.4. Considering the variations in cell wall thicknesses that were measured in each sample, the agreement is good.

foam	f_s (from strut area)	f_s (from cell wall thickness)	% difference from cell wall thickness calculation
Page #21	0.73	0.84	-13.1
Page #27	0.68	0.66	+ 3.0
NBE 785/206	0.65	0.71	- 8.5
NBE 819/16/1	0.77	0.83	- 7.2

Table 4.4: *Comparison of Fraction of Solid in Strut from Strut Area and from Cell Wall Thickness Measurements*

There are shortcomings to this method that have to be kept in mind. The most important is that usually 3 or 4 struts appear on any SEM photo with enough resolution to get an accurate measurement of area. So the method becomes time consuming and expensive in terms of SEM use to get a statistically large enough sample, which more than five strut areas appear to provide Other things that should be kept in mind are the assumptions used in the derivation, most importantly that all struts have the same cross sectional area. The benefits of this method include a greater confidence in the results than

from measuring cell wall thickness and a measurement technique that is less tedious than finding a suitable cell wall thickness at high magnification.

Several strut cross sectional area distributions and the SEM photos from which they were measured are in Appendix G. The fractions of solid in the struts derived from equation 4.22 and from the measured results for the six foams provided by ICI Polyurethanes are listed in Table 4.14 at the end of the chapter. The variation of f_s with cell size is shown in figure 4.18. With the possible exception of foam NBE 863/13/1 (f_s=0.48) , the redistribution of polymer from the struts to the cell walls as cell size decreases can be seen. The redistribution decreases the extinction due to the struts while at the same time increasing the extinction due to the cell walls. Whether this increases or decreases the total radiative conductivity depends upon the relative change in each component. The predicted radiative conductivity for constant f_s=0.8 and ρ_f=35kg/m^3 is plotted in figure 4.19 along with the predicted radiative conductivity with the measured mass fractions. Note that in the intermediate cell sizes, the measured redistribution of polymer decreases the radiative conductivity while increasing it at small cell sizes. How this redistribution affects solid conductivity will be discussed in Chapter 5.

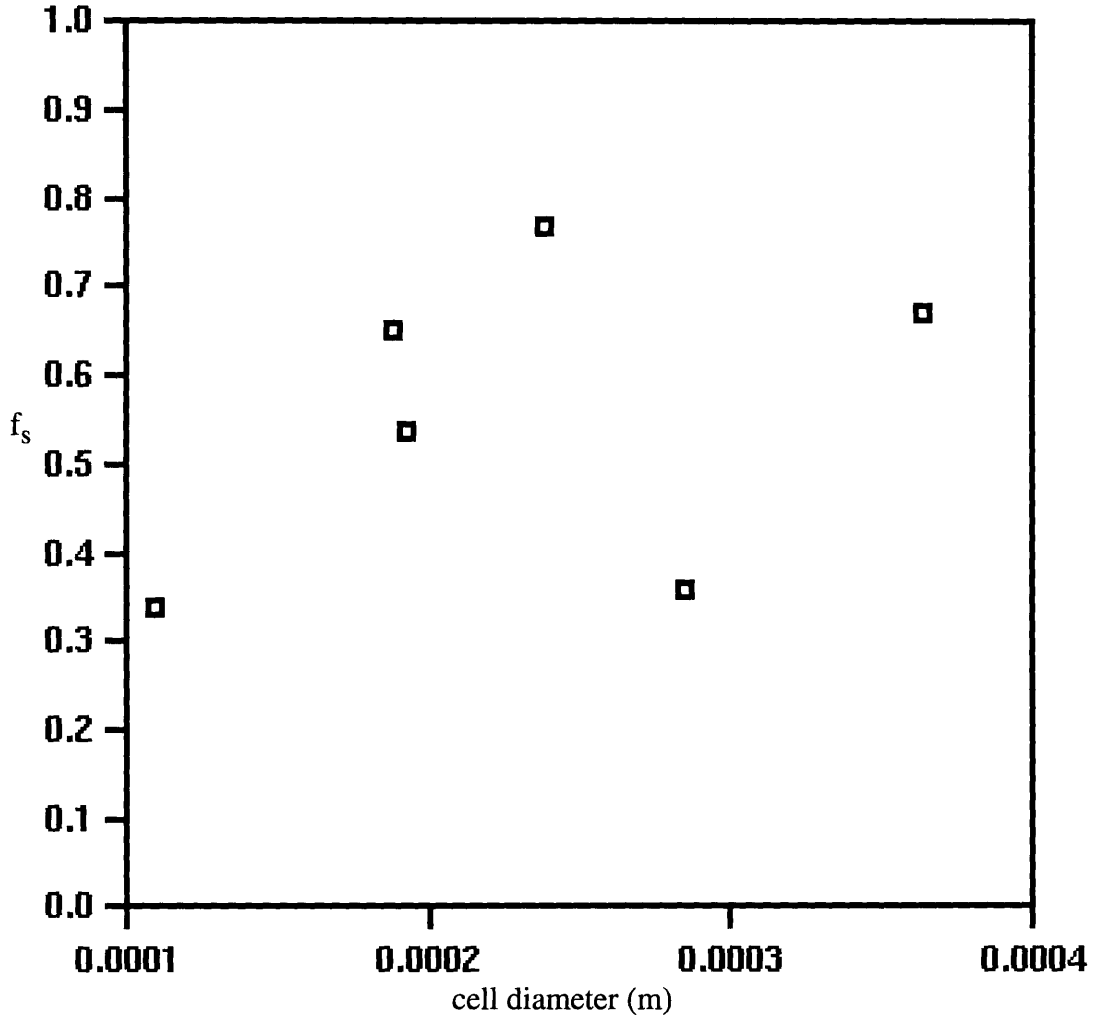

Figure 4.18: *Measured Fraction of Solid in Strut versus Foam Cell Size*

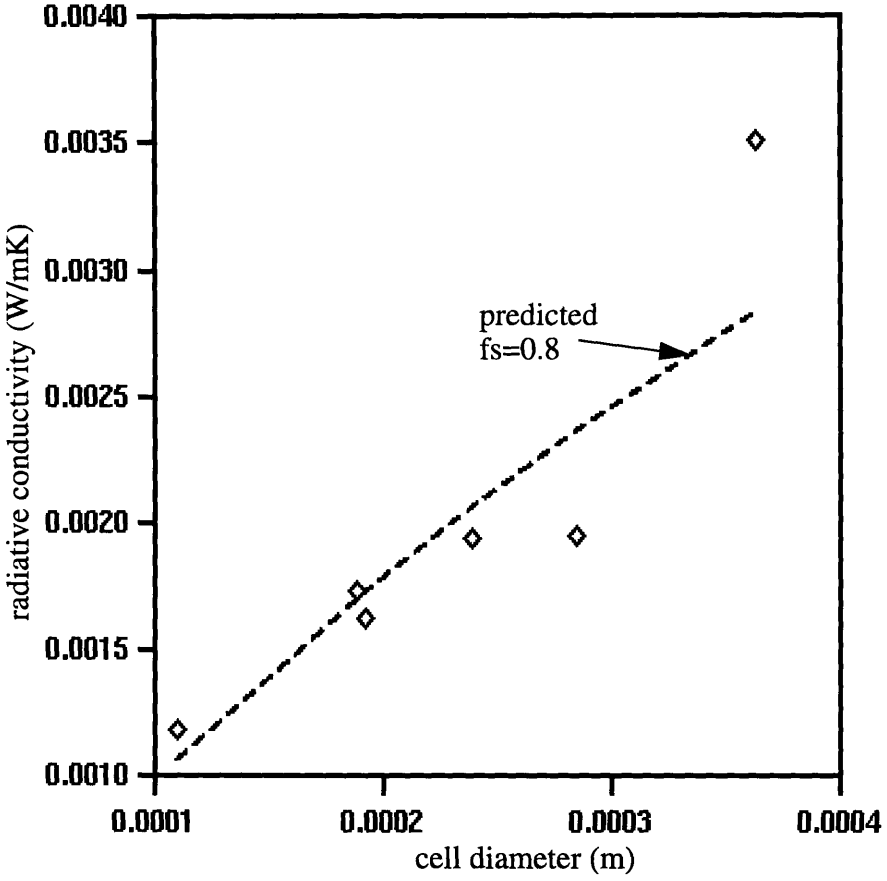

Figure 4.19: *Effect of Polymer Distribution on Radiative Conductivity for Six Foams Analyzed*

4.6 Comparison of Predicted and Measured Extinction Coefficients

Now that the fraction of solid in the strut and mean cell diameter have been measured, the extinction coefficient predicted from equation 2.50 can be compared to the measured extinction coefficients of Section 4.1. The extinction coefficients predicted from equation 2.50 and from the data in Table 4.14 are shown in Table 4.5. Both extinction coefficients are also plotted versus cell size in figure 4.20.

foam	mean cell diameter (mm)	$K_{measured}$ (cm^{-1})	$K_{predicted}$ from morphology (cm^{-1})
NBE 678/21/47	0.109	61.0	40.9
NBE 785/206	0.188	49.0	31.8
NBE 819/16/2	0.192	40.7	30.6
NBE 819/16/1	0.238	38.4	27.8
NBE 863/13/1	0.284	27.0	20.9
NBE 785/204	0.363	34.9	16.8

Table 4.5: *Extinction Coefficients from Transmission Measurements and from Morphology Calculations*

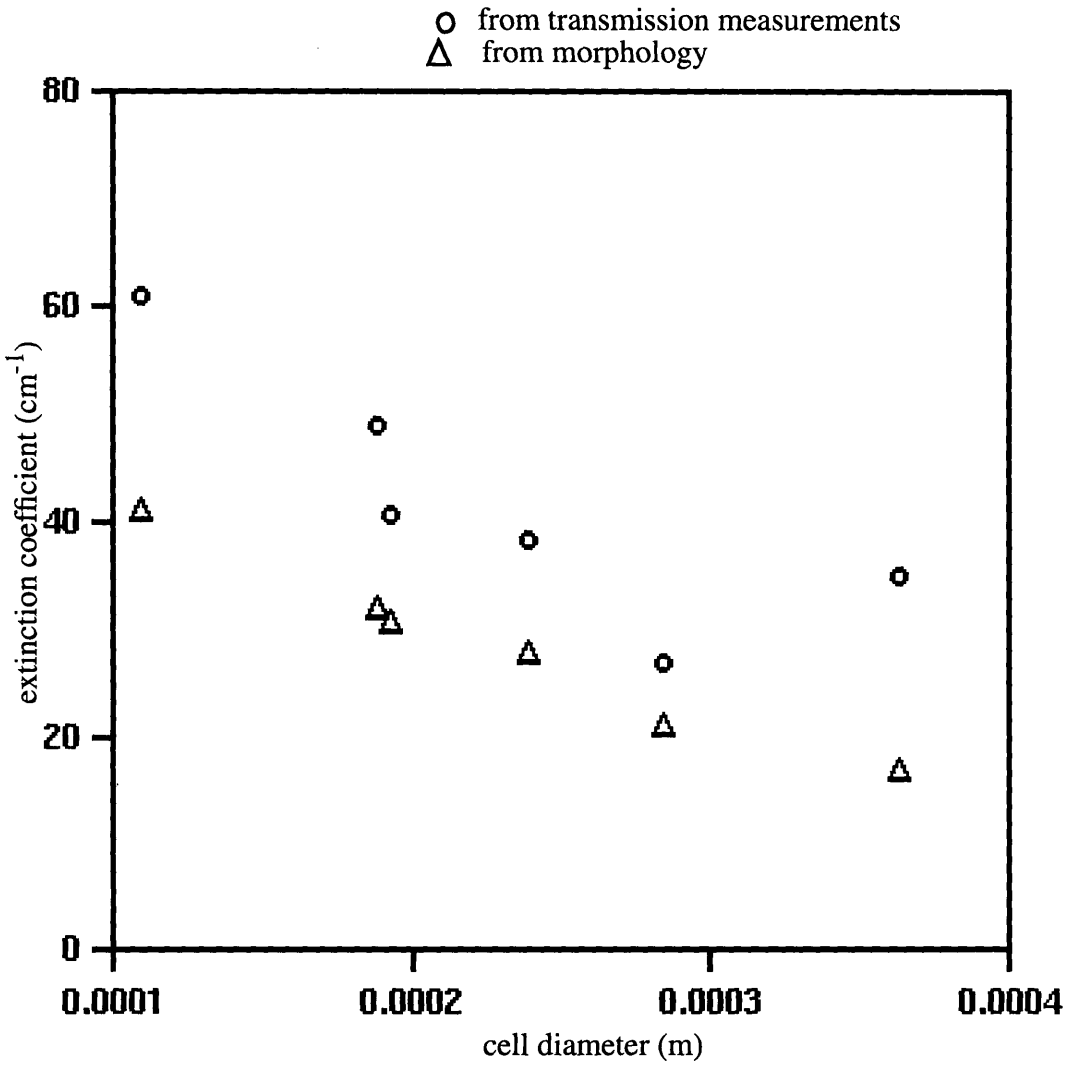

Figure 4.20: *Comparison of Extinction Coefficients from Morphology and from Transmission Measurements*

Notice that the morphology predictions underpredict the transmission measurements. Two possibilities for discrepancy were considered. The first is the possibility that highly anisotropic scattering might skew the transmission measurements. This is discussed in the following section. The second is the possibility that the extinction efficiency factor is not unity for the smaller celled foams. The analysis of the extinction efficiency factor from Mie Scattering Theory is discussed in Appendix H. Another possible cause of

discrepancy is additional scattering due to reflections at the cell wall surfaces. The impact of such reflections should be examined in future work.

4.7 Scaling of Measured Extinction Coefficients For Anisotropic Scattering

In the derivation of the Rosseland equation, isotropic scattering is assumed [15]. Scattering in foams is actually an anisotropic process as will be shown below. As described by Sinofsky [15] the measured extinction coefficient which includes anisotropic scattering can be scaled to the P-1 approximate extinction coefficient which can then be used with the isotropic Rosseland equation to describe the radiative behavior. If not scaled, for strongly forward scattering material, such as fiberglass, the Rosseland equation could underpredict radiation by as much as 60% [15].

The directional nature of scattering is represented by the phase function $\phi(\theta)$ which is the normalized ratio of intensity scattered in the θ direction to the intensity scattered in the same direction if scattering were isotropic. Consider energy scattered from an element oriented in the θ_i direction. Intensity scattered from this element in the θ direction is related to the total intensity scattered from the element

$$dI_{s\lambda}(\theta, \theta_i) = -dI_{s\lambda}(\theta_i) \frac{\phi_\lambda(\theta, \theta_i)}{4\pi} \tag{4.31}$$

The total intensity scattered from the θ_i element is

$$dI_{s\lambda}(\theta_i) = \int_{\omega_i=4\pi} dI_{s\lambda}(\theta, \theta_i)\, d\omega \tag{4.32}$$

integrated over the solid angle

$$d\omega = \sin\theta d\theta d\varphi \tag{4.33}$$

Then

$$\phi_\lambda(\theta, \theta_i) = \frac{dI_{s\lambda}(\theta, \theta_i)}{(\frac{1}{4\pi}) \int_{\omega_i=4\pi} dI_{s\lambda}(\theta, \theta_i)\, d\omega} \tag{4.34}$$

The denominator is actually the increase in intensity if scattering were isotropic, so

$$\phi_\lambda(\theta) = \frac{dI_{s\lambda}(\theta, \theta_i)}{dI_{s\lambda}(\theta, \theta_i)_{isotropic}} \tag{4.35}$$

The phase function is normalized so that

$$\frac{1}{4\pi} \int_{\omega_i=4\pi} \phi_\lambda(\theta)\, d\omega = 1 \tag{4.36}$$

Based on the phase function, one can define the fraction of energy scattered in the forward direction due to anisotropy. This is the forward fraction, F_λ

$$F_\lambda = \frac{\int_0^{\pi/2} \phi_\lambda(\theta) \sin\theta d\theta}{\int_0^{\pi} \phi_\lambda(\theta) \sin\theta d\theta} \tag{4.37}$$

If $F_\lambda > 0.5$, the material is forward scattering. If $F_\lambda < 0.5$, the material is backward scattering. If $F_\lambda = 0.5$, the scattering is isotropic.

The phase function for polyurethane foam at 9μm wavelength was measured by Schuetz and Glicksman[8] and found to be forward scattering.

Knowledge of the albedo, Ω_λ, is also needed to scale anisotropic measurements to be used with the isotropic Rosseland equation. The albedo is the relative size of scattering in a material or

$$\Omega_\lambda = \frac{\sigma_\lambda}{\sigma_\lambda + a_\lambda} \tag{4.38}$$

The albedo for small celled polyurethane foam was measured by Kuhn et al [33]. Their results indicate that a good approximation of the albedo is Ω_λ=0.6 for wavelengths less than 6μm and Ω_λ=0.2 for wavelengths greater than 6μm.

Now the P-1 extinction coefficient scales the extinction coefficient according to the severity and direction of anisotropy. If $F_\lambda > 0.5$, a material propagates more radiant energy than isotropically scattering media because more energy is directed in the forward direction. The P-1 extinction coefficient is therefore lower than the true extinction coefficient since less energy is attenuated with a forward scattering material.

From knowledge of albedo and phase function, a scaled spectral scattering coefficient can be defined [32]

$$\sigma_{\lambda P1} = \sigma_\lambda (1 - <\cos\theta>_\lambda) \tag{4.39}$$

where the asymmetry factor $<\cos\theta>_\lambda$ is

$$<\cos\theta>_\lambda = \frac{1}{2}\int_{-1}^{1} \phi_\lambda(\theta) \cos\theta d(\cos\theta) \tag{4.40}$$

The P-1 extinction coefficient is then

$$K_{\lambda P1} = \sigma_{\lambda P1} + a_\lambda \tag{4.41}$$

which can then be used with the Rosseland equation. Lee and Buchias [32] showed that this method is quite accurate.

From the phase function measured by Mark Schuetz for polyurethane foam [14], Mark Sinofsky determined the foam forward fraction to be F=0.68 [15]. The forward fraction F=0.75 was the closest to this value for which extinction ratios were presented for different albedos. Using the approximate albedo derived from Kuhn et al [33](see figure 4.21) and the ratios of $K_{measured}/K_{P\text{-}1}$ presented in Sinofsky [15] for a forward fraction of F=0.75, the spectral extinction coefficients were scaled. Then the Rosseland mean P-1 extinction coefficient was calculated. P-1 extinction coefficients for the six foams provided by ICI are listed in Table 4.6. Also shown in Table 4.6 are the extinction coefficients predicted from the morphology.

foam (mean cell diameter)	$K_{meas}/K_{P\text{-}1}$ $\lambda < 6\mu m$	$K_{meas}/K_{P\text{-}1}$ $\lambda > 6\mu m$	K_{meas} (cm^{-1})	$K_{P\text{-}1}$ (cm^{-1})	$K_{morphology}$ (cm^{-1})
NBE 678/21/47 (0.109mm)	1.20	1.09	61.0	54.6	40.9
NBE 785/206 (0.188mm)	1.20	1.09	49.0	44.7	31.8
NBE 819/16/2 (0.192mm)	1.20	1.09	40.7	37.1	30.6
NBE 819/16/1 (0.238mm)	1.20	1.09	38.4	35.0	27.8
NBE 863/13/1 (0.284mm)	1.20	1.09	27.0	24.6	20.9

Table 4.6: *P-1 Extinction Coefficients from Extinction Coefficients Calculated from Transmission Measurements*

foam (mean cell diameter)	K_{meas}/K_{P-1} $\lambda < 6\mu m$	K_{meas}/K_{P-1} $\lambda > 6\mu m$	K_{meas} (cm^{-1})	K_{P-1} (cm^{-1})	$K_{morphology}$ (cm^{-1})
NBE 785/204 (0.363mm)	1.20	1.09	34.9	31.8	16.8

Table 4.6: *P-1 Extinction Coefficients from Extinction Coefficients Calculated from Transmission Measurements*

The predictions of overall conductivity in Section 5.4 will use the uncorrected extinction coefficients measured from the transmission characteristics. In Section 5.9 the impact of scaling the measured extinction coefficients on predicted overall conductivities will be explored.

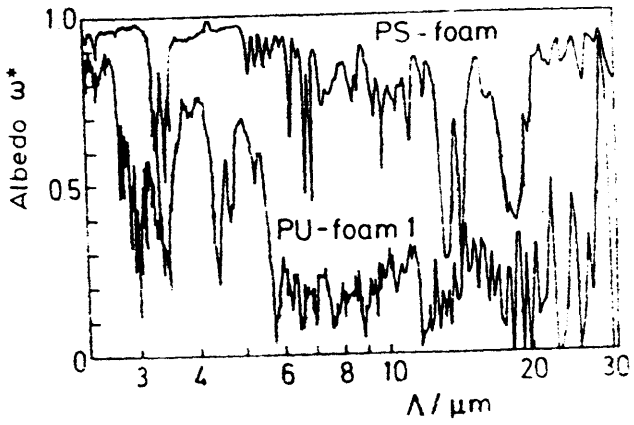

Figure 4.21: *Albedo of Polyurethane Foam Measured by Kuhn et al*[33]

4.8 Anisotropy Measurement and Effect on Conductivities

The degree of foam cell anisotropy and a first look at its affect on radiative conductivity was investigated. The influence on solid conductivity, as outlined in Chapter 2 will be discussed in Chapter 5. As outlined in Chapter 2, the affects of anisotropy can be included with the ratio of major to minor cell axes *a/b* where *a* and *b* are shown in figure 2.2. With oriented cells modeled as ellipses, this anisotropy factor is the same for any section cut by a plane parallel to the orientation axis. So the ratio of major to minor axes for sections such as SEM or confocal images should be the same as the ratio for the three dimensional cells. The anisotropy factor for oriented cells can then be computed from the measured quantities ($N_L//$ and $N_L\perp$). That is, the mean major axis ($2a$) is proportional to $1/N_L//$ while the mean minor axis ($2b$) is proportional to $1/N_L\perp$ with the same proportionality constant. Then the anisotropy factor can be derived

$$e = \frac{a}{b} = \frac{1/N_{L//}}{1/N_{L\perp}} = \frac{N_{L\perp}}{N_{L//}} \tag{4.42}$$

The anisotropy factor for the foams supplied by ICI are shown in Table 4.14 at the end of the chapter. One noticeable trend is that as the cell size becomes smaller, the degree of anisotropy decreases considerably. That is, the smaller celled foams are more isotropic than the larger celled foams.

Anisotropy of foam cells mean that the extinction coefficient varies with angle from the orientation axis. So the influence of anisotropy can be easily incorporated into the radiative heat transfer model by accounting for an extinciton coefficient that varies with angle. Going back to equation 2.32, it is assumed that the extinction coefficient K is not a function of θ to derive the Rosseland equation for a gray isotropic body. The integration yields

$$q_R = -\frac{4}{3K}\frac{de_b}{dx} \tag{4.43}$$

The integration can also be carried out for K that varies with θ, the situation when anisotropic foams are encountered. The first and third terms of $q_r(+x)$ and $q_r(-x)$ still cancel in expression 2.32 assuming that $K(\theta)$ equals $K(\theta+\pi)$. With $K(\theta)$ the net radiant flux in both directions is

$$q_R = -4\left(\frac{de_b}{dx}\right)_0 \int_0^{\pi/2} \frac{\cos^2\theta \sin\theta d\theta}{K(\theta)} \tag{4.44}$$

A measure of how well the isotropic Rosseland equation predicts the actual anisotropic radiative flux is the ratio q_{anis}/q_{isot}. That is, for some measured or calculated K, compare the ratio of flux predicted by equation 4.43 to the true anisotropic flux of equation 4.44. Note that the angular dependence of the extinction coefficient with respect to the orientation axis or rise direction has to be known. If known, or assumed, the ratio of fluxes can be written

$$\frac{q_{anis}}{q_{isot}} = \frac{-4\frac{de_b}{dx}\int_0^{\pi/2} \frac{\cos^2\theta \sin\theta d\theta}{K(\theta)}}{-4\frac{de_b}{dx}/3K} = \frac{\int_0^{\pi/2} \frac{\cos^2\theta \sin\theta d\theta}{K(\theta)}}{\left(\frac{1}{3K}\right)} \tag{4.45}$$

So the amount of error in predicted flux from using the isotropic Rosseland equation with some measured extinction coefficient can be quantified by the ratio q_{anis}/q_{isot}. This was done numerically for a simple assumed variation of $K(\theta)$. For simplicity of angular orientation, assume a harmonic function $K(\theta)$

$$K(\theta) = K_0 \cos^2\theta + K_{90} \sin^2\theta \tag{4.46}$$

where K_0 and K_{90} are the extinction coefficients in the rise direction and at right angles to the rise direction respectively. Axial symmetry around the rise direction axis is assumed. Note that the harmonic form reduces to the isotropic extinction coefficient K when the foam is isotropic, or $K_0=K_{90}=K$.

The first comparison looked at use of the isotropic Rosseland equation with extinction coefficients presently used in foam heat transfer analysis. The extinction coefficient measured parallel to the rise direction, or K_0, is currently used as the isotropic Rosseland extinction coefficient as described in section 4.1. For several ratios of K_0/K_{90} and the assumed harmonic distribution of $K(\theta)$, the radiative flux ratio q_{anis}/q_{isot} was determined. The results are shown in Table 4.7 and graphically in figure 4.22.

K_0/K_{90}	q_{anis}/q_{isot}
0.333	0.606
0.500	0.739
0.667	0.843
0.833	0.928
1.000	1.000
1.167	1.062
1.333	1.117
1.500	1.166
1.667	1.210
1.833	1.251
2.000	1.288

Table 4.7: *Ratio of Anisotropic to Isotropic Radiative Fluxes (Use Extinction Coefficient Measured Parallel to the Rise Direction in the Isotropic Rosseland Equation)*

K_0/K_{90}	q_{anis}/q_{isot}
2.167	1.322
2.333	1.353
2.500	1.383
2.667	1.410
2.833	1.436
3.000	1.460
3.167	1.483
3.333	1.505

Table 4.7: *Ratio of Anisotropic to Isotropic Radiative Fluxes (Use Extinction Coefficient Measured Parallel to the Rise Direction in the Isotropic Rosseland Equation)*

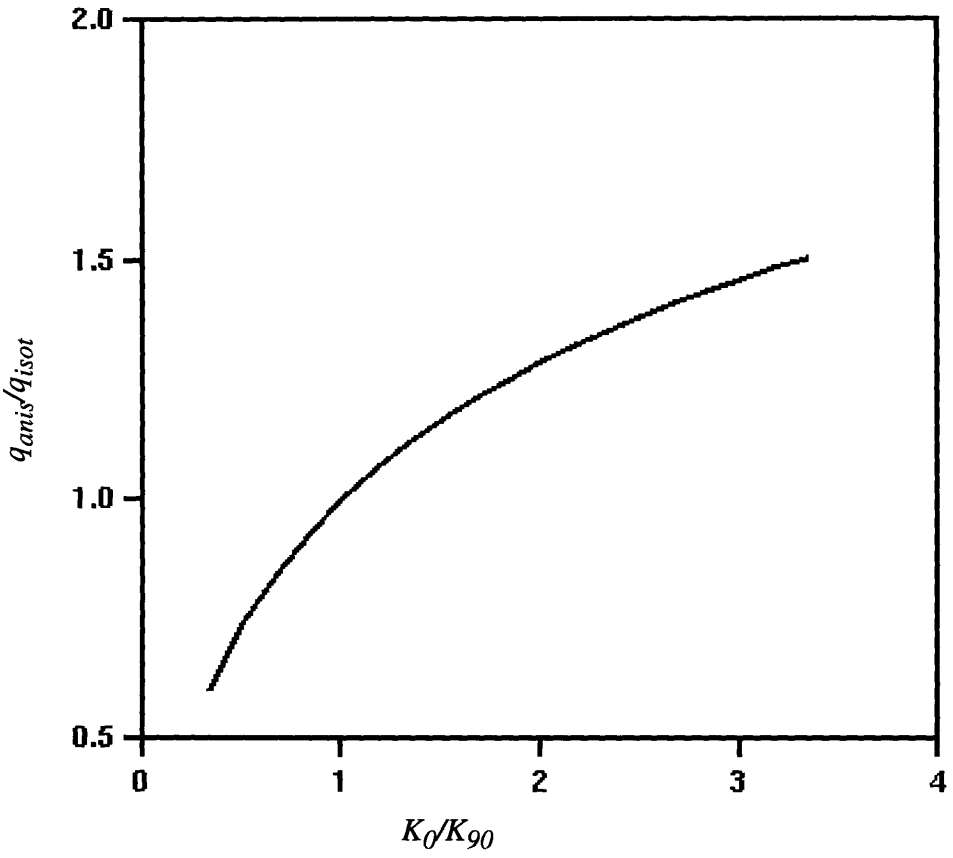

Figure 4.22: *Ratio of Approximate to Exact Radiative Flux (Use Extinction Coefficient Measured Parallel to the Rise Direction in Isotropic Rosseland Equation)*

As can be seen, substantial errors could result if the anisotropy resulted in an extinction coefficient of the form of equation 4.46 and one used K_0 with the isotropic Rosseland equation. If this were the case and K_0 were $2/3K_{90}$, the isotropic Rosseland equation would overpredict the actual anisotropic radiative flux by 18%.

Consider using the arithmetic average of the extinction coefficients parallel and perpendicular to the rise direction, K_0 and K_{90}, which can easily be measured. Errors are significantly reduced for the case of the harmonic function $K(\theta)$ if one were to use this average, $K_{avg}=1/2(K_0+K_{90})$, with the isotropic Rosseland equation. This can be seen in Table 4.8 and in figure 4.23 which again compares the anisotropic to the isotropic fluxes for different K_0/K_{90} ratios.

K_0/K_{90}	q_{anis}/q_{isot}
0.333	1.211
0.500	1.109
0.667	1.054
0.833	1.021
1.000	1.000
1.167	0.986
1.333	0.978
1.500	0.972
1.667	0.968
1.833	0.966
2.000	0.966
2.167	0.966
2.333	0.967
2.500	0.968
2.667	0.969

Table 4.8: *Ratio of Anisotropic to Isotropic Radiative Fluxes (Use K_{avg} in Isotropic Rosseland Equation)*

K_0/K_{90}	q_{anis}/q_{isot}
2.833	0.971
3.000	0.973
3.167	0.976
3.333	0.978

Table 4.8: *Ratio of Anisotropic to Isotropic Radiative Fluxes (Use K_{avg} in Isotropic Rosseland Equation)*

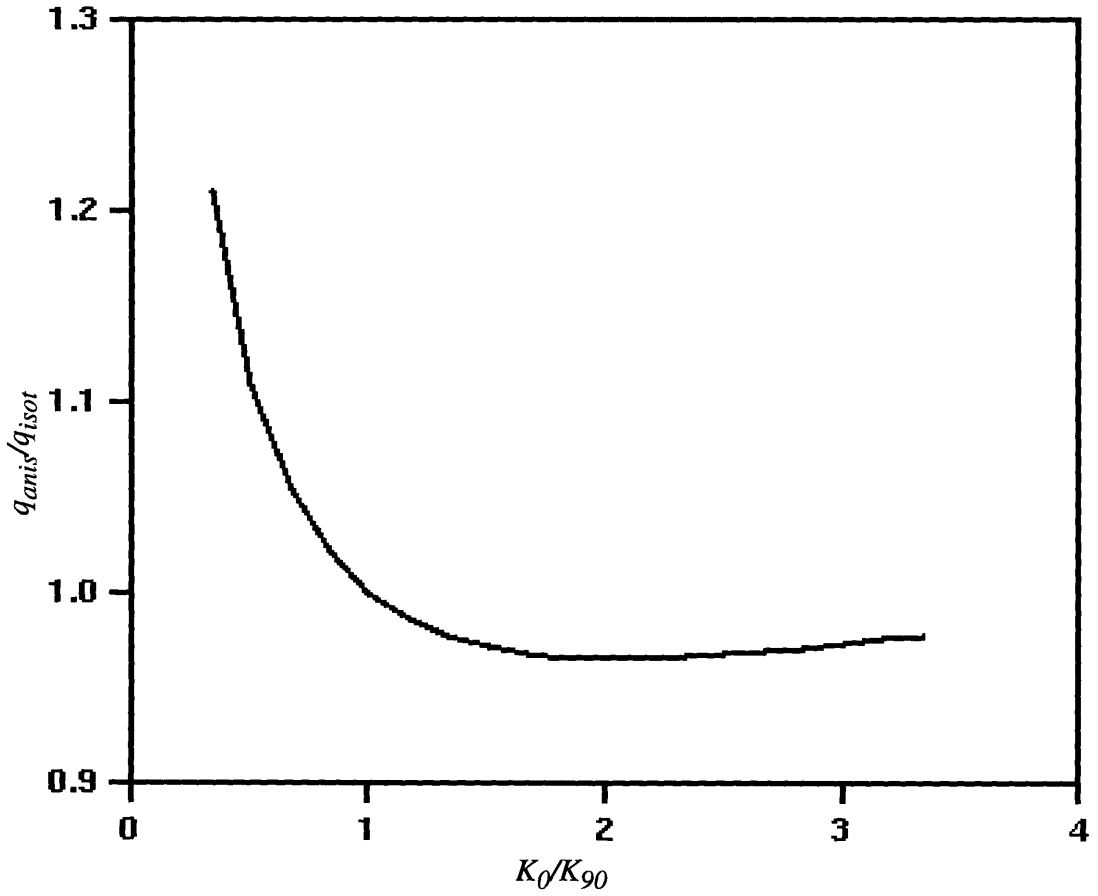

Figure 4.23: *Ratio of Approximate to Exact Radiative Flux Using K_{avg} in Isotropic Rosseland Equation*

The isotropic radiative flux is overpredicted by only 5% if K_0 is $2/3K_{90}$. For the special case of a harmonic function of $K(\theta)$, the arithmetic average extinction coefficient is the same as the P-1 approximate extinction coefficient

$$K_{p1} = 2\int_0^{\pi/2} K(\theta)\cos\theta\sin\theta d\theta \tag{4.47}$$

For other forms of $K(\theta)$ this equality would not be true and using K_{avg} and K_{p1} in the isotropic Rosseland equation would yield different results. The appeal of using K_{avg} with the isotropic Rosseland equation is that it should provide good agreement with the exact anisotropic radiative flux with only two measurements.

We next conducted a look at how the anisotropy of the cells affects the radiative properties of the actual foams provided by ICI. That is, for four foams of a measured anisotropy factor, we determined the difference between the extinction coefficients in the anisotropic (K_0) and in the isotropic directions (K_{90}). The results of the transmission measurements for these foams are provided in Table 4.9.

foam	mean cell diameter (mm)	anisotropy *a/b*	K_0 (cm^{-1})	K_{90} (cm^{-1})	K_0/K_{90}
NBE 678/21/47	0.109	1.35	61.0	65.0	0.94
NBE 819/16/2	0.192	1.80	40.7	50.5	0.81
NBE 863/13/1	0.284	1.70	27.0	35.5	0.76
NBE 785/204	0.363	1.29	34.9	36.9	0.95

Table 4.9: *Measured Extinction Coefficients Showing Influence of Anisotropy*

One apparent trend of the data in Table 4.9 is that foams with a smaller degree of anisotropy (*a/b*) have a lower variation of extinction coefficient between the isotropic and anisotropic directions.

Next we measured the extinction coefficient of two foams at 45° to the orientation axis (K_{45})to get an idea of the functional variation of $K(\theta)$. If $K(\theta)$ were harmonic, the extinction coefficient at 45° to the orientation axis should be equal to $K_{avg}=1/2(K_0+K_{90})$. The comparison between K_{avg} and K_{45} is provided in Table 4.10. From this data, $K(\theta)$ does not appear to be harmonic but more elliptical, meaning having a value closer to K_{90} for a wider range of θ. From Table 4.10 it is clear that the arithmetic average of the extinction coefficients K_0 and K_{90} in conjunction with the isotropic Rosseland equation would not provide a good approximation to the anisotropic flux.

Foams that show a large degree of anisotropy warrant a closer inspection of actual $K(\theta)$ variation to see how well the isotropic model handles anisotropic radiative flux and what combination of measurable extinction coefficients provide the best approximation to the actual anisotropic extinction coefficient.

foam	anisotropy *a/b*	K_0 (cm^{-1})	K_{90} (cm^{-1})	K_{avg} (cm^{-1})	K_{45} (cm^{-1})
NBE 819/16/2	1.8	40.7	50.5	45.6	47.4
NBE 863/13/1	1.70	27.0	35.5	31.3	35.0

Table 4.10: *Comparison of Extinction Coefficients Measured at 45° to Rise Direction and Values Predicted if Harmonic Function $K(\theta)$*

4.9 Statistical Distribution of Cell Sizes

With radiation treated as a local process related to the mean cell diameter of the foam the possibility exists that a widely varying distribution of cell sizes could greatly affect the extinction coefficient. If the cell sizes varied enough, the validity of a single extinction coefficient to represent the properties of the whole foam would be questionable. We carried out a first look at this to determine the influence of cell segregation. The details of this analysis are described in Section 4.10 after a description of how to determine the cell size distribution. Consider a segregated distribution between two cell sizes in parallel to the direction of heat flow (figure 4.24) with foam density constant in both sections. We compared the true foam conductivity of segregated cells and the foam conductivity using the average cell diameter as a function of volume fraction of cells of diameter d_1. Use of mean cell diameter underpredicts the true foam conductivity by as much as 9% if the volume fractions of cells of each diameter are equal (w_1=0.5, d_1=0.1mm, d_2=0.4mm in figure 4.24). So part of this project included an analysis of the cell size variation in a foam and how measured cell size variations would likely affect the extinction coefficient.

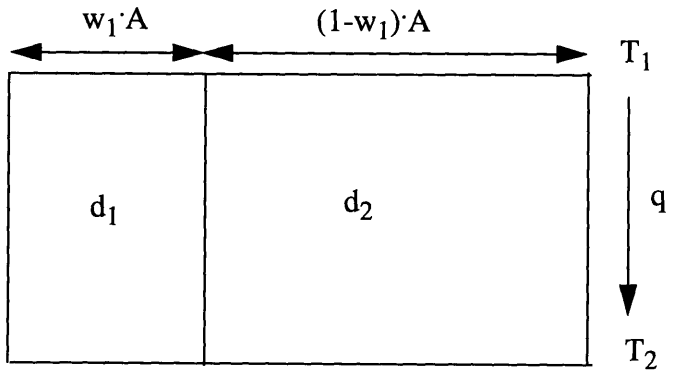

Figure 4.24: *Foam Consisting of Segregated Cells*

The calculation of foam cell size distribution from SEM or confocal micrographs is not as straightforward as measuring the distribution of diameters on the micrograph. Even if all foam cells are spheres with exactly the same diameters, a random section plane through the foam will cut cells at different section planes from the cell center yielding a distribution of sizes on the micrograph. This is depicted in figure 4.25. Adding complexity to the problem is an actual distribution of cell sizes. Now a random section plane will not only cut a sphere at different locations from the center, but will cut cells of different sizes at different locations from the centers. The problem created is depicted in figure 4.26. As shown in the figure, two cells of different diameter could yield a section of the same diameter.

Fortunately, methods to obtain actual size distributions from section planes were developed in the 1950s and 1960s primarily by metallurgists interested in the grain sizes of metals. Several techniques exist and are reviewed in Underwood's *Quantitative Stereology* [12]. The techniques cover diverse systems of measurement, from measuring section diameters, intercepted chord lengths, to measured section areas to develop the cell distribution and agree quite well with each other. The methods do vary considerably in assumptions necessary for the analysis and in complexity. The method chosen calculates size distribution from measured section areas. This method is most useful for a few reasons. Unlike many others, this method works for particles of nonspherical shapes. Previous work [9,10] indicate that polyurethane foam cells are best described by polyhedral shapes such as the pentagonal dodecahedron. Another important reason why this method was chosen is that it is a rather easy method to implement with computer code. Most of the other methods that could handle nonspherical shapes become unwieldy once a nonspherical shape is used.

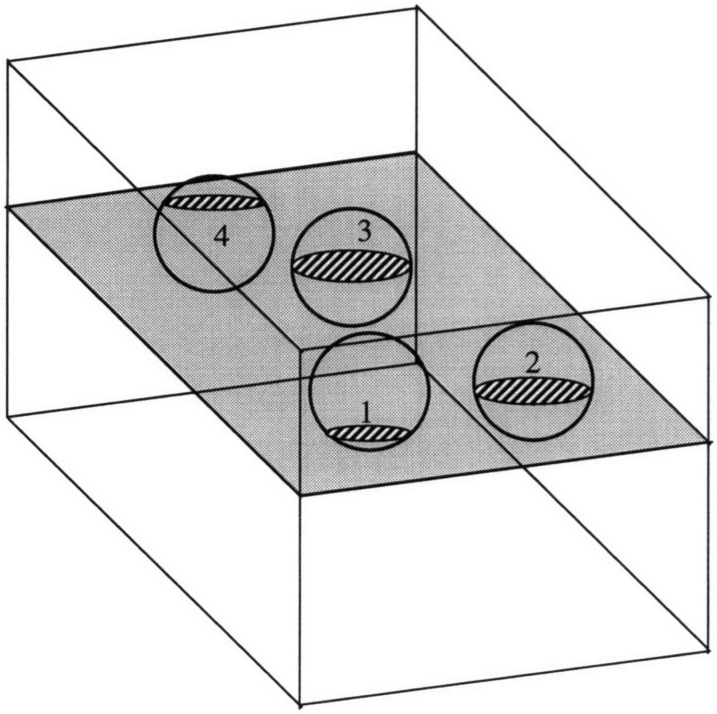

(a) Intersection of Plane with Volume Filled with Spheres of Radius R

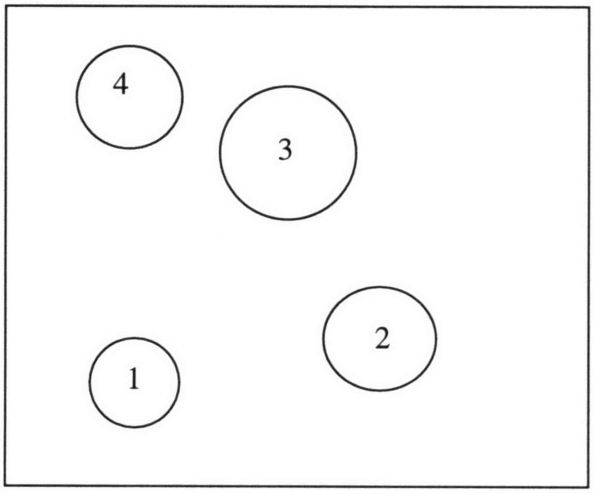

(b) Intersected Areas on Section Plane

Figure 4.25: *Distribution Resulting from Spheres of Same Diameter*

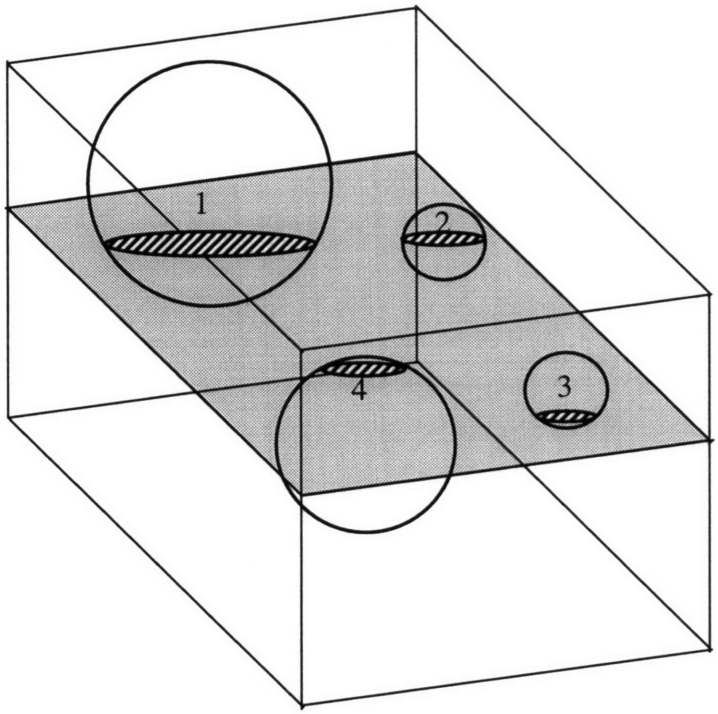

(a) Intersection of Plane with Volume Filled with Spheres of Different Radii

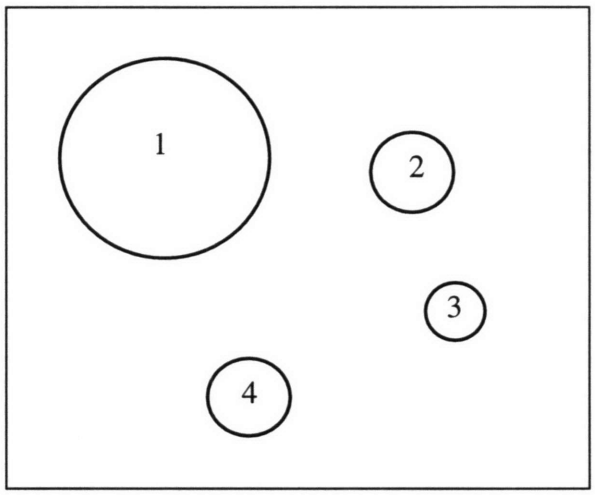

(b) Intersected Areas on Section Plane

Note: Spheres 2 and 4 have different radii but produce same section areas

Figure 4.26: *Distribution Resulting from Spheres of Different Diameters*

Assumptions in the method are for the most part flexible enough to encompass foam distributions. These include particles being of the same shape like a collection of spheres, a collection of cubes, or a collection of pentagonal dodecahedrons. The shape of the particle must be one such that a section plane intersects the body only once, which is true for all convex bodies. The distribution of particles in space have to be statistically uniform throughout the test volume to ensure that the frequency of cells of a certain size, the number per unit volume, has a constant value for a large enough sample. This assumption appears to be true in foams. The mean cell diameter for different SEM images and for different confocal microscope images for the same foam does not vary greatly and for the images examined, the foam cell diameters are concentrated in size around the mean cell diameter. This may not be true near the surface of foams but appears to be true in the foam interior. The last assumption is the only one that might be violated. This assumption is that the particles are randomly oriented in space. As has been pointed out in section 4.8, this is certainly not true for foams which have an orientation axis and elongated direction. However, an extension of the present method has been developed that allows the determination of cell size distribution of oriented cells based on sections perpendicular to the orientation axis. This method will be described in further detail.

The assumption of the cells having the same shape simplifies the analysis of the morphology considerably. With all cells of one shape, there is only one parameter that is needed to specify the size distribution. This parameter is the diameter of the cells (d). As is explained in *Quantitative Stereology*, it is the same diameter that has been defined in Chapter 2 or in Section 4.4 in the heat transfer equations as the cell diameter and is shown in figure 2.1.

With a parameter to define the particle cell sizes, the governing equation that relates number of particles of a certain size per section plane (N_A) to the number of particles per volume (N_V) is quite simple.

$$N_A = N_V d \tag{4.48}$$

The derivation of this is presented in Appendix A. Now since it would be impractical to measure the continuous section plane size distribution (N_A), the cell size distribution is for classes of particles. Characterizing each class is the section area. That is, particles with section areas within certain bounds are grouped into the same cell size class. Increasing the number of classes increases the approximation to the actual distribution, although it also increases the number of measurements necessary.

Now consider a single particle of a given shape as in figure 4.27. For all of the section planes through the particle there is a certain section plane that yields the maximum section area. That is, even though several section planes might intersect the particle giving the maximum section area, these sections must have the required shape. For a cubic cell as in figure 4.27 there are two section planes that yield the maximum section area. But both yield section areas that are rectangles with sides a and $a\sqrt{2}$ For a pentagonal dodecahedron, the maximum section area has a hexagonal shape. In measuring cell areas in the analysis, it is important to have a large enough number of sections to get the sectional area with both the greatest area and the shape of the maximum area through the body.

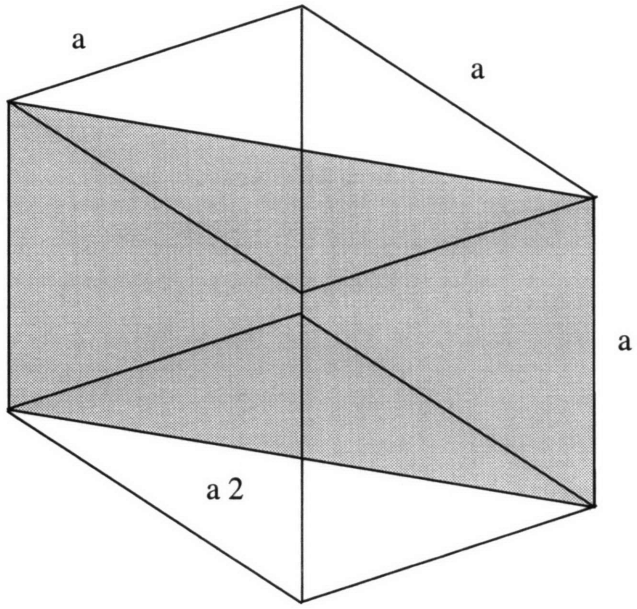

Figure 4.27: *Maximum Section Area Intersected by Section Plane for Cubic Cell*

Still consider a single particle that is intersected by a large number of random planes.. A number of intersected areas, or section areas will result. Grouping these section areas into class intervals, a distribution of section areas characteristic of and only dependent on a body shape will result. The section area distribution of a pentagonal dodecahedron is different from the section area distribution of a sphere and from the distribution describing any other shape as is shown in figures 4.28 and 4.29.

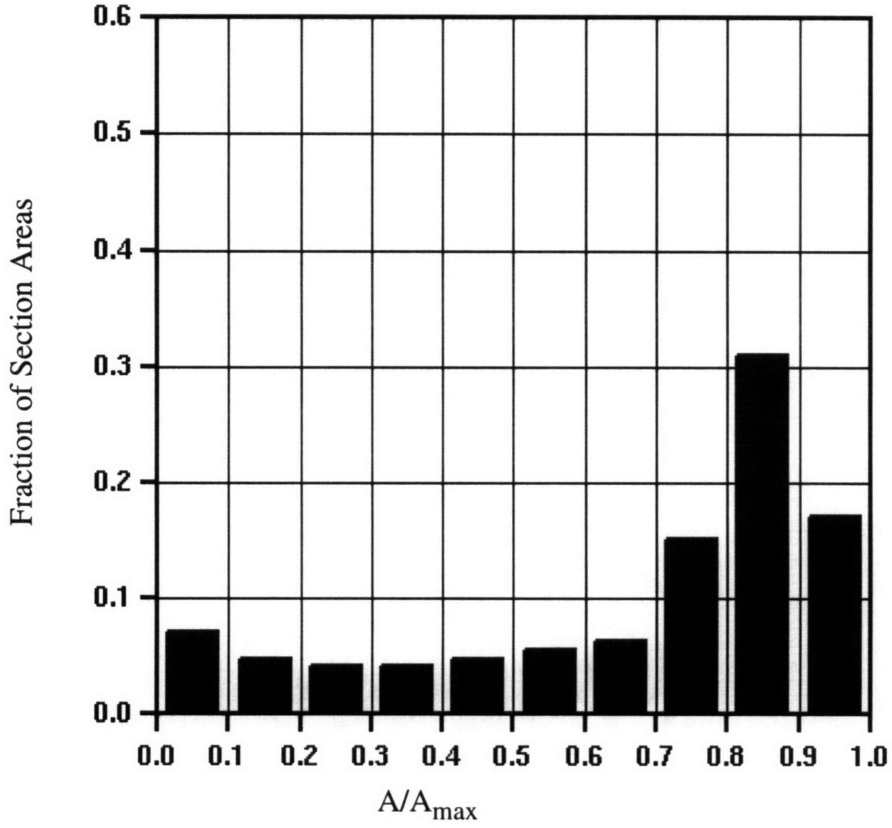

Figure 4.28: *Section Area Probability Distribution for Pentagonal Dodecahedron Derived from* [34]

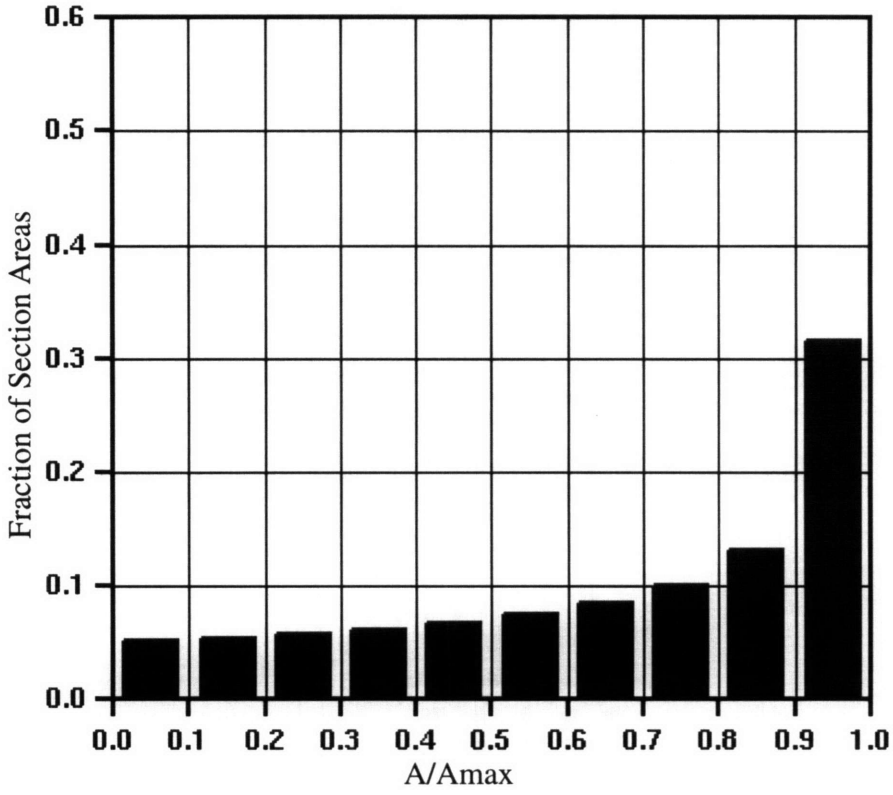

Figure 4.29: *Section Area Probability Distribution for Sphere Derived from* [12]

Important to the determination of cell size distribution is the fact that this area ratio distribution is applicable if a single particle is intersected by random planes or if a random plane intersects a large number of equal sized randomly oriented particles.

Again, the area distribution cut by a random plane, or number of particles per section plane (N_A) versus A/A_{max}, is unique and completely determined by the particle shape. F.C. Hull and W.J. Houk [34] determined experimentally the A/A_{max} distribution if pentagonal dodecahedrons are intersected by a random test plane. Their results are shown in figure 4.28.

In establishing the matrix equations derived from relationship 4.48 used to solve for the cell size distribution, the following subscript notation will apply.

- j: relating to sphere of diameter j (actual cell diameter)
- i: relating to section area diameter i (intersected section diameter)

Using these subscripts, equation 4.48 can be rewritten as

$$N_{Vj} = \frac{\sum_i (N_A)_{ij}}{d_j} \tag{4.49}$$

That is, the number of particles per unit volume of size j are equal to the number of sections of all sizes obtained from particles of size j divided by the cell diameter of size j. N_{Aij} is the number of sections of size i from particle j.

Now define the probability that a section plane will intersect a particle of size j to yield a section of diameter d_i, P_{ij}. From its definition, this probability is

$$P_{ij} = \frac{(N_A)_{ij}}{\sum_i (N_A)_{ij}} \tag{4.50}$$

Combining expressions 4.49 and 4.50, the following relationship can be established

$$N_{Aij} = P_{ij} N_{Vj} d_j \tag{4.51}$$

That is, the number of particles per unit area of section size i originating from particles of size j is equal to the probability of a section plane intersecting a particle of size j to yield a section of size i times the total number of sections per unit area from particles of size j,

which is the number of particles per unit volume of size j times the diameter of the particles of size j.

Summing over all particles gives the number per area of sections of size i, which is the measurable quantity from confocal or SEM images

$$N_{Ai} = \sum_j (N_A)_{ij} = \sum_j P_{ij} N_{Vj} d_j \tag{4.52}$$

This can be written in matrix notation as

$$[N_A] = [A]\,[N_V] \tag{4.53}$$

where

$$A_{ij} = P_{ij} d_j \tag{4.54}$$

Taking the number of class intervals i equal to the number of measured section intervals j, equation 4.53 is directly solvable as

$$[N_V] = [A]^{-1}\,[N_A] \tag{4.55}$$

Even though these equations do not deal with the anisotropy of the foam cells, they were used for a first look at the cell size distribution in foams. The procedure was as follows. First, section areas were measured using *IMAGE* 1.47 (described in Chapter 3). The maximum section area and total area of sections were calculated. Ten classes of A/A_{max} were formed and the number of sections per total area in each A/A_{max} class (N_{Ai}) were determined. The area of each class interval (A_j) is the mean A/A_{max} of each class times the maximum area (A_{max}). For a sphere, the class diameter (d_j) is

$$d_j = 2\sqrt{\frac{A_j}{\pi}} \tag{4.56}$$

and for a pentagonal dodecahedron it is

$$d_j = 2.57\sqrt{\frac{A_j}{5.161}} \tag{4.57}$$

calculated from Underwood's mean projected area and mean projected height data [12]. The probability of intercept (P_{ij}) is calculated from the assumed shape's N_A versus A/A_{max} curve.Then A_{ij} is calculated

$$A_{ij} = P_{ij}d_j \tag{4.58}$$

The distribution of cells (N_{Vj}'s) in the class intervals (d_j's) is solved using a matrix solver (MATLAB in this case) using equation 4.55.

Results of cell size distributions for three foams provided by ICI Polyurethanes are shown in figures 4.30 through 4.32. How these distributions affect the extinction coefficient will be discussed later in this section.

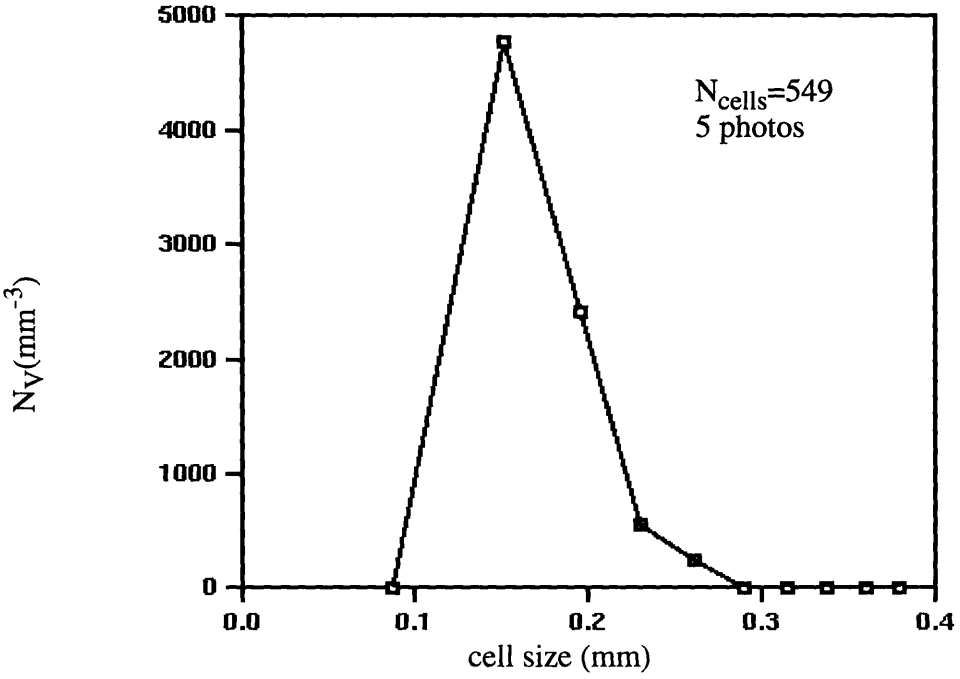

Figure 4.30: *Foam NBE 819/16/2 Cell Size Distribution*

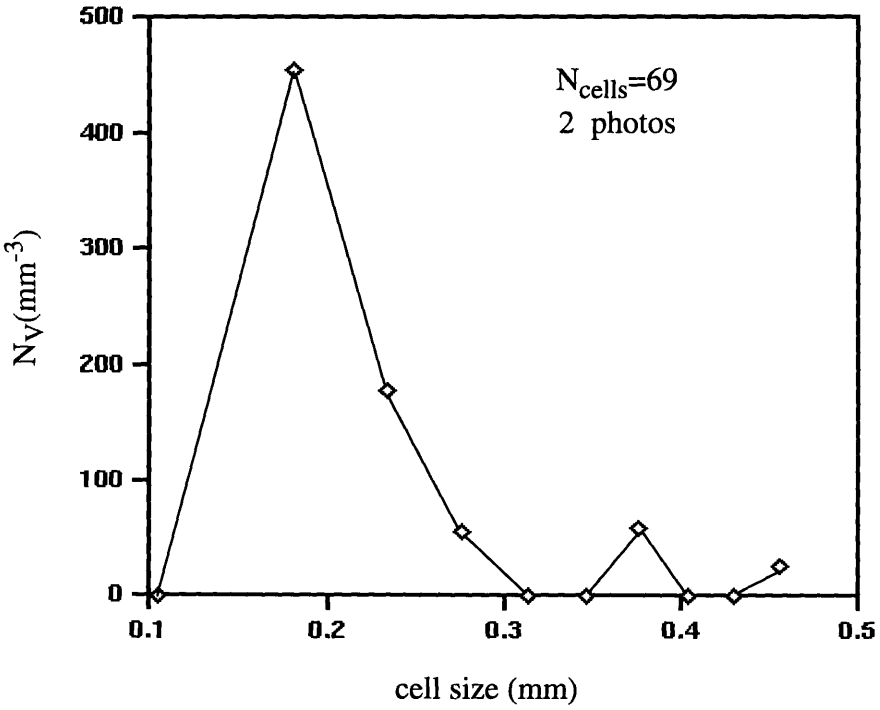

Figure 4.31: *Foam NBE 819/16/1 Cell Size Diatribution*

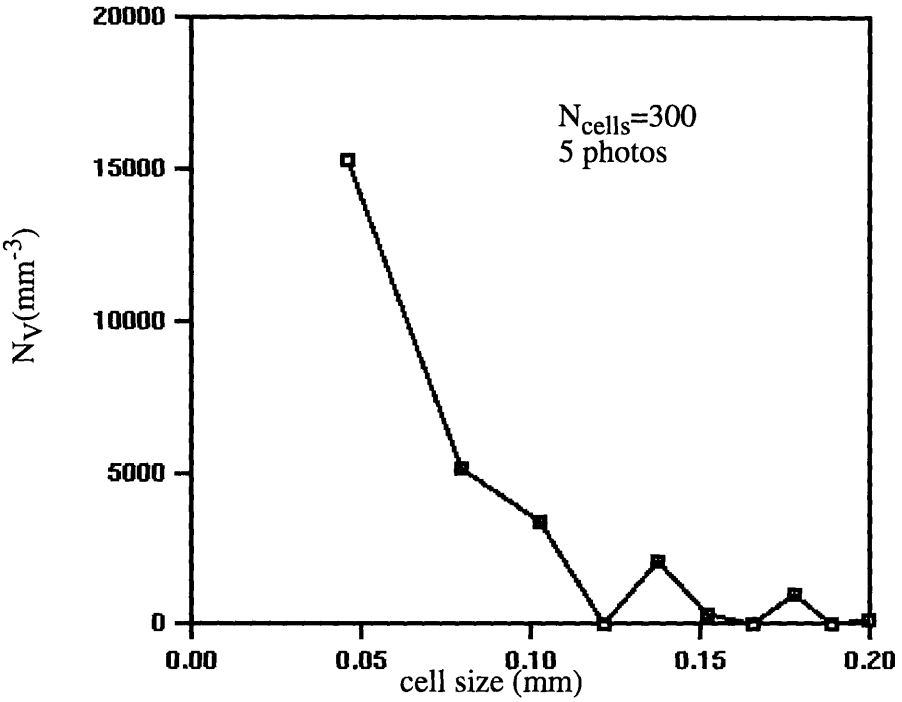

Figure 4.32: *Foam NBE 678/21/47 Cell Size Distribution*

With the cells well mixed in the foam, the same mean cell diameter as defined in Chapter 2 should be predicted from these results. The proper mean of the distribution should relate the extinction coefficient predicted by the distribution to that predicted by the mean cell diameter of Chapter 2. That is, from Chapter 2, the extinction coefficient is expressed as

$$\overline{K} = \frac{4.1\sqrt{f_s \rho_f / \rho_s}}{d_{avg}} + (1 - f_s)\frac{\rho_f}{\rho_s} K_w \tag{4.59}$$

For well mixed cells, the extinction coefficient is

$$\overline{K} = \sum_i w_i K_i \tag{4.60}$$

where w_i is the volume fraction of cells of size i or

$$w_i = \frac{N_{vi}\pi d_i^3/6}{\sum_j N_{vj}\pi d_j^3/6} = \frac{N_{vi}d_i^3}{\sum_j N_{vj}d_j^3} \tag{4.61}$$

and

$$K_i = \frac{4.1\sqrt{f_s \rho_f/\rho_s}}{d_i} + (1-f_s)\frac{\rho_f}{\rho_s}K_w \tag{4.62}$$

So for well mixed cells

$$\overline{K} = \sum_i \frac{N_{vi}d_i^3}{\sum_j N_{vj}d_j^3}\frac{4.1\sqrt{f_s \rho_f/\rho_s}}{d_i} + \sum_i \frac{N_{vi}d_i^3}{\sum_j N_{vj}d_j^3}\left((1-f_s)\frac{\rho_f}{\rho_s}K_w\right) \tag{4.63}$$

$$\overline{K} = (4.1\sqrt{f_s \rho_f/\rho_s})\sum_i \frac{N_{vi}d_i^2}{\sum_j N_{vj}d_j^3} + (1-f_s)\frac{\rho_f}{\rho_s}K_w \tag{4.64}$$

Equating the extinction coefficients for the well mixed case and for the mean cell diameter and rearranging yields

$$d_{avg} = \frac{\sum_j N_{vj} d_j^3}{\sum_j N_{vj} d_j^2} \tag{4.65}$$

This value calculated from the cell distribution should be equal to that calculated from the surface-to-volume ratio of Section 4.4. The comparison of the two for the cell distributions of figure 4.30, 4.31, and figure 4.32 is provided in Table 4.11.

foam	d_{avg} (from distribution) (mm)	d_{avg} (from surface-to-volume calculation) (mm)
NBE 819/16/2	0.187	0.192
NBE 678/21/47	0.113	0.109

Table 4.11: *Mean Cell Size from Distribution and Surface-To-Volume Measurement*

In actuality, the foam cells are not isotropic bodies, but rather oriented structures, which violates the assumption of random orientation. Therefore, the cell size distribution analysis was modified to account for oriented structures. That is, a method to describe the cell size distribution of ellipses of a known anisotropy factor (*a/b* in Section 4.9) was developed. This method employs examination of sections perpendicular to the rise direction (see figure 4.33) and use of the relation 4.48.

Just as with other assumed cell shapes like spheres and pentagonal dodecahedrons a means to determine the probability of intersecting an ellipse to yield a certain section area had to be developed. The development of this probability function is described in Appendix F. The probability of obtaining section areas in A/A_{max} classes is shown in figure 4.34.

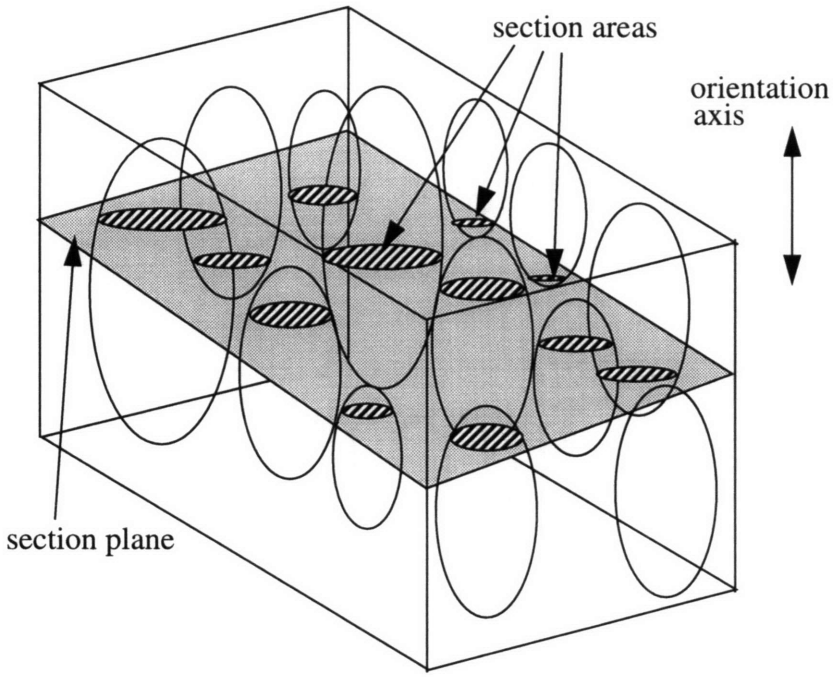

Figure 4.33: *Section Areas Used in Anisotropic Size Distribution Analysis*

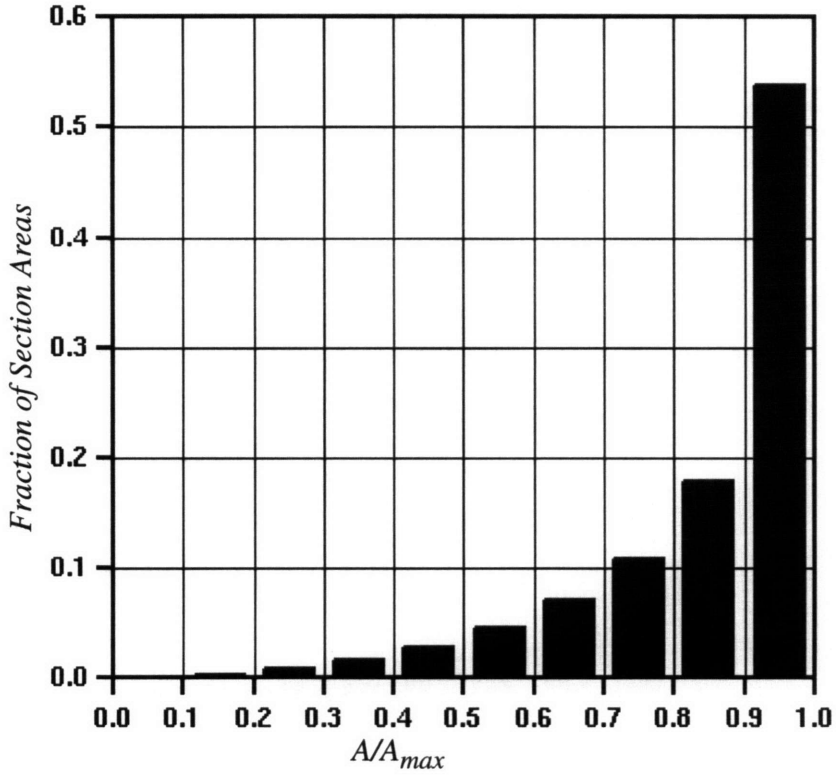

Figure 4.34: *Fraction of Section Areas of Size A/A_{max} When Ellipse Intersected by Planes Perpendicular to Orientation Axis*

Again, as with the method to measure isotropic distributions, section areas are measured, the difference being that only areas on section planes perpendicular to the orientation axis are measured. The number of sections per total area measured in each A/A_{max} class are calculated in the same manner as with the random section method.

The particle class diameters are found in the following manner. For each class interval j, the area representing that class is equal to the mean A/A_{max} of that interval multiplied by A_{max}. The minor axis radius, b_j, which was displayed in figure 2.2 is

$$b_j = \sqrt{\frac{A_j}{\pi}} \tag{4.66}$$

To relate the class diameters, d_j, to b_j first consider equation 2.5 which relates the cell diameter to the surface to volume ratio. Since the surface-to-volume ratio is 1/2 the ratio of surface area to volume of an individual particle, S_j/V_j (see internal surface area definition in Section 4.5), then the class diameter can be expressed as

$$d_j = \frac{3.46}{\frac{1}{2}S_v} = \frac{6.92}{S_j/V_j} \tag{4.67}$$

The surface area and the volume of a single elliptical particle are defined by Underwood [12] in terms of the major and minor axes radii. Therefore, S_j/V_j ca n be written as

$$\frac{S_j}{V_j} = \frac{2\pi\,(b_j)\;(b_j + \frac{a_j}{\varepsilon}\sin^{-1}\varepsilon)}{\frac{4}{3}\pi\,(a_j)\;(b_j^2)} \tag{4.68}$$

where ε is defined in terms of the anisotropy factor, e,

$$\varepsilon = \sqrt{1 - \frac{1}{e^2}} \tag{4.69}$$

and equation 4.68 can be rewritten in the form

$$\frac{S_j}{V_j} = \frac{3}{2eb_j}\,(1 + \frac{e}{\varepsilon}\sin^{-1}\varepsilon) \tag{4.70}$$

and the cell class diameter can be written as

$$d_j = \frac{6.92}{\frac{1.5}{eb_j}\left(1 + \frac{e}{\varepsilon}\sin^{-1}\varepsilon\right)} \tag{4.71}$$

So now that the class diameters are defined, the number of section areas per total area are defined, and the probability of intersecting ellipses perpendicular to the orientation axis (the major axis) to yield certain section area ranges are defined, the matrix equation 4.55 can now be solved. That is, matrix elements N_{Ai} are known, the elements A_{ij} equals $d_j P_{ij}$, and the number of cells in each class are

$$[N_V] = [A]^{-1}[N_A] \tag{4.72}$$

The cell size distributions based on the anisotropic cells approach were calculated for four of the foams provided by ICI. The distributions are shown in figures 4.35 and 4.36. Also shown in Table 4.12 is the comparison of mean cell diameter calculated from the distribution compared to the mean cell diameter calculated from the surface-to-volume ratio.

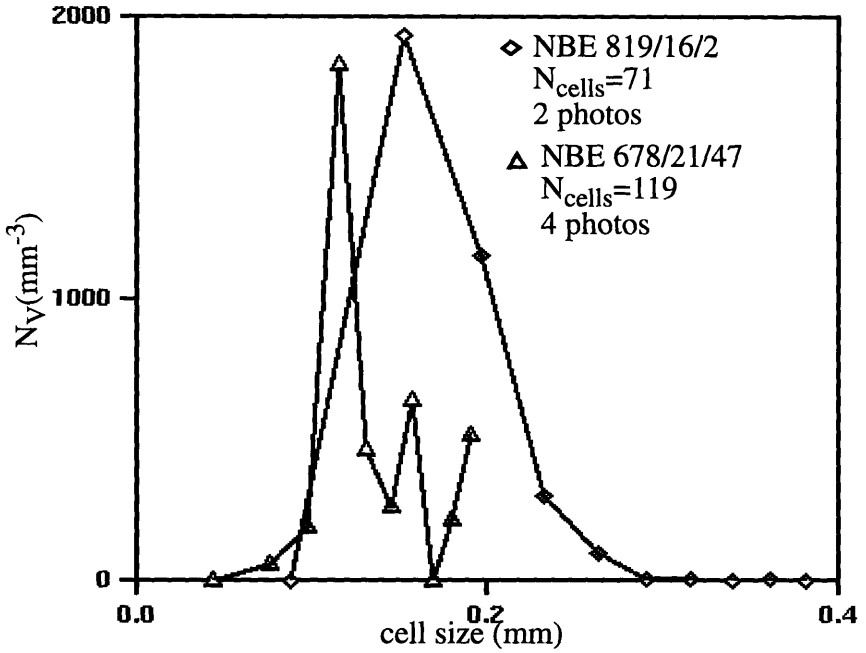

Figure 4.35: *Foam NBE 819/16/2 & NBE 678/21/47 Cell Size Distributions*

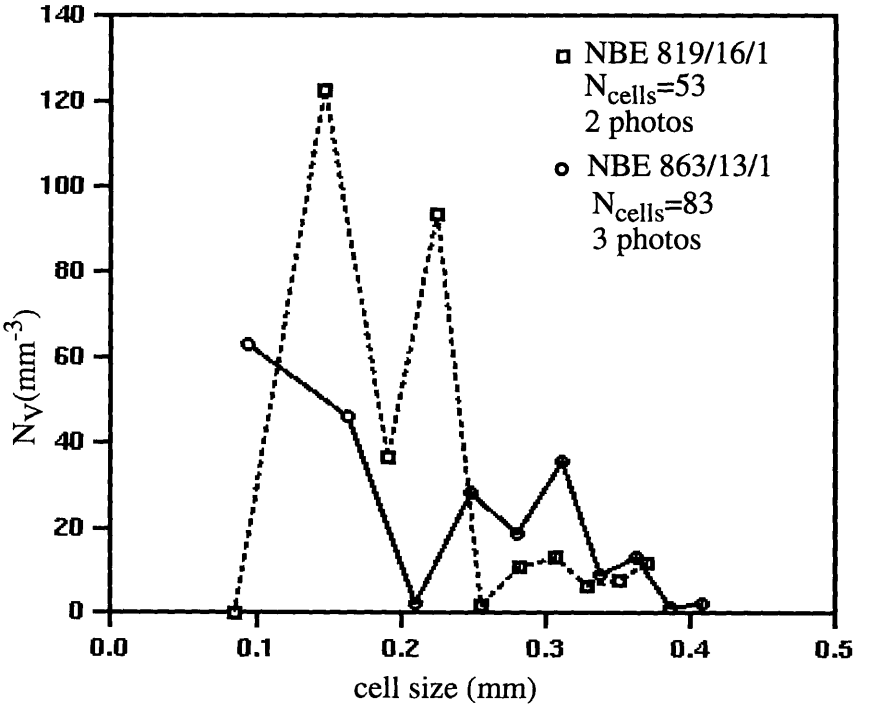

Figure 4.36: *Foam NBE 819/16/1 & NBE 863/13/1 Cell Size Distributions*

foam	d_{avg} (from distribution) (mm)	d_{avg} (from surface-to-volume calculation) (mm)
NBE 819/16/1	0.248	0.238
NBE 819/16/2	0.192	0.192
NBE 678/21/47	0.149	0.109
NBE 863/13/1	0.287	0.284

Table 4.12: *Mean Cell Size from Distribution and Surface-To-Volume Measurement*

4.10 Effect of Cell Distribution on Extinction Coefficient

How these cell size distributions might influence the extinction coefficient of the foams was analyzed. Worst case segregations where cells of different diameters are grouped into distinct regions are considered. The first considers regions with different cell diameters in parallel to the heat transfer as in figure 4.37(a) and the second considers these regions in series as in figure 4.37(b). In each section, the density is assumed to still be the overall foam density. The analysis only strictly holds for isotropic cells since the relation between the extinction coefficient and anisotropic cells has not been fully explored. But this restriction will be relaxed to also determine how the cell size distributions measured from the anisotropic cells might influence the overall extinction coefficient.

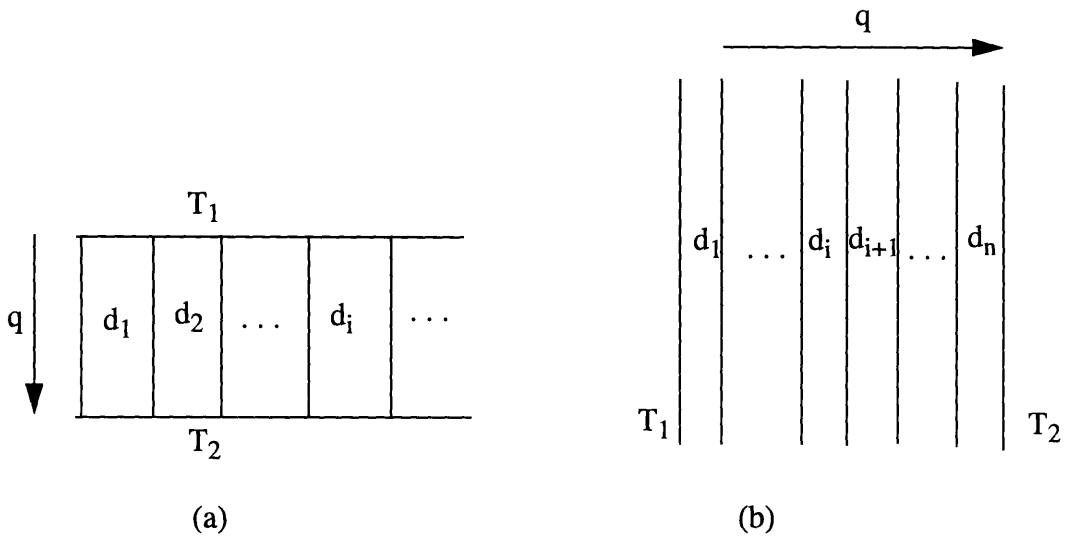

Figure 4.37: *Extreme Cases of Foam Cell Segregation*

To consider how the cell segregation affects the extinction coefficient of the first case, consider the flux across the cells.

$$q = q_1 + q_2 + \ldots = \sum_i q_i = A_{total} k_{avg} \frac{(T_1 - T_2)}{t} \tag{4.73}$$

where

$$q_i = A_i k_i \frac{(T_1 - T_2)}{t} \tag{4.74}$$

and

$$k_i = k_{solid} + k_{gas} + k_{radiation,i} \tag{4.75}$$

k_{solid} and k_{gas} can be seen in Chapter 2 to be independent of cell size, so they are the same for each section of cells. They are calculated in this analysis from equations 2.7 and 2.13. The radiation term is

$$k_{rad,i} = \frac{16\sigma T^3}{3K_i} \tag{4.76}$$

where

$$K_i = \frac{4.1\sqrt{f_s \rho_f / \rho_s}}{d_i} + (1 - f_s)\frac{\rho_f}{\rho_s} K_w \tag{4.77}$$

so combining equations 4.73 and 4.74

$$\sum_i A_i k_i \frac{(T_1 - T_2)}{t} = A_{total} k_{avg} \frac{(T_1 - T_2)}{t} \tag{4.78}$$

Rearranging yields

$$k_{avg} = \sum_i \frac{A_i}{A_{total}} k_i \tag{4.79}$$

Defining the volume fraction (w_i) as the total volume of cells of size i per total volume of foam and recognizing that the width (t) of each section is the same, one can write the relation

$$w_i = \frac{V_i}{V_{total}} = \frac{N_{vi} d_i^3}{\sum_j N_{vj} d_j^3} = \frac{A_i t}{A_{total} t} = \frac{A_i}{A_{total}} \tag{4.80}$$

Substituting this expression into equation 4.79

$$k_{avg} = \sum_i \frac{N_{vi} d_i^3}{\sum_j N_{vj} d_j^3} k_i \tag{4.81}$$

k_{avg} is now

$$k_{avg} = k_{solid} + k_{gas} + \frac{16\sigma T^3}{3K_{avg}} \tag{4.82}$$

and so the effect of segregated cells on the extinction coefficient can be written

$$K_{avg} = \frac{16\sigma T^3}{3\,(k_{avg} - k_{solid} - k_{gas})} \tag{4.83}$$

Doing a similar analysis for cells segregated in series to the heat transfer, the flux across the foam is

$$q = \frac{T_1 - T_2}{\sum_i \frac{w_i V_{total}}{k_i A}} = \frac{T_1 - T_2}{\frac{V_{total}}{k_{avg} A}} \tag{4.84}$$

where again

$$k_i = k_{solid} + k_{gas} + k_{radiation,\,i} \tag{4.85}$$

Rearranging, the average conductivity is

$$k_{avg} = \frac{1}{\sum_i \frac{w_i}{k_i}} \tag{4.86}$$

The effect of segregation on the extinction coefficient is again expressed by equation 4.83.

For the cell distributions from the isotropic shape factors and from the ellipse shape factor shown, the extinction coefficient due to segregated cells in these two worst case scenarios were calculated. They were also compared to the extinction coefficients from the mean cell diameter predictions and from the well mixed case (given by equation 4.77). These results are shown in Table 4.13. For each of the three cases, the percent error in K predicted from the mean cell diameter is also displayed.

foam	d_{avg} (mm)	K d_{avg} (cm^{-1})	K well mixed (cm^{-1}) / % error	K_{avg} in parallel (cm^{-1}) / % error	K_{avg} in series (cm^{-1}) / % error
NBE 863/13/1 ellipse	0.287	22.07	21.93 + 0.64%	21.02 + 5.00%	21.15 + 4.35%
NBE 819/16/1 ellipse	0.248	27.27	26.35 + 3.49%	24.58 +10.94%	24.85 + 9.74%
NBE 819/16/2 ellipse	0.192	31.50	31.60 - 0.32%	30.53 + 3.18%	30.67 + 2.71%
NBE 678/21/47 ellipse	0.149	42.60	32.73 +30.16%	31.72 +34.30%	31.86 +33.71%
NBE 819/16/2 pent. dodec.	0.187	31.50	32.40 - 2.78%	31.37 - 0.41%	31.51 - 0.03%

Table 4.13: *Cell Distribution Effects on Extinction Coefficient*

foam	d_{avg} (mm)	K d_{avg} (cm^{-1})	K well mixed (cm^{-1}) / % error	K_{avg} in parallel (cm^{-1}) / % error	K_{avg} in series (cm^{-1}) / % error
NBE 678/21/47 pent. dodec.	0.113	42.60	40.96 + 4.00%	36.44 +16.90%	36.63 +16.30%

Table 4.13: *Cell Distribution Effects on Extinction Coefficient*

As can be seen in Table 4.13, for most of the distributions the cells were concentrated so closely to the mean cell diameter that there is little impact in ignoring the distributions. In fact, in the foams other than NBE 678/21/47 the maximum error in K predicted from the mean cell diameter is 11%. The K overprediction using the mean cell diameter for foam NBE 678/21/47 is significant however. The differences could be partially accounted for by the difference in mean cell diameters predicted from the distribution and from the surface-to-volume ratio (see Tables 4.11 and 4.12). Further investigation into the effects of cell size distributions in smaller celled foams like NBE 678/21/47 would be recommended.

4.11 Statistical Look at Total Conductivity Versus T^3

All of the means to calculate radiative conductivity presented in this chapter involve the intermediate calculation of radiative conductivity from a model. That is, transmission measurements requires interpretation of the radiative behavior from Beer's Law and the Rosseland equation. Prediction from morphology measurements require the intermediate theory of the interaction of struts and cell walls with electromagnetic radiation to estimate the radiative conductivity. So in a vain similar to the attempts to measure the solid conductivity, direct measurement techniques of the radiative conductivity were examined. One of the most seemingly direct measurement techniques, calculation of radiative behavior from the temperature dependence of the measured overall conductivity was explored in detail.

Looking at the form of the total conductivity across a foam specimen,

$$k = \delta k_g + \frac{1-\delta}{3} k_p \left[f_s \sqrt{\frac{a}{b}} + 2(1-f_s)\left(\frac{a}{b}\right)^{1/4} \right] + \frac{16\sigma}{3K} T^3 \tag{4.87}$$

one can see that the radiative term can be determined from the variation of the total conductivity with temperature. That is, assuming that the gas and solid conductivity terms are independent of temperature, the slope of conductivity versus T^3 should give a measure of the extinction coefficient. Since

$$\frac{dk}{dT^3} = \frac{16\sigma}{3K} \tag{4.88}$$

the extinction coefficient of the foam should then be

$$K = \frac{16\sigma}{3\left(\frac{dk}{dT^3}\right)} \tag{4.89}$$

Ideally then, the radiative conductivity can be determined from the slope of the variation of conductivity with T^3. The practicality of this technique was explored.

It has to first be established that the gas and solid conductivity terms are not strong functions of temperature. If k_p and k_g are not functions of temperature, both solid and gas conduction terms can be treated as constant with temperature. Over the range where most foam conductivity measurements would be made, data published by. Bhattacharjee et al. [19] indicates that from T=0°F to T=150°F, k_g increases 20%. Torpey [16] measured the variation of k_p with temperature. Again in the range of temperatures where the foam conductivity change would be measured, the solid conductivity changes 20%. This is shown in figure 4.38. This is compared to roughly a 60% change in the radiative conductivity term in the same range. Even though the change in gas and solid conductivity with temperature is not insignificant, consider as a limiting case that all of the change in total conductivity with temperature is due to radiative conductivity.

A practical measurement problem arises even considering the ideal case of equation 4.87. The magnitude of the change in overall conductivity for most foams is small, on the order of the experimental uncertainty of some of the best thermal conductivity measuring instruments.

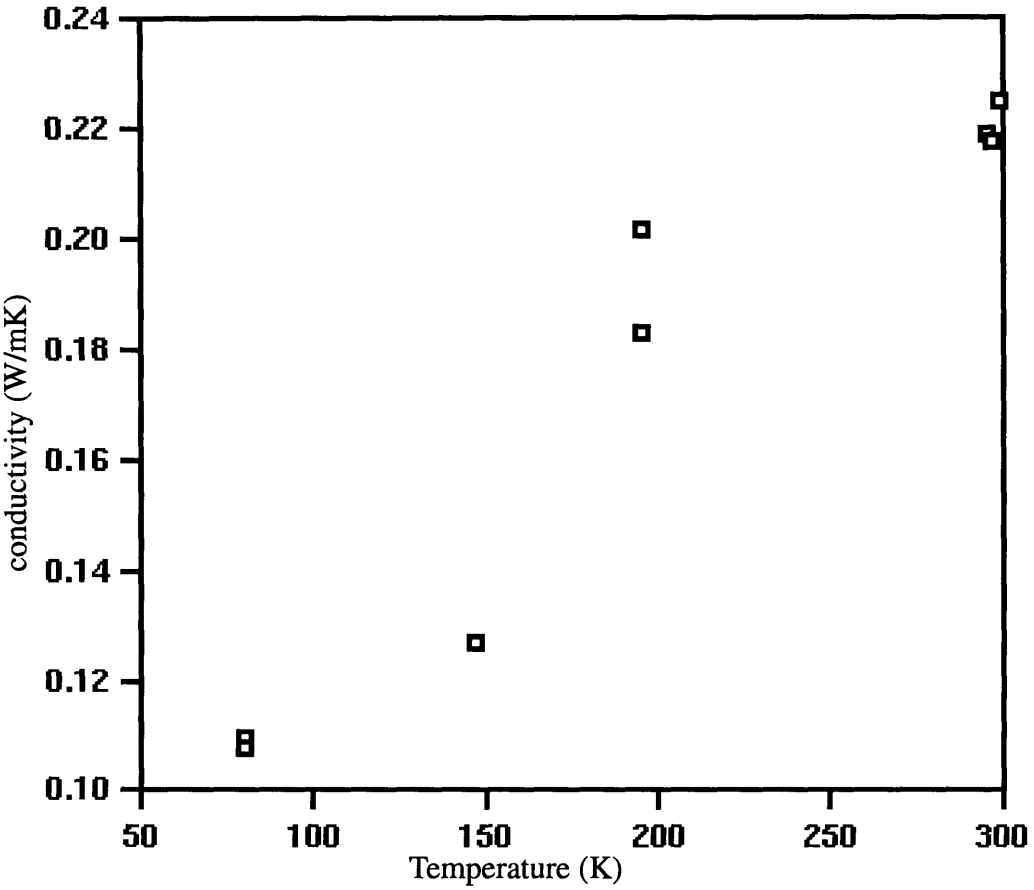

Figure 4.38: *Conductivity of Solid Polyurethane as Measured by Torpey* [16]

For a foam with the following typical parameters,

k_g = 13.5 mW/mK

k_p = 0.263 W/mK

$\delta = 0.9718$ ($\rho_f = 35 kg/m^3$)

$f_s = 0.8$

$a/b = 1.5$

$K = 2200\ m^{-1}$

conductivities calculated from equation 4.87 at T=256K and at T=300K are 0.0189 W/mK and 0.0204 W/mK respectively. The ratio of the conductivity change to the average conductivity (k_{avg}=19.65 mW /mK) is

$$\frac{\Delta k}{k_{avg}} = 7.15\% \tag{4.90}$$

which is on the same order of magnitude as the accuracy of the best equipment available. According to Yarbrough at Oak Ridge National Laboratory [35], such thermal conductivity measurement equipment usually have uncertainties on the order of 2%.

With the possibility of experimental errors overwhelming the accuracy of the technique, a numerical calculation was run to determine the number of measurements that would be needed to get an accurate measure of the radiative conductivity.

For typical property values, total conductivity values versus temperature were calculated from equation 4.87. For the most promising extreme, assume that k_g and k_p are constant with temperature. Next random errors are added to the conductivity values such that the standard deviation of the errors equals the uncertainty of typical measurement equipment. The procedure to add such random errors is as follows.

The normalized cumulative area under a normal distribution curve with standard deviation $\sigma(k)$ is shown in figure 4.39. Here $\sigma(k)$ os equivalent to the uncertainty of the measurement equipment, 2% for the Oak Ridge thermal conductivity measuring equipment. *F(k)* is the area under the normalized curve,

$$F(k) = \frac{1}{2} + \frac{1}{2} erf\left(\frac{k-\bar{k}}{\sigma\sqrt{2}}\right) \tag{4.91}$$

such that

$$\lim_{k \to \infty} F(k) = 1 \tag{4.92}$$

To add random errors that yield a standard deviation of $\sigma(k)$, random numbers are generated from 0 to 1 using a conventional random number generator, in this case the Fortran subroutine outlined in [41]. This value is equivalent to *F(k)*. Then equation 4.91 is solved for k with a given value of $\bar{k}$ the correct conductivity based on an assumed temperature, k_g, k_p, etc.

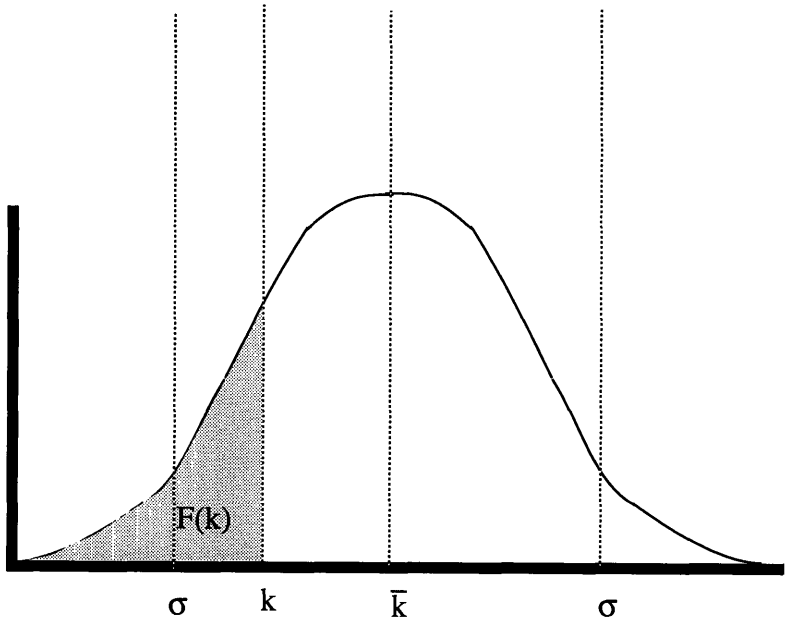

Figure 4.39: *Normal Distribution Curve Showing F(k) (shaded area)*

For the typical values of k_g, k_p, f_s, etc. given above(i.e.k_g = 13.5mW/mK, k_p = 0.263W/mK) , the conductivities at certain temperatures were calculated. For example, if looking at the slope from conductivities calculated at every 20K beginning at T=280K and ending at T=340K, at each temperature the conductivity would be (from equation 4.87)

$$k = (0.9718)\,(0.0135\frac{W}{mK}) + \frac{(1-0.9718)}{3}\,(0.263\frac{W}{mK})\,[0.8\sqrt{1.5} + 2\,(1-0.8)\,(1.5)^{1/4}] + \frac{16\sigma}{3K}T^3 \qquad (4.93)$$

$$k = 0.01312\frac{W}{mK} + 0.003517\frac{W}{mK} + 1.3745\times10^{-10}T^3 \qquad (4.94)$$

Then, using the procedure developed in the last paragraph, random errors are added to the conductivities at every temperature. The error at each temperature is derived from a normal distribution with the simulated conductivity as the mean and the accuracy of the conductivity testing equipment (2% in this case) as the standard deviation. Each simulated trial measurement of radiative conductivity consisted of one measurement at each temperature level. At each temperature, the simulated conductivity was determined as the true value plus the random error. A best fit line was obtained for these measurements at different temperatures. Note that when this trial is repeated, a different set of simulated data is obtained with a different best fit slope. The best fit slopes of all of the trials are then used to obtain a mean and standard deviation for the slope. The standard deviation of the slope gives a measure of the of the accuracy of the technique. For the example of four conductivities calculated at every 20K, the simulated conductivity versus temperature-cubed curve is shown in figure 4.40. Also displayed in the figure are four cases where random errors are introduced to the simulated conductivities.

The least squares best-fit slope through the points having random errors is determined. Assuming that for each sample that the tests with temperature could be run a few times to obtain a few slopes, the mean of the best-fit slopes is compared with the true slope, $16\sigma/3K$.

Two measurement parameters were varied to judge their impact on the final error in predicted extinction coefficient from the mean best fit slopes of conductivity versus temperature cubed. The first was the number and ranges of temperatures at which

conductivities would be measured to obtain a slope. The second was the number of best fit slopes used to obtain a mean best fit slope. Conductivities with simulated measurement errors at 280K, 300K, 320K, and 340K were first considered. The case of three simulated measurements at each of these temperatures was considered with the mean of the three slopes compared to the true slope, $16\sigma/3K$. The cases of 7, 15, and 30 simulated slopes were also considered, with the mean slope for the 7 simulated slopes, mean slope for the 15 simulated slopes, etc are compared to the true slope, $16\sigma/3K$. Next, conductivities were calculated at 10K intervals beginning at 270K and ending at 350K. Again random errors were added to obtain 3,7, and 15 best fit slopes and the mean slope in each case (3 best fit slopes, 7 best fit slopes, etc.) was compared to the true slope, $16\sigma/3K$. Conductivities were calculated at 30K intervals beginning at T=270K and ending at T=360K. Random errors were added to obtain cases with 2,3,5,7, 10, and 20 best fit slopes. Finally the conductivities at 10K intervals between 240K and 400K were used to look at errors in the mean of 2, 3, 5, and 7 best fit slopes.

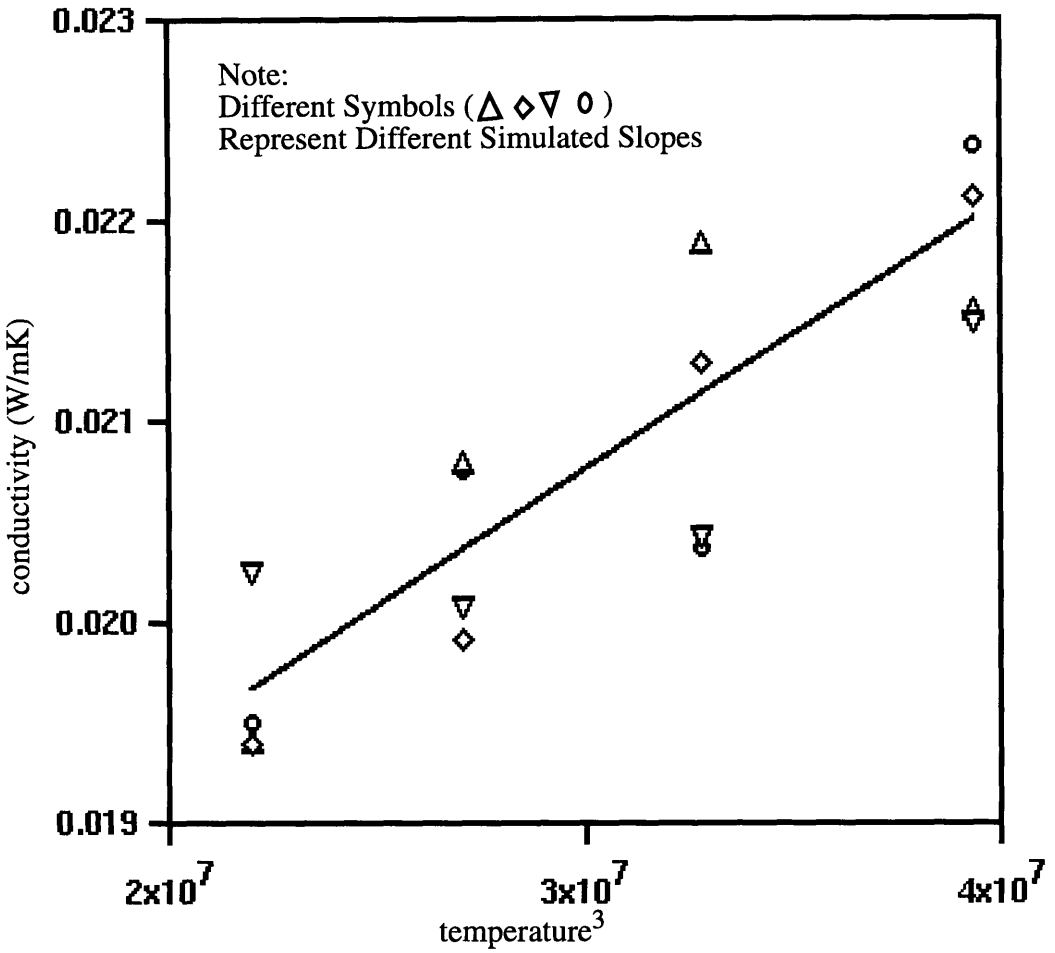

Figure 4.40: *Calculated Conductivities with Simulated Measurement Errors*

The error of the mean slope versus the number of measurements necessary, i.e. the number of temperatures at which measurements are taken per slope times the number of slopes measured, is shown in figure 4.41. Again, this is for 2% standard deviation in the thermal conductivity measuring equipment. The different cases are for different number of conductivity measurements per slope. For 10% accuracy then in calculating the radiative conductivity from the slope of k versus T^3, about 20 total measurements seem to be required. For 5% accuracy, about 40 to 80 total measurements are needed.

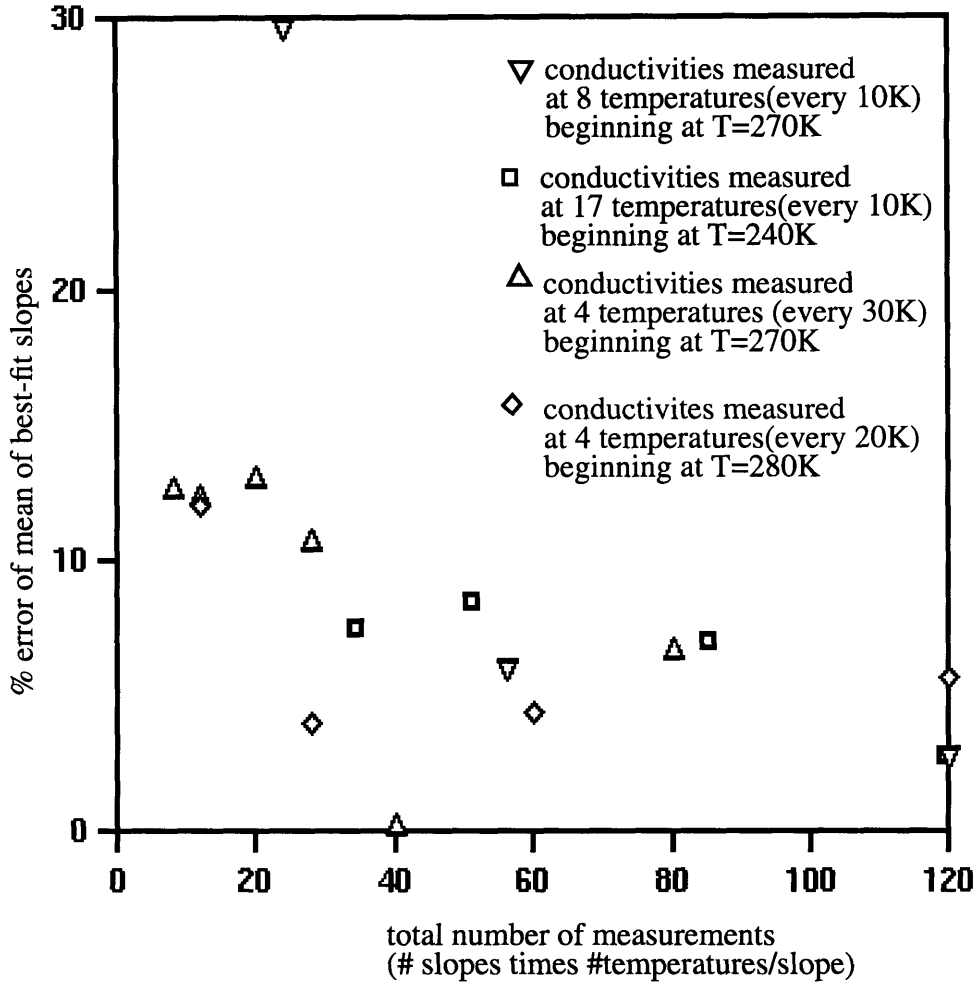

Figure 4.41: *Error in Predicted Slope Resulting from Simulated Measurement Error as a Function of Number of Conductivities Measured*

With each conductivity measurement taking one hour [42], the amount of time to determine the radiative conductivity of a foam to within 5% is approximately 40 to 80 hours. This is under ideal conditions:. one hour measurement time, equipment with 2% precision, and minimal change in the gas and solid conductivities with temperature. So it is likely that 40 to 80 hours is a conservative estimate of the time required to determine the radiative conductivity of one foam sample. In addition, this is the ideal case with k_g and k_p invariant with temperature. As was shown earlier, this is not the case, which

provides additional uncertainty in the results. Therefore, as a quick and simple way to determine the radiative contribution to total heat transfer, the measure of conductivity versus temperature-cubed does not appear to be a viable alternative.

foam	density (kg/m^3)	$K_{meas,//}$ (cm^{-1})	mean cell diameter (mm)	f_s	anisoropy *a/b*	k_{rad} (from K_{meas}) (W/mK)	k_{rad} (from morphology) (W/mK) equations 2.38 and 2.50
NBE 678/21/47	32.1	61.0	0.109	0.34	1.35	1.124E-3	1.675E-3
NBE 785/206	33.0	49.0	0.188	0.65	1.11	1.399E-3	2.156E-3
NBE** 819/16/2	35.0	40.7	0.192	0.54	1.80	1.684E-3	2.241E-3
NBE** 819/16/1	35.6	38.4	0.238	0.77	1.70	1.784E-3	2.467E-3
NBE** 863/13/1	35.9	27.0	0.284	0.36	1.70	2.539E-3	3.287E-3
NBE 785/204	29.2	34.9	0.363	0.67	1.29	1.964E-3	4.090E-3

Table 4.14: *Measured Transmission and Morphology Characteristics and Radiative Conductivities Predicted from Both*

**samples cut with razor at room temperature

Chapter 5

Total Conductivity

5.1 Overall Thermal Conductivity Measurements

The ultimate goal of the theory and measurements is to be able to predict the actual foam conductivity. The overall thermal conductivity measurements of the six foams provided by ICI will be examined. For these foams, the overall conductivity appears to reach a minimum at a cell diameter of 0.2mm rather than continue decreasing with cell size as can be seen in figure 5.1.

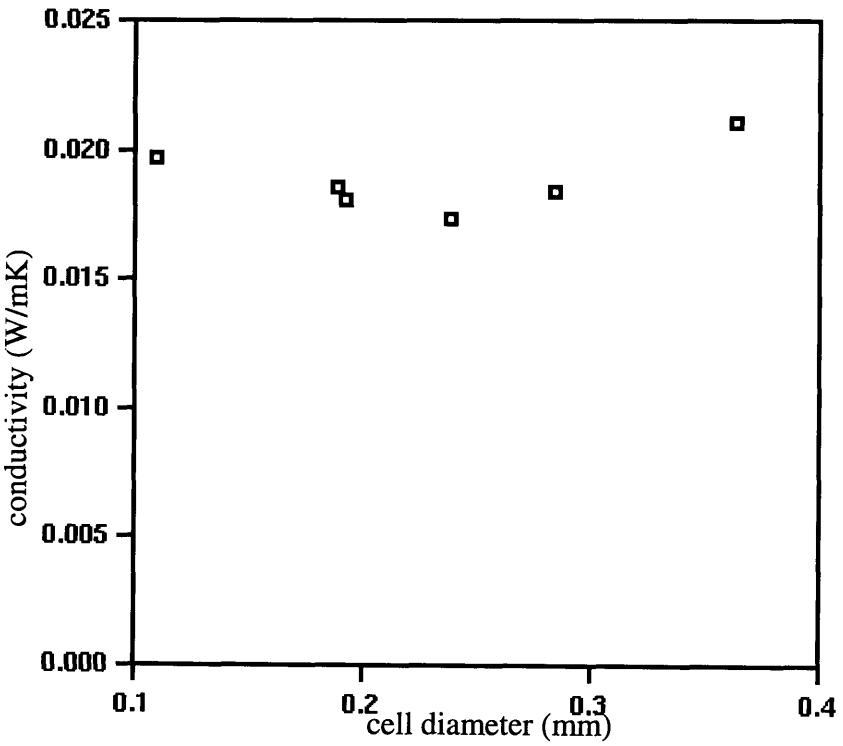

Figure 5.1: *Measured Overall Conductivity*

It is important to see what the conductivity model, equation 2.2, predicts will be the trend of conductivity with these foams.

5.2 Gas Conductivity Calculation

As was described in Chapter 2, three conductivity components are calculated with the model. The first is the dominant gas conductivity component. The Lindsay Bromley equation 2.8 is used for these calculations with the molar fractions provided by ICI. The molar fraction of gases at the time of conductivity testing are shown in Table 5.1. A uniform concentration throughout the foam was assumed.

foam	mol % Air	mol % CO2	mol % HCFC-141b	mol % perfluoro-pentane
NBE 678/21/47	40.73	3.38	---	55.89
NBE 785/206	0.00	31.30	---	68.70
NBE 819/16/2	3.77	35.05	61.18	---
NBE 819/16/1	3.32	32.08	64.60	---
NBE 863/13/1	4.18	26.16	69.66	---
NBE 785/204	2.90	97.10	---	---

Table 5.1: *Gas Composition of ICI Foams*

Since perfluoropentane and HCFC-141b have only recently been explored as foam blowing agents, the thermal properties on these gases are not as well defined as those of CFC blowing agents. The best data to date that could be found for these gases were used, but a certain amount of uncertainty arises. The properties important for calculation of the gas conductivity are the gas's thermal conductivity, boiling point, viscosity, and molecular weight. These properties are listed in Table 5.2.

gas	thermal conductivity (W/mK)	boiling point (K)	viscosity (kg/ms)	molecular weight
air [36]	2.45E-2	82	18.43E-6	29
CO2 [36]	1.51E-2	194.6	15E-6	44.01
HCFC-141b [39]	8.80E-3	305.2	11E-6	117
perfluoro-pentane [37]	1.05E-2	303	11E-6	288.04

Table 5.2: *Properties of Constituent Gases of ICI Foams*

Using the gas properties of Table 5.2 and the molar fractions quoted in Table 5.1, the Lindsay Bromley expression predicts the following gas mixture conductivities. The gas conductivities for the six foams are presented in Table 5.4 at the beginning of section 5.4 where all of the predicted foam thermal properties are listed.

foam	k_{mix} (mW/mK)
NBE 678/21/47	16.4
NBE 785/206	12.5
NBE 819/16/2	11.7
NBE 819/16/1	11.5
NBE 863/13/1	11.2
NBE 785/206	15.4

Table 5.3: *Predicted Gas Mixture Conductivities Assuming Uniform Concentration Throughout Foams*

5.3 Solid Conductivity Calculation

The solid conductivity component was next calculated from the model presented in Chapter 2 and from the morphology measurements of Chapter 4. The results of these calcuations are shown in Table 5.4.

Note the effect that polymer redistribution from struts to cell walls as cell size decreases has on the solid conductivity. This can be seen in figure 5.2 where the solid conductivity as predicted with a constant fraction of solid in the strut is compared to the solid conductivity predicted with the mass redistribution. The changing f_s increases the solid conductivity from what would be expected without polymer redistribution because more of the polymer is in the cell walls.

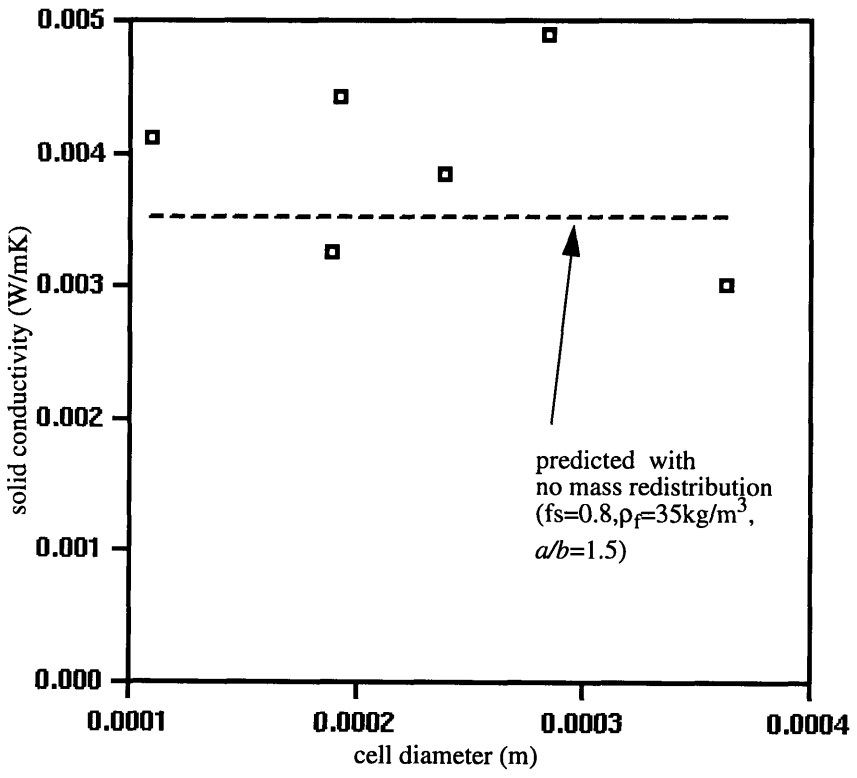

Figure 5.2: *Predicted Solid Conductivity Versus Cell Size*

5.4 Comparison of Predicted and Measured Total Conductivities

The calculated gas and solid conductivities are added to the predicted radiative conductivity component (see Table 4.14) to provide a predicted total conductivity. This predicted total conductivity is also displayed in Table 5.4.

foam (mean cell dameter)	k_{rad} from morphology equations 2.38 and 2.50 (mW/mK)	k_{rad} from transmission measurements (mW/mK)	predicted k_{solid} *mW/mK*	predicted k_{gas} *mW/mK*	overall k from morphology prediction of k_{rad} (mW/mK)	overall k from transmission prediction k_{rad} *(mW/mK)*	measured overall k mW/mK
NBE 678/21/47 (.109mm)	1.67	1.12	4.13	16.0	21.8 +10.7%	21.2 + 7.61%	19.7
NBE 785/206 (.188mm)	2.16	1.40	3.27	12.1	17.6 -5.38%	16.8 - 9.68%	18.6
NBE 819/16/2 (.192mm)	2.24	1.68	4.43	11.4	18.0 - 0.55%	17.5 - 3.31%	18.1
NBE 819/16/1 (.238mm)	2.47	1.78	3.85	11.1	17.4 + 0.00%	16.8 - 3.45%	17.4
NBE 863/13/1 (.284mm)	3.29	2.54	4.90	10.9	19.1 + 3.80%	18.3 - 0.54%	18.4
NBE 785/204 (.363mm)	4.09	1.96	3.02	15.0	22.2 + 5.21%	20.0 - 5.21%	21.1

Table 5.4: *Comparison of Predicted Overall Conductivities to Measured Overall Conductivities*

There are two calculated total conductivities listed for each foam. The first considers the case where the morphology measurements are used to predict the extinction coefficient. The second calculated conductivity considers the case where the transmission measurements are used to predict the extinction coefficient. The comparison of predicted

total conductivities with measured total conductivities are shown in figure 5.3.

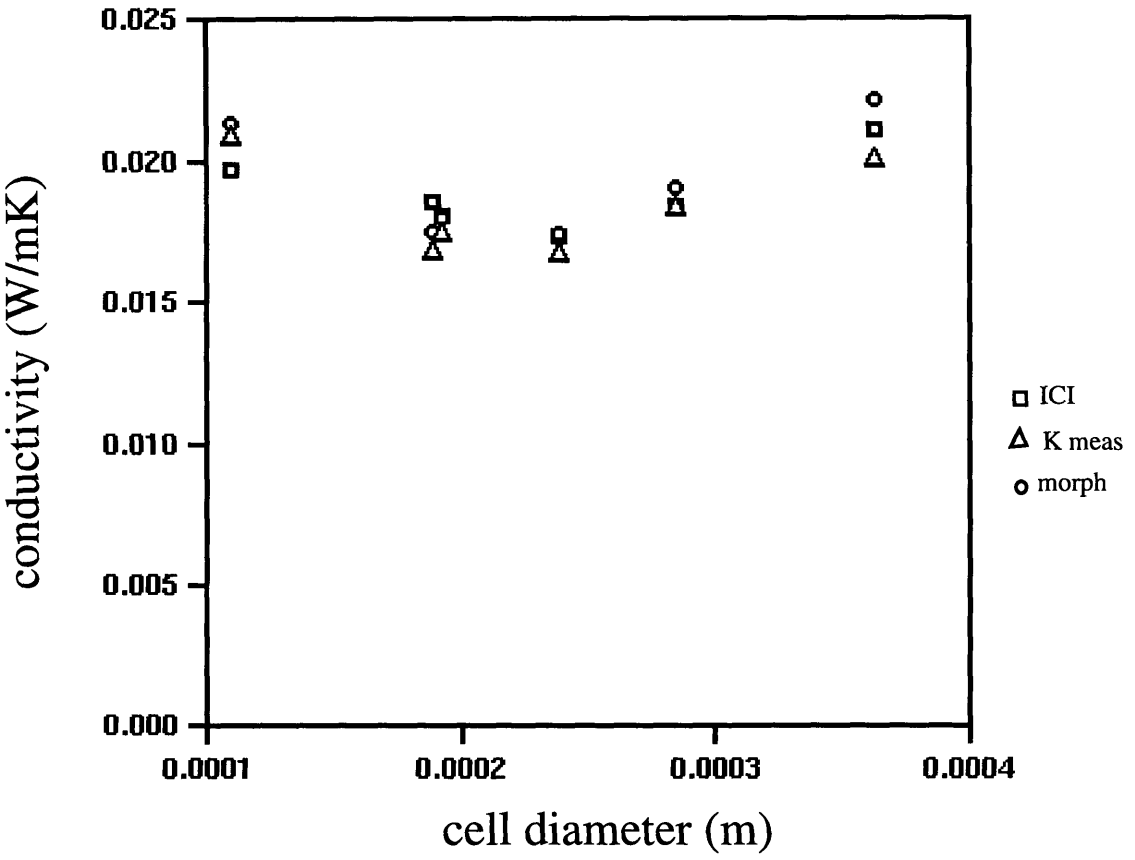

Figure 5.3: *Comparison of Predicted and Measured Overall Thermal Conductivities*

Predictions of the overall conductivity from both the morphology measurements and from the transmission measurements indicate the lack of thermal improvement with smaller cell sizes. The lack of improvement can be seen to stem from both the increase in solid conductivity due to polymer redistribution as well as from changes in the gas conductivity component in Table 5.4 as well as in figure 5.4 where predicted overall conductivity, solid conductivity, gas conductivity, and radiative conductivity from the morphology measurements are displayed. Note for the smallest foams, radiation is far less important than solid conduction Uncertainties in radiation have a modest influence on overall conductivity while solid conduction shifts due to lower percentage of solid in the struts

has a much larger effect. It can be seen from Table 5.4 that most of the predicted conductivities are within 6% of the measured conductivities and that all of the values are within 11%. The predicted values capture the trend in the measured data. An analysis of the error and measurement uncertainties follow in the next section.

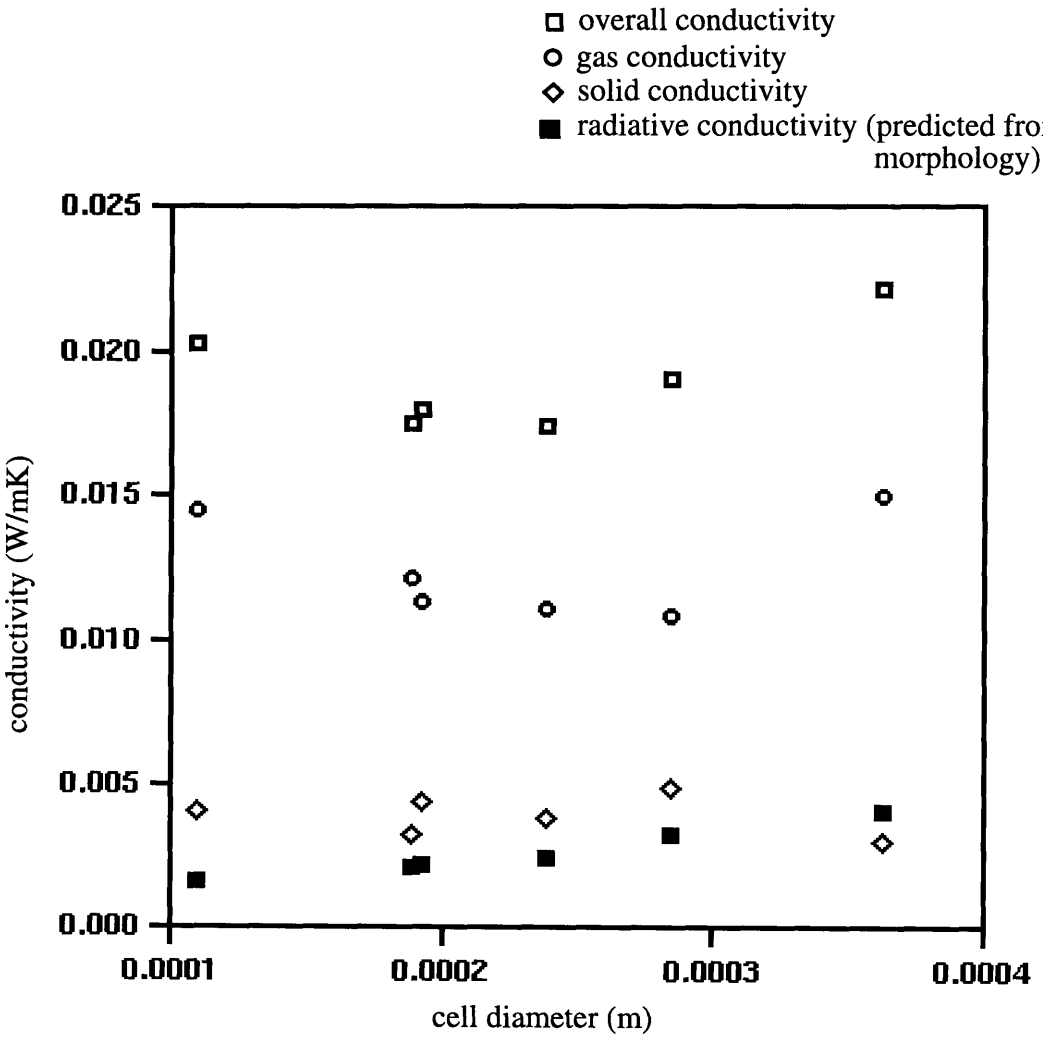

Figure 5.4: *Predicted Conductivity Components from Morphology*

5.5 Uncertainty In Measured Overall Thermal Conductivity

First consider the uncertainty in the measured overall thermal conductivity. Correspondence with Yarbrough at Oak Ridge National Laboratory indicates that the

precision of the best thermal conductivity measuring equipment is roughly 2% [35] . This will be used as a conservative estimate for the measured overall thermal conductivity.

5.6 Uncertainty in Predicted Gas Conductivity

Next consider the errors in the measurements leading to the predicted thermal conductivity. The largest source of error is the uncertainty in the gas thermal conductivity component. There is an error in considering the gas composition to be uniform throughout the foam. Numerical work by Glicksman et al. [1] has indicated that using the average gas concentrations, as was done in this analysis, can lead to uncertainties of 6%. However, a greater amount of error is likely due to uncertainties in the component gas properties as will be outlined below.

The properties for air and CO_2 are well defined in most standard heat transfer textbooks [36]. So for these conductivity components, the 2% precision of measurement equipment can be taken as a conservative estimate of the uncertainty in their values. The same cannot also be said of the blowing agents HCFC-141b or perfluoropentane.

For HCFC-141b, most sources in the literature quoted a thermal conductivity of 10.0mW/mK measured at 25°C [38]. Property data obtained from ICI also indicated this value, as well as a value of 8.8mW/mK measured at 10°C. Since overall conductivity measurements were carried out at 10°C, the HCFC-141b thermal conductivity reported at this temperature was used. The difference between the value reported in the literature and the value reported at 10°C, 1.2mW/mK, can be considered an estimate of the uncertainty.

Foams blown with perfluoropentane have a much greater uncertainty associated with them. Since perfluoropentane is not widely used as a blowing agent, little is reported of its properties. An approximate value of the thermal conductivity of this gas, 10.5mW/mK, was quoted from ICI Polyurethanes but this was stressed to be an approximate value [39]. Nor did contacted suppliers of the gas have data available on either thermal conductivity or viscosity. So, a conservative estimate of the uncertainty in the gas thermal conductivity

is roughly 10% until more information becomes available in the literature.

Error bounds for the foam gas conductivity component is calculated from the gas conductivity uncertainties in the following manner. Consider the gases in the lower error bounds to have a conductivity equal to the reported value minus the precision error. Use these gas conductivities with the Lindsay Bromley equation. The same is done for the upper error bounds except that the conductivity of the component gases are set equal to the reported value plus the uncertainty. Error bounds for the gas conductivity of the six foams are shown in Table 5.5. Note that uncertainties in the conductivity of air and CO_2 do not greatly affect the results but those of HCFC-141b and perfluoropentane do. This can be seen directly in the narrow error bounds for foam NBE 785/204 which is composed entirely of air and CO_2 and in the larger error bounds for all of the other foams.

foam	lower bounds k_{gas} (mW/mK)	predicted value of k_{gas} (mW/mK)	upper bounds k_{gas} (mW/mK)
NBE 678/21/47	15.2	16.0	16.8
NBE 785/206	11.4	12.1	12.9
NBE 819/16/2	10.5	11.4	12.1
NBE 819/16/1	10.2	11.1	11.9
NBE 863/13/1	9.9	10.9	11.7
NBE 785/204	14.7	15.0	15.3

Table 5.5: *Uncertainties in Predicted Gas Conductivities*

It should again be stressed that this gas uncertainty analysis only considered the likely

dominant source of error. It is therefore a conservative estimate of uncertainty since factors like gas concentration gradients, open cells at the surface, and uncertainties in using the Lindsay Bromley expression have not been included. For a further discussion of such errors, the reader is referred to [1].

5.7 Uncertainty in Predicted Solid Conductivity

For the solid conductivity component, the largest source of error is the fraction of solid in the strut, f_s, calculation. Even though measurement of strut areas provide greater precision in determining f_s, there is still considerable uncertainty due to variation in measured areas. Therefore, the impact of the strut area distribution on calculated f_s and on the predicted solid conductivity was analyzed. Since f_s depends on the mean area measured, determine the uncertainty from the standard deviation of the strut area distribution. That is, multiply an area one standard deviation below the mean by the correction factor used to determine A from A_{int} . Use this corrected area value with equation 4.22 to determine a lower limit f_s. Do the same with an area one standard deviation above the mean to calculate an upper limit to f_s. The upper and lower limit fraction of solid in the strut are displayed in Table 5.6. A greater fraction of solid in the strut decreases the solid conductivity since it decreases the contribution from the cell walls. So the upper limit f_s provides a lower limit estimate of the solid conductivity while the lower limit f_s provides an upper limit estimate of the solid conductivity. These

estimates are shown in Table 5.6.

foam	mean strut area (μm^2)	standard deviation (μm^2)	lower limit f_s	upper limit f_s	lower limit k_s (mW/mK)	upper limit k_s (mW/mK)
NBE 678/21/ 47	15.74	3.27	0.27	0.406	3.98	4.28
NBE 785/206	92.93	26.56	0.47	0.84	2.83	3.69
NBE 819/16/2	102.72	43.20	0.31	0.76	3.90	4.98
NBE 819/16/1	168.70	46.98	0.55	0.98	3.33	4.39
NBE 863/13/1	150.46	65.24	0.20	0.51	4.53	5.30
NBE 785/204	279.98	47.08	0.56	0.79	2.78	3.25

Table 5.6: *Uncertainties in Predicted Solid Conductivities*

5.8 Uncertainty in Radiative Conductivity Predicted from Morphology

Two parameters contribute to the uncertainty in the radiative conductivity predicted from equation 2.38 and 2.50. The first is the measured mean cell diameter, d, and the second is the calculated fraction of solid in the struts, f_s. To determine the uncertainty in the mean cell diameter, the mean cell diameter from surface to volume meaurements were carried out for several SEM and confocal images. The average mean cell diameter as well as the standard deviations in measured values are reported in Table 5.7. Note that for each foam, there is not more than a 9% standard deviation in the calculated mean cell diameter.

foam	mean cell diameter (mm)	standard deviation (mm)	% stamdard deviation
NBE 678/21/47	0.109	0.009	8.2
NBE 785/204	0.188	0.015	7.9
NBE 819/16/2	0.192	0.012	6.3
NBE 819/16/1	0.238	0.008	3.4
NBE 863/13/1	0.284	0.022	7.7
NBE 785/206	0.363	0.008	2.3

Table 5.7: *Uncertainties in Measured Mean Cell Diameters*

From the values reported in Table 5.7 and in Table 5.6, one can see that errors in the calculation of fraction of solid in the strut dominate the errors in predicted radiative conductivity. So how the upper and lower limits of f_s affect the radiative conductivity will be considered. That is, consider the radiative conductivity lower limit with the upper limit f_s and the radiative conductivity upper limit with the lower limit f_s. How the uncertainty bounds of f_s affects the extinction coefficient predicted from the morphology, and how this changes the radiative conductivity is displayed in Table 5.8. Notice from the table that there is at most a 16% uncertainty in the radiative conductivity due to the dominant measurement error of f_s.

foam	extinction coefficient from morphology (cm^{-1})	lower limit f_s	upper limit f_s	extinction coefficient from upper limit f_s(cm^{-1}) ---------- % error k_{rad}	extinction coefficient from lower limit f_s(cm^{-1}) ---------- % error k_{rad}
NBE 678/21/47	40.9	0.27	0.41	43.9 ---------- - 7%	37.8 ---------- + 8%
NBE 785/204	31.8	0.47	0.84	34.0 ---------- - 6%	29.1 ---------- +10%
NBE 819/16/2	30.6	0.31	0.76	33.6 ---------- - 9%	26.5 ---------- +16%
NBE 819/16/1	27.8	0.55	0.98	29.1 ---------- - 4%	26.0 ---------- + 7%
NBE 863/13/1	20.9	0.20	0.51	22.3 ---------- - 6%	18.8 ---------- +11%
NBE 785/206	16.8	0.56	0.79	17.1 ---------- - 2%	16.5 ---------- + 2%

Table 5.8: *Uncertainties in Radiative Conductivities Predicted from Morphology Measurements*

5.9 Uncertainty in Radiative Conductivity Predicted from Transmission Measurements

The largest source of error in predicting the radiative conductivity from transmission measurements appears to stem from neglecting anisotropic scattering. Mozgowiec calculated the uncertainty in the extinction coefficient associated with transmissivity and foam slice thickness measurements. He found such uncertainty to be between 3.3% and

8% [18]. As seen in the calculation of P-1 extinction coefficients in Section 4.7, the uncertainty due to neglecting anisotropic scattering is closer to 10%. Therefore, let the P-1 extinction coefficient represent a conservative lower bounds for the uncertainty in the extinction coefficient. Similarly, let the extinction coefficients measured parallel to the orientation axis represent the upper bounds of the extinction coefficient.

5.10 Comparison of Measured and Predicted Values Accounting for Uncertainties

The three conductivity components with their uncertainties accounted for with error bars are displayed for the two predicted results in figures 5.5 and 5.6. The predicted total conductivities with uncertainties are also compared to measured total conductivities with uncertainties in these figures. Figure 5.5 shows the predicted results with uncertainties with the radiative conductivity predicted from morphology while figure 5.6 shows the predicted results with the radiative conductivity predicted from transmission data. The uncertainties in the predicted overall conductivities are the root-mean-squares of the uncertainties of each of the components. That is, for uncertainties σ_g for the gas conductivity, σ_s for the solid conductivity,σ_{r1} for the radiative conductivity predicted from morphology measurements, and σ_{r2} for the radiative conductivity predicted from transmission measurements, the overall uncertainty is

$$\sigma_{total} = \sqrt{\sigma_g^2 + \sigma_s^2 + \sigma_r^2} \tag{5.1}$$

where σ_r is either σ_{r1} or σ_{r2} depending on whether the predictions from morphology measurements or from transmission measurements are being calculated. Note that even with conservative estimates of uncertainties, the ranges of predicted and measured overall conductivities overlap in all but two cases and the predicted values follow the overall measured trend.

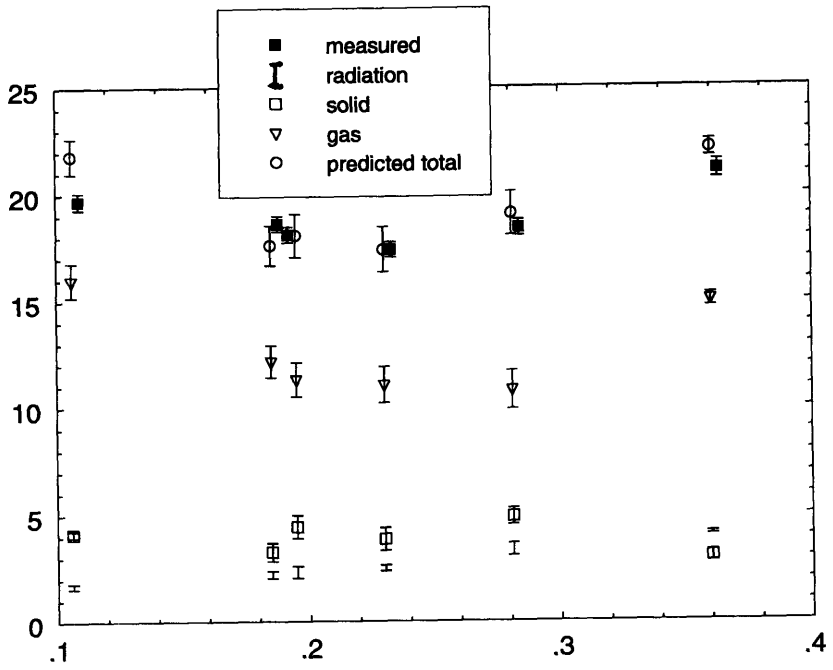

Figure 5.5: *Comaprison of Total Conductivity Measured and Predicted from Morphology Measurements (Note: Uncertainties in Gas Conductivity, Solid Conductivity, and Radiative Conductivity Components Also Shown)*

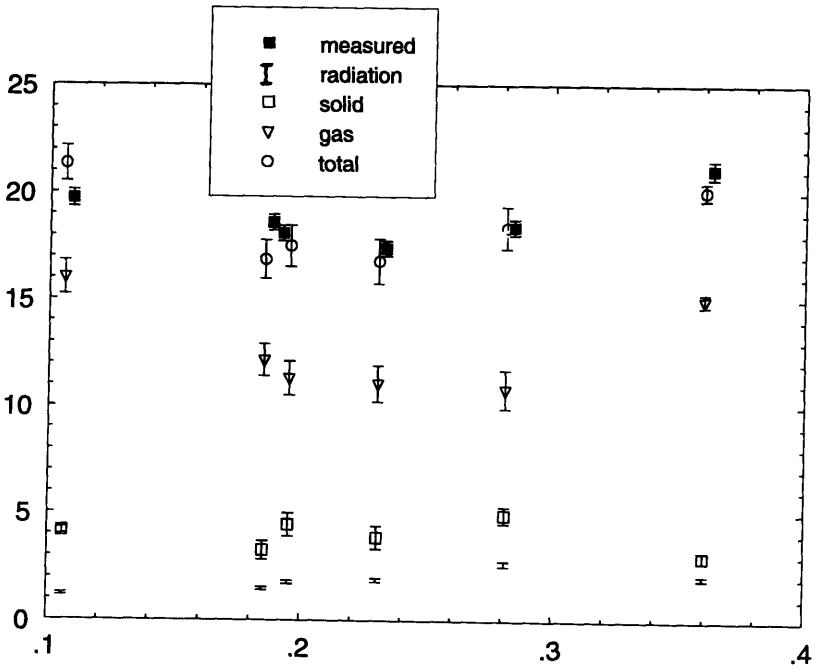

Figure 5.6: *Comaprison of Total Conductivity Measured and Predicted from Transmission Measurements (Note: Uncertainties in Gas Conductivity, Solid Conductivity, and Radiative Conductivity Components Also Shown)*

Chapter 6

Conclusions and Recommendations

1. As cell size decreases, radiative conductivity decreases. Anisotropic scattering might have a greater impact on the radiative flux, but the radiative conductivity is negligibly small compared to the other components. Therefore, increased scattering does not account for the lack of thermal improvement at smaller cell sizes as suggested by Kuhn et al. [33]. A lack of thermal improvement at smaller cell sizes results from an increase in gas conductivity and from a redistribution of polymer from the struts to the cell walls. This redistribution increases the solid conductivity component offsetting any gains from a decrease in radiative conductivity.

2. A program that calculates the effective two-dimensional solid conductivity from actual confocal microscope images of a foam's structure has been developed. Predictions of solid conductivity for test cases of simple geometries agree with analytical solutions. Results from foams indicate that they are markedly affected by anisotropy. Foams showing a high degree of anisotropy (*a/b* of about 1.7) display great disparity between conductivity in the direction parallel to the rise direction and conductivity in the direction perpendicular to the rise direction. Foams of little anisotropy (*a/b* of about 1.3) show little differences in two-dimensional solid conductivity for the two directions. Once two-dimensional images showing all of the cell walls with little-depth of field can be confidently produced with the confocal microscope, the solid conductivity program should be extended to automate the determination of nodes and borders as well as characteristics like the border thicknesses.

3. The confocal microscope provides an adequate two-dimensional image of the foam structure if foams are stained with fluorescent dyes. However, cell walls are not clear enough at the present for the solid conductivity program to automate the determination of nodes and borders. With some manual inputs, images from the confocal microscope can be used to obtain a two-dimensional picture of the foam. Future work should explore some combination of dyes, computer imaging filters, or some other means to improve the images from the confocal microscope. Initial investigation into shattering of the foam at cryogenic temperatures (using liquid nitrogen) and staining with a fluorescent dye suggests improvement in confocal microscope images. Such improved images without the depth-of-field problem posed by the SEM will allow automation of calculations like the effective two-dimensional solid conductivity and cell size distributions.

4. The dielectric nature of polyurethane as well as sensitivity to humidity and impurities makes the calculation of solid conductivity from electrical conductivity measurements impractical.

5. Determination of solid polymer extinction coefficient from thin film transmission measurements indicate a value of $300cm^{-1}$ ($337cm^{-1}$ with a spectrometer wavelength range of 2μm to 25μm and $280cm^{-1}$ with a spectrometer wavelength range of 2μm to 33μm).

6. A method to determine the fraction of solid in the strut from SEM photographs of strut cross-sectional areas has been formulated. f_s calculations from this technique were found to agree within 15% to calculations from cell wall thickness measurements. This method is recommended instead of the conventional cell wall thickness measurement technique. Strut areas are easier to detect than cell wall thicknesses (which must be viewed perpendicular to the width of the cell walls). Cross-sectional areas also do not

show the wide distribution in measured values found with cell wall thickness measurements.

7. Numerical analysis indicates that ignoring anisotropy in radiative conductivity can lead to a considerable overprediction of the radiative flux. Measurements indicate that foams with larger degrees of anisotropy have larger variations in extinction coefficients parallel and perpendicular to the rise direction. Further analysis of how the extinction coefficient varies with direction is recommended. This will provide information on how well the isotropic Rosseland equation predicts the anisotropic flux as well as what combination of measured extinction coefficients should be used for greatest accuracy.

8. Measurement of cell area distributions appearing on SEM or confocal images provides a means to calculate the true cell size distribution in the foam. A technique to calculate the cell size distribution for anisotropic foams from SEM or confocal photographs perpendicular to the rise direction has been formulated.

9. Considerations of nonopaque struts, Q not equal to unity, does not account for the discrepancy between extinction coefficients calculated from the morphology and from the transmission measurements. Analysis of the extinction efficiency does reveal that the extinction efficiency is not less than unity for very small cell sizes as indicated by Kuhn et al [33] but is instead larger than unity. This would indicate that the actual radiative conductivity predicted by theory and an extinction efficiency of unity overpredicts the actual radiative conductivity.

References

[1] Glicksman, L.R. "Heat Transfer in Foams", Chapter V in "The Physics of Cellular Plastics",N.C. Hilyard and A. Cunningham (eds.), Elsevier Science Publishing Ltd. in press, 1991.

[2] Doherty, D.J., Hurd, R. & Lester, G.R. Chem. and Industry, 30, 1962, p.1340.

[3] Skochdopole, R.E. Chem. Eng. Progress, 57, 10, 1961, p. 55.

[4] Glicksman, L.R., Schuetz, M. & Sinofsky, M. International Journal of Heat and Mass Transfer, 30, 1, 1987, pp 187-197.

[5] Williams R.J.J. & Aldo G.M. Polymer Engineering and Science, 23, April 1983, pp.293-298.

[6] Glicksman, L.R. & Torpey, M.R. "The Influence of Cell Size and Foam Density on the Thermal Conductivity of Foam Insulation". Proceedings of the Polyurethane World Congress, Aachen, W. Germany, 1987, pp 80-84.

[7] Glicksman, L.R., Mozgowiec, M. & Torpey, M.R. Proceedings Ninth International Heat Transfer Conference, Jerusalem, 1990.

[8] Schuetz, M.A. & Glicksman, L.R. Journal of Cellular Plastics, 20, 2, 1984, pp. 114-121.

[9] Gibson, L.J. & Ashby, M.F. Cellular Solids: Structure and Properties, Pergamon, 1988..

[10] Cunningham, A. "A Structural Model of Heat Transfer Through Rigid Polyurethane Foam", Unpublished, 1992.

[11] Reitz, D.W. A Basic Study of Gas Diffusion in Foam Insulation. M.S. Thesis, M.I.T., Cambridge, Massachusetts, 1984.

[12] Underwood, E.E. Quantitative Stereology. Addison-Wesley Publishing Company, Reading, Massachusetts, 1970.

[13] Page, M.C. Effects of Alternate Blowing Agents on the Aging of Closed-Cell Foam Insulation. M.S. Thesis, M.I.T., Cambridge, Massachusetts, 1991.

[14] Schuetz, M.A. Heat Transfer in Foam Insulation. M.S. Thesis, M.I.T., Cambridge, Massachusetts, 1982.

[15] Sinofsky, M. Property Measurement and Thermal Performance Prediction of Foam Insulation. M.S. Thesis, M.I.T., Cambridge, Massachusetts, 1984.

[16] Torpey, M.R. A Study of Radiative Heat Transfer Through Foam Insulation. M.S.Thesis, M.I.T., Cambridge, Massachusetts, 1987.

[17] Siegel, R. and Howell, J.R. Thermal Radiation Heat Transfer. 3rd edition. Hemisphere Publishing Corporation, Washington, D.C., 1992.

[18] Mozgowiec, M.D. The Use of Small Cells to Reduce Radiation Heat Transfer in Foam Insulation. M.S. Thesis, M.I.T., Cambridge, Massachusetts, 1990.

[19] Bhattacharjee, D., King, J.A., and Whitehead, K.N. "Thermal Conductivity of PU/PIR Foams as a Function of Mean Temperature". Journal of CELLULAR PLASTICS, 27, May 1991, pp 240-251.

[20] Shuman, H., Murray, J.M., and DiLullo, C. "Confocal Microscopy: An Overview". BioTechniques, 7, 2, 1989, pp. 154-163.

[21] Shugg, W.T. Handbook of Electrical and Electronic Insulating Materials. Van Nostrand Reinhold. 1986.

[22] Lemlich, R. "A Theory for the Limiting Conductivity of Polyhedral Foam at Low Density". Journal of Colloid and Interface Science, 64, 1, March 15, 1978, pp107-110.

[23] Chang, K. and Lemlich, R. "A Study of the Electrical Conductivity of Foam". Journal of Colloid and Interface Science, 73, 1, January 1980, pp 224-229.

[24] Harrop, P.J. Dielectrics. Butterworths, London, 1972

[25] International Electrotechnical Commission. Encyclopedia of Electrical Insulating Materials: Classification, Synoptic Tables, and Descriptive Sheets. American Institute of Electrical Engineers, New York, 1958.

[26] Clark, F.M. Insulating Materials for Design and Engineering Practice. Wiley, New York, 1962.

[27] Scott, A.H. "Measurement of Multimegohm Resistors". Journal of Research of the National Bureau of Standards, 50, 3, March 1953, pp. 147-152.

[28] Engineering Dielectrics Volume IIB Electrical Properties of Solid Insulating Materials: Measurement Techniques. Bartnikas, R. (editor). American Society for Testing and Materials, Philadelphia, Pennsylvania. Special Technical Publication 926, 1987.

[29] Mopsik, Fred. National Institute of Standards and Technology, Gaithersburg, Maryland, Personal Communication, June 30, 1993.

[30] Eeckhaut, G. ICI Polyurethanes, Everberg, Belgium, Personal Communication, January 19, 1994.

[31] Cunningham, A. and Sparrow, D.J. Cellular Polymers, 5, 1986, pp. 327-342.

[32] Lee, H. and Buckins, R.O. Journal of Heat Transfer, 104, p. 68.

[33] Kuhn, J., Ebert, H., Fricke, J., et al. "Thermal Transport in Polystyrene and Polyurethane Foam Insulations". International Journal of Heat and Mass Transfer, 35, 7, 1992, pp 1795-1801.

[34] Hull, F.C. and Houk, W.J. "Statistical Grain Structure Studies: Plane Distribution Curves of Regular Polyhedrons". Transactions AIME: Journal of Metals. April 1953, pp. 565-572.

[35] Yarbrough, D.W., Materials Thermal Analyses Group, Oak Ridge National Laboratory, Oak Ridge, Tennessee, Personal Communication, May 14, 1993.

[36] Mills, A.F. Heat Transfer. Irwin, Homewood, Illinois, 1992, pp. 824-825.

[37] Shankland, I. "CFC Alternatives for Thermal Insulation Foams". Rev. Int. Froid, 13, 1990, p 115.

[38] Clatty, J.R. Journal of CELLULAR PLASTICS, 26, July 1990, pp 325.

[39] Cunningham, A. ICI Polyurethanes, Everberg, Belgium. Personal Communication, September 7, 1993.

[40] IMPACT IR44 Sales Brochure, Nicholett Instrument Corporation, 1993.

[41] Kerker, M. The Scattering of Light and Other Electromagnetic Radiation. Academic Press, New York, 1969.

[42] Eastes, W. Owens Corning Fiberglass, Columbus, Ohio, Personal Communication, January 24, 1994

[43] Solomou, N., Boston, Massachusetts, Personal Communication, January 20, 1994.

Appendix A Derivation of Mean Intercepted Height

The relationship

$$N_A = N_V d \tag{A.1}$$

is derived from an inspection of how section planes intercept a particle or cell in space. The derivation is based on one presented in *Quantitative Stereology* [12].

A sample cube of length l is cut from a polydispersed system of convex particles in space. Consider n_T parallel test planes of total area

$$A_T = n_T l^2 \tag{A.2}$$

that penetrate the cube as shown in figure A.1. All of the test planes are parallel to one side of the cube. A projection plane is next erected perpendicular to the test planes and parallel to two cube faces. This projection plane is also displayed in figure A.1.

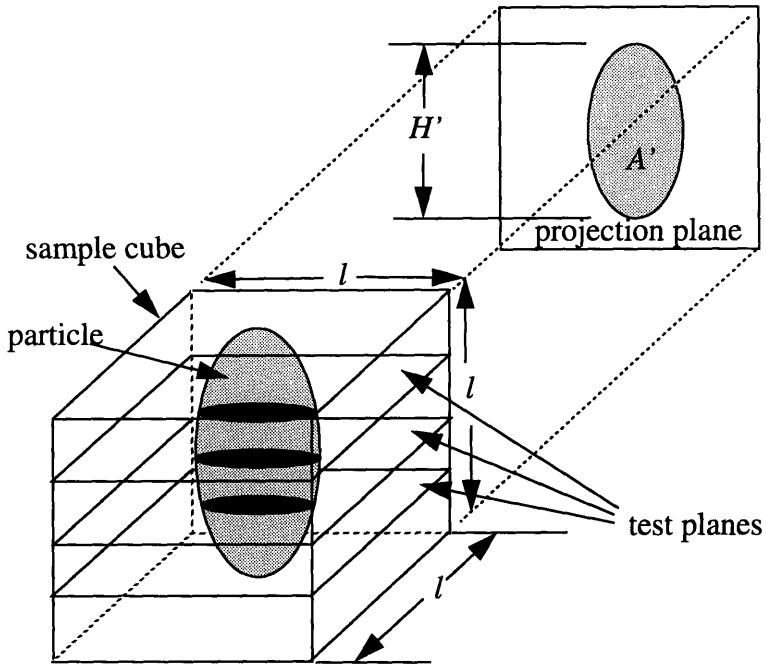

Figure A.1: *Particle Intersected by Test Planes and Projection of Particle on Projection Plane*

Consider one particle inside the cube. The number of test planes intersecting this one particle (n_x) is equal to some fraction f of the total number of test planes (n_T) or

$$n_x = n_T f \tag{A.3}$$

The fraction f is a lineal ratio defined by the ratio

$$f = \frac{H'}{l} \tag{A.4}$$

Where, as depicted in figure A.1, H' is the projected height of the particle in the test cube on the projection plane.

Now look at the ratio n_x/A_T, or the number of planes intersecting the particle per total area of intersecting planes. This ratio can be expressed in terms of the projected height of

the particle and the length of the sample cube from expressions A.2 and A.3. That is,

$$\frac{n_x}{A_T} = \frac{n_T H'/l}{n_T l^2} = \frac{H'}{l^3} \tag{A.5}$$

To look at the mean projected height of a system of convex particles, first group the particles into class intervals based on size. Then the number of intersections of N_i particles in the ith class interval per unit area of test planes (N_{Ai}) is, from equation A.5

$$(N_A)_i = \frac{1}{V_T}(N_i H'_i) \tag{A.6}$$

Summing over particles of all classes, the total number of intersections with particles of every class (N_A) is

$$N_A = \sum (N_A)_i = \frac{1}{V_T}\sum N_i H'_i \tag{A.7}$$

Dividing both sides of equation A.7 by N, the total number of particles in the test sample,

$$\frac{N_A}{N} = \frac{1}{V_T}\left[\frac{N_1 H'_1 + N_2 H'_2 + N_3 H'_3 + \ldots}{N}\right] \tag{A.8}$$

The expression in brackets is an arithmetic average of the projected heights or the mean projected height $\overline{H}'$. It is this quantity we have described as the mean cell diameter. By rearranging expression A.8

$$N_A = \frac{N}{V_T}\overline{H}' = N_V \overline{H}' = N_V d \tag{A.9}$$

one can see that the mean projected height relates the total number of particles per unit volume (N_V) to the number of particles intersected per unit test area (N_A).

Appendix B Solid Conductivity Matrix Program

Recall the final form of the two-dimensional solid conductivity matrix equations relating node temperatures to fluxes at the nodes (Section 3.4)

$$[M]\ [T]\ =\ [b] \tag{B.1}$$

Here

$$M_{ij} = \begin{cases} \sum_k \dfrac{k_{ik}A_{ik}}{L_{ik}} & i=j, \text{ summed over nodes } k \text{ directly connected to node } i \\ -\dfrac{k_{ij}A_{ij}}{L_{ij}} & \text{nodes } i \text{ and } j \text{ are connected and } i \neq j \\ 0 & \text{nodes } i \text{ and } j \text{ are not connected} \end{cases} \tag{B.2}$$

$$b_i = \begin{cases} 0 & \text{if node } i \text{ is not a boundary node} \\ q_{out,\,i} & \text{if node } i \text{ is a boundary node} \end{cases} \tag{B.3}$$

T_i is the temperature at node i. Both vectors [T] and [b] are comprised of unknown and known values.

To set up the matrices in a form solvable by a direct matrix solver like a Gauss-Seidel routine, rearrange the matrix equation so that it is a matrix times a vector of unknowns equals a vector of knowns. This intermediate form of the equations will be dimensionally inhomogeneous, but easier for common routines to solve. To rearrange the vectors, look at the energy equations at the boundaries

$$\left(\sum \frac{k_{ij}A_{ij}}{L_{ij}}\right)T_i + \ldots - \left(\frac{k_{ik}A_{ik}}{L_{ik}}\right)T_k \ldots - \left(\frac{k_{i(k+1)}A_{i(k+1)}}{L_{i(k+1)}}\right)T_{(k+1)} \ldots = q_{out,\,i} \qquad \text{(B.4)}$$

Rearrange these equations such that all of the knowns are on the left hand side and all of the unknowns are on the right hand side. This form of the equation looks like

$$-q_{out,\,i} + \ldots - \left(\frac{k_{ik}A_{ik}}{L_{ik}}\right)T_k \ldots - \left(\frac{k_{i(k+1)}A_{i(k+1)}}{L_{i(k+1)}}\right)T_{(k+1)} \ldots = -\left(\sum \frac{k_{ij}A_{ij}}{L_{ij}}\right)T_i \qquad \text{(B.5)}$$

For every boundary node i, the above equation is appended to the matrix equation. The appended matrix equation then becomes

$$[Y]\,[x] = [Z] \qquad \text{(B.6)}$$

where

$$Y_{ij} = \begin{cases} -1 & i=j \text{ and node } i \text{ is a boundary node} \\ \displaystyle\sum_k \frac{k_{ik}A_{ik}}{L_{ik}} & i=j, \text{ summed over nodes } k \text{ directly connected to node } i \text{ (node } i \text{ is not a boundary node)} \\ \displaystyle -\frac{k_{ij}A_{ij}}{L_{ij}} & \text{nodes } i \text{ and } j \text{ are connected and } i \neq j \\ 0 & \text{nodes } i \text{ and } j \text{ are not connected} \end{cases} \qquad \text{(B.7)}$$

$$x_i = \begin{cases} T_i & \text{if node } i \text{ is not a boundary node} \\ q_{out,\,i} & \text{if node } i \text{ is a boundary node} \end{cases} \qquad \text{(B.8)}$$

$$Z_i = \begin{cases} 0 & \text{if node } i \text{ is not a boundary node} \\ \left(-\sum_k \frac{k_{ik}A_{ik}}{L_{ik}}\right)T_i & \text{if node } i \text{ is a boundary node} \end{cases} \quad \text{(B.9)}$$

This is the system of linear equations that is solved by the matrix solver in the solid conductivity program listed next.

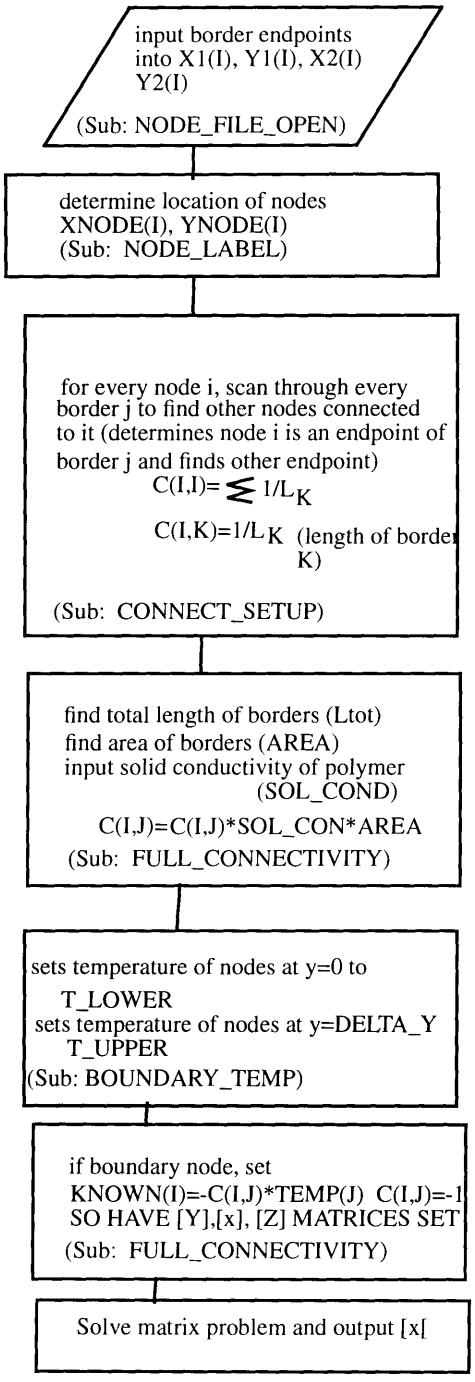

Figure B.1: *Flowchart for Program "Solid_Conductivity"*

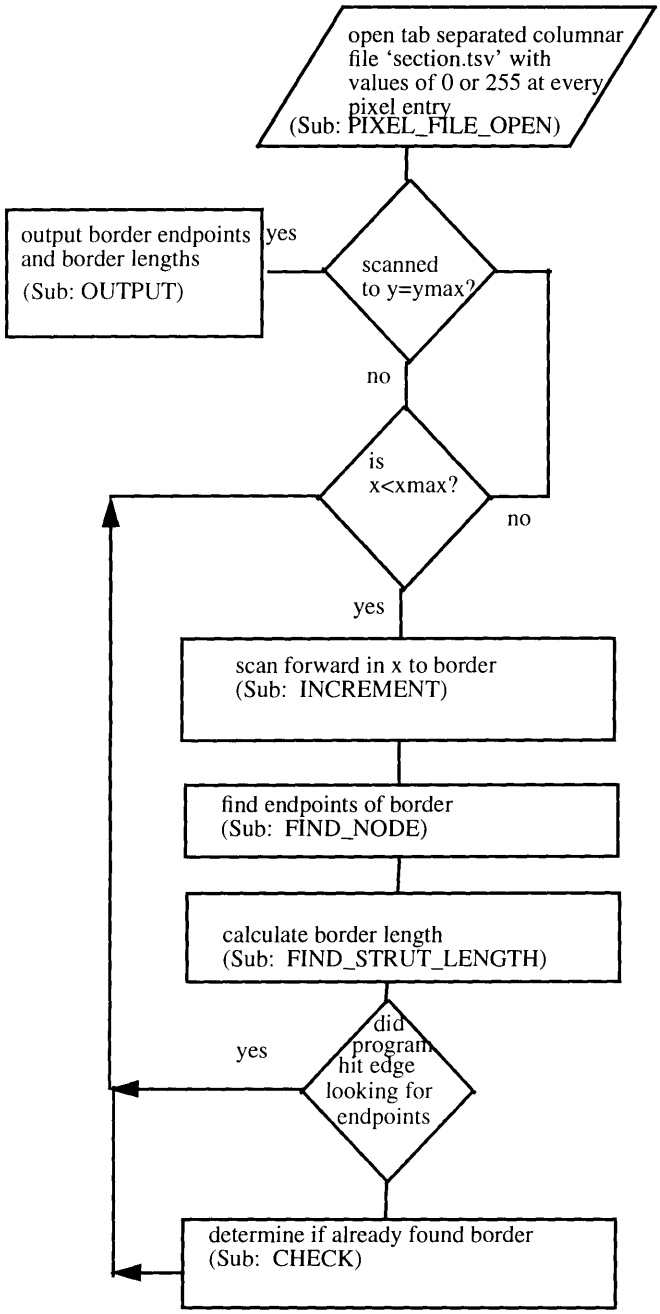

Figure B.2: *Flowchart for Program "Connect"*

```
PROGRAM SOLID_CONDUCTIVITY
PARAMETER(MAX_STRUT=1200,MAX_NODES=600)
REAL X1(MAX_STRUT),X2(MAX_STRUT),Y1(MAX_STRUT),Y2(MAX_STRUT)
REAL XNODE(MAX_NODES),YNODE(MAX_NODES),C(MAX_NODES,MAX_NODES)
REAL AREA,SOLID_COND,KNOWN(MAX_NODES),TEMP(MAX_NODES)
```

```
INTEGER ICOUNT

CALL INPUT(NUM_NODES)
NUM_STRUTS=NUM_NODES/2.
CALL NODE_FILE_OPEN(X1,X2,Y1,Y2,NUM_STRUTS)
CALL NODE_LABEL(X1,X2,Y1,Y2,NUM_NODES,XNODE,YNODE,ICOUNT)
CALL CONNECT_SETUP(X1,X2,Y1,Y2,XNODE,YNODE,ICOUNT,NUM_NODES,C)
CALL FULL_CONNECTIVITY(C,ICOUNT,X1,X2,Y1,Y2,NUM_STRUTS)
CALL BOUNDARY_TEMP(TEMP,ICOUNT,XNODE,YNODE)
CALL BOUNDARY(C,ICOUNT,KNOWN,XNODE,YNODE,TEMP)
CALL MATRIX(C,KNOWN,ICOUNT)
END

SUBROUTINE INPUT(NUM_NODES)
C-----------------------------------------------
C    Input of number of border endpoints marked in IMAGE.  That is, if 140 borders are marked,
C    there are 280 nodes in the file.  The true number of nodes will be less than this since several
C    border mark each node.
C-----------------------------------------------
INTEGER NUM_NODES
WRITE(6,*) 'ENTER THE NUMBER OF NODES IN FILE (NUMBER OF XY PTS)'
READ(6,*) NUM_NODES
RETURN
END

SUBROUTINE NODE_FILE_OPEN(X1,X2,Y1,Y2,NUM_STRUTS)
C-----------------------------------------------
C  Opens file having x-y endpoints of borders marked.  Reads both endpoints of each border (file
C     is sequential list of borders)
C-----------------------------------------------
PARAMETER(SCALE_FACTOR = 1.E-6)
REAL X1(NUM_STRUTS),X2(NUM_STRUTS),Y1(NUM_STRUTS),Y2(NUM_STRUTS)

OPEN(UNIT=27,FILE='strut_nodes',STATUS='UNKNOWN')
REWIND(27)
DO 10 I=1,NUM_STRUTS
READ(27,*) X1(I),Y1(I)
READ(27,*) X2(I),Y2(I)
X1(I) = X1(I) * SCALE_FACTOR
X2(I) = X2(I) * SCALE_FACTOR
Y1(I) = Y1(I) * SCALE_FACTOR
Y2(I) = Y2(I) * SCALE_FACTOR
 10CONTINUE
CLOSE(27)
RETURN
END


SUBROUTINE NODE_LABEL(X1,X2,Y1,Y2,NUM_NODES,XNODE,YNODE,ICOUNT)
C-----------------------------------------------
C  Determines actual number of nodes in image by mrking nodes, checking if unknown node has
C       already been marked, and if not, marking it as a node
C-----------------------------------------------
PARAMETER(SCALE_FACTOR = 1.E-6)
```

```
REAL X1(NUM_NODES),X2(NUM_NODES),Y1(NUM_NODES),Y2(NUM_NODES)
REAL XNODE(NUM_NODES),YNODE(NUM_NODES)
REAL XERR,YERR,XDIF,YDIF
INTEGER FOUND,NUM_NODES,NUM_STRUTS

WRITE(6,*) 'WHAT ERROR BOUNDS FOR X OF NODES (m)?'
READ(6,*) XERR
WRITE(6,*) 'WHAT ERROR BOUNDS FOR Y OF NODES (m)?'
READ(6,*) YERR

ICOUNT=0
NUM_STRUTS=NUM_NODES/2.
DO 10 I=1,NUM_STRUTS
FOUND = 0
 DO 20 J=1,ICOUNT
XDIF=ABS(X1(I) - XNODE(J))
YDIF=ABS(Y1(I) - YNODE(J))
IF(XDIF.LE.XERR.AND.YDIF.LE.YERR) THEN
FOUND=1
ENDIF
 20CONTINUE
IF(FOUND.NE.1) THEN
ICOUNT=ICOUNT+1
XNODE(ICOUNT) = X1(I)
YNODE(ICOUNT) = Y1(I)
ENDIF
FOUND = 0
DO 30 J=1,ICOUNT
XDIF=ABS(X2(I) - XNODE(J))
YDIF=ABS(Y2(I) - YNODE(J))
 IF(XDIF.LE.XERR.AND.YDIF.LE.YERR) THEN
FOUND=1
ENDIF
 30CONTINUE
IF(FOUND.NE.1) THEN
ICOUNT=ICOUNT+1
XNODE(ICOUNT)=X2(I)
YNODE(ICOUNT)=Y2(I)
ENDIF
 10CONTINUE
RETURN
END


SUBROUTINE CONNECT_SETUP(X1,X2,Y1,Y2,XN,YN,ICOUNT,NN,C)
C-------------------------------------------------
C    COMBINATION OF SUBROUTINES CONNECT_SETUP AND FULL_CONDUCTIVITY
C      For every node found in subroutine NODE_LABEL, determines the elements Yij (of
C      [Y][x]=[Z]) for all nodes connected to it.  This is determined by finding what borders have
C      the node as an endpoint
C-------------------------------------------------
PARAMETER(MAX=600,SCALE_FACTOR = 1.E-6)
REAL C(MAX,MAX),X1(NN),X2(NN),Y1(NN),Y2(NN)
REAL XN(NN),YN(NN)
```

```
REAL XERR,YERR,XDIF,YDIF,NUM_STRUTS,XDIF2,YDIF2,DIST,INVLEN
INTEGER ICOUNT,NN

DO 10 I = 1,ICOUNT
DO 20 J=1,ICOUNT
C(I,J) = 0.0
 20 CONTINUE
 10CONTINUE
WRITE(6,*) 'WHAT ERROR BOUNDS FOR X OF NODES (m)?'
READ(6,*) XERR
WRITE(6,*) 'WHAT ERROR BOUNDS FOR Y OF NODES (m)?'
READ(6,*) YERR

NUM_STRUTS=NN/2.
DO 30 I=1,ICOUNT
DO 40 J=1,NUM_STRUTS
XDIF=ABS(X1(J)-XN(I))
YDIF=ABS(Y1(J)-YN(I))
IF(XDIF.LE.XERR.AND.YDIF.LE.YERR) THEN
DO 50 K=1,ICOUNT
XDIF2=ABS(X2(J)-XN(K))
YDIF2=ABS(Y2(J)-YN(K))
IF(XDIF2.LE.XERR.AND.YDIF2.LE.YERR) THEN
DIST=SQRT((X1(J)-X2(J))*(X1(J)-X2(J))+(Y1(J)-Y2(J))*(Y1(J)-Y2(J)))
INVLEN = 1./DIST
C(I,K)=C(I,K) - INVLEN
C(I,I)=C(I,I) + INVLEN
ENDIF
 50CONTINUE
ENDIF
 40CONTINUE
 30CONTINUE
DO 55 I=1,ICOUNT
DO 60 J=1,NUM_STRUTS
XDIF=ABS(X2(J)-XN(I))
YDIF=ABS(Y2(J)-YN(I))
IF(XDIF.LE.XERR.AND.YDIF.LE.YERR) THEN
DO 70 K=1,ICOUNT
XDIF2=ABS(X1(J)-XN(K))
YDIF2=ABS(Y1(J)-YN(K))
IF(XDIF2.LE.XERR.AND.YDIF2.LE.YERR) THEN
DIST=SQRT((X1(J)-X2(J))*(X1(J)-X2(J))+(Y1(J)-Y2(J))*(Y1(J)-Y2(J)))
INVLEN = 1. / DIST
C(I,K)=C(I,K) - INVLEN
C(I,I)=C(I,I) + INVLEN
ENDIF
 70CONTINUE
ENDIF
 60CONTINUE
 55CONTINUE
RETURN
END
```

```
SUBROUTINE FULL_CONNECTIVITY(C,ICOUNT,X1,X2,Y1,Y2,NUM_STRUTS)
PARAMETER(MAX=600)
REAL C(MAX,MAX),AREA,SOLID_COND,DELX,DELY,VF
INTEGER ICOUNT,NUM_STRUTS
REAL X1(MAX),X2(MAX),Y1(MAX),Y2(MAX),DIST,LTOT

WRITE(6,*) 'ENTER X DIMENSION OF PICTURE (m)'
READ(6,*) DELX
WRITE(6,*) 'ENTER Y DIMENSION OF PICTURE (m)'
READ(6,*) DELY
WRITE(6,*) 'ENTER VOID FRACTION OF FOAM'
READ(6,*) VF
WRITE(6,*) 'ENTER SOLID POLYMER CONDUCTIVITY (W/mK)'
READ(6,*) SOLID_COND

LTOT=0.0
DO 5 I=1,NUM_STRUTS
DIST=SQRT((X1(I)-X2(I))*(X1(I)-X2(I))+(Y1(I)-Y2(I))*(Y1(I)-Y2(I)))
LTOT=LTOT+DIST
 5CONTINUE
AREA = (1-VF)*DELX*DELY/LTOT
WRITE(6,*) 'CELL WALL THICKNESS FOR 2-D MODEL = ',AREA

DO 10 I=1,ICOUNT
DO 20 J=1,ICOUNT
C(I,J)=C(I,J)*SOLID_COND*AREA
 20CONTINUE
 10CONTINUE
RETURN
END

SUBROUTINE BOUNDARY(C,ICOUNT,KNOWN,XNODE,YNODE,TEMP)
PARAMETER(MAX=600,INIT=-1.)
REAL C(MAX,MAX),KNOWN(MAX),XNODE(MAX),YNODE(MAX)
INTEGER ICOUNT,NBOUNDARY,INODE
REAL TEMP(MAX)

OPEN(UNIT=15,FILE='node_locations.dat',STATUS='UNKNOWN')
REWIND(15)
DO 5 I=1,ICOUNT
WRITE(15,*) 'NODE',I,'  AT',XNODE(I),YNODE(I)
 5CONTINUE
CLOSE(15)
DO 10 I=1,ICOUNT
KNOWN(I)=0.
 10CONTINUE
DO 30 I=1,ICOUNT
DO 40 J=1,ICOUNT
IF(TEMP(J).NE.INIT.AND.I.EQ.J) THEN
KNOWN(I)=-C(I,J)*TEMP(J)
C(I,J)=-1.
ELSE IF(TEMP(J).NE.INIT.AND.I.NE.J) THEN
KNOWN(I)=KNOWN(I) - C(I,J)*TEMP(J)
C(I,J) = 0.
```

```
ENDIF
 40CONTINUE
 30CONTINUE
RETURN
END

SUBROUTINE BOUNDARY_TEMP(TEMP,ICOUNT,XNODE,YNODE)
C-----------------------------------------------
C   Determines which nodes are boundary nodes and rearranges knowns to known vector [Z] and
C   unknowns to unknown vector [x]
C-----------------------------------------------
PARAMETER(MAX=600,T_LOWER=290.,DELTA_X_TOTAL=0.0254)
PARAMETER(DELTA_T_TOTAL=50,YERR=7.E-6,INIT=-1.)
REAL TEMP(MAX),HTRATE,DELTA_Y,DELTA_T,T_UPPER
REAL XNODE(MAX),YNODE(MAX)
INTEGER ICOUNT

WRITE(6,*) 'ENTER TOTAL PICTURE LENGTH IN HEAT TRANSFER DIRECTION'
WRITE(6,*) 'in m.'
READ(6,*) DELTA_Y

HTRATE=DELTA_T_TOTAL/DELTA_X_TOTAL
DELTA_T=HTRATE*DELTA_Y
T_UPPER=T_LOWER+DELTA_T

DO 5 I=1,ICOUNT
TEMP(I)=INIT
 5CONTINUE
DO 10 I=1,ICOUNT
YDIF=ABS(YNODE(I)-0.0)
IF(YDIF.LE.YERR) THEN
TEMP(I)=T_LOWER
WRITE(6,*) 'NODE',I,XNODE(I),YNODE(I)
WRITE(6,*) 'ON LOWER BORDER, TEMP = ',TEMP(I)
ENDIF

YDIF=ABS(YNODE(I) - DELTA_Y)
IF(YDIF.LE.YERR) THEN
TEMP(I)=T_UPPER
WRITE(6,*) 'NODE',I,XNODE(I),YNODE(I)
WRITE(6,*) 'ON UPPER BORDER, TEMP = ',TEMP(I)
ENDIF
 10CONTINUE
RETURN
END




SUBROUTINE MATRIX(C,KNOWN,ICOUNT)
C-----------------------------------------------
C   Gauss Matrix Solver determining unknown elements of [x]
C-----------------------------------------------
```

```
PARAMETER(MAX=600,LIMAUG=MAX+1)
REAL A(MAX,LIMAUG),X(MAX),C(MAX,MAX),KNOWN(MAX)
INTEGER N

WRITE(6,*) 'IN SUBROUTINE MATRIX ...'
CALL MATRIX_SET(A,KNOWN,ICOUNT,C)
CALL GAUSS(A,X,ICOUNT)
CALL OUTPUT(X,ICOUNT)
END

SUBROUTINE MATRIX_SET(A,C,N,CPREV)
PARAMETER(MAX=600,LIMAUG=MAX+1)
REAL A(MAX,LIMAUG),C(MAX),CPREV(MAX,MAX)
INTEGER N
DO 10 I=1,N
DO 20 J=1,N
A(I,J)=CPREV(I,J)
 20CONTINUE
 10 CONTINUE

DO 30 I=1,N
A(I,N+1) = C(I)
WRITE(6,*) A(I,N+1)
 30 CONTINUE
RETURN
END


SUBROUTINE GAUSS(AUG,X,N)
PARAMETER(MAX=600,LIMAUG=MAX+1)
REAL AUG(MAX,LIMAUG),X(MAX),MULT
INTEGER N,I,J,K,PIVOT

DO 70 I=1,N
IF(AUG(I,I).EQ.0) THEN
PIVOT=0
J=I+1
 30IF((PIVOT.EQ.0).AND.(J.NE.N)) THEN
IF(AUG(J,I).NE.0) PIVOT = J
J=J+1
GO TO 30
ENDIF
IF(PIVOT.EQ.0) THEN
WRITE(6,*) 'MATRIX IS SINGULAR'
STOP
ELSE
DO 40 J=1,N+1
TEMP=AUG(I,J)
AUG(I,J)=AUG(PIVOT,J)
AUG(PIVOT,J)=TEMP
 40CONTINUE
ENDIF
ENDIF
DO 60 J=I+1,N
```

```
MULT=-AUG(J,I)/AUG(I,I)
DO 50 K=I,N+1
AUG(J,K)=AUG(J,K)+MULT*AUG(I,K)
 50CONTINUE
 60CONTINUE
 70CONTINUE

X(N)=AUG(N,N+1)/AUG(N,N)
DO 90 J=N-1,1,-1
X(J)=AUG(J,N+1)
DO 80 K=J+1,N
X(J)=X(J)-AUG(J,K)*X(K)
 80CONTINUE
 X(J)=X(J)/AUG(J,J)
 90CONTINUE
RETURN
END


SUBROUTINE OUTPUT(X,N)
C-----------------------------------------------
C  Ouputs temperature (for internal nodes) or flux (for boundary nodes) for every node.  Fluxes
C   at boundaries are then summed to determine solid conductivity.
C-----------------------------------------------
PARAMETER(MAX=600)
REAL X(MAX)
INTEGER N

WRITE(6,*) 'IN SUBROUTINE OUTPUT ...'
OPEN(UNIT=13,FILE='conductivity_solution.dat',STATUS='UNKNOWN')
REWIND(13)
DO 10 I=1,N
WRITE(13,*) 'X ',I,' = ',X(I)
 10 CONTINUE
CLOSE(13)
RETURN
END
```

The following Fortran code listed is a routine that determines the borders and nodes directly from the image file. The image file is considered a text file where the pixel value in black (255) or white(0) is an element in a 768x512 array which is the same size as the array of pixels in the image. In the future, this input routine can be expanded to directly read the unaltered binary image file. the following algorithm is used. The program scans from left to right until it hits a border. The program scans up and down the border until it hits the border's end nodes. The end nodes are recorded. Then the program checks whether the border has already been found (if so, the duplicate is erased). Then the

program goes back to the original scanning line and continues to scan for other borders. Once the end of the picture is hit, the program moves up one pixel and begins to scan again from left to right. Once completed, all of the borders and nodes are recorded in a file to be used with the program 'SOLID_CONDUCTIVITY'

```
PROGRAM CONNECT
PARAMETER(MAXX=600,MAXY=600,MAXSTRUT=900,XERR=10,YERR=10)
PARAMETER(BORDER=0,BACKGROUND=255,SEP_ERROR=5)
PARAMETER(PIXEL_SHIFT=5)
COMMON/BLOCK1/XMAX,YMAX

INTEGER PIXEL(MAXY,MAXX),ISTRUT,HIT_EDGE,X,Y
INTEGER XN1(MAXSTRUT),XN2(MAXSTRUT),YN1(MAXSTRUT)
INTEGER YN2(MAXSTRUT)
INTEGER XMAX,YMAX
REAL STRUT_LENGTH(MAXSTRUT)

ISTRUT=1
CALL INITIALIZE(XN1,XN2,YN1,YN2,STRUT_LENGTH,PIXEL)
CALL PIXEL_FILE_OPEN(PIXEL)
Y=1

DO WHILE(Y.LE.YMAX.AND.ISTRUT.LE.300)
X=1
DO WHILE(X.LT.XMAX)
CALL INCREMENT(X,Y,PIXEL)
IF(X.LT.XMAX) THEN
HIT_EDGE=0
cWRITE(6,*) 'x = ',X,'XMAX = ',XMAX
cWRITE(6,*) '    y = ',Y,'    YMAX =',YMAX
cWRITE(6,*) 'NUMBER OF STRUTS',ISTRUT
CALL FIND_NODE(XN1,XN2,YN1,YN2,PIXEL,ISTRUT,HIT_EDGE,X,Y)
CALL FIND_STRUT_LENGTH(STRUT_LENGTH,ISTRUT,XN1,XN2,YN1,YN2)
IF(HIT_EDGE.NE.1) THEN
CALL CHECK(XN1,XN2,YN1,YN2,ISTRUT)
ENDIF
ENDIF
X=X+PIXEL_SHIFT
ENDDO
Y=Y+1
ENDDO
CALL OUTPUT(XN1,XN2,YN1,YN2,STRUT_LENGTH,ISTRUT)
END


SUBROUTINE INITIALIZE(X1,X2,Y1,Y2,LENGTH,PIXEL)
PARAMETER(MAXX=600,MAXY=600,MAXSTRUT=900,XERR=10,YERR=10)
PARAMETER(BORDER=0,BACKGROUND=255,SEP_ERROR=5)
PARAMETER(PIXEL_SHIFT=5)
COMMON/BLOCK1/XMAX,YMAX
```

```
INTEGER I,J,X1(MAXSTRUT),X2(MAXSTRUT),Y1(MAXSTRUT),Y2(MAXSTRUT)
INTEGER PIXEL(MAXY,MAXX)
INTEGER XMAX,YMAX
REAL LENGTH(MAXSTRUT)

 WRITE(6,*) 'IN SUBROUTINE INITIALIZE ...'
DO 10 I=1,MAXSTRUT
X1(I)=0
X2(I)=0
Y1(I)=0
Y2(I)=0
LENGTH(I)=0
 10CONTINUE

DO 20 I=1,YMAX
 DO 30 J=1,XMAX
PIXEL(I,J)=0
 30CONTINUE
 20 CONTINUE
RETURN
END


SUBROUTINE PIXEL_FILE_OPEN(PIXEL)
C-------------------------------------------------
C    Subroutine that opens digitized black/white image 'section.tsv'
C-------------------------------------------------
PARAMETER(MAXX=600,MAXY=600,MAXSTRUT=900,XERR=10,YERR=10)
PARAMETER(BORDER=0,BACKGROUND=255,SEP_ERROR=5)
PARAMETER(PIXEL_SHIFT=5)
COMMON/BLOCK1/XMAX,YMAX

INTEGER PIXEL(MAXY,MAXX),I,J
INTEGER XMAX,YMAX
WRITE(6,*) 'IN SUBROUTINE PIXEL_FILE_OPEN ...'

OPEN(UNIT=19,FILE='section.tsv',STATUS='UNKNOWN')
REWIND(19)
READ(19,*) YMAX,XMAX
DO 10 I=1,YMAX
READ(19,*) (PIXEL(I,J),J=1,XMAX)
 10CONTINUE

CLOSE(19)
RETURN
END


SUBROUTINE INCREMENT(X,Y,PIXEL)
C-------------------------------------------------
C  Subroutine that increments from left to right until border is hit
C-------------------------------------------------
PARAMETER(MAXX=600,MAXY=600,MAXSTRUT=900,XERR=10,YERR=10)
PARAMETER(BORDER=0,BACKGROUND=255,SEP_ERROR=5)
```

```
PARAMETER(PIXEL_SHIFT=5)
COMMON/BLOCK1/XMAX,YMAX

INTEGER FIND_BORDER_FORWARD,X,Y,PIXEL(MAXY,MAXX)
INTEGER XMAX,YMAX

cWRITE(6,*) 'IN SUBROUTINE INCREMENT ...'
X=FIND_BORDER_FORWARD(X,Y,PIXEL)

RETURN
END


INTEGER FUNCTION FIND_BORDER_FORWARD(X,Y,PIXEL)
C-----------------------------------------------
C  Function that moves location to right until border is hit
C-----------------------------------------------
PARAMETER(MAXX=600,MAXY=600,MAXSTRUT=900,XERR=10,YERR=10)
PARAMETER(BORDER=0,BACKGROUND=255,SEP_ERROR=5)
PARAMETER(PIXEL_SHIFT=5)
COMMON/BLOCK1/XMAX,YMAX

INTEGER FOUND,X,Y,PIXEL(MAXY,MAXX)
INTEGER XMAX,YMAX

FOUND=-1
DO WHILE(X.LT.XMAX.AND.FOUND.EQ.(-1))
IF(PIXEL(Y,X).EQ.BACKGROUND) THEN
X=X+1
ELSE IF(PIXEL(Y,X).EQ.BORDER) THEN
FOUND=1
ENDIF
ENDDO
IF(X.GE.XMAX)THEN
X=XMAX
ENDIF
FIND_BORDER_FORWARD = X
RETURN
END


INTEGER FUNCTION FIND_BORDER_REVERSE(X,Y,PIXEL)
C-----------------------------------------------
C  Function that moves location to left until border is hit
C-----------------------------------------------
PARAMETER(MAXX=600,MAXY=600,MAXSTRUT=900,XERR=10,YERR=10)
PARAMETER(BORDER=0,BACKGROUND=255,SEP_ERROR=5)
PARAMETER(PIXEL_SHIFT=5)
COMMON/BLOCK1/XMAX,YMAX

INTEGER FOUND,X,Y,PIXEL(MAXY,MAXX)
INTEGER XMAX,YMAX

FOUND=-1
```

```
DO WHILE(X.GT.1.AND.FOUND.EQ.(-1))
IF(PIXEL(Y,X).EQ.BACKGROUND) THEN
X=X-1
ELSE IF(PIXEL(Y,X).EQ.BORDER) THEN
FOUND=1
ENDIF
ENDDO
IF(X.LE.1) THEN
X=1
ELSE IF(X.GE.XMAX) THEN
X=XMAX
ENDIF
FIND_BORDER_REVERSE = X
RETURN
END


SUBROUTINE FIND_NODE(X1,X2,Y1,Y2,PIXEL,ISTRUT,HIT_EDGE,X,Y)
C-------------------------------------------------
C Subroutine that moves up and down border until comes to border endpoint.  This is found by looking
C  at the nearest neighbor border and where the 2 converge is the endpoint of the border -- or a node.
C-------------------------------------------------
PARAMETER(MAXX=600,MAXY=600,MAXSTRUT=900,XERR=10,YERR=10)
PARAMETER(BORDER=0,BACKGROUND=255,SEP_ERROR=5)
PARAMETER(PIXEL_SHIFT=5)
COMMON/BLOCK1/XMAX,YMAX

INTEGER X1(MAXSTRUT),X2(MAXSTRUT),Y1(MAXSTRUT),Y2(MAXSTRUT)
INTEGER PIXEL(MAXY,MAXX),ISTRUT,HIT_EDGE,X,Y
INTEGER FIND_BORDER_FORWARD,FIND_BORDER_REVERSE
INTEGER XT1,XT2,XT3,YT1,YT2,YT3,DIST12,DIST13,DIST,ODIST,XORIG,YORIG
INTEGER BORDER_WIDTH_FORWARD,BORDER_WIDTH_REVERSE
INTEGER XMAX,YMAX

cWRITE(6,*) 'IN SUBROUTINE FIND_NODE ...'
XORIG=X
YORIG=Y

XT1=X
X=X+BORDER_WIDTH_FORWARD(XT1,Y,PIXEL)
IF(X.GT.XMAX) THEN
HIT_EDGE=1
X = XORIG
Y = YORIG
RETURN
ENDIF

XT2=FIND_BORDER_FORWARD(X,Y,PIXEL)
IF(XT2.GE.XMAX) THEN
HIT_EDGE=2
XT2 = XMAX
ENDIF

DIST12= XT2 - (XT1+BORDER_WIDTH_FORWARD(XT1,Y,PIXEL))
```

```
X=XT1 - BORDER_WIDTH_REVERSE(XT1,Y,PIXEL)
XT3=FIND_BORDER_REVERSE(X,Y,PIXEL)
DIST13= (XT1-BORDER_WIDTH_REVERSE(XT1,Y,PIXEL)) - XT3

IF(DIST12.LE.DIST13) THEN
DIST = DIST12
ELSE
DIST = DIST13
ENDIF
ODIST = DIST

DO WHILE(DIST.GT.SEP_ERROR)
Y=Y+1
IF(Y.GT.YMAX) THEN
HIT_EDGE=1
X = XORIG
Y = YORIG
RETURN
ENDIF
X= XT1 - PIXEL_SHIFT
IF(X.LT.1) THEN
HIT_EDGE=1
X = XORIG
Y = YORIG
RETURN
ENDIF

XT1 = FIND_BORDER_FORWARD(X,Y,PIXEL)
IF(XT1.GT.XMAX) THEN
HIT_EDGE=1
X = XORIG
Y = YORIG
RETURN
ENDIF

X=XT1 + BORDER_WIDTH_FORWARD(XT1,Y,PIXEL)
XT2=FIND_BORDER_FORWARD(X,Y,PIXEL)
IF(XT2.GE.XMAX) THEN
HIT_EDGE=2
XT2 = XMAX
ENDIF
DIST12 = XT2 - (XT1+BORDER_WIDTH_FORWARD(XT1,Y,PIXEL))

X = XT1 - BORDER_WIDTH_REVERSE(XT1,Y,PIXEL)
XT3= FIND_BORDER_REVERSE(X,Y,PIXEL)
DIST13 = (XT1-BORDER_WIDTH_REVERSE(XT1,Y,PIXEL)) - XT3

ODIST=DIST
IF(DIST12.LE.DIST13) THEN
DIST=DIST12
ELSE
DIST=DIST13
ENDIF
```

```
ENDDO

X1(ISTRUT) = XT1
Y1(ISTRUT) = Y

X=XORIG
Y=YORIG
XT1 = X
X = X + BORDER_WIDTH_FORWARD(XT1,Y,PIXEL)

XT2 = FIND_BORDER_FORWARD(X,Y,PIXEL)
DIST12 = XT2 - (XT1+BORDER_WIDTH_FORWARD(XT1,Y,PIXEL))

X = XT1 - BORDER_WIDTH_REVERSE(XT1,Y,PIXEL)
XT3=FIND_BORDER_REVERSE(X,Y,PIXEL)
DIST13 = (XT1-BORDER_WIDTH_REVERSE(XT1,Y,PIXEL)) - XT3

IF(DIST12.LE.DIST13) THEN
DIST=DIST12
ELSE
DIST=DIST13
ENDIF
ODIST = DIST

DO WHILE(DIST.GT.SEP_ERROR)
Y = Y-1
IF(Y.LT.1) THEN
HIT_EDGE=1
X = XORIG
Y = YORIG
RETURN
ENDIF
X = XT1 - PIXEL_SHIFT

IF(X.LT.1) THEN
HIT_EDGE=1
X = XORIG
Y = YORIG
RETURN
ENDIF

XT1 = FIND_BORDER_FORWARD(X,Y,PIXEL)
IF(XT1.GT.XMAX) THEN
HIT_EDGE=1
X = XORIG
Y = YORIG
RETURN
ENDIF

X = XT1 + BORDER_WIDTH_FORWARD(XT1,Y,PIXEL)
XT2 = FIND_BORDER_FORWARD(X,Y,PIXEL)
IF(XT2.GT.XMAX) THEN
HIT_EDGE = 2
XT2 = XMAX
```

```
ENDIF
DIST12 = XT2 -( XT1+BORDER_WIDTH_FORWARD(XT1,Y,PIXEL))

X = XT1 - BORDER_WIDTH_REVERSE(XT1,Y,PIXEL)
XT3 = FIND_BORDER_REVERSE(X,Y,PIXEL)
DIST13 = (XT1-BORDER_WIDTH_REVERSE(XT1,Y,PIXEL)) - XT3

ODIST = DIST
IF(DIST12.LE.DIST13) THEN
DIST = DIST12
ELSE
DIST = DIST13
ENDIF
ENDDO

X2(ISTRUT) = XT1
Y2(ISTRUT) = Y

IF(DIST.LE.SEP_ERROR) THEN
ISTRUT= ISTRUT + 1
ENDIF
X = XORIG
Y = YORIG

RETURN
END


SUBROUTINE FIND_STRUT_LENGTH(LENGTH,ISTRUT,X1,X2,Y1,Y2)
C-----------------------------------------------
C  Determines length of border that was just determined
C-----------------------------------------------
PARAMETER(MAXX=600,MAXY=600,MAXSTRUT=900,XERR=10,YERR=10)
PARAMETER(BORDER=0,BACKGROUND=255,SEP_ERROR=5)
PARAMETER(PIXEL_SHIFT=5)
PARAMETER(SLMIN=20.0)
COMMON/BLOCK1/XMAX,YMAX

REAL LENGTH(MAXSTRUT),DELTA_X,DELTA_Y
INTEGER ISTRUT,X1(MAXSTRUT),X2(MAXSTRUT),Y1(MAXSTRUT),Y2(MAXSTRUT)
INTEGER XMAX,YMAX

cWRITE(6,*) 'IN SUBROUTINE FIND_STRUT_LENGTH ...'
DELTA_X = X2(ISTRUT-1) - X1(ISTRUT-1)
DELTA_Y = Y2(ISTRUT-1) - Y1(ISTRUT-1)
LENGTH(ISTRUT-1) = SQRT(DELTA_X*DELTA_X + DELTA_Y*DELTA_Y)

IF(LENGTH(ISTRUT-1).LT.SLMIN) THEN
ISTRUT=ISTRUT-1
ENDIF
RETURN
END
```

```
SUBROUTINE CHECK(X1,X2,Y1,Y2,ISTRUT)
C-------------------------------------------------
C  Subroutine that determines if border is already found
C-------------------------------------------------
PARAMETER(MAXX=600,MAXY=600,MAXSTRUT=900,XR=10,YR=10)
PARAMETER(BORDER=0,BACKGROUND=255,SEP_ERROR=5)
PARAMETER(PIXEL_SHIFT=5)
PARAMETER(SLMIN=10.0)
COMMON/BLOCK1/XMAX,YMAX

INTEGER X1(MAXSTRUT),X2(MAXSTRUT),Y1(MAXSTRUT),Y2(MAXSTRUT),ISTRUT
INTEGER L_STRUT,I
INTEGER XD1,XD2,XD3,XD4,YD1,YD2,YD3,YD4
INTEGER XMAX,YMAX
REAL LENGTH

cWRITE(6,*) 'IN SUBROUTINE CHECK ...'
L_STRUT = ISTRUT - 1

DO 10 I = 1,L_STRUT-1
XD1=ABS(X1(L_STRUT) - X1(I))
XD2=ABS(X2(L_STRUT) - X2(I))
XD3=ABS(X1(L_STRUT) - X1(I))
XD4=ABS(X2(L_STRUT) - X1(I))

YD1=ABS(Y1(L_STRUT) - Y1(I))
YD2=ABS(Y2(L_STRUT) - Y2(I))
YD3=ABS(Y1(L_STRUT) - Y1(I))
YD4=ABS(Y2(L_STRUT) - Y1(I))

IF(XD1.LE.XR.AND.XD2.LE.XR.AND.YD1.LE.YR.AND.YD2.LE.YR) THEN
ISTRUT = ISTRUT - 1
RETURN
ELSEIF(XD3.LE.XR.AND.XD4.LE.XR.AND.YD3.LE.YR.AND.YD4.LE.YR)THEN
ISTRUT = ISTRUT - 1
RETURN
ENDIF
 10CONTINUE

IF(X1(L_STRUT).EQ.X2(L_STRUT).AND.Y1(L_STRUT).EQ.Y2(L_STRUT)) THEN
ISTRUT = ISTRUT -1
ENDIF

RETURN
END


SUBROUTINE OUTPUT(X1,X2,Y1,Y2,LENGTH,ISTRUT)
C-------------------------------------------------
C  Outputs borders found, length of border, and (x,y) coordinates of border's endpoints
C-------------------------------------------------
PARAMETER(MAXX=600,MAXY=600,MAXSTRUT=900,XERR=10,YERR=10)
PARAMETER(BORDER=0,BACKGROUND=255,SEP_ERROR=5)
PARAMETER(PIXEL_SHIFT=5)
```

```
COMMON/BLOCK1/XMAX,YMAX

INTEGER X1(MAXSTRUT),X2(MAXSTRUT),Y1(MAXSTRUT),Y2(MAXSTRUT),ISTRUT
REAL LENGTH(MAXSTRUT)
INTEGER I,J,LAST_STRUT
INTEGER XMAX,YMAX


WRITE(6,*) 'IN SUBROUTINE OUTPUT ...'
LAST_STRUT=ISTRUT - 1

OPEN(UNIT=11,FILE='connect_output.dat',STATUS='UNKNOWN')
REWIND(11)
WRITE(11,*) 'NUMBER OF STRUTS = ',LAST_STRUT
DO 10 I = 1,LAST_STRUT
WRITE(11,*) 'STRUT ',I,'STRUT LENGTH = ',LENGTH(I)
WRITE(11,*) 'XNODE1 = ',X1(I),'YNODE1 = ',Y1(I)
WRITE(11,*) 'XNODE2 = ',X2(I),'YNODE2 = ',Y2(I)
 10CONTINUE
CLOSE(11)
RETURN
END


INTEGER FUNCTION BORDER_WIDTH_FORWARD(XT1,Y,PIXEL)
C-------------------------------------------------
C  Increments forward to end of border so that border of mroe than 1 pixel width is not treated as
C  2 borders really close
C-------------------------------------------------
PARAMETER(MAXX=600,MAXY=600,MAXSTRUT=900,XERR=10,YERR=10)
PARAMETER(BORDER=0,BACKGROUND=255,SEP_ERROR=5)
PARAMETER(PIXEL_SHIFT=5)
COMMON/BLOCK1/XMAX,YMAX

INTEGER XT1,Y,PIXEL(MAXY,MAXX)
INTEGER A,AINC
INTEGER XMAX,YMAX

AINC = 1
A = XT1 + AINC
FOUND = -1

DO WHILE(A.LT.XMAX.AND.FOUND.EQ.(-1))
IF(PIXEL(Y,A).EQ.BORDER) THEN
AINC = AINC + 1
A = XT1 + AINC
ELSE IF(PIXEL(Y,A).EQ.BACKGROUND) THEN
BORDER_WIDTH_FORWARD = AINC
FOUND = 1
ENDIF
ENDDO
RETURN
END
```

```
INTEGER FUNCTION BORDER_WIDTH_REVERSE(XT1,Y,PIXEL)
C-------------------------------------------------
C  Increments backward to end of border so that border of mroe than 1 pixel width is not treated as
C  2 borders really close
C-------------------------------------------------
PARAMETER(MAXX=600,MAXY=600,MAXSTRUT=900,XERR=10,YERR=10)
PARAMETER(BORDER=0,BACKGROUND=255,SEP_ERROR=5)
PARAMETER(PIXEL_SHIFT=5)
COMMON/BLOCK1/XMAX,YMAX

INTEGER XT1,Y,PIXEL(MAXY,MAXX)
INTEGER A,AINC
INTEGER XMAX,YMAX

AINC = 1
A = XT1 - AINC
FOUND = -1

DO WHILE(A.GT.1.AND.FOUND.EQ.(-1))
IF(PIXEL(Y,A).EQ.BORDER) THEN
AINC = AINC + 1
A = XT1 - AINC
ELSE IF(PIXEL(Y,A).EQ.BACKGROUND) THEN
BORDER_WIDTH_REVERSE = AINC
FOUND = 1
ENDIF
ENDDO
RETURN
END
```

Appendix C Schuetz's 2D Solid Conductivity Analysis

Consider for the two-dimensional solid conductivity the case where the solid is in the form of sticks oriented at every angle. The total length of sticks in any direction within a small angle dθ is constant. This is what is meant by "random sticks".

Look at the upper limit of conductivity on this geometry, isotherms are assumed horizontal. That is, the conductivity of the solid is assumed infinite in the direction perpendicular to heat flow. This is displayed in figure C.1. Because the isotherms are horizontal lines, the temperature gradient must be constant under steady state conditions. All sticks at the same angle θ may be lined up end to end with no effect on the heat transfer so as to form continuous "bridges" crossing the thickness of the sample. Because there is an equal length of sticks at any θ, there are more bridges at small angles than at large angles. The heat flow across a single bridge at angle θ is given by:

$$q(\theta) = k_p \frac{t(T_1 - T_2)}{(\frac{L}{\cos\theta})} \tag{C.1}$$

If $n(\theta)$ is the number of bridges at θ per unit angle per unit volume, and if $l(\theta)$ is the length of a bridge at θ, define a constant, λ, such that:

$$\lambda = n(\theta)\, l(\theta) = constant \tag{C.2}$$

From the geometry of the situation

$$l(\theta) = \frac{L}{\cos\theta} \tag{C.3}$$

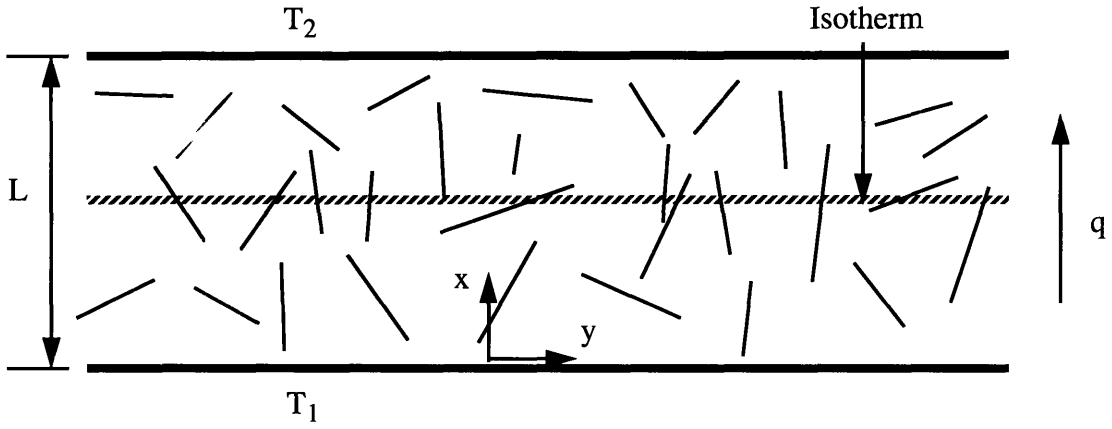

(a) Random Sticks (Reproduced from [14])

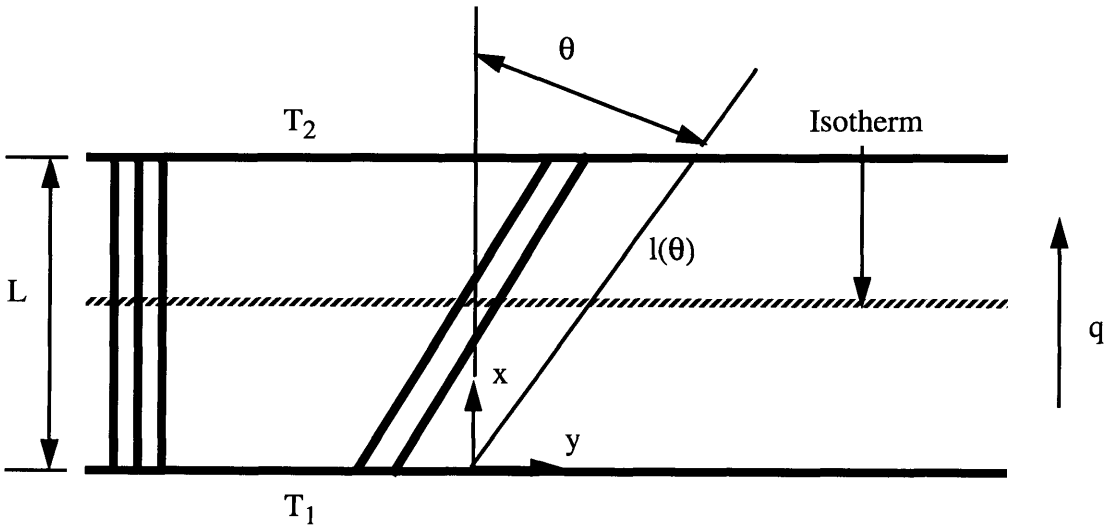

(b) Sticks Aligned to Form Bridges (Reproduced from [14])

Figure C.1: *Geometry Showing Upper Limit Conductivity of Random Sticks*

therefore

$$n(\theta) = \frac{\lambda \cos\theta}{L} \tag{C.4}$$

Physically, λ is the total length of all sticks at θ per unit volume, per unit angle, and is therefore a constant for random sticks, as defined here. The total solid conduction is the integral of the heat flow per bridge, times the number of bridges per unit volume per unit angle, times the volume, over all angles θ.

$$q_{solid} = \int_{\theta=0}^{2\pi} (A \bullet L) \left(\frac{k_p t (T_1 - T_2) \cos\theta}{L}\right) \left(\lambda \frac{\cos\theta}{L}\right) d\theta \tag{C.5}$$

Integrating we find:

$$q_{solid} = \frac{A (T_1 - T_2)}{L} \pi k_p t \lambda \tag{C.6}$$

But λ is related to the foam porosity.

$$1 - \delta = t\lambda \int_{\theta=0}^{2\pi} d\theta = t\lambda 2\pi \tag{C.7}$$

Solving for λ and substituting into equation C.6,

$$q_{solid} = \frac{A (T_1 - T_2)}{L} k_p \left(\frac{1 - \delta}{2}\right) \tag{C.8}$$

For the gas (ignoring the volume of the solid):

$$q_{gas} = \frac{A (T_1 - T_2)}{L} k_g \tag{C.9}$$

But in our analysis, just looking at the solid conductivity component to compare to the

solid conductivity program, ignore the gas conductivity (effectively treating k_g as zero).

Then from equations C.8, we may find the effective solid conductivity of the medium, given by:

$$k_{solid} = k_p \left(\frac{1-\delta}{2}\right) \tag{C.10}$$

If one were considering both effective conductivity components (k_{gas}+k_{solid}) this could be determined by combining equations C.8 and C.9 to yield

$$k_{solid} + k_{gas} = k_p \left(\frac{1-\delta}{2}\right) + k_g \tag{C.11}$$

It is the two-dimensional solid conductivity predicted by equation C.10 that is compared to the results of the solid conductivity matrix program of Section 3.9.

Appendix D Rosseland Extinction Coefficient Program

First shown in this appendix is a sample transmission data file from the spectrometer. Next is the modified transmission data file. This modified data file is input to the Fortran code listing which follows, "Rosseland", which calculates the Rosseland average extinction coefficient.

```
INSTRUMENT = IR44
FILETYPE = UNSPECIFIED
FIRST PT = 4800.47
LAST PT = 399.32
# POINTS = 4564
# SCANS = 256
DATE = 8/12/93
TIME = 10:23:41
SAMPLE NAME =
SAMPLE FORM =
CHEMIST NAME =
ZEROFILL = 1
APODIZATION = WENDEL RHINE
DATA =
0.0197  0.0199  0.0199  0.0195  0.0198  0.0189
0.0179  0.0184  0.0185  0.0185  0.0189  0.0192
0.0190  0.0194  0.0196  0.0195  0.0187  0.0179
                .
                .  761 Rows of Transmissivities
                .
0.0151  0.0143  0.0150  0.0159  0.0158  0.0156
0.0155  0.0151  0.0150  0.0158  0.0168  0.0164
0.0163  0.0178  0.0177  0.0175
```

Figure D.1: *Sample Transmission Data File from the Spectrometer*

sample thickness (inches)

```
0.028
0.0197 0.0199 0.0199 0.0195 0.0198 0.0189
0.0179 0.0184 0.0185 0.0185 0.0189 0.0192
0.0190 0.0194 0.0196 0.0195 0.0187 0.0179
                .
                . 761 Rows of Transmissivities
                .
0.0151 0.0143 0.0150 0.0159 0.0158 0.0156
0.0155 0.0151 0.0150 0.0158 0.0168 0.0164
0.0163 0.0178 0.0177 0.0175
```

Figure D.2: *Sample Modified Transmission Data File*

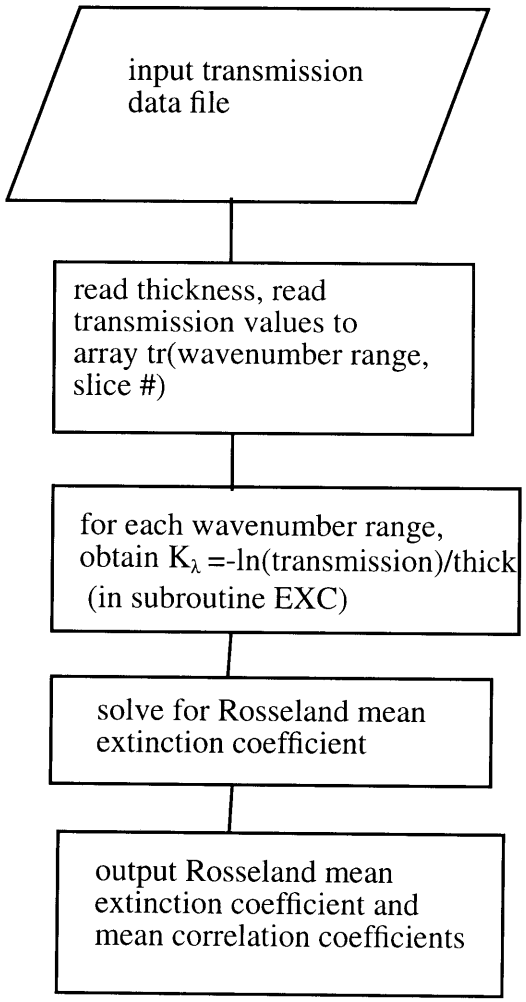

Figure D.3: *Flowchart for Program "Rosseland"*

```
      program rosseland
c
cThis program calculates the Rosseland mean extinction coefficient
cfor foam samples.  The input data is obtained from a Nicolet IR44
cinfrared spectrometer, which records transmissivities as a function
cof wavenumber.
c
c
cVARIABLE LIST
c
cnsam    number of sample slices for a particular foam
c w      thickness of each slice
ctr      transmissivity of a particular foam slice at a
c         particular wavenumber
cn       number of wavenumber intervals used in the integration
ceta     wavenumber
cdeta    wavenumber interval length
ckfeta   wavenumber-specific extinction coefficient, obtained
c          by force-fit method (see subroutine)
ckbeta   wavenumber-specific extinction coefficient, obtained
c          by a best-fit method
cc1,c2   constants used in the integral
csb      Stefan-Boltzmann constant
ct       temperature of sample in degrees Rankine, taken as
c          room temperature
ckrf,krb  final Rosseland mean extinction coefficients obtained
c           by force-fit and best-fit methods, respectively
ccorrf   wavenumber-specific correlation coefficients to check
c corrb  the validity of the force-fit and best-fit methods
c
c
      real tr(15,2000),trs(15),kbeta,krb,w(15),kfeta,krf,a,b
      character*(15) filename
c
cThe following files are obtained from the IR44 software. Each file
crepresents transmission data for a single foam slice. The first number
cin the file is the slice thickness in inches, and the remaining number
care the transmissivities for successive wavenumber intervals.
c
      write(6,*) 'INPUT NUMBER OF TRANSMISSION FILES'
      read(6,*) nsam
      idummy=10
      do 4 i=1,nsam
```

```
 write(6,*) 'INPUT NAME OF FILE (place 1 space before name)'
 read(6,3) filename
 write(6,2) filename
3format(1x,a15)
2format(//,'Filename is',a20,/)
 open(idummy,file=filename,status='old')
 idummy=idummy+1
4continue
data c1,c2,t/.18892e8,25898,528./
data sb,n,deta/1.712e-9,276,5.7872/
pi = acos(-1.)

open(6,file='f18.out',status='unknown')
write(*,5)
 5format(t4,'K(forced)',t18,'Corr.',t30,'K(best fit)',t45,'Corr.',/)
c
CSlice thicknesses are stored in an array
c
      do 10 i1=10,nsam+9
read(i1,*)w(i1-9)
 10continue
c
cTransmissivities are stored in a two-dimensional array.  The first
cindex is the slice number, and the second is the transmissivity for
ceach wavenumber interval.
c
do 30 iw=1,760
do 20 is=10,(nsam+9)
i1=is-9
i2=iw-484
c
cThe spectrometer file contains transmissivities at wavenumbers outside
cthe desired range. These values are read into dummy variable(q).
C
if(iw.le.484) then
read(is,*)q
else
read(is,*)tr(i1,i2)
endif
 20continue
 30continue
c
c
cThe following loop numericallly integrates wavenumber-specific
cextinction coefficients to obtain two Rosseland mean coefficients:
cone for the force-fit slope and one for the actual-fit slope.
```

```
c
do 50 j1=1,n
do 40 j2=1,nsam
trs(j2)=tr(j2,j1)
 40continue
c
cObtain the extinction coefficient for each wavenumber interval.
c
call exc(trs,w,nsam,kfeta,corrf,kbeta,corrb)

c
 eta=2000.-j1*deta
a=(pi*c1*c2*((eta/10000)**4))/(2.*sb*(t**5))
b=exp(c2*(eta/10000)/t)
sumkb=sumkb+((a*b)/(kbeta*(b-1.)*(b-1.)))*deta
sumkf=sumkf+((a*b)/(kfeta*(b-1.)*(b-1.)))*deta
sum=sum+((a*b)/((b-1.)*(b-1.)))*deta
C
cSum correlation coefficients for force-fit and actual-fit extinction
ccoefficients to be averaged later.
c
sumcorrf=sumcorrf+corrf
sumcorrb=sumcorrb+corrb
c
write(6,45) kfeta,corrf,kbeta,corrb
 45format(t6,f6.2,t17,f6.4,t33,f6.2,t44,f6.4)
 50continue
c
cThe Rosseland mean extinction coefficient is actually the ratio of
ctwo integrals (see analysis).
c
krf=sum/sumkf
krb=sum/sumkb
c
write(6,60)krf
write(6,70)sumcorrf/n
write(6,80)krb
write(6,70)sumcorrb/n
 60format(//,t3,'extinction coefficeint - force fit: ',f6.2)
 70format(t3,'average correlation: ',f6.4,//)
 80format(t3,'extinction coefficeint - actual fit: ',f6.2)
stop
end
c
c
cSubroutine exc calculates the extinction coefficient from the slopes
```

```
cof lines fitting the -ln(transmissivity) vs. thickness data in two
cways: one (kf) uses a line that is forced through the origin, and the
cother (kb) uses the conventional least-sqares best-fit line without
cregard to its intercept. The correlation coefficients for these two
ccases (rf,rb) are also calculated.
c
subroutine exc(tau,x,n,kf,rf,kb,rb)
real kb,tau(15),x(15),kf,icept

sumx2=0.
sumxy=0.
sumx=0.
sumy=0.
sumym=0.
sumycb=0.
sumycf=0.
c
cObtain sums from data points for force-fit and best-fit slope
cequations.
c
do 100 j=1,n
if(tau(j).le. .0001) then
tau(j) = .0001
endif
y=-log(tau(j))
sumx2=sumx2+(x(j)*x(j))
sumxy=sumxy+(y*x(j))
sumy=sumy+y
sumx=sumx+x(j)
 100continue
c
c
kf=sumxy/sumx2
kb=(n*sumxy-sumx*sumy)/(n*sumx2-sumx*sumx)

c
c'icept'is the y-intercept of the best-fit line. It is not needed in
cthis program, but is included for completeness.
c
icept=(sumy*sumx2-sumxy*sumx)/(n*sumx2-sumx*sumx)
ym=sumy/n
c
cObtain sums of deviations to obtain correlation coefficients
c
do 110 i=1,n
if(tau(i).le. .0001) then
```

```
 tau(i)=.0001
 endif
 y=-log(tau(i))
 ycf=kf*x(i)
 ycb=kb*x(i)+icept
 sumym=sumym+(y-ym)*(y-ym)
 sumycb=sumycb+(y-ycb)*(y-ycb)
 sumycf=sumycf+(y-ycf)*(y-ycf)
  110continue
 sigy2=sumym/(n-1)
 sigyxb2=sumycb/(n-2)
 sigyxf2=sumycf/(n-2)
 Cwrite(6,112) sigyxb2,sigyxf2,sigy2
  112format(t5,f5.4,t15,f5.4,t25,f5.4)
 if(sigyxf2.ge.sigy2) then
 rf=0.
 if(sigyxb2.ge.sigy2) then
   rb=0.
 goto 130
 endif
 go to 120
       endif
 if(sigyxb2.ge.sigy2) then
 rb=0.
 rf=(1.-(sigyxf2/sigy2))**0.5
 goto 130
 endif

 c
 ccorrelation coefficients
 C
 rf=(1.-(sigyxf2/sigy2))**0.5
  120rb=(1.-(sigyxb2/sigy2))**0.5
  130return
 end
```

Appendix E Extinction Coefficient of 1.5μm Film Accounting for Reflectivity

A first account of the influence of reflectivity on the measured transmissivity for a solid sample is carried out in the following manner. The relationship between extinction coefficient and transmissivity (equation 4.3)

$$K_\lambda = \frac{-ln(\tau_\lambda)}{t} \tag{E.1}$$

assumes that all of the attenuation of energy is due to absorption or scattering by the bulk material. That is, the intensity incident on the material is considered after any energy has been reflected from the surface as in figure E.1.

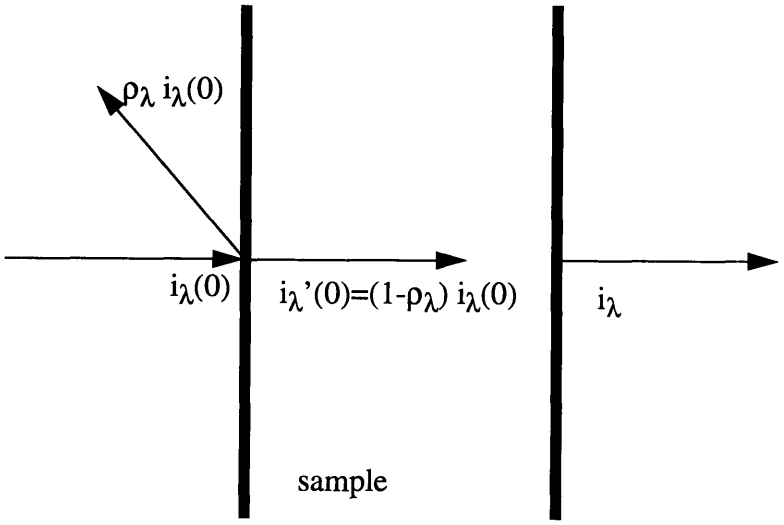

Figure E.1: *Intensities Before and After Reflection from Sample Surface*

Then the transmissivity appropriate to use with equation E.1 to calculate the extinction coefficient is

$$\tau_\lambda = \frac{i_\lambda}{i_\lambda{}'(0)} = \frac{i_\lambda}{(1-\rho_\lambda)\, i_\lambda(0)} \tag{E.2}$$

The spectrometer in calculating the transmissivity does not account for reflections off of the surface but measures the "apparent transmissivity"

$$\tau_{a,\lambda} = \frac{i_\lambda}{i_\lambda(0)} \tag{E.3}$$

So to relate the transmissivity used with equation E.1 to the transmittance outputted from the spectrometer in cases where reflectivity is important, rearrange expressions E.2 and E.3 to yield

$$\tau_\lambda = \frac{\tau_{a,\lambda}}{1-\rho_\lambda} \tag{E.4}$$

The reflectivity is a quantity dependent upon several parameters such as incident angle and whether the surface reflects in a diffuse or bidirectional fashion. An approximate estimate of this quantity in terms of the complex index of refraction of solid polyurethane ($\bar{n}_{\lambda 2}=n_{\lambda 2}+i\kappa_{\lambda 2}$) can be derived if one considers radiation normally incident to the surface with reflectivity being a bidirectional process and radiation leaving the surface also normal to the surface. This relation is presented in Siegel and Howell [17]

$$\rho_{\lambda n} = \frac{(n_{\lambda 2}-n_{\lambda 1})^2 + (\kappa_{\lambda 2}-\kappa_{\lambda 1})^2}{(n_{\lambda 2}+n_{\lambda 1})^2 + (\kappa_{\lambda 2}+\kappa_{\lambda 1})^2} \tag{E.5}$$

where $\bar{n}_{\lambda 1}=n_{\lambda 1}+i\kappa_{\lambda 1}$ is the complex index of refraction of air which is approximately $\bar{n}_{\lambda 1}=1+i(0)$. So the spectral reflectivity is roughly equivalent to

$$\rho_{\lambda n} = \frac{(n_{\lambda 2} - 1)^2 + (\kappa_{\lambda 2})^2}{(n_{\lambda 2} + 1)^2 + (\kappa_{\lambda 2})^2} \tag{E.6}$$

The values of the complex index of refraction of solid polyurethane measured by Mark Torpey were used and are presented along with the wavelength in Table E.1. Also in Table E.1 are the spectral reflectivities calculated from equation E.6, the apparent transmissivities of the 1.5μm solid polyurethane film, and the transmissivity adjusted for reflectivity calculated from equation E.4.

λ (μm)	$n_{\lambda 2}$	$\kappa_{\lambda 2}$	ρ_λ	$\tau_{a\lambda}$	τ_λ
6.5	1.4169	0.2450	0.040	0.61	0.64
7.0	1.516	0.0857	0.043	0.74	0.77
7.5	1.458	0.0718	0.036	0.77	0.80
8.0	1.4111	0.1874	0.035	0.73	0.76
8.5	1.5644	0.0805	0.049	0.72	0.76
9.0	1.4809	0.1944	0.043	0.68	0.71
9.5	1.6600	0.1257	0.064	0.69	0.74
10.0	1.6574	0.0557	0.062	0.77	0.82
11.0	1.6201	0.0072	0.056	0.85	0.90
12.0	1.6398	0.0216	0.059	0.86	0.91
13.0	1.7798	0.0294	0.079	0.86	0.93
14.0	1.7394	0.0082	0.073	0.89	0.96
15.0	1.8504	0.0	0.089	0.89	0.98
16.0	1.8921	0.0	0.095	0.87	0.96
18.0	1.9718	0.0	0.107	0.90	1.01

Table E.1: *Adjustment of 1.5*μm *Thin Film Transmissivity for Reflections from Surface*

λ (μm)	$n_{\lambda 2}$	$\kappa_{\lambda 2}$	ρ_λ	$\tau_{a\lambda}$	τ_λ
19.0	1.9985	0.0	0.111	0.90	1.01
20.0	2.1098	0.0	0.127	0.91	1.04
21.0	2.0976	0.0	0.126	0.90	1.03
22.0	2.1121	0.0	0.128	0.90	1.03
23.0	2.2656	0.0	0.150	0.93	1.09
24.0	2.2556	0.0	0.149	0.93	1.09
25.0	2.2751		0.152	0.94	1.11
30.0	2.4454		0.176	0.95	1.15

Table E.1: *Adjustment of 1.5*μm *Thin Film Transmissivity for Reflections from Surface*

Since the transmissivities at wavelengths above 16μm are greater than unity when accounting for approximate reflectivities, only extinction coefficients in the wavelength range 6μm to 16μm (the spectral range within which roughly 60% of the blackbody energy from a source at 300K lies) were Rosseland averaged. The extinction coefficient accounting for approximate reflectivity is 612cm^{-1} rather than the 1100cm^{-1} reported without accounting for reflectivity. This value is even lower if one approximates the transmissivities to be near unity in the wavelength range above 16μm.

Appendix F Derivation of Section Probability Distribution for Ellipse

Consider an elliptical cell with both minor axes b and a major axis a as displayed in figure F.1. The probability of sections perpendicular to the major axis (the orientation axis) having areas between area A_1 and A_2 is equivalent to the fraction of total section areas that these areas represent. That is

$$P(A{:}A_1 > A > A_2) = \frac{A\Delta x}{\sum A\Delta x} \tag{F.1}$$

This is the same as considering the surface of revolution of the ellipse and determining the area fraction of the shaded region in figure F.2. The probability of a section lying in this shaded region is

$$P(A{:}A_1 > A > A_2) = \frac{\bar{y}\Delta x}{\sum \bar{y}\Delta x} \tag{F.2}$$

Due to symmetry, this is the same problem as finding the fraction in figure F.3

$$P(A{:}A_1 > A > A_2) = \frac{y\Delta x}{\sum y\Delta x} \tag{F.3}$$

Now the surface of revolution is given by

$$\frac{x^2}{a^2} + \frac{y^2}{b^2} = 1 \tag{F.4}$$

This means that in the differential limit for Δx,

$$\sum y\Delta x = \int_{x=0}^{a} y(x)\,dx = \frac{\pi ab}{4} \tag{F.5}$$

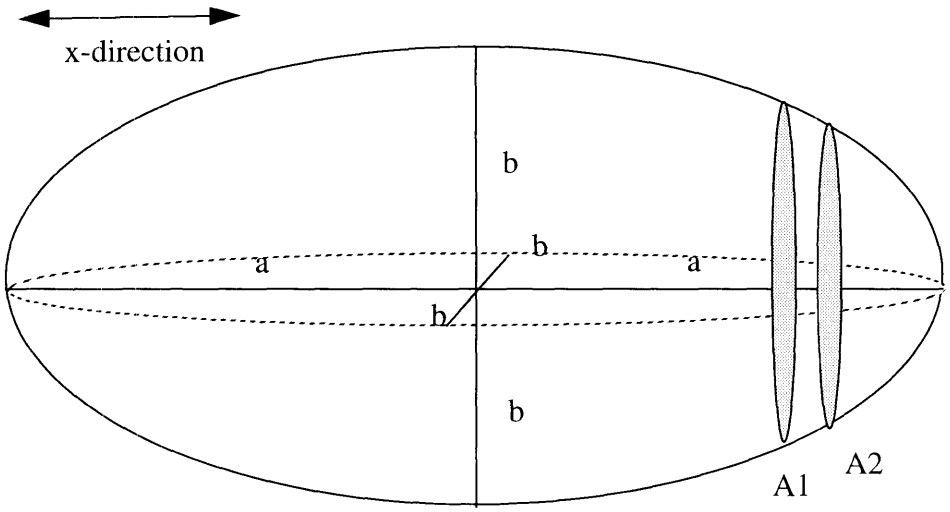

Figure F.1: *Elliptical Cell*

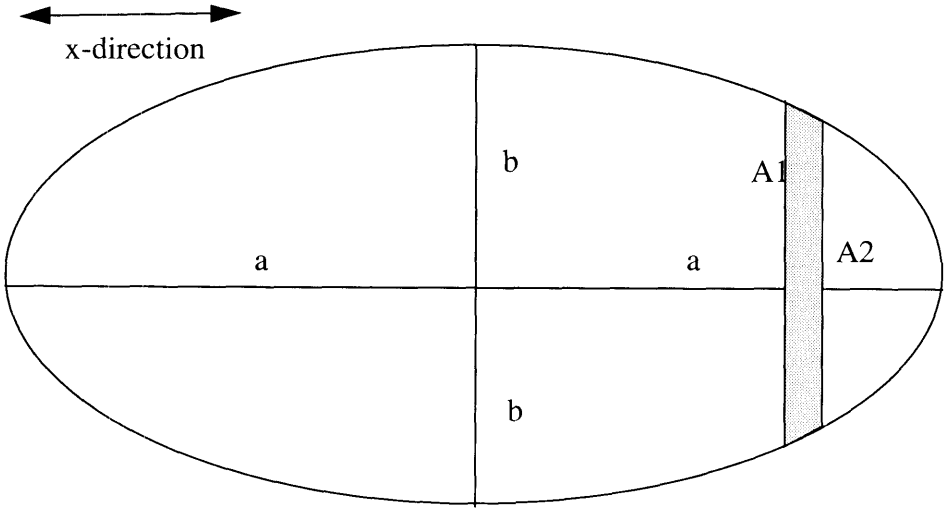

Figure F.2: *Ellipsoid Surface of Revolution*

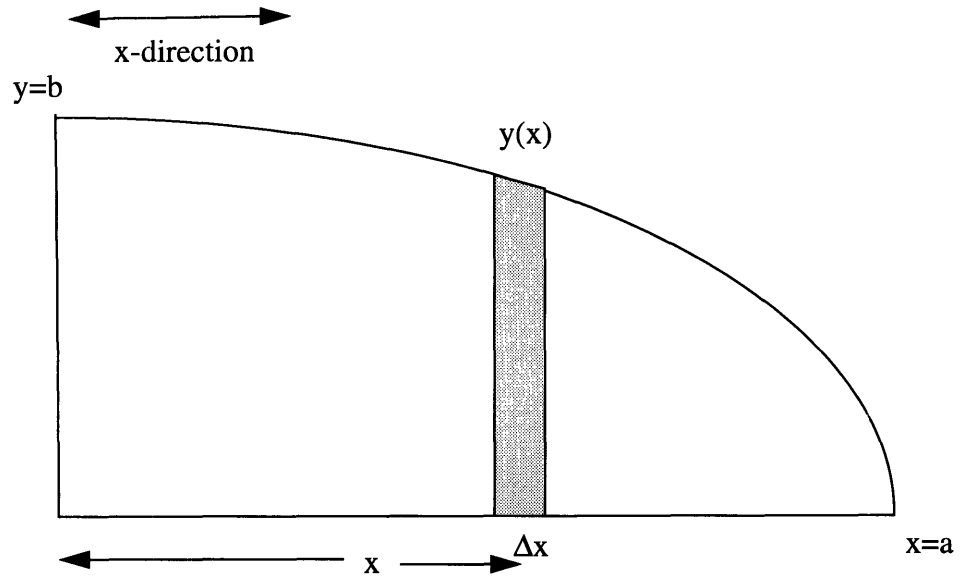

Figure F.3: *Symmetrical Portion of Surface of Revolution*

To determine y(x)Δx, consider the differential case where the slope of y(x) can be approximated as a linear slope

$$y(x)\,\Delta x \approx y(x)\,\Delta x + \frac{1}{2}\,[y(x) - y(x+\Delta x)\,]\,\Delta x = y(x)\,\Delta x + \frac{1}{2}\,(\frac{dy}{dx})\,\Delta x^2 \tag{F.6}$$

So the probability that the section area is in the range of A_1 and A_2, given by equation F.3 can be rewritten using equations F.5 and F.6 as

$$P(A{:}A_1 > A > A_2) = \frac{4}{\pi}\frac{\Delta x}{a}\frac{y}{b} + \frac{4}{2\pi}\frac{(dy/dx)\,\Delta x^2}{ab} \tag{F.7}$$

From equation F.4, the following relations can be incorporated into expression F.7

$$\frac{dy}{dx} = -\frac{b^2}{ay}\sqrt{1 - \frac{y^2}{b^2}} \tag{F.8}$$

$$\Delta x = -\frac{ay}{b^2}\frac{\Delta y}{\sqrt{1-\frac{y^2}{b^2}}} \tag{F.9}$$

Define z=y/b (dz=dy/b and $\Delta z=\Delta y/b$) such that for the region considered, z goes from unity to zero as x goes from 0 to a. Then using the expressions F.8 and F.9 and the definition of z, the probability that a section area lies in the differential area class A_1 to A_2 is

$$P(A:A_1 > A > A_2) = -\frac{4}{\pi}\frac{z\Delta z}{\sqrt{\frac{1}{z^2}-1}} - \frac{2z\Delta z^2}{\pi\sqrt{1-z^2}} \tag{F.10}$$

So using a spreadsheet with $\Delta z=0.001$ ($\Delta z<<1$) the probability of a section area lying in a certain differential diameter range was calculated. Then, the probabilities that section diameters lie within diameter ranges for A/A_{max} classes described in Section 4.9 were determined by summing the probability distributions for the differential diameter classes within that range. The results are shown in Section 4.9.

Appendix G SEM Photographs and Measurements

This appendix is organized by foam. That is, relevent data for the results in chapters three and four are presented for foam NBE 678/21/47, then for foam NBE 785/206, etc. For each foam, the following data is presented

(1) The results of the transmission measurements for the six foams analyzed. The plots of -ln(transmissivity) versus sample thickness are shown . Here, the transmission is calculated from the peak areas from the spectrometer as described in Section 4.1. Also in these figures are the slopes that represent the calculated Rosseland mean extinction coefficients. There are ten plots, one for each foam where the transmission was measured parallel to the rise direction, or direction of heat transfer. There are also plots for measurements made perpendicular to the rise direction for four foams.

(2) SEM photographs from which mean cell diameters and anisotropy are calculated. Sample calcuations are provided for mean cell diameter and anisotropy. Listed are the image from which calculations are made, the mean number of intersections per length of line parallel to the heat transfer direction, the mean number of intersections per length of line perpendicular to the heat transfer direction, the calculated surface-to-volume ratio, the mean cell diameter from equation 2.5 and the degree of anisotropy from equation 4.42.

(3) The SEM photographs showing strut cross sectional areas used in estimating f_s. The strut cross sectional area distributions measured from such SEM photographs as well as the mean strut cross sectional areas mesured, the ratio R of maximum to mean measured areas (as described in Section 4.5), the calculated true strut cross sectional area (from equation 4.30), and the resulting

fraction of solid in the strut.

(5) Characteristics of section area distributions used to calculate the cell size distributions of section 4.9 with ellipse shape factors. The maximum section area is presented as well as the number of section areas per total area for ten classes of A/A_{max}.

(7) After all of the data presented for the foams, the solid polyurethane extinction coefficient measured by ICI Polyurethanes is presented as a function of wavelength.

Foam NBE 678/21/47

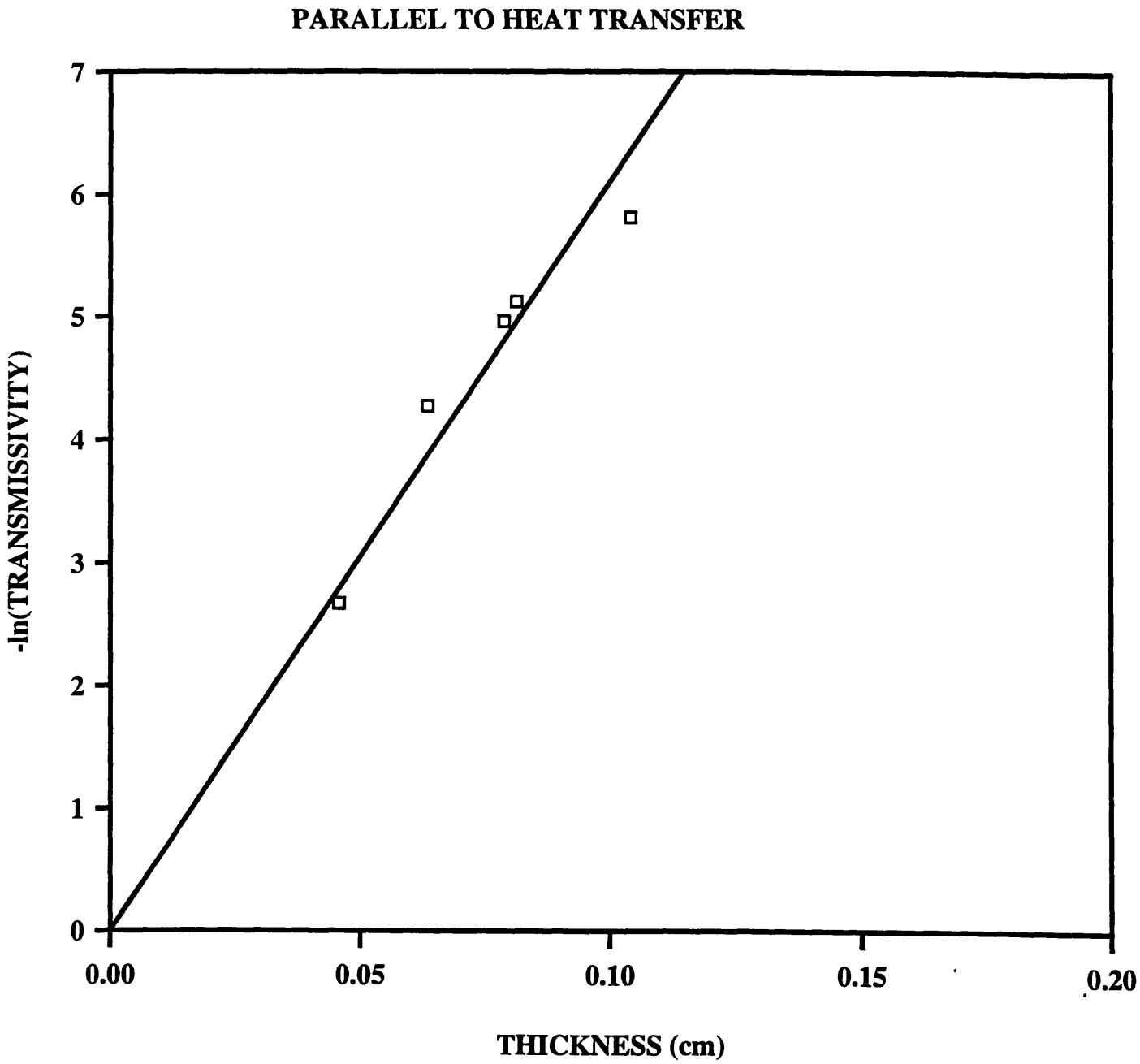

Figure G.1: *Transmission Data for Samples Tested*

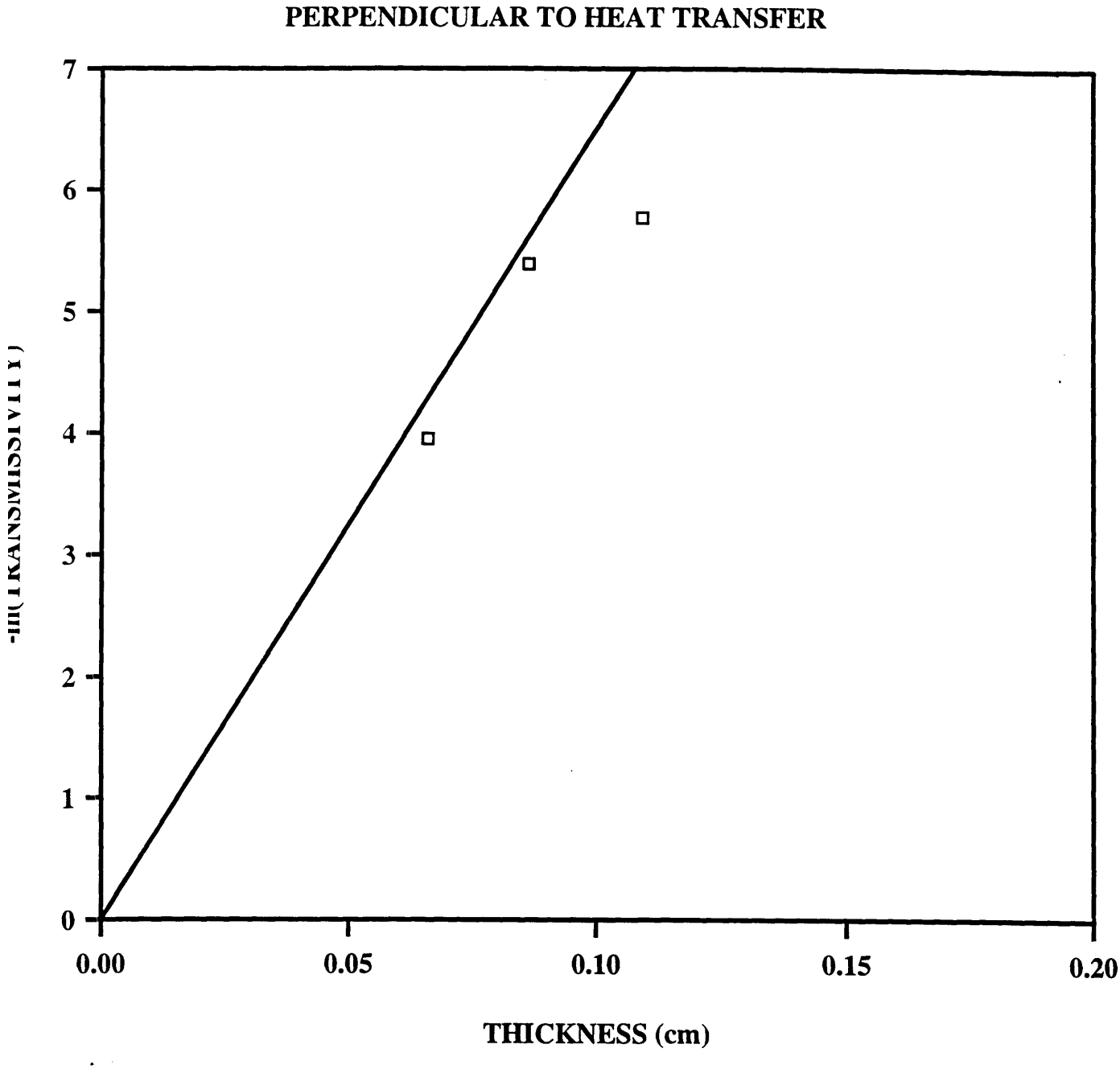

Figure G.2: *Transmission Data for Samples Tested*

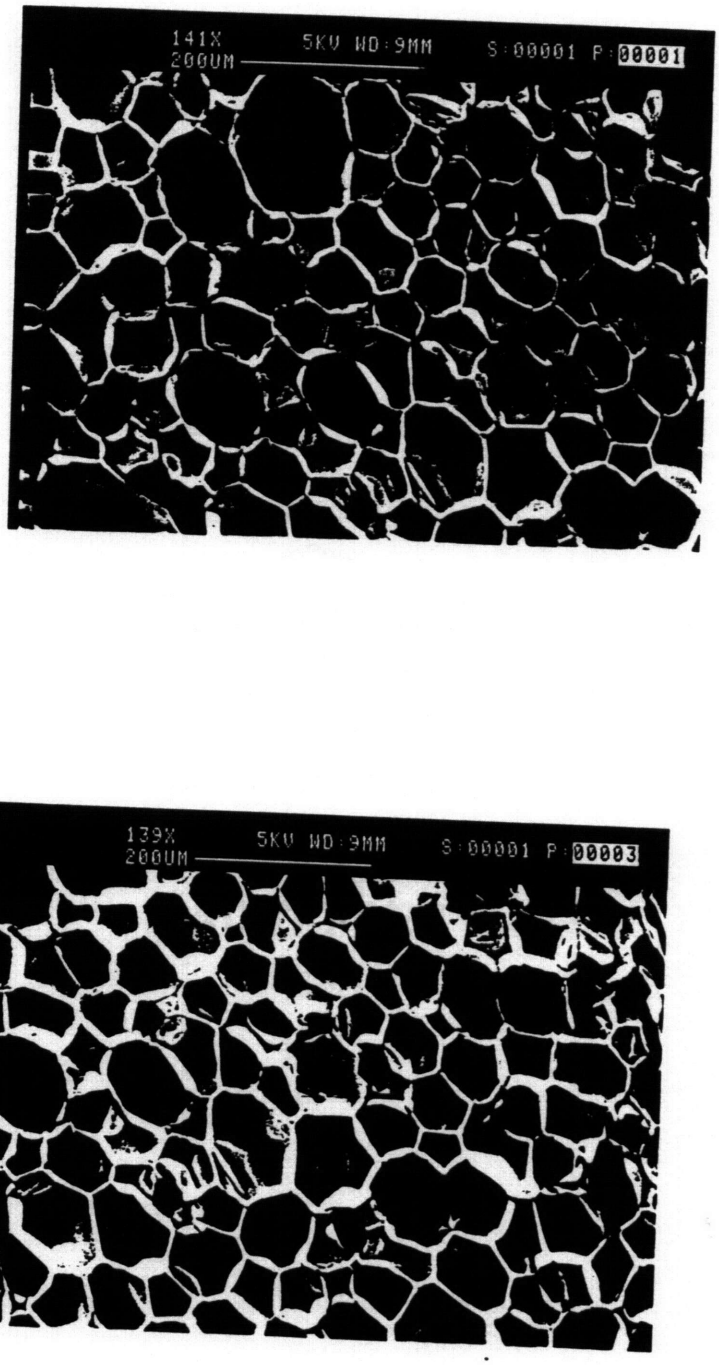

Figure G.3: *SEM Photographs of Mean Cell Diameter and Anisotropy*

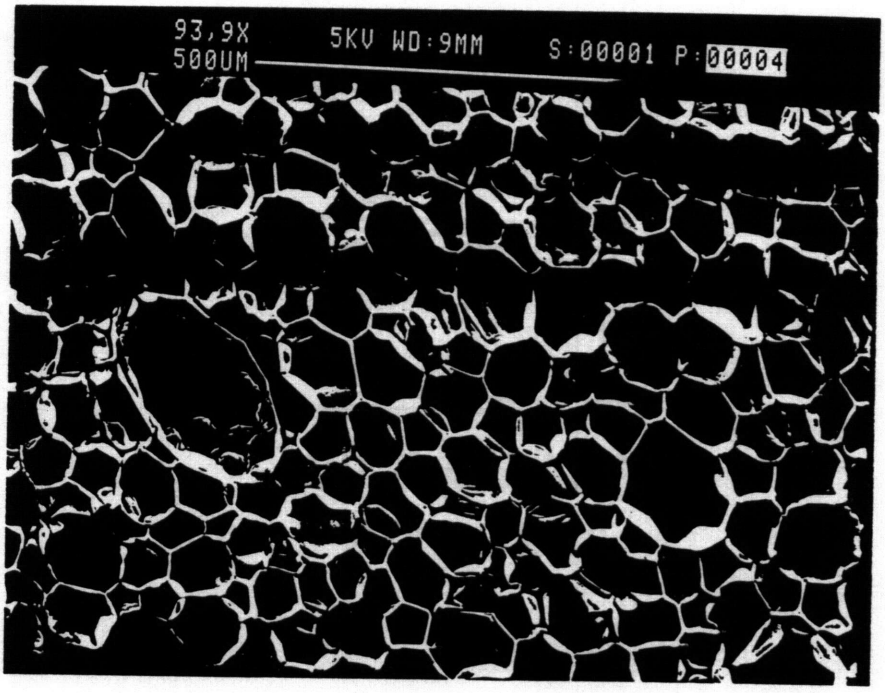

Figure G.4: *SEM Photographs of Mean Cell Diameter and Anisotropy*

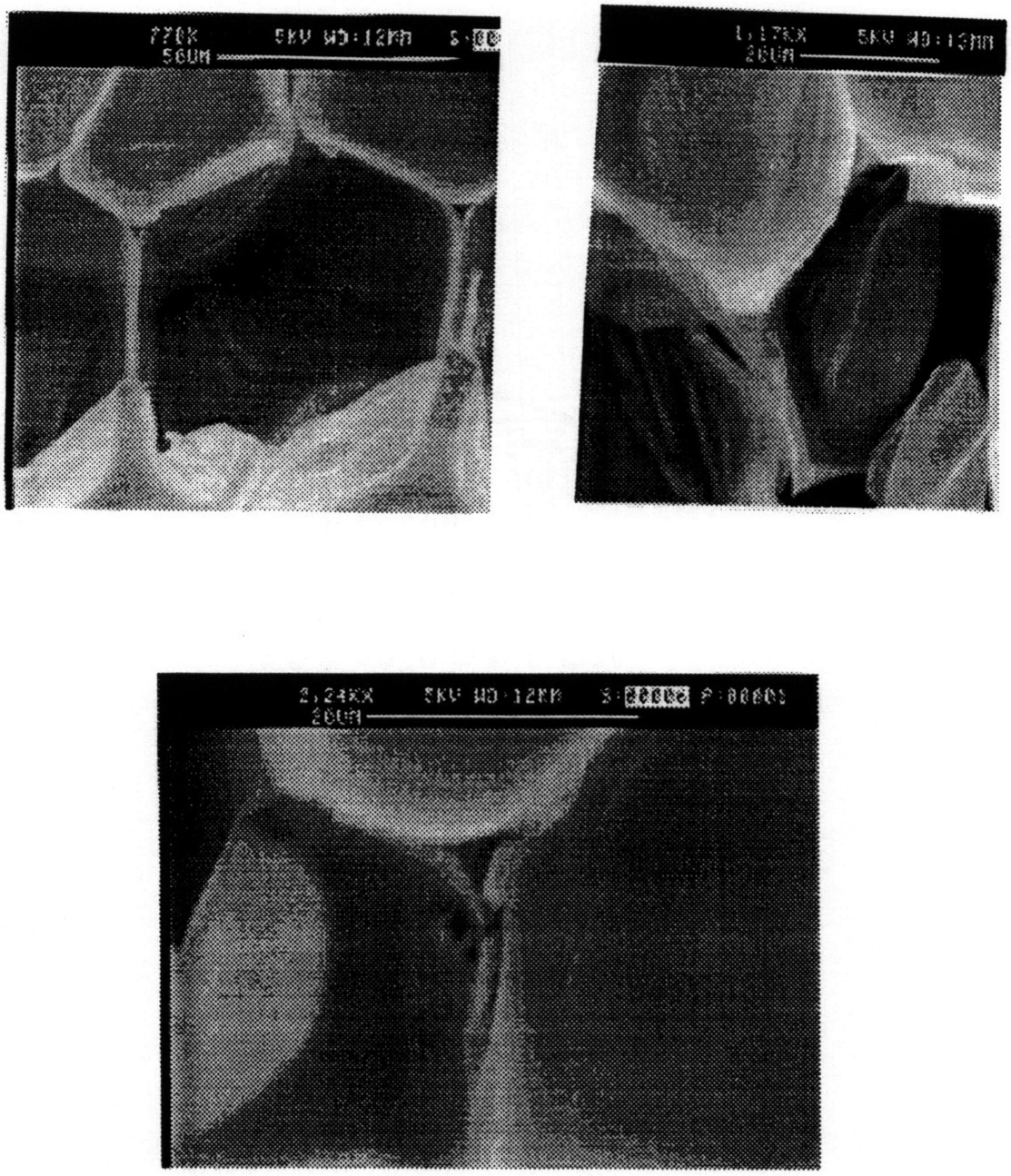

Figure G.5: *SEM Photographs of Strut Cross Sectional Areas*

Table G.1: *Cell Morphology Measurements*

image	$N_{L//}$ (mm^{-1})	$N_{L\perp}$ (mm^{-1})	S_V (mm^{-1})	mean cell diameter (mm)	anisotropy *a/b*
G.4	13.85	15.60	30.45	0.114	1.13

Table G.2: *Measured Strut Area Distribution*

strut cross sectional areas (μm^2)
18.17
13.63
12.12
16.97
21.22
17.82
15.84
10.64
15.28

Table G.3: *Parameters in Calculation of f_s from Strut Cross Sectiional Area Distribution*

mean measured area (μm^2)	ratio of maximum to mean area R	calculated strut cross sectional area (equation 4.30) (μm^2)	fraction of solid in the strut (equation 4.22)
15.74	1.35	11.98	0.34

Table G.4: *Measured Section Areas Perpendicular to Rise Direction (A_{max}=18878μm^2)*

A/A_{max}	N/A (μm^{-2})
0.9-1.0	3.896e-5
0.8-0.9	3.033e-5
0.7-0.8	1.331e-5
0.6-0.7	5.0848e-5
0.5-0.6	3.9204e-5
0.4-0.5	4.81411e-5
0.3-0.4	1.1204e-4
0.2-0.3	6.1592e-5
0.1-0.2	4.5536e-5
0.0-0.1	2.4506e-5

Foam NBE 785/206

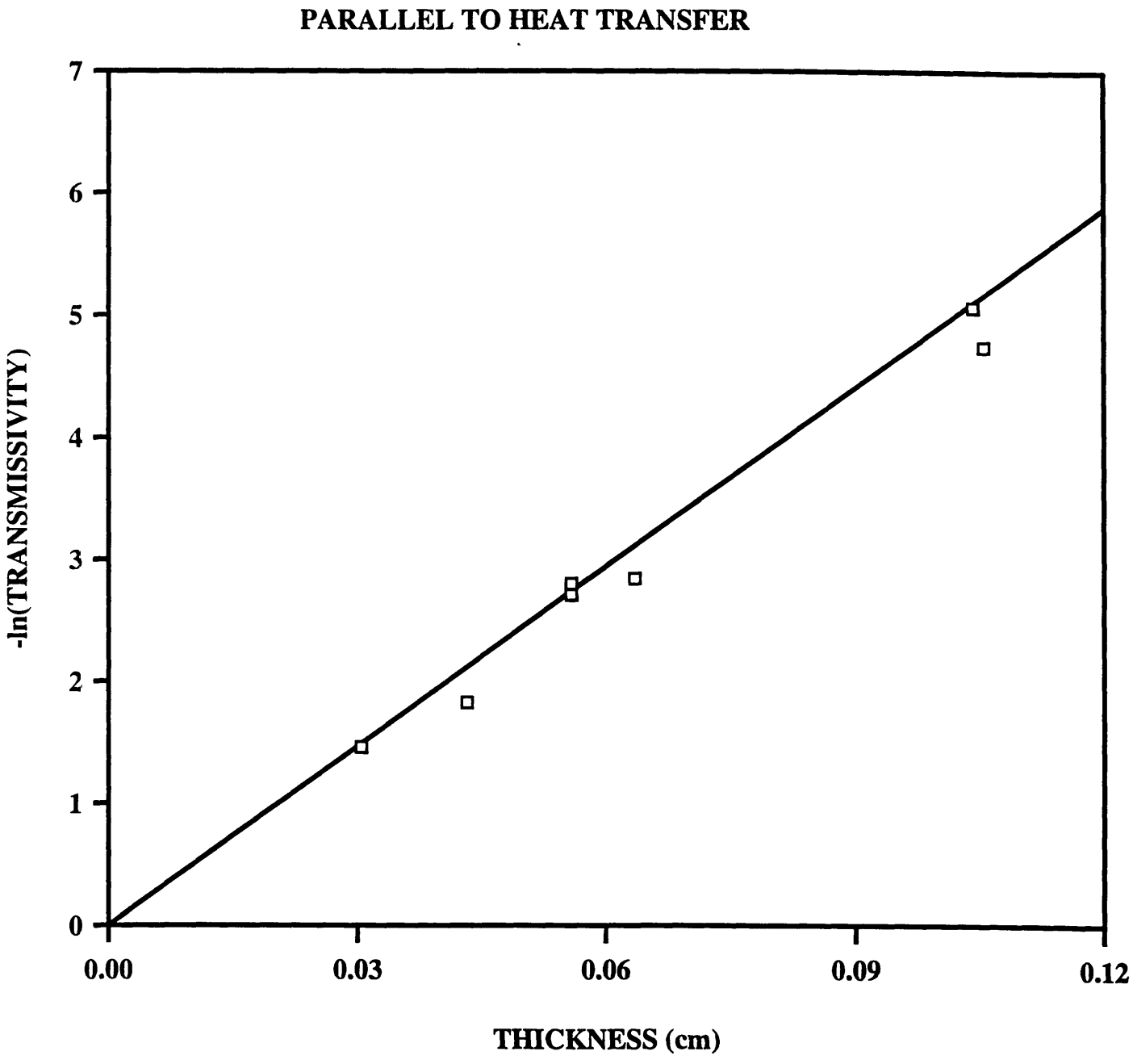

Figure G.6: *Transmission Data for Samples Tested*

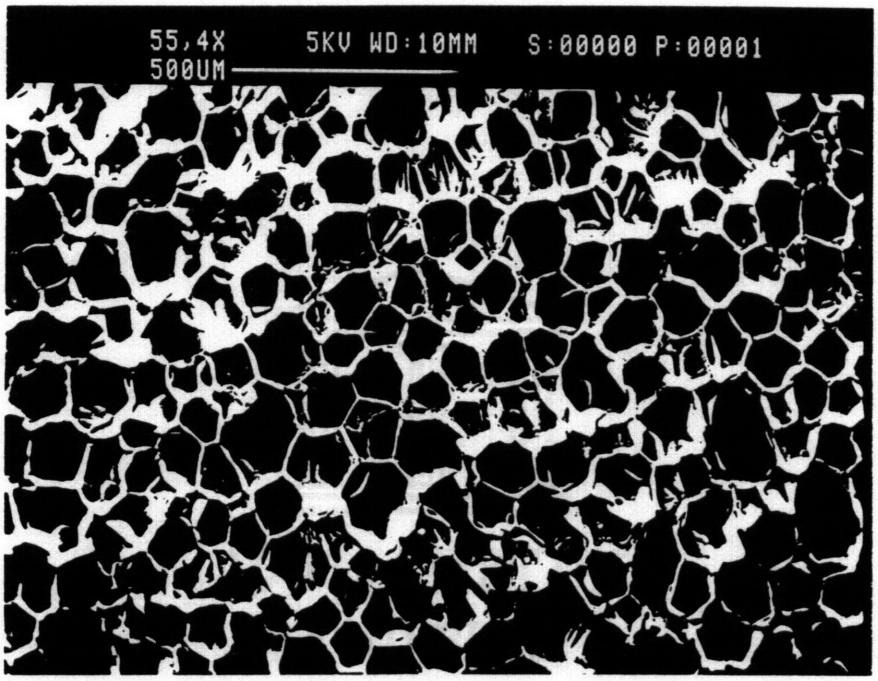

Sit 2

Figure G.7: *SEM Photographs of Mean Cell Diameter and Anisotropy*

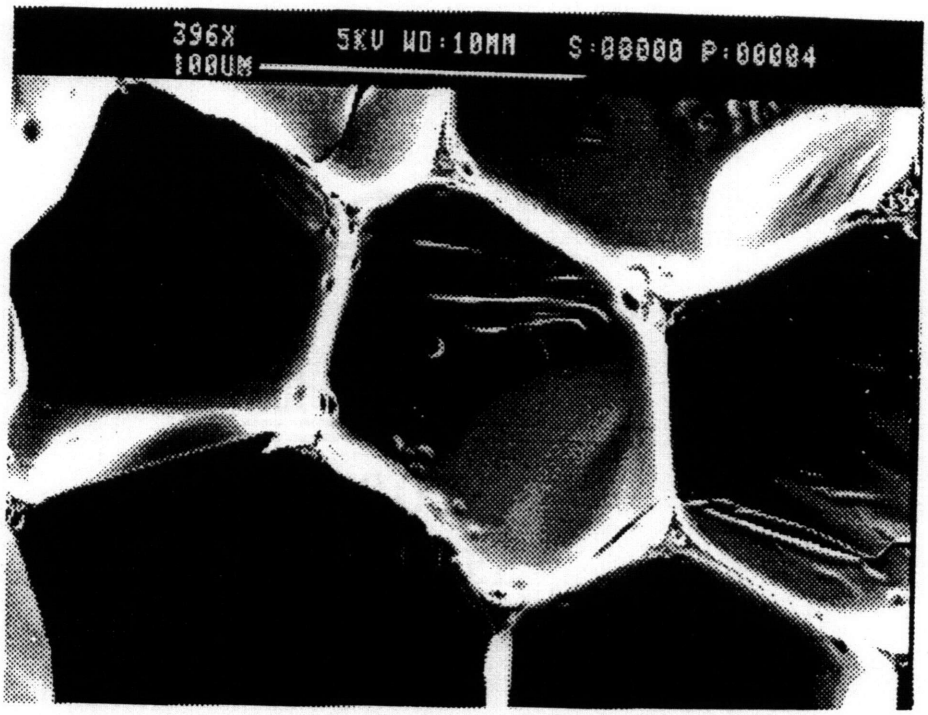

Figure G.8: *SEM Photographs of Strut Cross Sectional Areas*

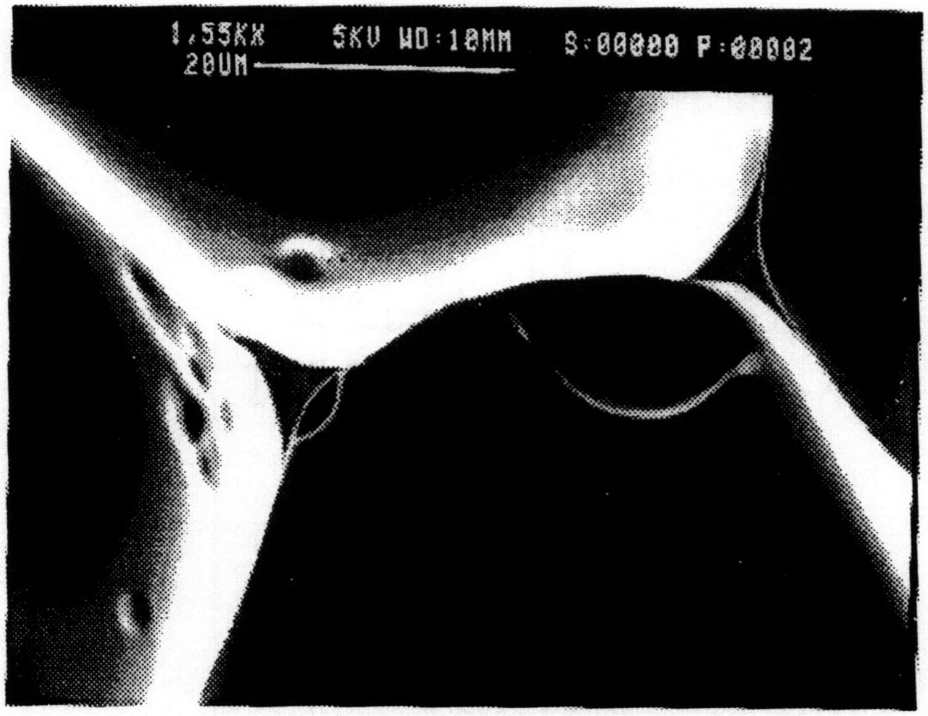

Figure G.9: *SEM Photographs of Strut Cross Sectional Areas*

Table G.5: *Cell Morphology Measurements*

image	$N_{L//}$ (mm^{-1})	$N_{L}\perp$ (mm^{-1})	S_V (mm^{-1})	mean cell diameter (mm)	anisotropy *a/b*
G.7	7.53	7.91	15.66	0.221	1.05

Table G.6: *Measured Strut Area Distribution*

strut cross sectional areas (μm^2)
117.77
81.87
124.96
71.81
68.22

Table G.7: *Parameters in Calculation of f_s from Strut Cross Sectiional Area Distribution*

mean measured area (μm^2)	ratio of maximum to mean area R	calculated strut cross sectional area (equation 4.30) (μm^2)	fraction of solid in the strut (equation 4.22)
92.93	1.34	71.17	0.65

Foam NBE 819/16/2

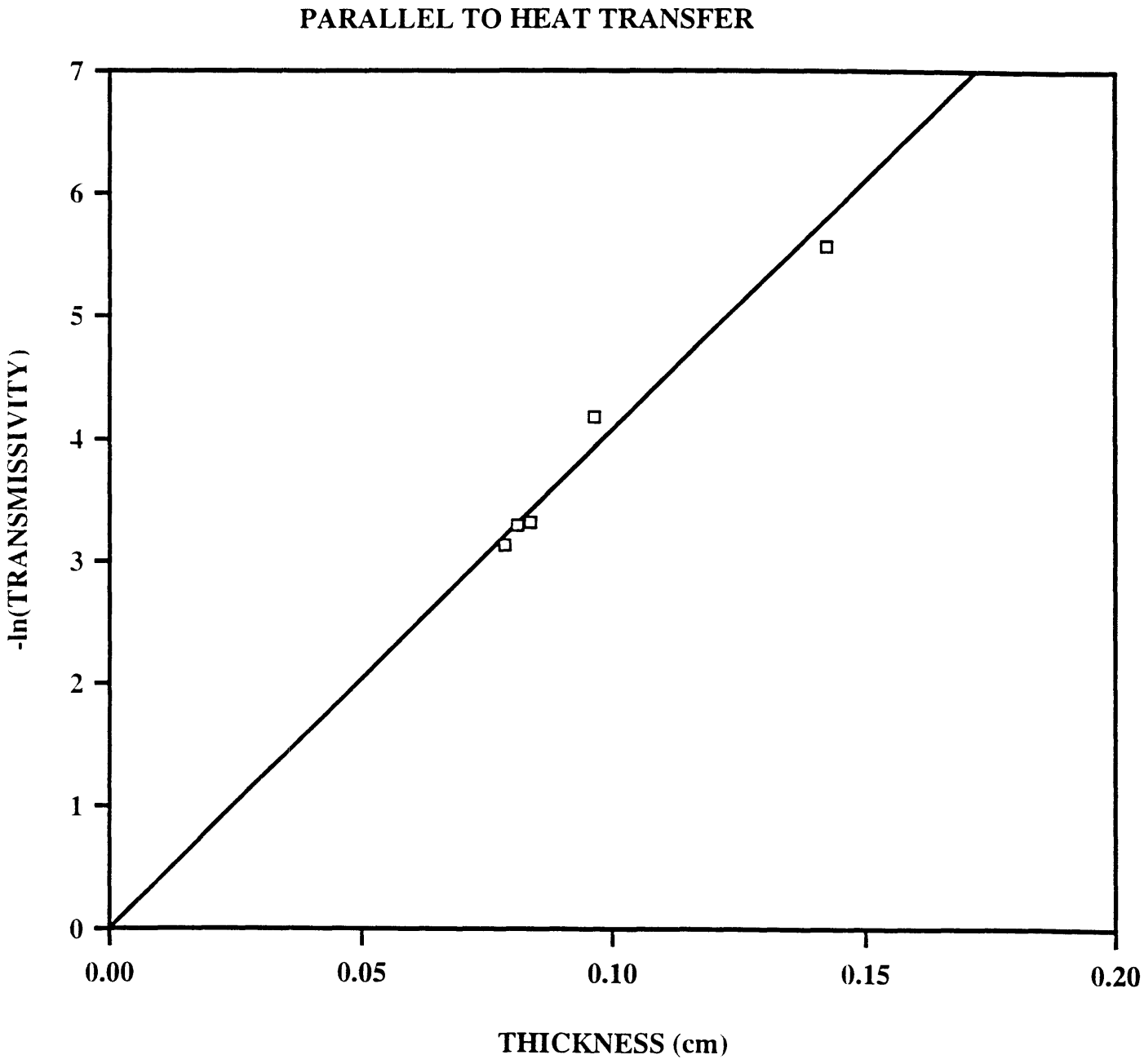

Figure G.10: *Transmission Data for Samples Tested*

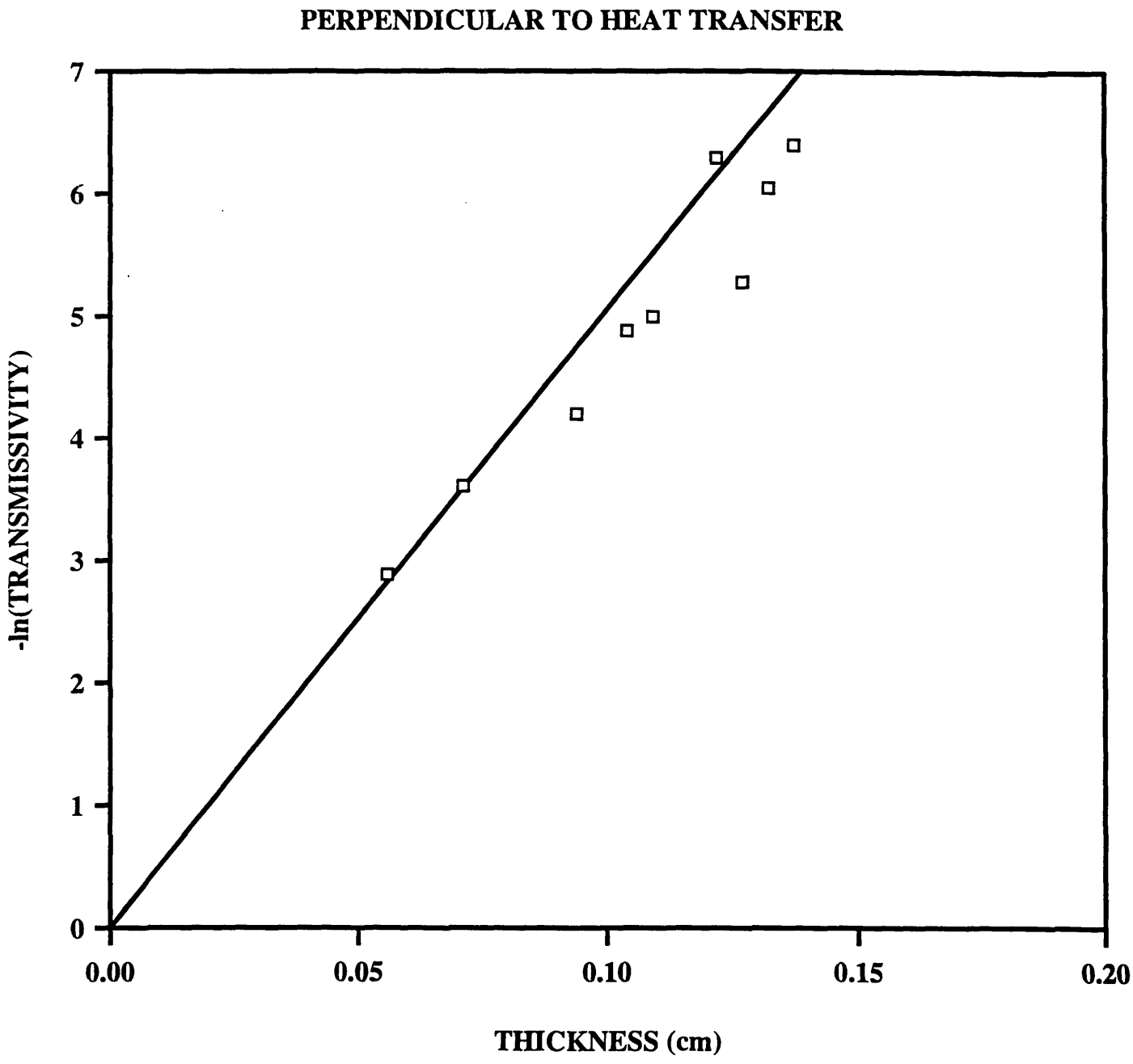

Figure G.11: *Transmission Data for Samples Tested*

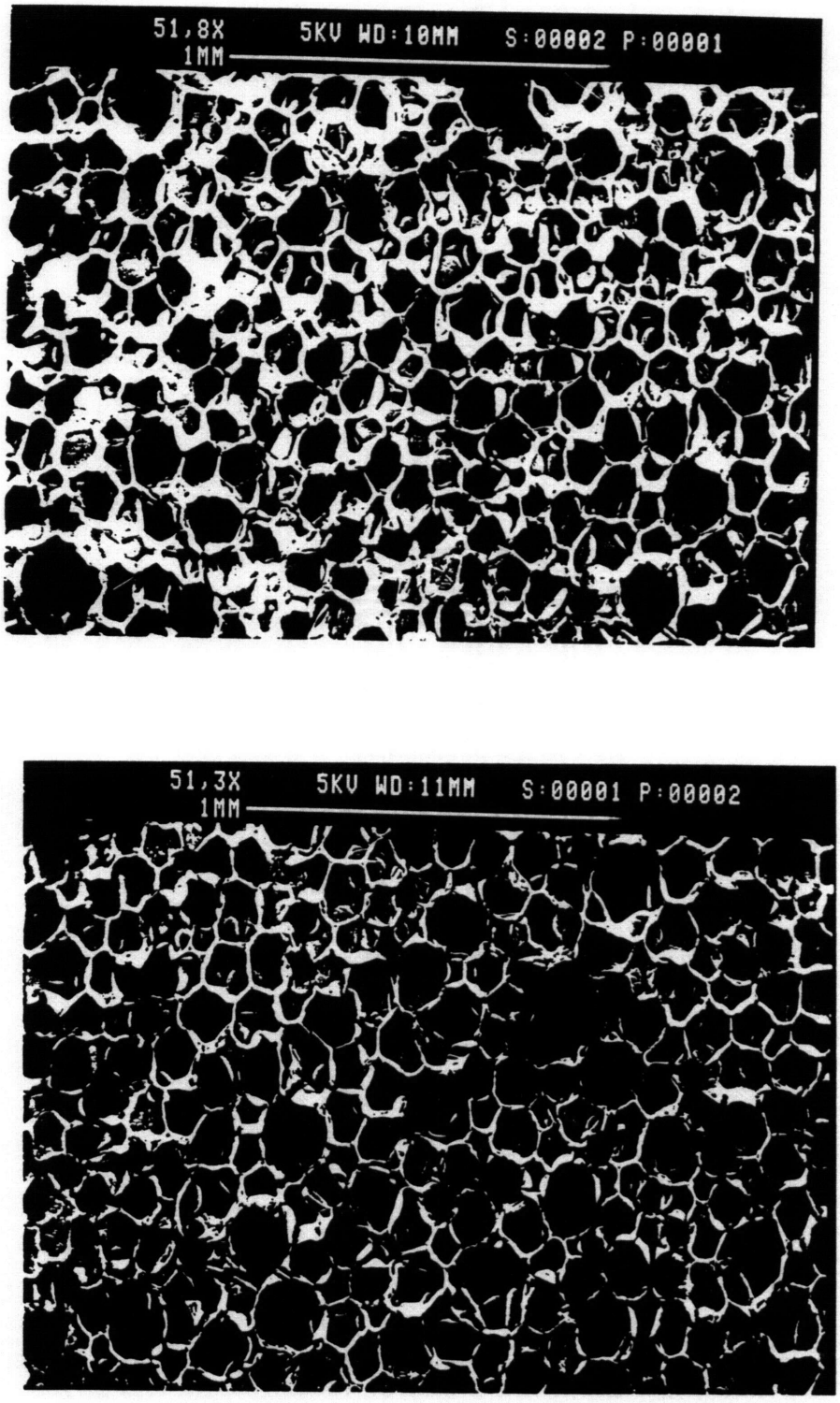

Figure G.12: *SEM Photographs of Mean Cell Diameter and Anisotropy*

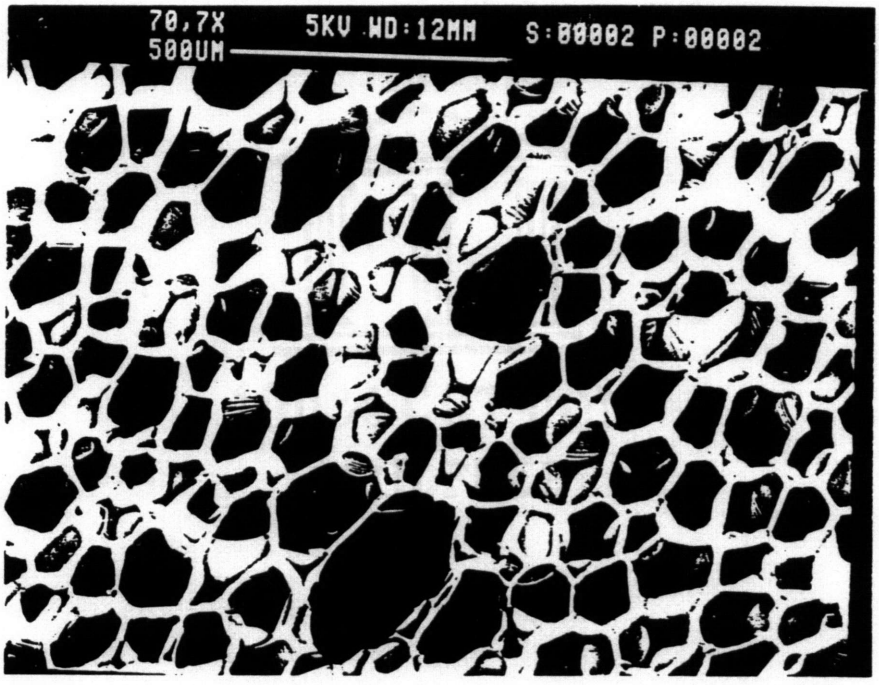

Figure G.13: *SEM Photographs of Mean Cell Diameter and Anisotropy*

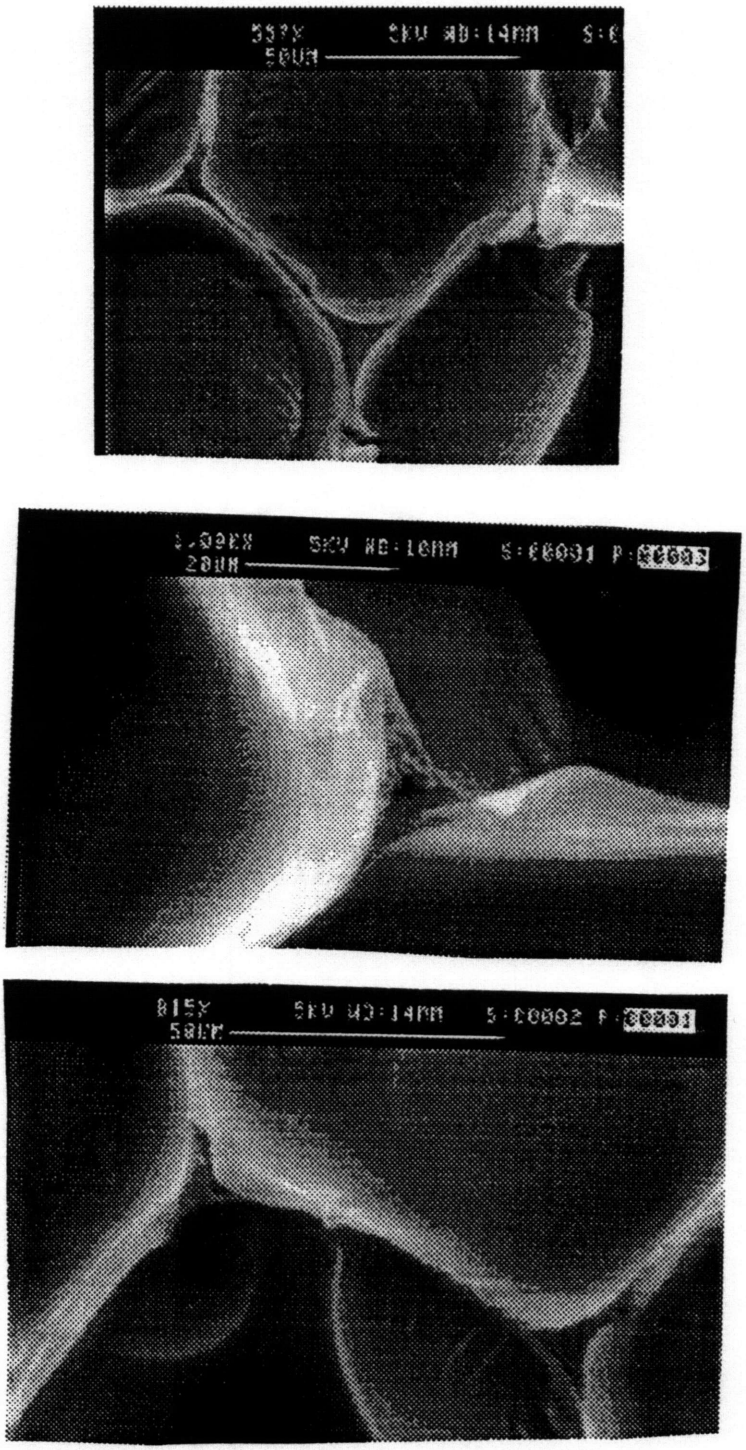

Figure G.14: *SEM Photographs of Strut Cross Sectional Areas*

There is no text material missing here.
Pages have been incorrectly numbered.

Table G.8: *Cell Morphology Measurements*

image	$N_{L//}$ (mm^{-1})	$N_L\perp$ (mm^{-1})	S_V (mm^{-1})	mean cell diameter (mm)	anisotropy *a/b*
G.13	7.48	10.70	20.02	0.173	1.43

Table G.9: *Measured Strut Area Distribution*

strut cross sectional areas (μm^2)
98.94
176.80
64.88
87.87
85.10

Table G.10: *Parameters in Calculation of f_s from Strut Cross Sectiional Area Distribution*

mean measured area (μm^2)	ratio of maximum to mean area R	calculated strut cross sectional area (equation 4.30) (μm^2)	fraction of solid in the strut (equation 4.22)
102.72	1.72	64.85	0.54

Table G.11: *Measured Section Areas Perpendicular to Rise Direction (A_{max}=0.0681mm^2)*

A/A_{max}	N/A (mm^{-2})
0.9-1.0	0.7758
0.8-0.9	1.5618
0.7-0.8	0.0
0.6-0.7	1.0946
0.5-0.6	1.5531
0.4-0.5	11.50195
0.3-0.4	32.43357
0.2-0.3	103.7919
0.1-0.2	161.4312
0.0-0.1	46.70818

Foam NBE 819/16/1

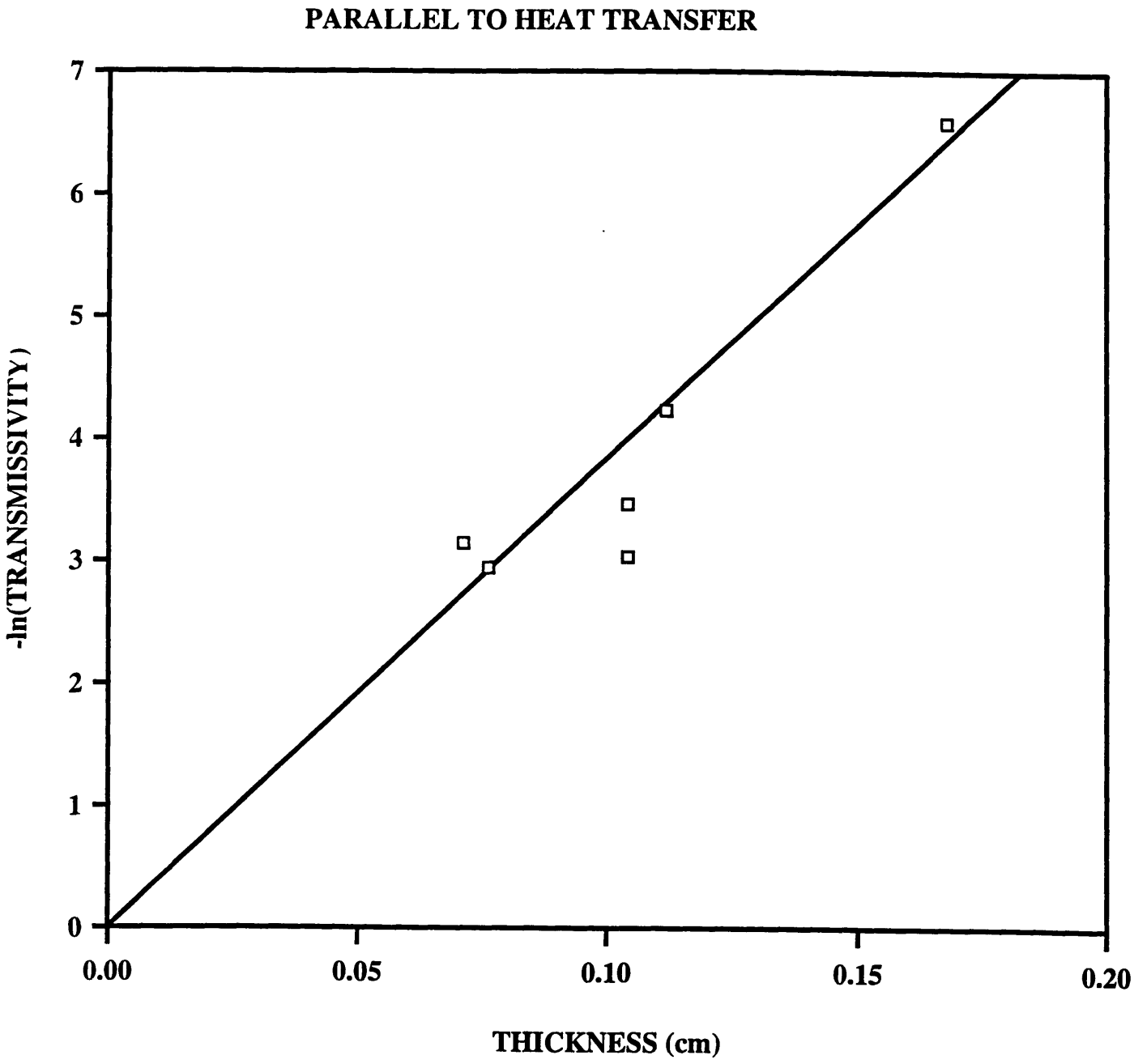

Figure G.16: *Transmission Data for Samples Tested*

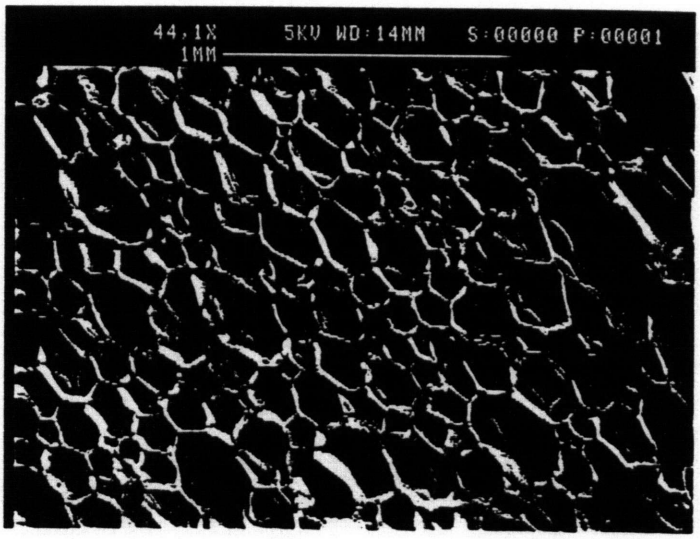

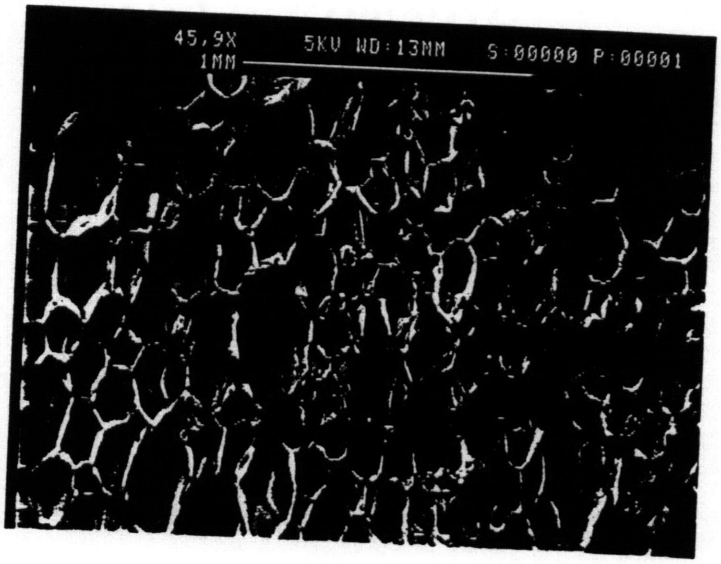

#1

Figure G.17: *SEM Photographs of Mean Cell Diameter and Anisotropy*

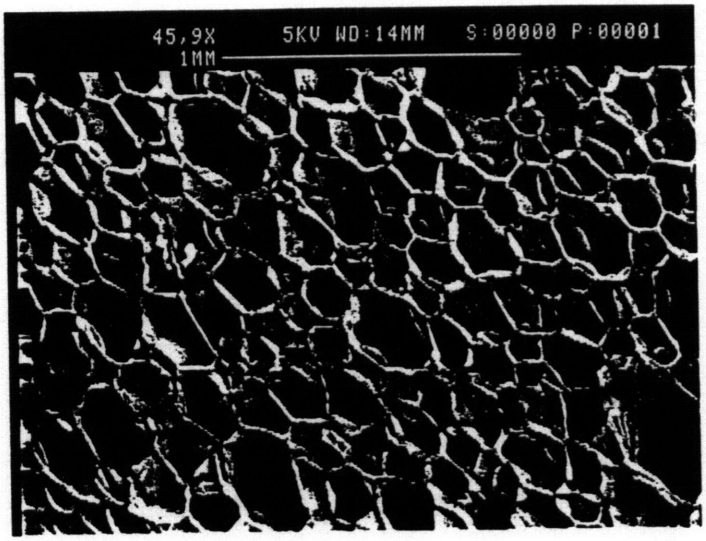

#2

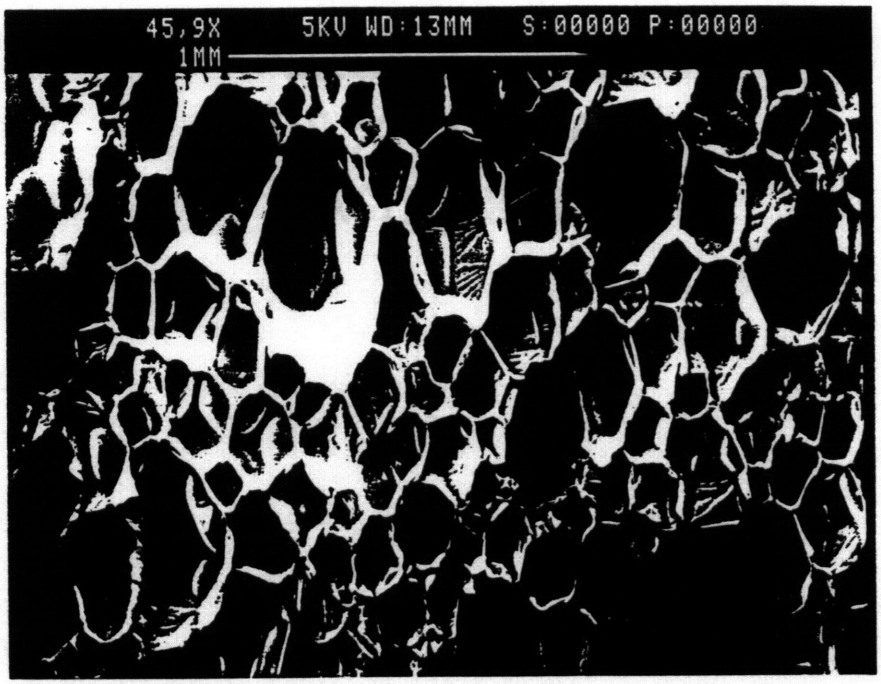

Figure G.18: *SEM Photographs of Mean Cell Diameter and Anisotropy*

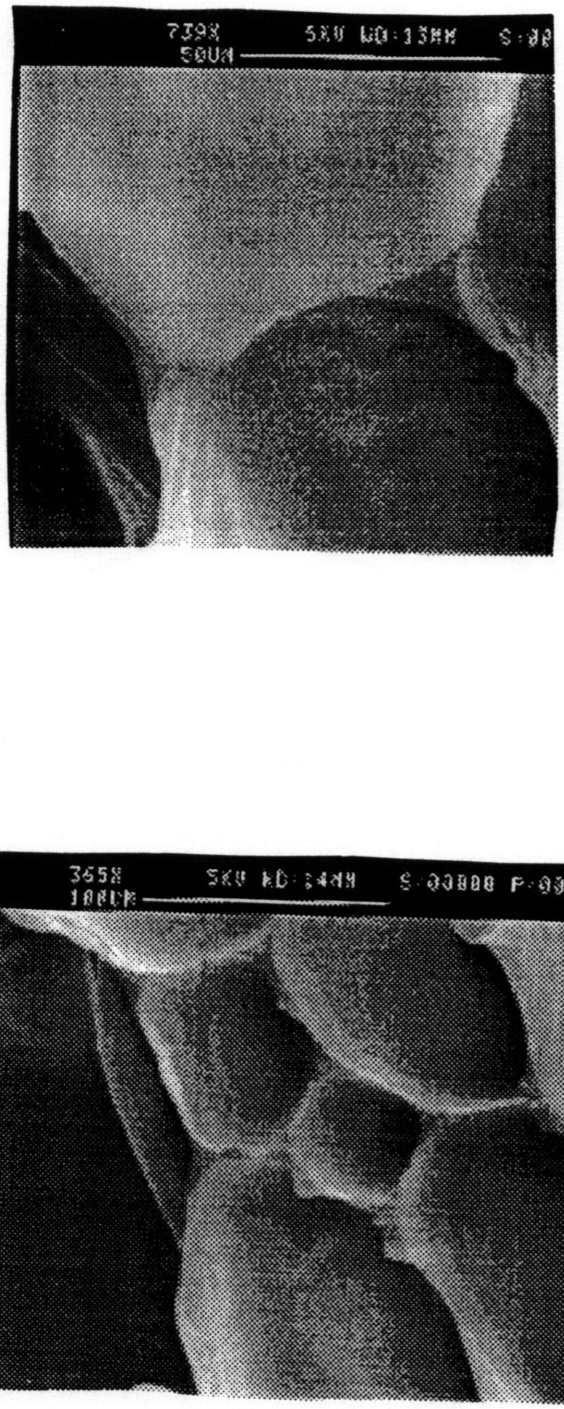

Figure G.19: *SEM Photographs of Strut Cross Sectional Areas*

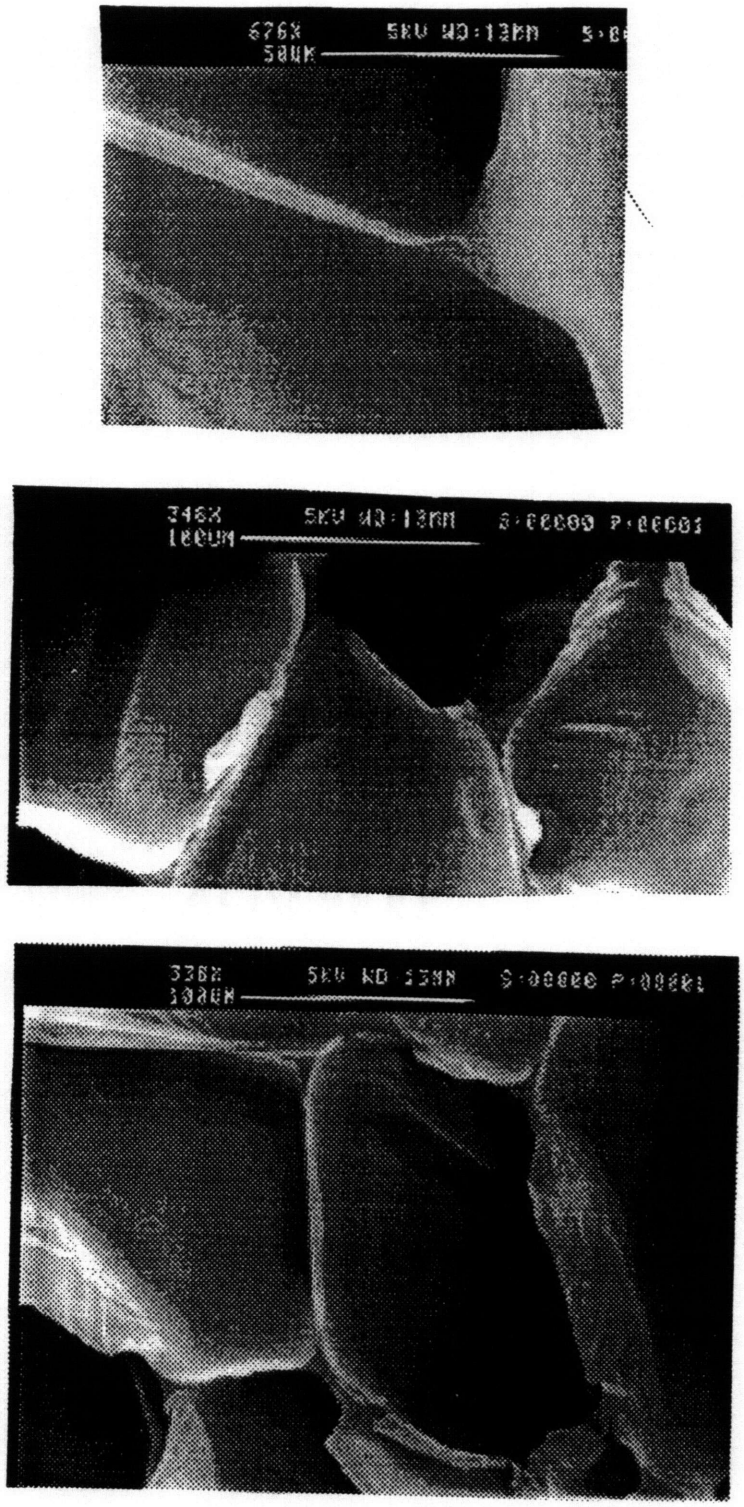

Figure G.20: *SEM Photographs of Strut Cross Sectional Areas*

Table G.12: *Cell Morphology Measurements*

image	$N_{L//}$ (mm^{-1})	$N_L\perp$ (mm^{-1})	S_V (mm^{-1})	mean cell diameter (mm)	anisotropy *a/b*
G.18(b)	5.94	7.82	14.83	0.233	1.32

Table G.13: *Measured Strut Area Distribution*

strut cross sectional areas (μm^2)
144.13
142.90
203.72
181.41
150.19
205.20
207.50
153.94
136.28
146.37
97.16
112.30
191.80
194.32
139.77
160.53

Table G.14: *Parameters in Calculation of f_s from Strut Cross Sectiional Area Distribution*

mean measured area (μm^2)	ratio of maximum to mean area R	calculated strut cross sectional area (equation 4.30) (μm^2)	fraction of solid in the strut (equation 4.22)
168.70	1.23	139.0	0.77

Foam NBE 863/13/1

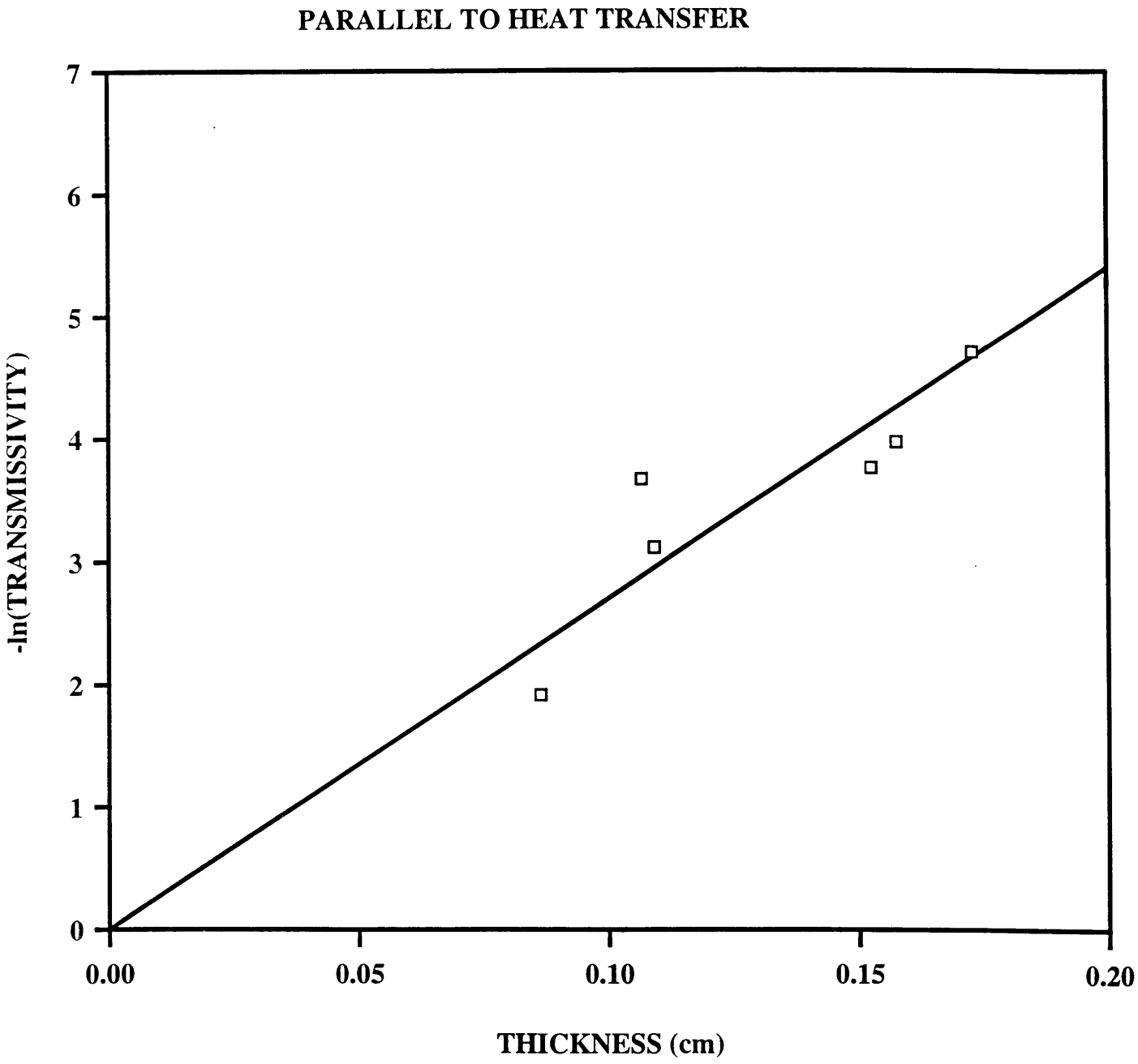

Figure G.21: *Transmission Data for Samples Tested*

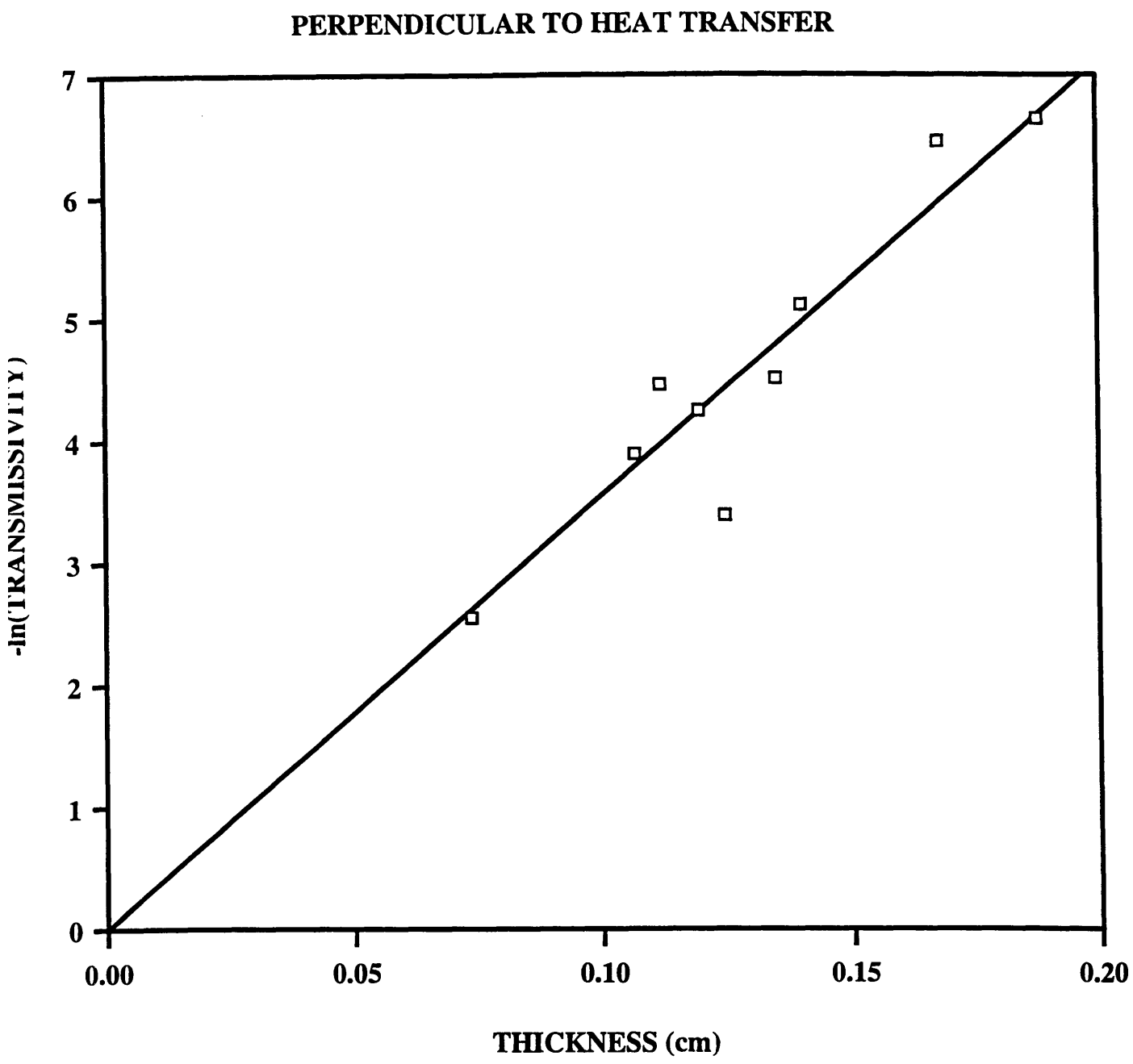

Figure G.22: *Transmission Data for Samples Tested*

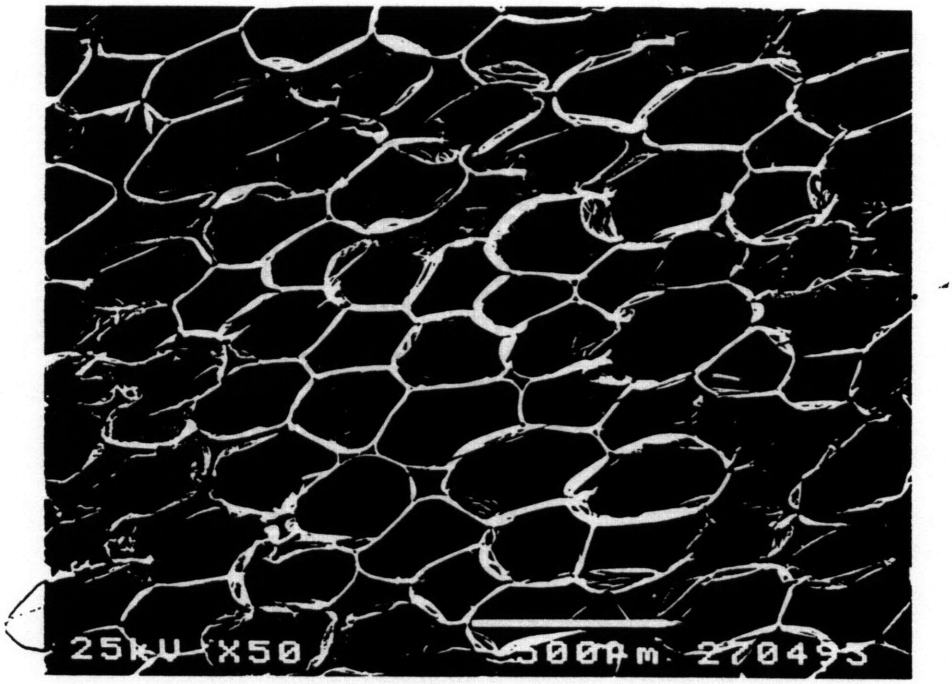

Figure G.23: *SEM Photographs of Mean Cell Diameter and Anisotropy*

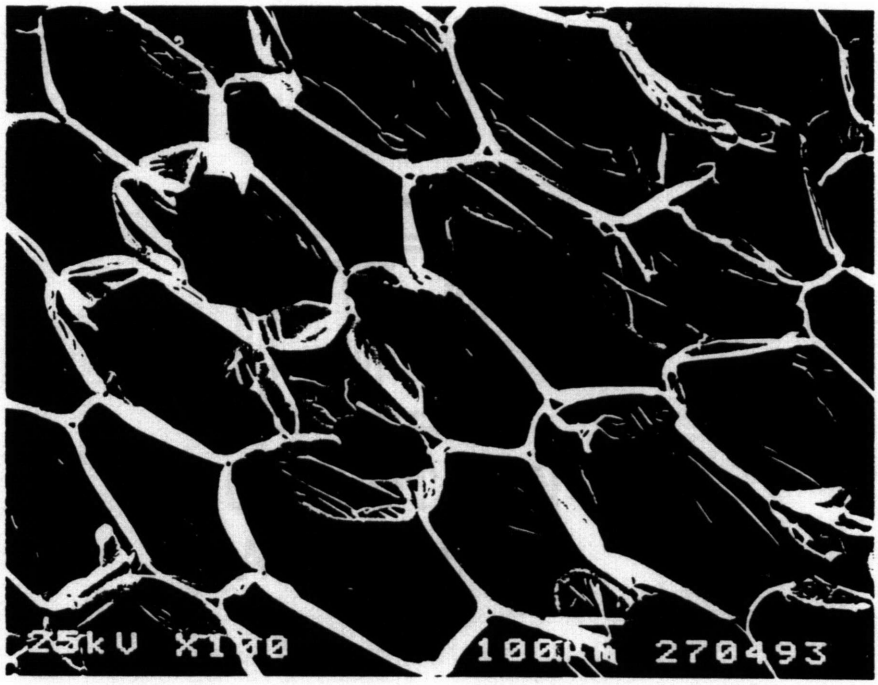

Figure G.24: *SEM Photographs of Mean Cell Diameter and Anisotropy*

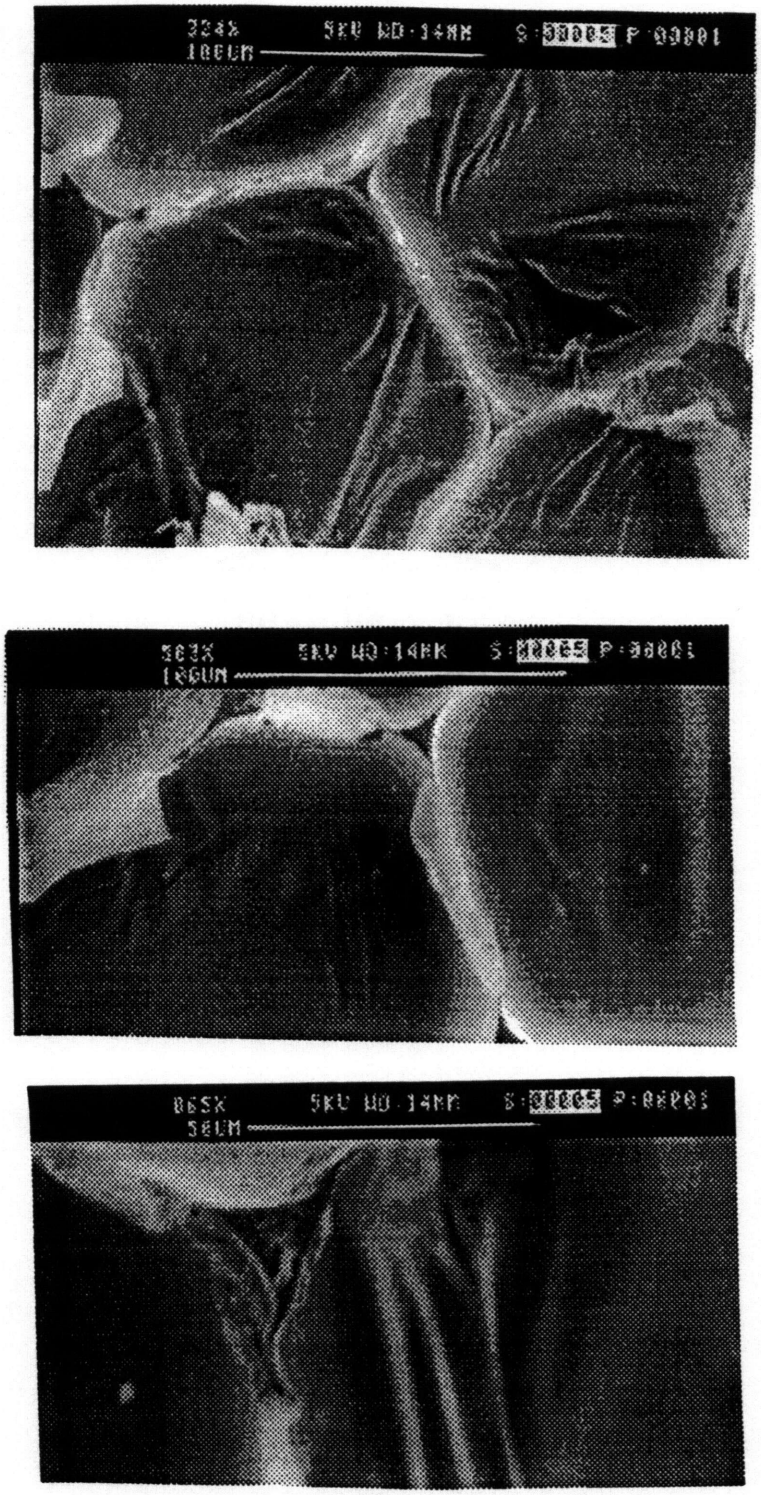

Figure G.25: *SEM Photographs of Strut Cross Sectional Areas*

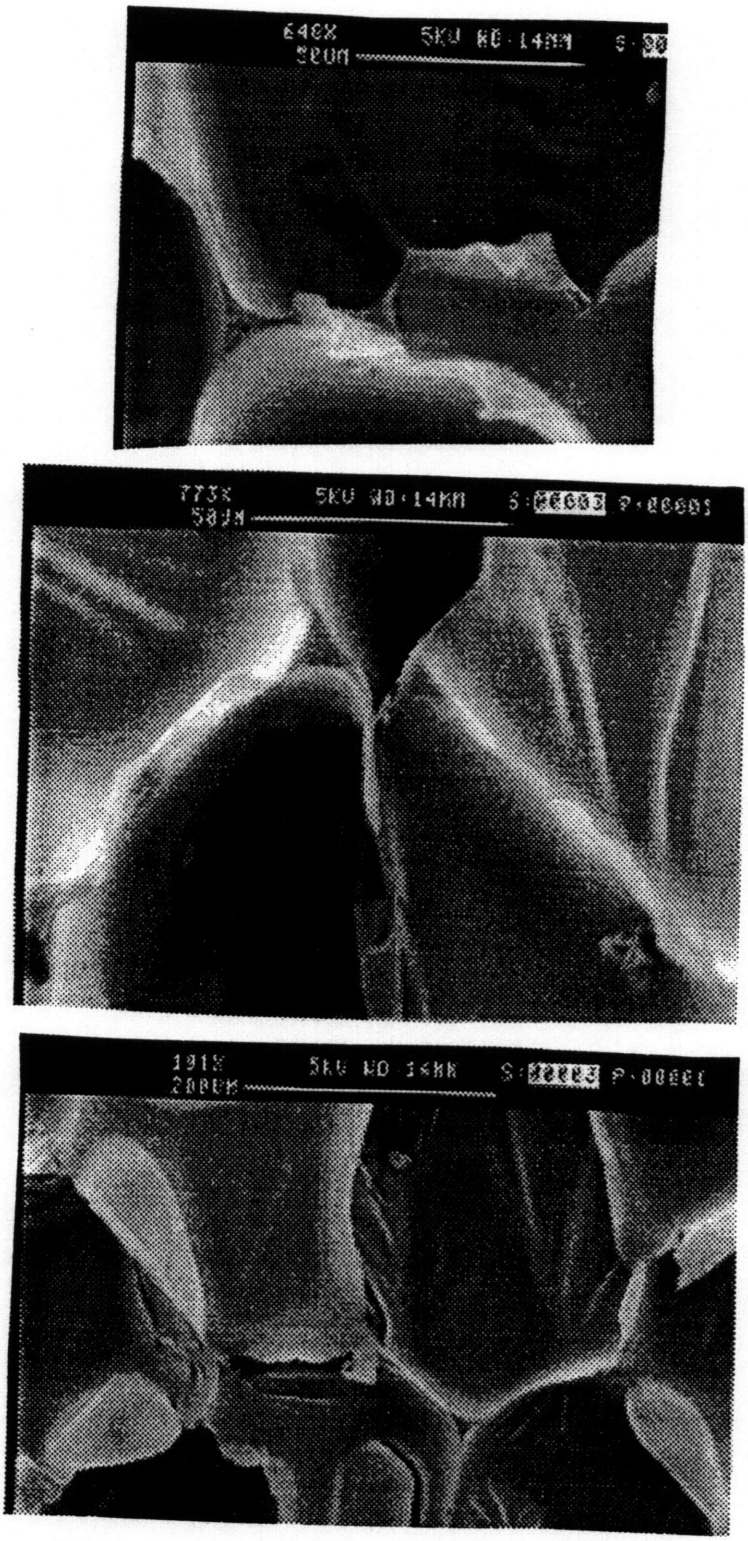

Figure G.26: *SEM Photographs of Strut Cross Sectional Areas*

Table G.15: *Cell Morphology Measurements*

image	$N_{L//}$ (mm^{-1})	$N_{L\perp}$ (mm^{-1})	S_V (mm^{-1})	mean cell diameter (mm)	anisotropy *a/b*
G.24	3.75	6.76	12.20	0.283	1.80

Table G.16: *Measured Strut Area Distribution*

strut cross sectional areas (μm^2)
84.63
104.11
129.77
225.89
169.82
253.23
221.16
133.11
88.74
221.85
108.10
65.13

Table G.17: *Parameters in Calculation of f_s from Strut Cross Sectiional Area Distribution*

mean measured area (μm^2)	ratio of maximum to mean area R	calculated strut cross sectional area (equation 4.30) (μm^2)	fraction of solid in the strut (equation 4.22)
150.46	1.68	96.67	0.36

Table G.18: *Measured Section Areas Perpendicular to Rise Direction (A_{max}=79271.1μm^2)*

A/A_{max}	N/A (μm^{-2})
0.9-1.0	4.2456e-7
0.8-0.9	4.2456e-7
0.7-0.8	2.1228e-6
0.6-0.7	2.1228e-6
0.5-0.6	5.51928e-6
0.4-0.5	4.67016e-6
0.3-0.4	5.51928e-6
0.2-0.3	3.39648e-6
0.1-0.2	5.51928e-6
0.0-0.1	5.51928e-6

Foam NBE 785/204

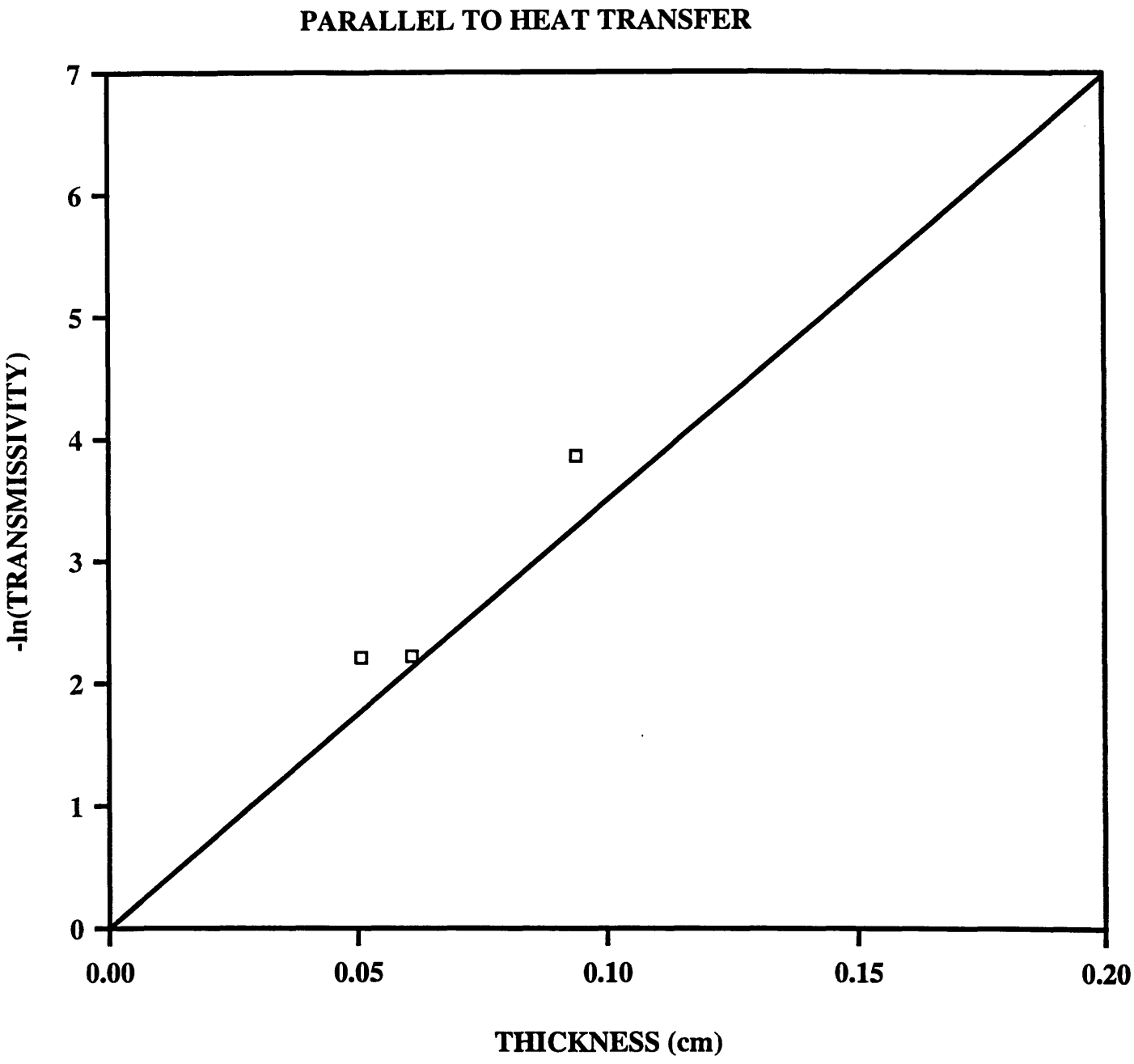

Figure G.27: *Transmission Data for Samples Tested*

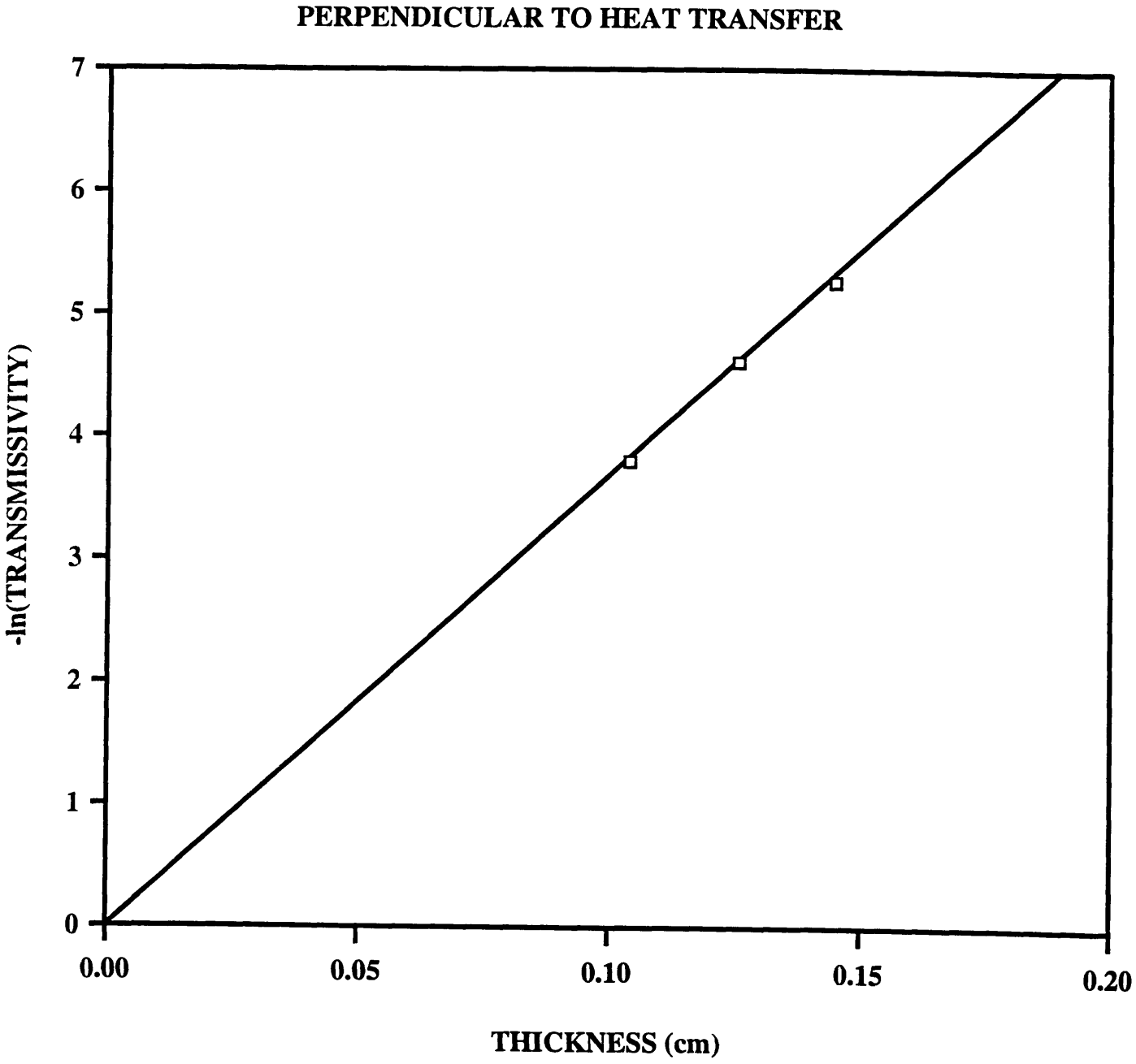

Figure G.28: *Transmission Data for Samples Tested*

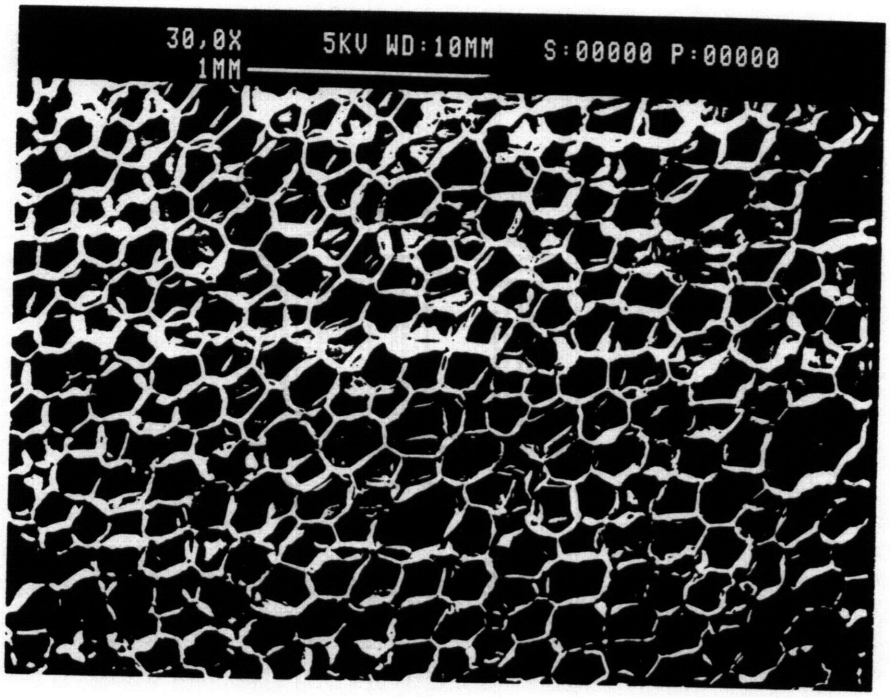

Figure G.29: *SEM Photographs of Mean Cell Diameter and Anisotropy*

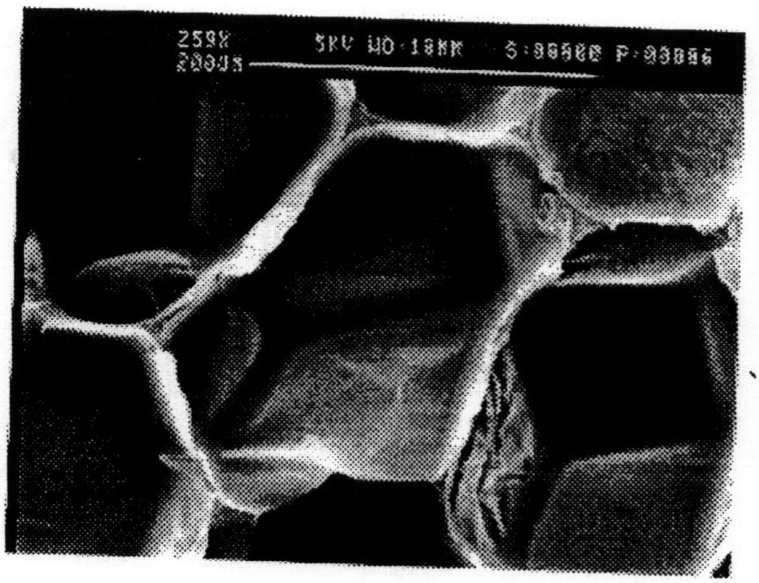

Figure G.30: *SEM Photographs of Strut Cross Sectional Areas*

Table G.19: *Cell Morphology Measurements*

image	$N_{L//}$ (mm^{-1})	$N_{L\perp}$ (mm^{-1})	S_V (mm^{-1})	mean cell diameter (mm)	anisotropy *a/b*
G.29	4.47	5.58	10.68	0.324	1.25

Table G.20: *Measured Strut Area Distribution*

strut cross sectional areas (μm^2)
237.04
326.54
314.44
241.88

Table G.21: *Parameters in Calculation of f_s from Strut Cross Sectiional Area Distribution*

mean measured area (μm^2)	ratio of maximum to mean area R	calculated strut cross sectional area (equation 4.30) (μm^2)	fraction of solid in the strut (equation 4.22)
279.98	1.17	241.92	0.67

Appendix H Mie Analysis of Extinction Coefficient

The extinction efficiency, considered unity in the present analysis of extinction coefficient, was examined in closer detail. There were two motivations for studying this parameter more closely.

The first motivation is the discrepancy between measured and predicted extinction coefficients seen in figure 4.20. That is, if the extinction efficiency is greater than unity, the possibility exists that neglecting this parameter in the predictions of extinction coefficients from morphology underpredicts the actual extinction coefficient. If the extinction efficiency is anything other than unity, the expression 2.50 is

$$K = \frac{4.1\sqrt{fs\rho_f/\rho_s}}{d}Q + \frac{(1-f_s)\rho_f}{\rho_s}K_w \tag{H.1}$$

The second motivation is the possibility of the extinction efficiency being much lower than unity which would indicate a much higher radiative conductivity than predicted by theory. That is, consider the strut diameters of the foams analyzed. The struts will be considered circular cylinders so that theoretical analysis of extinction efficiency can be carried out (there is no known theoretical model of the interaction of electromagnetic waves with cylinders of triangular cross section). Since the true cross sectional areas of the struts are closer to triangular shape rather than circular, this analysis is not strictly true and future work should consider the influence of the actual triangular cross section of the struts on this analysis. The strut diameters can be related to the measured strut cross sectional areas measured in Appendix G

$$d = \sqrt{\frac{4}{\pi}A_{xs}} \tag{H.2}$$

For the smallest celled foam NBE 678/21/47 this translates to a diameter of 3.9μm. A

rough estimate of the optical thickness of this foam yields $t_2=K_w d=0.13$. It is therefore questionable (see Section 2.8) whether struts of this size can be treated as opaque. For nonopaque bodies, the extinction efficiency Q is not likely to be unity. Analysis of this parameter then requires the exact interaction of such particles with electromagnetic waves.

For particles of size on the order of the wavelength of the electromagnetic radiation, a detailed description of the interaction with electromagnetic radiation is given by the Mie Scattering Theory which is decribed in detail in [41]. The concern from Mie theory is that at very small strut diameter, the extinction efficiency approaches zero which would indicate that a decrease in cell size is accompanied by an increase in the radiative flux. Kuhn et al [33] report such a trend with polystyrene foams at strut diameters smaller than 4μm. It was therefore important to see whether the efficiency factors for the small celled polyurethane foams were much smaller than unity and approaching zero.

As can be seen in the derivation of Mie analysis [41], calculation of the extinction efficiency is a very complex analysis for a single particle, let alone for a collection of randomly oriented particles. A code developed at Owens Corning does however determine the extinction efficiency and resulting radiative conductivity for a collection of randomly oriented struts based on Mie Scattering Theory[42] . So calculations from this code were obtained for struts ranging in diameter from 3μm to 20μm.

The necessary input for the Owens Corning calculations is the complex index of refraction of polyurethane. The complex index of refraction can be calculated from reflection and transmission measurements of solid polyurethane [16]. This parameter was therefore calculated from reflection data obtained by Torpey [16] and from the transmission data described in Section 4.2. The calculated complex index of refraction used with the Owens Corning Mie analysis is listed as a function of wavenumber at the end of the appendix.

Using the complex index of refraction, the extinction efficiency of foams of different diameters were calculated at Owens Corning. The results are shown in Table H.1 where

the strut diameters, the extinction efficiencies Q, the radiative conductivity calculated from the exact electromagnetic interaction [41], and the radiative conductivity calculated from the theory with an extinction efficiency of unity are listed. The theoretical prediction for struts of circular cross section is developed by Torpey [16] and given by

$$k_{rad} = \frac{16}{3}\left(\frac{\rho_s}{\rho_f}\right)\sigma T^3 D \tag{H.2}$$

where for the Owens Corning calculations the solid density ρ_s is 62.4 pcf, the foam density ρ_f is 0.55 pcf, the temperature T is 300K, and the strut diameter D is varied.

strut diameter (μm)	extinction efficiency	radiative conductivity predicted by Mie Theory (Btu in/ft^{2}F)	radiative conductivity predicted by equation H.2 (Btu in/ft^{2}F)
3.05	1.459	0.0286	0.0196
4.06	1.225	0.0319	0.0260
5.08	1.111	0.0362	0.0326
6.10	1.012	0.0397	0.0392
7.11	0.957	0.0437	0.0457
8.13	0.9373	0.0490	0.0523
9.14	0.9398	0.0550	0.0585
10.16	0.9406	0.0614	0.0653
12.19	0.9520	0.0745	0.0783
14.22	0.9710	0.0887	0.0913
16.26	0.9890	0.1033	0.1044
18.29	1.003	0.1178	0.1174
20.32	1.013	0.1322	0.1305

Table H.1: *Extinction Efficiencies of Struts Calculated by Mie Theory*

Notice that the extinction efficiencies have not begun to approach zero, but are instead increasing. This would indicate lower radiative flux at smaller cell sizes than predicted from equation 2.50 until the extinction efficiency begins to decrease and approach zero at some smaller strut diameter.

How this would affect the six small celled foams was next considered. That is, the extinction coefficients calculated from the morphology characteristics and equation H.1 were compared to the extinction coefficients calculated without regards to extinction efficiency and from the transmisison measurements. These results are listed in Table H.2 where the extinction efficiencies for the foams are linearly interpolated from the strut ranges of Table H.1.

foam	A_{xs} (μm^2)	strut diameter (μm)	Q	K (Q=1) (cm^{-1})	K measured (cm^{-1})	K (Q from Mie Theory) (cm^{-1})
NBE 678/21/47	11.98	3.90	1.262	40.9	61.0	50.3
NBE 785/206	71.17	9.52	0.940	31.8	49.0	30.1
NBE 819/16/2	64.85	9.09	0.9397	30.6	40.7	29.1
NBE 819/16/1	139.0	13.30	0.9620	27.8	38.4	26.9
NBE 863/13/1	96.67	11.09	0.9460	20.9	27.0	20.2
NBE 785/204	241.92	17.55	0.998	16.8	34.9	16.8

Table H.2: *Extinction Efficiency Influence on Predicted Extinction Coefficient*

Two results can be seen in Table H.2. The addition of extinction efficiency to theory does not account for the discrepancy between extinction coefficients measured from

spectrometer data and those predicted from morphology. Further investigation is needed into the cause of this discrepancy. Also radiative flux at these lower cell sizes which is inversely related to the extinction coefficient has not been underpredicted by theory if one assumes opaque struts, but has actually been overpredicted. It appears that the extinction efficiency should be incorporated into further analysis of small celled foams because even though the radiative flux has not been underpredicted, the extinction efficiency does begin to differ greatly from unity.

wavenumber (cm^{-1})	real part of complex index of refraction	imaginary part of complex index of refraction
300.99	2.56476	0
304.85	2.52626	0
308.71	2.50291	0
312.56	2.51554	0
316.42	2.55003	0
320.28	2.63095	0
324.14	2.71406	0
328	2.65727	0
331.86	2.48505	0
335.72	2.46284	0
339.58	2.45515	0
343.43	2.39397	0
347.29	2.34759	0
351.15	2.33385	0
355.01	2.4419	0
358.87	2.40286	0

Table H.3: *Complex Index of Refraction Used with Mie Scattering Code*

wavenumber (cm^{-1})	real part of complex index of refraction	imaginary part of complex index of refraction
362.73	2.28268	0
366.59	2.32862	0
370.45	2.38385	0
374.31	2.40024	0
378.16	2.37843	0
382.02	2.35252	0
385.53	2.3681	0
389.74	2.35151	0
393.6	2.31832	0
397.46	2.269	0
401.32	2.27825	0
409.03	2.28888	0
416.75	2.25558	0
420.81	2.21759	0
424.47	2.22563	0
428.33	2.34426	0
432.19	2.34858	0
436.05	2.22585	0
439.91	2.22266	0
443.76	2.16439	0
447.52	2.08796	0
451.48	2.09436	0
455.34	2.11698	0
459.2	2.11821	0
463.06	2.11664	0
466.92	2.06055	0

Table H.3: *Complex Index of Refraction Used with Mie Scattering Code*

wavenumber (cm^{-1})	real part of complex index of refraction	imaginary part of complex index of refraction
470.78	2.04092	0
474.63	2.09754	0
478.49	2.09768	0
482.35	2.11005	0
486.21	2.14564	0
490.07	2.15247	0
493.93	2.11225	0
497.79	2.10353	0
501.65	2.11444	0
505.51	2.13099	0
509.36	2.10735	0
513.22	2.08724	0
524.8	1.98982	0
528.66	2.01213	0
532.52	1.98475	0
536.38	1.99505	0
540.23	2.03055	0
544.09	1.99374	0
547.05	1.96325	0
551.81	1.95239	0
555.67	1.97181	0
559.53	2.00632	0
563.39	1.98574	0
567.25	1.95142	0
571.11	1.92327	0
574.96	1.90924	0

Table H.3: *Complex Index of Refraction Used with Mie Scattering Code*

wavenumber (cm^{-1})	real part of complex index of refraction	imaginary part of complex index of refraction
578.82	1.93641	0
582.68	1.91078	0
586.54	1.90439	0
590.4	1.93802	0
594.26	1.94902	0
598.12	1.95947	0
601.98	1.95329	0
605.33	1.94902	0
609.69	1.93139	0
617.41	1.91844	0
621.27	1.90588	0
625.13	1.89164	0
628.99	1.90716	0
632.85	1.90051	0
636.7	1.86816	0
640.56	1.88265	0
648.28	1.86097	0
656	1.87569	0
659.86	1.88252	0
663.72	1.86402	0
667.58	1.81643	0
671.43	1.80985	0
675.29	1.81807	0
679.15	1.78334	0
683.01	1.79948	0
686.87	1.82466	0

Table H.3: *Complex Index of Refraction Used with Mie Scattering Code*

wavenumber (cm^{-1})	real part of complex index of refraction	imaginary part of complex index of refraction
694.59	1.78425	0
698.45	1.7701	0
702.3	1.77624	0
706.16	1.7851	0
710.02	1.77507	0
713.88	1.73992	0.00805
725.46	1.72575	0.01185
729.32	1.72019	0.01361
733.18	1.73522	0.00771
737.03	1.72595	0.01118
744.75	1.74039	0.01192
748.61	1.73359	0.01784
756.33	1.71434	0.02965
760.19	1.72497	0.03054
764.05	1.74844	0.03004
767.9	1.72472	0.04089
771.76	1.69445	0.0464
775.62	1.70046	0.03659
779.48	1.72154	0.02348
783.34	1.71427	0.02053
787.2	1.70599	0.02007
791.06	1.6935	0.02298
794.92	1.6808	0.0268
818.07	1.69996	0.02786
821.93	1.69157	0.02486
825.79	1.67829	0.02127

Table H.3: *Complex Index of Refraction Used with Mie Scattering Code*

wavenumber (cm^{-1})	real part of complex index of refraction	imaginary part of complex index of refraction
829.65	1.64975	0.02267
833.5	1.63983	0.02158
837.36	1.60686	0.02785
841.22	1.50093	0.05231
845.08	1.42405	0.05895
848.94	1.51136	0.04717
852.8	1.56034	0.03514
856.66	1.5443	0.03956
864.38	1.58182	0.03207
868.23	1.59613	0.02888
872.09	1.58514	0.03072
875.95	1.59775	0.02666
883.67	1.63264	0.01492
891.39	1.58037	0.02052
895.25	1.59269	0.01478
902.86	1.60151	0.00956
906.82	1.62661	0.00505
910.68	1.61561	0.00867
914.54	1.60473	0.013
918.4	1.62521	0.01217
922.26	1.65087	0.01047
926.12	1.62703	0.01551
929.98	1.59765	0.02366
945.41	1.62627	0.01934
953.13	1.61423	0.02125
960.85	1.60457	0.02241

Table H.3: *Complex Index of Refraction Used with Mie Scattering Code*

wavenumber (cm^{-1})	real part of complex index of refraction	imaginary part of complex index of refraction
964.7	1.59726	0.02304
968.56	1.63151	0.01785
972.42	1.64889	0.01614
976.28	1.63011	0.01958
980.14	1.66067	0.01749
984	1.65047	0.02175
987.86	1.63351	0.02874
991.72	1.66128	0.03372
995.67	1.65232	0.04571
999.43	1.65743	0.05509
1011.01	1.67839	0.05076
1014.87	1.69155	0.05144
1018.73	1.70226	0.05409
1022.69	1.69329	0.05662
1030.3	1.7137	0.06362
1034.16	1.70265	0.07872
1038.02	1.69462	0.08559
1041.88	1.69341	0.09661
1045.74	1.68143	0.10785
1049.6	1.66515	0.11815
1053.46	1.65817	0.12794
1057.32	1.67585	0.13754
1061.17	1.6813	0.14856
1065.03	1.63125	0.16264
1068.89	1.6237	0.17391
1072.75	1.59901	0.18476

Table H.3: *Complex Index of Refraction Used with Mie Scattering Code*

wavenumber (cm^{-1})	real part of complex index of refraction	imaginary part of complex index of refraction
1076.61	1.52877	0.19757
1080.47	1.50433	0.20539
1084.33	1.51088	0.20789
1088.19	1.5257	0.20744
1092.05	1.51264	0.20858
1095.9	1.49723	0.20957
1099.76	1.51362	0.20615
1119.06	1.45564	0.18509
1122.92	1.43918	0.17864
1126.77	1.43047	0.16874
1130.63	1.43367	0.13529
1134.49	1.48599	0.13961
1138.35	1.52051	0.12407
1142.21	1.5172	0.11288
1146.07	1.50649	0.10458
1149.93	1.52816	0.09852
1153.79	1.57988	0.09358
1157.65	1.5886	0.09147
1161.5	1.5587	0.09015
1169.22	1.54416	0.08192
1173.08	1.51635	0.08048
1176.94	1.56441	0.08053
1180.8	1.57377	0.08849
1184.66	1.51666	0.10341
1188.52	1.52149	0.11419
1192.37	1.53373	0.1183

Table H.3: *Complex Index of Refraction Used with Mie Scattering Code*

wavenumber (cm^{-1})	real part of complex index of refraction	imaginary part of complex index of refraction
1196.23	1.51809	0.12324
1200.09	1.56961	0.1347
1203.85	1.62348	0.14282
1207.81	1.66827	0.15669
1211.67	1.6406	0.17789
1215.53	1.66095	0.20745
1219.89	2.07625	0.22251
1223.25	1.33615	0.26736
1227.1	1.43521	0.31277
1230.86	1.35229	0.32176
1234.82	1.30894	0.31168
1238.68	1.35172	0.23442
1238.68	1.35172	0.23442
1242.64	1.34796	0.2588
1246.4	1.38333	0.21378
1250.26	1.41109	0.1874
1254.12	1.42089	0.16358
1257.97	1.41026	0.14825
1261.83	1.41939	0.1375
1265.69	1.42777	0.12956
1269.55	1.41468	0.12481
1273.41	1.4258	0.12056
1281.13	1.43122	0.11565
1284.99	1.46248	0.1098
1288.85	1.47566	0.1049
1292.7	1.49512	0.10085

Table H.3: *Complex Index of Refraction Used with Mie Scattering Code*

wavenumber (cm^{-1})	real part of complex index of refraction	imaginary part of complex index of refraction
1296.56	1.51975	0.09768
1304.28	1.51044	0.09255
1306.14	1.49196	0.09215
1312	1.48427	0.09171
1319.72	1.46429	0.09128
1323.57	1.43816	0.08985
1331.29	1.4534	0.07721
1335.15	1.46315	0.06936
1339.01	1.47059	0.06314
1342.87	1.48874	0.05926
1362.16	1.50911	0.06211
1366.02	1.51809	0.0656
1369.98	1.52693	0.07183
1373.74	1.51352	0.08096
1377.6	1.4996	0.08766
1381.46	1.50911	0.08698
1385.82	1.5208	0.08219
1389.17	1.53701	0.07712
1393.03	1.55187	0.07471
1416.19	1.54133	0.10472
1420.04	1.53877	0.09708
1423.9	1.51731	0.08951
1427.76	1.51096	0.0855
1431.62	1.53715	0.08843
1435.48	1.55095	0.08664
1439.34	1.54331	0.09481

Table H.3: *Complex Index of Refraction Used with Mie Scattering Code*

wavenumber (cm^{-1})	real part of complex index of refraction	imaginary part of complex index of refraction
1443.2	1.54353	0.10521
1447.06	1.53963	0.11721
1450.92	1.5324	0.12375
1454.77	1.52735	0.12394
1458.63	1.53802	0.11622
1462.49	1.53291	0.10986
1466.35	1.54637	0.10471
1470.21	1.55265	0.10493
1477.93	1.56765	0.10838
1485.54	1.59486	0.10341
1489.3	1.62221	0.10536
1493.36	1.60512	0.11141
1497.22	1.60329	0.11954
1501.08	1.6205	0.1324
1504.94	1.6387	0.14195
1508.3	1.53854	0.15078
1512.56	1.63165	0.17624
1516.52	1.6099	0.1881
1520.37	1.51459	0.19798
1524.23	1.55295	0.21212
1528.09	1.49581	0.23015
1531.95	1.44303	0.24489
1535.81	1.41922	0.25181
1539.67	1.41508	0.24645
1543.53	1.40943	0.23358
1547.39	1.39777	0.21233

Table H.3: *Complex Index of Refraction Used with Mie Scattering Code*

wavenumber (cm^{-1})	real part of complex index of refraction	imaginary part of complex index of refraction
1551.24	1.40521	0.18799
1555.1	1.42095	0.15213
1558.96	1.44062	0.13314
1562.82	1.45342	0.10359
1566.68	1.45255	0.09953
1570.54	1.67633	0.07569
1574.4	1.48237	0.06929
1578.26	1.49353	0.05872
1582.12	1.51778	0.07294
1585.97	1.51499	0.08373
1589.83	1.49692	0.09883
1593.69	1.46335	0.11442
1597.55	1.46993	0.12341
1601.41	1.47582	0.13434
1605.27	1.4586	0.13533
1609.13	1.47442	0.1297
1612.99	1.49797	0.11226
1616.84	1.49795	0.10801
1620.7	1.48437	0.09681
1624.56	1.49213	0.08359
1628.42	1.50512	0.07953
1632.28	1.52182	0.0636
1651.57	1.53215	0.06715
1655.43	1.55645	0.06915
1663.15	1.54921	0.07696
1667.01	1.56784	0.07927

Table H.3: *Complex Index of Refraction Used with Mie Scattering Code*

wavenumber (cm^{-1})	real part of complex index of refraction	imaginary part of complex index of refraction
1670.87	1.57414	0.08473
1697.86	1.55191	0.14737
1701.74	1.55602	0.15973
1705.6	1.54482	0.16937
1709.46	1.53514	0.17397
1713.32	1.5291	0.17402
1717.17	1.53994	0.16981
1728.75	1.50813	0.15564
1732.61	1.50667	0.18962
1736.47	1.48254	0.11362
1740.33	1.46357	0.08951
1744.19	1.49472	0.05699
1748.94	1.50166	0.04797
1751.9	1.51497	0.08451
1755.76	1.52897	0.02671
1763.48	1.52603	0.02094
1767.84	1.5334	0.01893
1821.36	1.52702	0.01592
1832.94	1.5239	0.01622
1844.61	1.51594	0.01562
1867.61	1.51974	0.01672
1886.96	1.54934	0.01384
1902.4	1.55158	0.01829
1925.55	1.54945	0.01349
1960.28	1.53151	0.01599
1979.57	1.55243	0.01125

Table H.3: *Complex Index of Refraction Used with Mie Scattering Code*

wavenumber (cm^{-1})	real part of complex index of refraction	imaginary part of complex index of refraction
1998.87	1.52162	0.0156
2014.3	1.54424	0.01225
2056.75	1.57077	0.00678
2072.19	1.54727	0.00994
2095.34	1.49604	0.0157
2130.07	1.55793	0.00586
2160.94	1.52215	0.00903
2180.23	1.55558	0.00306
2199.53	1.54794	0.00293
2207.24	1.51818	0.00695
2222.68	1.565	0
2272.84	1.53587	0.00109
2280.56	1.55692	0
2303.71	1.51194	0.00229
2323.01	1.56093	0
2353.88	1.53527	0
2404.04	1.51852	0
2423.34	1.4871	0
2431.06	1.53181	0
2454.21	1.56532	0
2477.36	1.55485	0
2496.66	1.54899	0
2531.38	1.57655	0
2546.82	1.55772	0
2569.97	1.57044	0
2608.56	1.56373	0

Table H.3: *Complex Index of Refraction Used with Mie Scattering Code*

wavenumber (cm^{-1})	real part of complex index of refraction	imaginary part of complex index of refraction
2647.15	1.53144	0
2701.17	1.54451	0
2712.75	1.55069	0
2743.52	1.52494	0
2770.53	1.55853	0
2793.78	1.52915	0
2835.23	1.54583	0.00585
2847.81	1.50881	0.01452
2867.1	1.52666	0.02938
2882.64	1.49304	0.02867
2913.41	1.47461	0.02769
2932.7	1.47905	0.03144
2955.85	1.48335	0.02557
2990.58	1.52419	0.02391

Table H.3: *Complex Index of Refraction Used with Mie Scattering Code*